Universität
Augsburg
University

Dissertation

zum Erlangen des akademischen Grades
Dr. rer. nat.

Optical and dispersion forces experienced by spherical objects

eingereicht an der
Mathematisch-Naturwisschenschaftlich-Technischen Fakultät
der Universität Augsburg

von

Tanja Schoger

Augsburg, 05. April 2024

Erstgutachter: Prof. Dr. Gert-Ludwig Ingold
Zweitgutachter: Prof. Dr. Abhinav Sharma
Drittgutachter: Prof. Felipe Siqueira de Souza da Rosa, Ph.D.

Tag der mündlichen Prüfung: 09. Juli 2024

Zusammenfassung

In dieser Arbeit untersuchen wir optische Kräfte und Dispersionskräfte, die auf kugelförmige Objekte wirken. Speziell betrachten wir die Dispersionswechselwirkung zwischen makroskopischen Körpern, die auch Casimir-Kraft genannt wird.

Befindet sich ein Objekt in einem Lichtfeld, so wirkt eine Kraft auf dieses. Bereits Kepler erkannte bei der Beobachtung der Schweife von Kometen, dass der Lichtdruck, der durch die Sonne entsteht, eine Krümmung des Schweifs verursacht. Diese Eigenschaft von Licht wird beispielsweise beim Einfangen und der Manipulation von Objekten in sogenannten optischen Pinzetten eingesetzt. Ursprünglich umfassten optische Pinzetten einen fokussierten Laserstrahl mit einem gaußförmigen Intensitätsprofil. Objekte können dann in der Nähe des Fokus, dem Punkt höchster Intensität, eingefangen werden. Seither entwickelten sich jedoch viele neue Realisierungen, dieses ursprünglich von Ashkin [1] eingeführten Aufbaus. Insbesondere strukturierte Lichtfelder, wie zum Beispiel Wirbelfelder, haben in den letzten Jahren steigendes Interesse erfahren. Bei Fokussierung von Wirbelfeldern entsteht ein ringförmiges Intensitätsprofil und Objekte können zusätzlich einen Bahndrehimpuls erfahren [2]. Im Rahmen dieser Arbeit betrachten wir einerseits die Eigenschaften dieser Wirbelfelder und andererseits die Möglichkeiten, diese zur Charakterisierung der eingefangenen Objekte zu nutzen. Speziell betrachten wir die Wechselwirkung von kugelförmigen Objekten mit dem Lichtfeld. Optische Pinzetten haben vielseitige Einsatzgebiete und eines davon ist als Kraftsensor mit einer Genauigkeit, die in den Femtonewtonbereich geht. Dadurch sind optische Pinzetten auch geeignet, Dispersionskräfte zwischen makroskopischen Objekten zu messen [3, 4].

Dispersionskräfte treten als dominante Kraft zwischen neutralen, nicht-polarisierten Objekten auf, auch wenn keine externen Felder vorhanden sind. Ihr Ursprung liegt in den Fluktuationen des quantisierten elektromagnetischen Feldes. Als Erstes wurde diese Kraft, bei Temperatur Null, zwischen zwei perfekt-leitenden Platten von Casimir [5] berechnet. Eine einfache Erklärung für die anziehende Kraft zwischen den Platten erfolgt beispielsweise mit dem oben angesprochenen Strahlendruck. Aufgrund der Randbedingungen sind zwischen den Platten nicht alle elektromagnetischen Feldmoden realisierbar, wodurch der Strahlendruck zwischen den Platten geringer ist als der von außen, was schließlich zu einer anziehenden Kraft führt. Bei endlichen Temperaturen tragen aber nicht nur die Quantenfluktuationen zu der Kraft bei, sondern auch thermische Fluktuationen, die im Limes hoher Temperaturen den dominanten Beitrag liefern und damit den Effekt zu einem rein klassischen Effekt machen [6]. Wir untersuchen diesen Hochtemperaturbereich der Casimir-Kraft für verschiedene Modellsysteme und zeigen auf, dass die Casimir-Wechselwirkung auch in biologischen Systemen zu relevanten, langreichweitigen Kräften führt. Die Casimir-Kraft wird hauptsächlich mit einer anziehenden Kraft in Verbindung gesetzt; in speziellen Fällen kann die Kraft allerdings auch repulsiv sein. Eine repulsive Casimir-Kraft wird beispielsweise zwischen nicht reziproken Materialien, also Materialien, in denen die Zeitumkehr-Symmetrie gebrochen ist, ermöglicht [7]. Wir untersuchen die Casimir-Kraft anhand eines idealisierten, nicht-reziproken Modellsystems von perfekten elektromagnetischen Leitern [8]. Wir zeigen auf, wie geometrische und thermische Effekte das Vorzeichen der Casimir-Kraft beeinflussen können. Als Modellsystem für die Casimir-Wechselwirkung betrachten wir, wie auch für die optische Pinzette, kugelförmige Objekte. Kugelförmige Objekte sind speziell für experimentelle Realisierungen der Casimir-Kraft relevant. Im Gegensatz zu der Platte-Platte-Geometrie, treten für Kugeln keine Probleme bei der parallelen Ausrichtung auf, weshalb diese häufig in Experimenten Anwendung finden [9, 10].

Contents

Introduction and Outline

Electromagnetic fields have the ability to transfer momentum, which means they can exert a force on an object. Even if there is no external source field $\langle E_i \rangle = 0$, forces between neutral, unpolarised and unmagnetised objects can still emerge due to fluctuations of the quantum electromagnetic vacuum $\langle E_i E_j \rangle \neq 0$. The forces are called dispersion forces. Dispersion forces between microscopic objects (like atom-atom interaction) are usually referred to as London-van-der-Waals interaction [11], which are mostly considered in the non-retarded regime. If one macroscopic object is present, like in an atom wall setup, we refer to the force as Casimir-Polder interaction [12]. Dispersion forces between macroscopic objects are usually called Casimir or Casimir-Lifshitz forces. Casimir computed in his seminal work [5] the force between perfect electric conductor plates arising from the vacuum fluctuations. Later, Lifshitz [13, 14] extended the calculation to materials which account for losses. The nomenclature for the dispersion forces in the different regimes might vary across communities; for an overview, see the recent review by Fiedler *et al.* [15]. In this work, we will focus on the latter, the interaction between macroscopic objects induced by quantum and also thermal fluctuations of the quantum electromagnetic field.

Since its original proposal by Casimir, it has taken several decades for the first reliable observation of the effect. Earlier experiments (see e. g. Ref. [16]) tried to probe the Casimir interaction between planar surfaces. However, it was only much later that accurate measurements of the Casimir interaction became possible [9, 17, 18]. In the earlier experiments, the perfect parallel alignment between plates presented a challenge, which was circumvented by using a setup consisting of a metallic spherical object and plate. Since then, rapid progress has been made to probe the Casimir interaction for various systems, including two-sphere setups in Refs. [19] and [3, 4], where the latter probed the Casimir interaction by using optical tweezers (see Fig. 2). For readers interested in recent developments, we refer to Ref. [20]. Due to its experimental relevance, we study the Casimir interaction between spherical objects in this work, as schematically illustrated in Fig. 1.

Considerable progress has been made on both the experimental and theoretical sides. Numerous theoretical methods aim to calculate the Casimir interaction for various experimental setups. On the forefront is the so-called scattering approach [21–23]. In this approach, the force resulting from the fluctuations of the quantum electromagnetic field is reduced to a classical scattering problem based on the T-matrix of the system. This method, in principle, allows for the calculation of the Casimir force between arbitrarily shaped geometries and various materials.

Nevertheless, exact analytical results for the Casimir force are still rare and usually limited to specific geometries and idealized materials. The high-temperature limit is one regime, where the main contribution to the Casimir force comes from thermal fluctuations. For the experimentally relevant systems of a metallic sphere and plate described by the Drude model, Bimonte and Emig [24] were able to determine an exact expression for the Casimir free energy. Later, Zhao *et al.* [25] found an analytical expression for two equally-sized spheres. However, it was doubted whether similar calculations could be extended to two spheres of dissimilar size [26]. This work aims to demonstrate that the scattering approach can be used to determine an analytical expression for the two-sphere setup.

The thermal Casimir effect also plays a role in systems involving dielectric objects in an electrolytic solution, which are usually not associated with Casimir interactions. This type of setup is commonly found in colloidal and biophysical science, such as interacting lipid layers or filaments. The Casimir

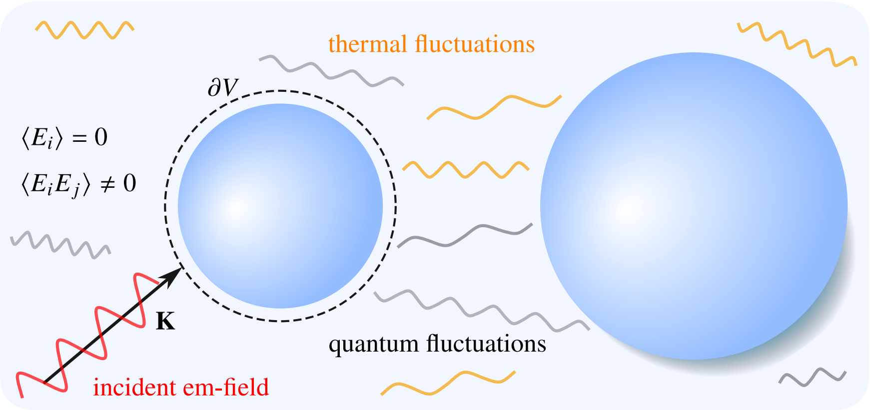

Figure 1: The electromagnetic field can transfer momentum while interacting with an object. The momentum flow can originate from an incident external light field, illustrated by the incident wave with wave vector **K**. However, if a second object is placed in close proximity, the quantum vacuum fluctuations and thermal fluctuations $\langle E_i E_j \rangle$ of the electromagnetic field can also cause a momentum transfer to both objects, resulting in an attractive or repulsive force.

interaction has potential relevance for self-assembly and cohesion in such systems [27, 28]. Until recently, it was assumed that long-range interactions due to low-frequency fluctuations are completely screened in these scenarios. However, it was shown in Ref. [27] and experimentally verified in Ref. [4] that low-frequency transverse magnetic modes are not screened, as it was considered up to that point [29]. Therefore, we are interested in computing the Casimir interaction from the low-frequency fluctuations between dielectric spherical objects in an electrolyte. We aim to find a simple expression that allows calculating the Casimir contribution in these systems without relying on extensive numerical calculations.

Computing the T-matrix for arbitrary-shaped systems is highly non-trivial, which is why approximation methods are usually applied when dealing with more complicated geometries than plates or spheres. Methods which are commonly used are the pairwise summation (PWS) approximation [30] and the proximity force approximation (PFA) [14], to name two. Within the PWS approximation, the Casimir force is evaluated by summing over van-der-Waals interactions between volume elements of the respective objects. Conversely, PFA approximates the surfaces by infinitesimal planar elements and the interaction between these planes is calculated via the Lifshitz formula [14]. However, due to the non-additivity of dispersion forces, both approximations are limited in their applicability [31, 32]. Studies of the Casimir interaction between dielectric spherical objects revealed that the PFA result is obtained from an asymptotic approximation of the scattering formula for large sphere radii [33]. Subsequently, leading corrections to PFA were determined, which helped to estimate the validity of the PFA [34, 35]. There is no polarisation mixing upon scattering in the PFA regime for dielectric objects, the two polarisation channels of the electromagnetic field thus contributed independently to the Casimir force. In this work, we study materials that mix polarisation upon scattering. We aim to analyse whether the PFA result could still be obtained from an asymptotic expansion of the scattering formula and whether we find corrections to the PFA result. We use bi-isotropic materials as a model, which allows for an exact calculation of the scattering at spherical objects.

Polarization-mixing materials have received more attention in recent years [36, 37] since they might lead to a reduction of the attractive Casimir force or even a repulsive force. The Casimir interaction becomes the dominant force between neutral objects on nano-length scales. Hence,

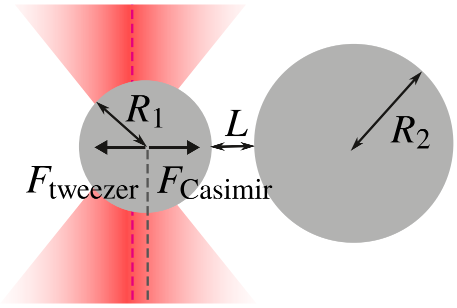

Figure 2: Illustration of the experimental setup in Refs. [4, 58] with two spheres of radii R_1 and R_2 in distance L, where one sphere is trapped by an optical tweezer. The Casimir force F_{Casimir} leads to a displacement of the trapped sphere, which in turn results in a restoring force from the tweezer F_{tweezer}. The Casimir force can be determined from the displacement of the trapped sphere from its axial equilibrium position.

an attractive Casimir force can influence the functionality of micro- and nano-electromechanical systems. To avoid phenomena like stiction [38], which is the adhesion of surfaces by dispersion forces, it would be advantageous to be able to control the strength or even the sign of the Casimir force. Unfortunately, a no-go theorem stated that the Casimir interaction between a mirror-symmetric setup is always attractive [39]. Later, it was found that reciprocal objects in a vacuum always attract each other [40]. Nevertheless, Casimir repulsion can be achieved for objects in a medium. Dielectric objects of relative permittivity ϵ_1 and ϵ_2, which are immersed in a liquid of permittivity ϵ_3 can repel each other if the permittivities fulfil $\epsilon_1(\mathrm{i}\xi) > \epsilon_3(\mathrm{i}\xi) > \epsilon_2(\mathrm{i}\xi)$ at imaginary frequencies ξ [14]. The first experimental realization was carried out by Munday *et al.* [10] and various theoretical studies [41, 42] examined the effect of geometry and temperature on the sign of Casimir interaction in these setups.

It is also possible to achieve Casimir repulsion without a mediating medium by combining magnetic and non-magnetic objects. This was already observed by Boyer in 1974 [43], who studied the Casimir interaction between a perfect electric and magnetic conductor plate at zero temperature. Since then, Casimir repulsion was examined between various systems involving meta-materials [44–46], topological insulators [47–52], Weyl semi-metals [53, 54] or magneto-electric materials [55–57]. Recently, it was also shown more generally that non-reciprocal materials, which break time-reversal symmetry, might lead to a repulsive Casimir force [7].

The studies [41, 42] of objects in a medium have shown that the sign of the Casimir force can change with distance, leading to equilibrium configurations. Furthermore, it was revealed that the equilibrium distance changes with temperature. In this work, we want to extend this study to polarisation-mixing material in vacuum for the experimentally relevant setup of spherical objects.

Earlier, we mentioned that recent Casimir experiments have used optical tweezers to probe the Casimir interaction between spheres [4, 58]. The high sensitivity of optical tweezers (in the femtonewton range) allowed the measurement of the Casimir force at much larger distances than in previous experiments. Usually the aspect ratio of sphere radius and distance L lies between 100 and 5000 [59], for the above-mentioned optical tweezers experiment, the Casimir interaction was probed for ratios below 10.

In fact, optical tweezers have many uses beyond measuring forces. They can, for example, also be used to manipulate and characterize trapped objects [60]. Since the original proposal by Ashkin in 1979 [1, 61], a wide range of applications of optical tweezers has emerged [62]. The original setup [61] involves a strongly focused laser beam with a high numerical aperture and an axial intensity profile. This setup allows for trapping close to the focal spot with a single beam. In recent years, there has been progress and increasing interest in using structured light fields (see e.g. Refs. [63–65] for review), where the amplitude, phase or polarisation of the beam is modulated. Examples of such fields are vortex beams, in which the photons carry orbital angular momentum in addition to the spin angular momentum associated with the polarisation. The focusing of such beams leads to a ring-shaped focal spot [66, 67] and thus to a different trapping behaviour compared to the earlier-mentioned single focal spot. We are interested in the trapping behaviour of spherical objects in a vortex beam. The additional orbital angular momentum can enhance the torque exerted on the trapped object [68]. This torque is dependent on the characteristics of the trapped object (see e. g. [69]), and we aim to investigate how this dependence can be utilized to measure different quantities of the trapped particle.

In summary, we investigate dispersion and optical forces on spherical objects and how temperature and material properties of the sphere affect these forces. Both forces share the same problem of solving the scattering of an electromagnetic field by a spherical object. However, the main difference is that optical forces typically operate in a specific frequency range, depending on the application. In contrast, when considering dispersion forces, fluctuations of the electromagnetic field at all frequencies and wave vectors must be taken into account (schematically depicted in Fig. 1 by the different wavelengths of the fluctuations). This broadband character of the Casimir effect makes it inherently more complex.

This work is divided into three main parts. We start in Part I by recalling the basics of classical electrodynamics in media and the extension to quantum electromagnetic fields. In Chap. 1, we introduce a specific class of media, called bi-isotropic materials [70], which allows for cross-susceptibilities and thus for polarisation-mixing upon scattering of electromagnetic waves. Bi-isotropic materials can model chiral and also non-reciprocal systems. Optical and dispersion forces on an arbitrary-shaped body can be computed through a volume integral over the electromagnetic force density (Chap. 2). Dispersion forces arise from the quantum field fluctuations between at least two objects and the fluctuation-dissipation theorem relates the fluctuations to the T-matrix of the system. We use the Lippmann-Schwinger equation to determine the T-matrix and arrive at the famous scattering formula for the Casimir interaction between macroscopic objects. The scattering formula constitutes the basis of this work, which we use to derive the Casimir force. Alternatively, forces induced by electromagnetic fields can also be computed from a surface integral over electromagnetic stresses. The surface is chosen such that it surrounds the object (see Fig. 1), and the change of the momentum flux through this surface is considered. We will use this approach as a starting point for the calculation of the optical force on a spherical object in a structured light field. Solutions for the Maxwell equations are presented in Chap. 3. In Chap. 4, we introduce the reflection matrix elements of a bi-isotropic sphere for an incoming spherical or plane wave. The expressions are derived for imaginary frequencies and analysed in several limiting cases.

Part II deals with optical forces experienced by illuminated spherical objects. Specifically, we provide the force expressions for dielectric and chiral objects in a focused Laguerre-Gaussian beam. We start in Chap. 5 by modelling the structured light field based on the Debye-Wolf diffraction integral, which results in an angular spectrum representation of the field at the exit of the focusing system. To account for optical aberrations present in most experimental setups, we employ the method of vectorial ray tracing. We apply our theory in Chap. 6, where we analyse the trapping of dielectric and chiral particles in a vortex field. We conclude Part II by introducing a method that utilizes vortex beams to measure the size of trapped dielectric beads (see Chap. 7).

Part III of this work deals with the Casimir interaction between two spherical objects. First, we recall the scattering approach for our specific geometry in Chap. 8. We examine the Casimir interaction for high temperatures in Chap. 9. The studied systems are metallic spheres in vacuum and dielectric spheres in an electrolytic solution. In the following Chap. 10, we discuss the Casimir interaction between two dissimilar bi-isotropic spheres. We analyse the Casimir interaction in the experimentally relevant regime of short distances or equivalently large sphere radii. We show that the leading asymptotic expansion agrees with the PFA result for polarisation-mixing materials. Additionally, general expressions for the leading PFA corrections are derived. To analyse the dependence of the sign of the Casimir force with distance, we also compute expressions for the Casimir free energy in the dipole-dipole or dipole-plane limit. Chapter 11 uses the results for small and large distances to study the Casimir interaction between an idealized class of non-reciprocal materials, namely so-called perfect electromagnetic conductors.

We summarize our results from the discussion of the optical tweezers setup and Casimir calculation in Chap. 12. Further details and technical calculations for the main body of this work can be found in the appendices.

Part I

Spherical particles in the presence of the electromagnetic field and its fluctuations

This thesis connects the behaviour of macroscopic objects for classical and quantum electromagnetic fields by examining both optical and dispersion forces on spheres. Both cases have in common that we need to solve the scattering problem at a spherical object. Hence, the first Part of the thesis introduces various theoretical concepts needed to discuss the optical and dispersion forces. We start in Chap. 1 by formulating the macroscopic electromagnetic field equations for bi-isotropic media. Chap. 2 evaluates the force on an object in an electromagnetic field. We discuss how the scattering formula for the Casimir interaction can be obtained from the Lorentz force. This method constitutes one of many ways of deriving the scattering formula. An alternative would be to examine the Maxwell stress tensor, which we will discuss in the context of optical forces. To solve the scattering problem of a spherical object, it is practical to expand the electromagnetic field in an orthonormal basis set. This is done in Chap. 3. We present the solutions for the scattering coefficient of a bi-isotropic sphere in an isotropic medium in Chap. 4 and analyse the results in the limit of large sphere radii and low frequencies.

1 | Electromagnetic field in a bi-isotropic medium

A classical electromagnetic field is described by the Maxwell equations [71]. For a quantized field, this still holds for a linear system, however, the electric field $\hat{\mathbf{E}}$, the magnetic induction $\hat{\mathbf{B}}$, the electric displacement $\hat{\mathbf{D}}$ and the magnetic field $\hat{\mathbf{H}}$ all become Hermitian operators [72, 73]. We consider systems without any excess charges, which means that both the displacement field and the magnetic induction field are divergence-free

$$\nabla_{\mathrm{r}} \cdot \hat{\mathbf{D}}(\mathbf{r}, t) = 0\,, \qquad \nabla_{\mathrm{r}} \cdot \hat{\mathbf{B}}(\mathbf{r}, t) = 0\,. \tag{1.1}$$

The fields are all functions of space $\mathbf{r}$ and time t. Moreover, we are mostly interested in systems with no free currents, which means that the curl equations are according to Maxwell given by

$$\nabla_{\mathrm{r}} \times \hat{\mathbf{E}}(\mathbf{r}, t) = -\partial_t \hat{\mathbf{B}}(\mathbf{r}, t)\,, \qquad \nabla_{\mathrm{r}} \times \hat{\mathbf{H}}(\mathbf{r}, t) = \partial_t \hat{\mathbf{D}}(\mathbf{r}, t)\,. \tag{1.2}$$

The equations above are defined in the time domain. Since we consider time harmonic excitation, it is more convenient to work with the equations in the frequency domain. The relation between the electric field in the time and frequency domain is, for example, given by

$$\hat{\mathbf{E}}(\mathbf{r}, t) = \int_0^\infty \frac{\mathrm{d}\omega}{2\pi} \left[\hat{\mathbf{E}}(\mathbf{r}, \omega)\mathrm{e}^{-\mathrm{i}\omega t} + \mathrm{h.c.}\right]\,, \tag{1.3}$$

where we denote the Fourier transform $\hat{\mathbf{E}}(\mathbf{r}, \omega)$ of $\hat{\mathbf{E}}(\mathbf{r}, t)$ just by the arguments. The same definition also holds for all other vector fields. If not stated otherwise, all fields are, from now on, considered in the frequency domain. Generally, the electric displacement and the magnetic field are respectively related to the electric field and the magnetic induction through the following equations

$$\hat{\mathbf{D}} = \epsilon_0 \hat{\mathbf{E}} + \hat{\mathbf{P}}\,, \qquad \hat{\mathbf{H}} = \hat{\mathbf{B}}/\mu_0 - \hat{\mathbf{M}}\,, \tag{1.4}$$

where ϵ_0 and μ_0 define the vacuum permittivity and permeability, respectively. $\hat{\mathbf{P}}$ and $\hat{\mathbf{M}}$ define the polarisation and magnetization, which account for the bound charge density $\hat{\rho} = -\nabla_r \cdot \hat{\mathbf{P}}$ and current density $\hat{\mathbf{j}} = -\mathrm{i}\omega\hat{\mathbf{P}} + \nabla_{\mathrm{r}} \times \hat{\mathbf{M}}$ in the medium. We consider a local and bi-isotropic medium [74] in the following, where both the polarisation and the magnetization show a linear response to the electric and magnetic field according to [75, 76]

$$\hat{\mathbf{P}} = \epsilon_0 \left(\epsilon - 1 - \alpha\beta\mu^{-1}\right) \hat{\mathbf{E}} + Z_0^{-1}\alpha\mu^{-1}\hat{\mathbf{B}}\,, \qquad \hat{\mathbf{M}} = Z_0^{-1}\beta\mu^{-1}\hat{\mathbf{E}} + \mu_0 \left(1 - \mu^{-1}\right) \hat{\mathbf{B}} \tag{1.5}$$

with the vacuum impedance $Z_0 = \sqrt{\mu_0/\epsilon_0}$. The parameters $\epsilon = \epsilon(\omega)$ and $\mu = \mu(\omega)$ respectively define the relative permittivity and permeability of the material. The cross-components $\alpha = \alpha(\omega)$ and $\beta = \beta(\omega)$ describe the electro-to-magnetic and magneto-to-electro coupling. The cross-couplings are zero in the limiting case of isotropic materials. Materials with a chiro-optical response can also be modeled by the above-given equations by considering the limit $\alpha = -\beta = -\mathrm{i}\kappa$, where κ is the so-called chirality parameter. These materials are reciprocal since $\alpha = -\beta$. Bi-isotropic materials, however, also include media which do not fulfil Onsager's reciprocity relation [77]. These kinds of systems are of interest in Casimir physics since they may lead to a repulsive Casimir interaction [7, 52]. An idealized system of non-reciprocal materials is a perfect electromagnetic conductor (PEMC) which interpolates between a perfect electric conductor (PEC) ($\epsilon \longrightarrow \infty$) and a perfect magnetic conductor (PMC) ($\mu \longrightarrow \infty$). By choosing the material parameters as [8, 78]

$$\alpha = \beta = q\,, \qquad \epsilon = q\cot(\theta)\,, \qquad \mu = q\tan(\theta) \tag{1.6}$$

with $q \longrightarrow \infty$ one obtains a PEMC, parameterized by the angle θ taking values between 0 and $\pi/2$ respectively accounting for the limiting cases of a PEC and a PMC. By inserting the relations (1.5) for the polarisation and magnetisation into Eq. (1.4), one obtains the following constitutive equations for the vector fields [70]

$$\begin{pmatrix} \hat{\mathbf{D}} \\ \hat{\mathbf{B}} \end{pmatrix} = \begin{pmatrix} \epsilon_0\epsilon & \alpha/c \\ \beta/c & \mu_0\mu \end{pmatrix} \begin{pmatrix} \hat{\mathbf{E}} \\ \hat{\mathbf{H}} \end{pmatrix}, \tag{1.7}$$

where $c = 1/\sqrt{\epsilon_0\mu_0}$ defines the speed of light in vacuum. Without any cross-couplings ($\alpha = 0 = \beta$), so for a linear isotropic medium, the constitutive equations take on the usual form with $\hat{\mathbf{D}} = \epsilon_0\epsilon\hat{\mathbf{E}}$, $\hat{\mathbf{B}} = \mu_0\mu\hat{\mathbf{H}}$. The Maxwell equations (1.2) thus yield

$$\nabla_\mathrm{r} \times \begin{pmatrix} \hat{\mathbf{E}} \\ \hat{\mathbf{H}} \end{pmatrix} = \mathrm{i}\omega \begin{pmatrix} \beta/c & \mu_0\mu \\ -\epsilon_0\epsilon & -\alpha/c \end{pmatrix} \begin{pmatrix} \hat{\mathbf{E}} \\ \hat{\mathbf{H}} \end{pmatrix}. \tag{1.8}$$

We switch to a basis where the material matrix in the equation above is diagonal by performing the following linear transformation [79, 80]

$$\begin{pmatrix} \hat{\mathbf{E}} \\ \hat{\mathbf{H}} \end{pmatrix} = \begin{pmatrix} 1 & a_\mathrm{R} \\ a_\mathrm{L} & 1 \end{pmatrix} \begin{pmatrix} \hat{\mathbf{Q}}_\mathrm{L} \\ \hat{\mathbf{Q}}_\mathrm{R} \end{pmatrix}, \qquad a_\mathrm{L} = \frac{n_\mathrm{L} - \mathrm{i}\beta}{\mathrm{i}c\mu}\,, \quad a_\mathrm{R} = \frac{n_\mathrm{R} - \mathrm{i}\alpha}{\mathrm{i}c\epsilon}\,, \tag{1.9}$$

where the indices denote left (L) and right (R) polarised light. The effective refractive indices for a bi-isotropic medium are defined by

$$n_\mathrm{L,R} = \sqrt{\epsilon\mu - \frac{(\alpha+\beta)^2}{4}} \pm \mathrm{i}\frac{\beta - \alpha}{2}\,, \tag{1.10}$$

where the sign $+(-)$ corresponds to the index L(R). For an isotropic material, we get the well-known expression $n = \sqrt{\epsilon\mu}$ for the refractive index. Each vector field $\hat{\mathbf{Q}}_\mathrm{L,R}$ fulfils the Helmholtz equation

$$\left(\Delta_\mathrm{r} + \frac{\omega^2 n_\mathrm{L,R}^2}{c^2}\right)\hat{\mathbf{Q}}_\mathrm{L,R} = 0 \tag{1.11}$$

with the Laplace operator $\Delta_\mathrm{r} = \nabla_\mathrm{r}^2$. The auxiliary fields are divergence free $\nabla_\mathrm{r} \cdot \hat{\mathbf{Q}}_\mathrm{L,R} = 0$ and the curl of the vector fields fulfil the relation $\nabla_\mathrm{r} \times \mathbf{Q}_\mathrm{L,R} = \pm(\omega n_\mathrm{L,R}/c)\hat{\mathbf{Q}}_\mathrm{L,R}$. The solutions of Eq. (1.11) are thus given by plane waves with wave vectors, which fulfil the dispersion relation

$$|\mathbf{K}_\mathrm{L,R}| = K_\mathrm{L,R} = \frac{\omega n_\mathrm{L,R}}{c}\,. \tag{1.12}$$

Hence, the general electromagnetic field in a bi-isotropic medium is a superposition of waves traveling with wave vector $\mathbf{K}_\mathrm{L}$ and $\mathbf{K}_\mathrm{R}$. In the following, we are thus going to discuss the solutions of the Helmholtz equations only in isotropic medium, the solution for a bi-isotropic follows directly from Eq. (1.9).

2 | Induced forces on objects and the scattering formalism

The Maxwell equations introduced in the previous Chapter describe both classical fields and fluctuations of the vacuum electromagnetic field and the material. Without any external fields, the quantum averages of the fields and sources vanish, e. g. the expectation value of the electric field and the sources in the vacuum ground state yield zero $\langle \hat{\mathbf{E}} \rangle = 0$, $\langle \hat{\rho} \rangle = 0$. The same holds for the magnetic field and the currents. However, both the fields and the body experience fluctuations, e.g. $\langle \hat{\mathbf{E}}^2 \rangle \neq 0$ and $\langle \hat{\rho}^2 \rangle \neq 0$, which are correlated and thus lead to a non-vanishing net force on an object [76]. Casimir first determined in Ref. [5] the force between two perfect electric conductor plates at zero temperature, which arises from these electromagnetic field fluctuations. Due to the imposed boundaries by the plates the vacuum energy density changes, thus leading to an attractive force [81]. Since its original proposal, several approaches have been developed to evaluate the Casimir force on arbitrarily shaped objects, materials which include losses and finite temperature. The theoretical approaches are based on the electromagnetic stress-energy tensor or the quantization of path integrals [22, 23]. We follow in this Chapter the derivation introduced by [82, 83], where the computation of the forces arising from fluctuations reduces to solving the classical scattering problem by means of the fluctuation-dissipation theorem [84].

In this Chapter, we will discuss forces exerted on arbitrarily shaped objects induced by the electromagnetic field and its fluctuations. The objects are in thermal equilibrium with their environment. We will concentrate on magneto-electric bodies in vacuum that do not intersect. The resulting force expressions are also valid for objects immersed in a dispersive dielectric medium [85] or for bi-isotropic materials [7]. We will start in Sec. 2.1 with the Casimir force on an object due to the presence of another object, which we obtain from a volume integral over the electromagnetic force density. From there, the well-known scattering formula to the Casimir interaction can be derived, which accounts for the reverberations of the electromagnetic field between the two objects. The scattering problem is solved by using the so-called Lippmann-Schwinger equation. Equivalent to the volume integral approach, the force on an object in an electromagnetic field can also be computed from a surface integral over the electromagnetic energy-stress tensor, presented in Sec. 2.2, which we will apply to determine the force on an object in an external source field, which is relevant for the optical tweezers analysis in this thesis.

2.1 Volume integral approach

In general, the force on a body is given by the volume integral over the quantum symmetrized average of the electromagnetic force density [76]

$$\mathbf{F} = \int_V \mathrm{d}^3\mathbf{r}\, \langle \hat{\rho}(\mathbf{r},t)\hat{\mathbf{E}}(\mathbf{r},t) + \hat{\mathbf{j}}(\mathbf{r},t) \times \hat{\mathbf{B}}(\mathbf{r},t) \rangle_{\mathrm{sym}} \,, \tag{2.1}$$

where $\hat{\rho}$ and $\hat{\mathbf{j}}$ define the charge and current density within a magneto-electric body of volume V. The symmetrized average of two operators $\hat{A}$ and $\hat{B}$ is given by $\langle \hat{A}\hat{B} \rangle_{\mathrm{sym}} = \frac{1}{2} \langle \hat{A}\hat{B} + \hat{B}\hat{A} \rangle$.

There exist several approaches to evaluate the average of the quantum Lorentz force [76]. We follow the calculation by [82, 86], where it is noticed that in stationary conditions, the correlators above do not depend on time, and can be expressed as

$$\mathbf{F} = \int_V \mathrm{d}^3\mathbf{r} \int_{-\infty}^{\infty} \frac{\mathrm{d}\omega}{2\pi} \langle \rho(\mathbf{r})\mathbf{E}^*(\mathbf{r}) + \mathbf{j}(\mathbf{r}) \times \mathbf{B}^*(\mathbf{r}) \rangle_\omega \,, \tag{2.2}$$

where $\langle \cdot \rangle_\omega$ defines spectral density for frequency ω, since there is no correlations between different frequency components. We assume that the internal charge and current density of the body obey the continuity equation $\nabla_\mathrm{r} \cdot \mathbf{j} = \mathrm{i}\omega\rho$ and we also apply the Maxwell equation (1.2) to replace the magnetic field. We specifically use $[\mathbf{j} \times (\nabla_\mathrm{r} \times \mathbf{E}^*)]_i = j_k \partial_{r_i} E_k - j_k \partial_{r_k} E_i$, where we employ the summation convention, that we sum over indices that appear twice. Furthermore, we assume that there are no surface currents. We can thus omit the surface term and obtain

$$\mathbf{F} = \int_V \mathrm{d}^3\mathbf{r} \int_{-\infty}^{\infty} \frac{\mathrm{d}\omega}{2\pi} \frac{1}{\mathrm{i}\omega} \hat{\mathbf{e}}_i \left\langle j_k \left(\partial_{r_i} E_k^*\right) \right\rangle_\omega \,, \tag{2.3}$$

where $\hat{\mathbf{e}}_i$ defines the unit vector in $\mathbf{r}_i$-direction. We consider a linear response between the sources and the electric field. Using the Green's function formalism, the electric field generated by the currents is given by $\mathbf{E} = \mathrm{i}\omega\mu_0\mathbb{G}_0\mathbf{j}$ (see, e. g. Ref. [71]), where $\mathbb{G}_0$ defines the free Green's function $\left[\nabla_\mathrm{r} \times \nabla_\mathrm{r} \times -\mathbb{I}\omega^2/c^2\right] \mathbb{G}_0(\mathbf{r}, \mathbf{r}') = \mathbb{I}\delta(\mathbf{r} - \mathbf{r}')$ with the unitary matrix $\mathbb{I}_{i,j} = \delta_{i,j}$. Open face symbols like $\mathbb{G}_0, \mathbb{I}, \ldots$ represent 3×3-matrices in position space. With the notation $\mathbb{G}_0\mathbf{j}$, we abbreviate spatial convolutions between a tensor of two spatial arguments and a vector

$$\mathbf{E}(\mathbf{r}) = \mathrm{i}\omega\mu_0 \left[\mathbb{G}_0\mathbf{j}\right](\mathbf{r}) = \mathrm{i}\omega\mu_0 \int \mathrm{d}^3\mathbf{r}' \mathbb{G}_0(\mathbf{r}, \mathbf{r}')\mathbf{j}(\mathbf{r}') \,. \tag{2.4}$$

Hence, the electric field at a position $\mathbf{r}$ is generated by a source at position $\mathbf{r}'$ within the body. The force expression thus involves the spectral density of the electric field. At thermal equilibrium, the correlations are defined by the fluctuation-dissipation theorem [87, 88] which relates the fluctuations of the field to the response of the body as follows

$$\langle E_j(\mathbf{r}) E_k^*(\mathbf{r}') \rangle_\omega = \mathrm{sign}(\omega) 2\pi\hbar\mu_0\omega^2 \left[\frac{1}{2} + n(\omega, T)\right] \mathrm{Im}\left(\mathbb{G}_{j,k}(\mathbf{r}, \mathbf{r}')\right) \,, \tag{2.5}$$

where the first term in the bracket accounts for the vacuum fluctuations, while the second part originates from thermal fluctuations, with the population of the field modes described by the Bose distribution $n(\omega, T) = \left[\exp\left(\hbar\omega/k_\mathrm{B}T\right) - 1\right]^{-1}$. $\mathbb{G}_{j,k}$ defines the components of the dyadic retarded Green's tensor via the wave equation

$$\left[\nabla_\mathrm{r} \times \nabla_\mathrm{r} - \frac{\omega^2}{c^2}\mathbb{I} - \mathbb{V}\right] \mathbb{G}(\mathbf{r}, \mathbf{r}') = \delta(\mathbf{r} - \mathbf{r}')\mathbb{I} \,, \tag{2.6}$$

where $\mathbb{V}$ defines the potential introduced by the presence of a scatterer, also referred to as collective susceptibility [89]

$$\mathbb{V}(\mathbf{r}, \omega) = \mathbb{I}\frac{\omega^2}{c^2} \left(\epsilon(\mathbf{r}, \omega) - 1\right) + \nabla_\mathrm{r} \times \left(1 - \frac{1}{\mu(\mathbf{r}, \omega)}\right) \nabla_\mathrm{r} \times \,. \tag{2.7}$$

The expression above can be derived from the Maxwell equations (1.1) and (1.2), assuming a linear response with $\mathbf{D} = \epsilon_0\epsilon(\mathbf{r}, \omega)\mathbf{E}$ and $\mathbf{B} = \mu_0\mu(\mathbf{r}, \omega)\mathbf{H}$, where ϵ and μ take the values of the permittivity and permeability of the scatterer, e.g. $\epsilon(\mathbf{r},\omega) = \epsilon(\omega)$ for $\mathbf{r} \in V$ and $\epsilon(\mathbf{r},\omega) = 1$ everywhere else. Hence, the potential $\mathbb{V}$ is only non-zero in the presence of the body and vanishes everywhere else. For $\mathbb{V} = 0$, the Green's function $\mathbb{G}$ coincides with the free Green's function $\mathbb{G}_0$. Introducing the relation for the spectral density into the force expression, we obtain

$$\mathbf{F} = \hbar \mathrm{Im} \int_0^\infty \frac{\mathrm{d}\omega}{2\pi} \coth\left(\frac{\hbar\omega}{2k_\mathrm{B}T}\right) \mathrm{tr}\big|_V \left(\nabla \mathbb{G}\mathbb{G}_0^{-1}\right) , \tag{2.8}$$

where we used that the trace over an operator is given by $\mathrm{tr}\big|_V \mathbb{A} = \sum_i \int_V \mathrm{d}^3\mathbf{r}\mathbb{A}_{ii}(\mathbf{r},\mathbf{r})$. Note also that the derivative ∇ is taken with respect to the first argument of the Greens function. Hence, according to the fluctuation-dissipation theorem, the calculation of the dispersion force reduces to finding the Green's function of the system. In the following, we discuss how the Green's function for a system of two scatterers can be derived.

2.1.1 Solving the scattering problem between two objects

We assume that $\mathbf{E}_0$ is the solution to the Helmholtz equation in free space, while $\mathbf{E}$ is the field in the presence of one body. The two fields are related through the Green's tensor by [82]

$$\mathbf{E} = \mathbb{G}\mathbb{G}_0^{-1}\mathbf{E}_0 . \tag{2.9}$$

The Green's function can iteratively be constructed by the Lippmann-Schwinger equation [90], where the electric field in the presence of a body is given by the field in free space and the field scattered by the object

$$\mathbf{E} = \mathbf{E}_0 + \mathbb{G}_0\mathbb{V}\mathbf{E} . \tag{2.10}$$

By solving the equation above for the scattered field, we get $\mathbf{E} = (1 - \mathbb{G}_0\mathbb{V})^{-1}\,\mathbf{E}_0$. To single out the free field, we introduce this expression in Eq. (2.10) and thus get the well-known relation of the field in terms of the $\mathbb{T}$-matrix, which is also illustrated in Fig. 2.1a

$$\mathbf{E} = (1 + \mathbb{G}_0\mathbb{T})\,\mathbf{E}_0 , \qquad \mathbb{T} = \mathbb{V}\,(\mathbb{I} - \mathbb{G}_0\mathbb{V})^{-1} . \tag{2.11}$$

From the definition (2.7) of the potential $\mathbb{V}$, follows that $\mathbb{T} = \mathbb{T}(\mathbf{r},\mathbf{r}')$ is only non-zero if $\mathbf{r}$ and $\mathbf{r}'$ are within the body, which we will exploit later on. A comparison with Eq. (2.9), allows one to read of the Green's tensor for one scatterer as

$$\mathbb{G} = \mathbb{G}_0 + \mathbb{G}_0\mathbb{T}\mathbb{G}_0 , \qquad \mathbb{G} = [\mathbb{I} - \mathbb{G}_0\mathbb{V}]^{-1}\,\mathbb{G}_0 . \tag{2.12}$$

In the second equation, we expressed the Green's tensor in terms of the potential $\mathbb{V}$. From the above solution, it is clear that in thermal equilibrium, there is no force displacing the object.

The situation changes, however, if at least one additional object is added. We thus consider two scatterers described by potentials $\mathbb{V}_1$ and $\mathbb{V}_2$. The solution of the wave equation for object 1 in the presence of object 2 can again be constructed iteratively as

$$\mathbf{E}_1 = \tilde{\mathbf{E}}_1 + \mathbb{G}_1\mathbb{V}_2\mathbf{E}_1 , \tag{2.13}$$

where the first term accounts for the field of the isolated object 1 with $\tilde{\mathbf{E}}_1 = \mathbb{G}_1\mathbb{G}_0^{-1}\mathbf{E}_0$. The second

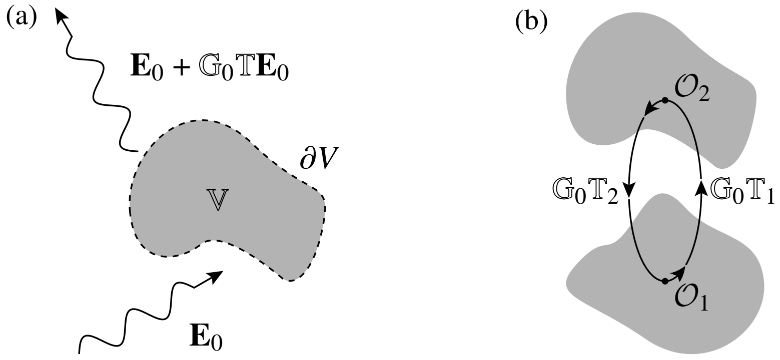

Figure 2.1: (a) Scattering of the free electromagnetic field at an object, described by the potential $\mathbb{V}$. The initial and scattered field are related through the $\mathbb{T}$-matrix, which is defined in Eq. (2.11). (b) Illustration of the round-trip operator $\mathbb{M}_{1,2} = \mathbb{G}_0\mathbb{T}_1\mathbb{G}_0\mathbb{T}_2$ for two objects.

term represents the field scattered from object 2 to object 1. We determine the Green's function $\mathbb{G}$ of the system with $\mathbf{E}_1 = \mathbb{G}\mathbb{G}_0^{-1}\mathbf{E}_0$. Therefore, we first express the Green's function $\mathbb{G}_1$ in terms of the potential $\mathbb{V}_1$ (2.12) and then solve for $\mathbf{E}_1$, which leads to the following expression

$$[\mathbb{I} - \mathbb{G}_0 (\mathbb{V}_1 + \mathbb{V}_2)]\, \mathbf{E}_1 = (\mathbb{I} - \mathbb{G}_0\mathbb{V}_1)\, \tilde{\mathbf{E}}_1 \,. \tag{2.14}$$

We again employ the definition of the Green's function (2.12), but now represent the potential in terms of the Green's function with $\mathbb{V}_i = \mathbb{G}_0^{-1} - \mathbb{G}_i^{-1}$ for $i = 1, 2$. Additionally, we use the matrix identity $(\mathbb{A}\mathbb{B})^{-1} = \mathbb{B}^{-1}\mathbb{A}^{-1}$ and multiply both sides of the equation with $\mathbb{G}_1\mathbb{G}_0^{-1}$ from the left, which in total yields

$$\left(-\mathbb{G}_1\mathbb{G}_0^{-1}\mathbb{G}_2\mathbb{G}_0^{-1} + \mathbb{G}_2\mathbb{G}_0^{-1} + \mathbb{G}_1\mathbb{G}_0^{-1}\right)\left(\mathbb{G}_2\mathbb{G}_0^{-1}\right)^{-1} \mathbf{E}_1 = \tilde{\mathbf{E}}_1 \tag{2.15}$$

with $\mathbb{G}_i = (\mathbb{I} + \mathbb{G}_0\mathbb{T}_i)\,\mathbb{G}_0$, we find for the Green's function

$$\mathbb{G} = (\mathbb{I} + \mathbb{G}_0\mathbb{T}_2)\left(\mathbb{I} - \mathbb{M}_{1,2}\right)^{-1}(\mathbb{I} + \mathbb{G}_0\mathbb{T}_1)\,\mathbb{G}_0 \,, \tag{2.16}$$

where we introduced the matrix

$$\mathbb{M}_{1,2} = \mathbb{G}_0\mathbb{T}_1\mathbb{G}_0\mathbb{T}_2 \,, \tag{2.17}$$

which accounts for the multiple scattering processes between the two objects as depicted in Fig. 2.1b. We are only interested in the interaction force, hence only terms with even numbers of the $\mathbb{T}$-operators are relevant. After inserting Eq. (2.16) into Eq. (2.8), we thus obtain for the force on object 1 [7, 82]

$$\mathbf{F}_1 = \frac{\hbar}{\pi}\mathrm{Im}\int_0^\infty d\omega \coth\left(\frac{\hbar\omega}{2k_\mathrm{B}T}\right) \mathrm{tr}\left[\nabla\mathbb{G}_0\mathbb{T}_2\left(\mathbb{I} - \mathbb{M}_{1,2}\right)^{-1}\mathbb{G}_0\mathbb{T}_1\right] \,. \tag{2.18}$$

The $\mathbb{T}_1$-operator is only defined within the body. We thus extended the trace integral over the whole space. The force on object 2 can similarly derived, one only needs to interchange the indices of the operators from 1 to 2 and vice versa. We want to express the force on object 2 in terms $\mathbb{M}_{1,2}$ and thus apply the identity $\left[\mathbb{I} - \mathbb{M}_{2,1}\right]^{-1}\mathbb{G}_0\mathbb{T}_2 = \mathbb{G}_0\mathbb{T}_2\left[\mathbb{I} - \mathbb{M}_{1,2}\right]^{-1}$, which then results in the following expression for the force on body 2

$$\mathbf{F}_2 = \frac{\hbar}{\pi}\mathrm{Im}\int_0^\infty \mathrm{d}\omega \coth\left(\frac{\hbar\omega}{2k_\mathrm{B}T}\right) \mathrm{tr}\left[\nabla\mathbb{G}_0\mathbb{T}_1\mathbb{G}_0\mathbb{T}_2\left(\mathbb{I}-\mathbb{M}_{1,2}\right)^{-1}\right] . \tag{2.19}$$

In thermal equilibrium $\mathbf{F}_1 = -\mathbf{F}_2$, we can thus introduce $\mathbf{F} = (\mathbf{F}_1 - \mathbf{F}_2)/2$. Taking into consideration that the trace is invariant under cyclic permutation and that we can move the derivative past the free Green's function, we find

$$\mathbf{F} = \frac{\hbar}{2\pi}\mathrm{Im}\int_0^\infty \mathrm{d}\omega \coth\left(\frac{\hbar\omega}{2k_\mathrm{B}T}\right) \mathrm{tr}\left[\left(\mathbb{I}-\mathbb{M}_{1,2}\right)^{-1}\mathbb{G}_0\left(\mathbb{T}_1\nabla\mathbb{G}_0 - \nabla\mathbb{T}_1\mathbb{G}_0\right)\mathbb{T}_2\right] . \tag{2.20}$$

The derivatives are only taken with respect to components located in object 1. The derivatives can thus also be rewritten as total derivatives with respect to the position O_1 of the object [82], see also auxiliary calculation in Sec. B.1. Making use of the identity $(\mathbb{I}-\mathbb{M}_{1,2})^{-1}\nabla_{O_1}\mathbb{M}_{1,2} = -\nabla_{O_1}\log(\mathbb{I}-\mathbb{M}_{1,2})$, we get

$$\mathbf{F} = -\frac{\hbar}{2\pi}\int_0^\infty \mathrm{d}\omega \coth\left(\frac{\hbar\omega}{2k_\mathrm{B}T}\right) \mathrm{Im}\left[\mathrm{tr}\nabla_{O_1}\log(\mathbb{I}-\mathbb{G}_0\mathbb{T}_1\mathbb{G}_0\mathbb{T}_2)\right] . \tag{2.21}$$

The expression above constitutes the well-known TGTG formula for the Casimir force [39]. The same expression can be found for non-reciprocal scatterers, as shown in Ref. [7]. The interaction free energy $\mathcal{F}$, which we will be considering throughout this work is given by $\mathbf{F} = -\nabla_{O_1}\mathcal{F}$. Furthermore, we note that within a partial-wave expansion the free Green's function and the $\mathbb{T}$-operator can respectively replaced by operators $\mathcal{T}_{ij}$, which describe the translation of the electromagnetic field form object j to i and by reflections operators $\mathcal{R}_i$, which describe the reflection at body i at a reference point within the object (see e. g. [23, 82]), as it is depicted for the two-body setup in Fig. 2.1b. The Casimir free energy thus reads

$$\mathcal{F} = \frac{\hbar}{2\pi}\int_0^\infty \mathrm{d}\omega \coth\left(\frac{\hbar\omega}{2k_\mathrm{B}T}\right) \mathrm{Im}\left[\mathrm{tr}\log\left(\mathcal{I}-\mathcal{M}(\omega)\right)\right] , \tag{2.22}$$

where $\mathcal{M} = \mathcal{T}_{21}\mathcal{R}_1\mathcal{T}_{12}\mathcal{R}_2$ is known as the so-called round-trip operator.

2.1.2 Analysis in imaginary frequencies, the Matsubara formalism

Due to the rapidly oscillating integrand, expression (2.22) is not practical for evaluations of the Casimir free energy. To avoid these oscillations, a Wick rotation to imaginary frequencies is usually performed [14]. We are thus examining the integrand of Eq. (2.22) in the complex frequency plane $z = \omega + \mathrm{i}\xi$. We define $e(\omega) = \mathrm{tr}\log(1-\mathcal{M}(\omega))$ and note that since the fields are real the following relation $e^*(\omega) = e(-\omega)$ holds, according to the Schwarz reflection principle. As a consequence, the imaginary part of $e(\omega)$ is an odd function in ω, which allows us to extend the integration in Eq. (2.22) over the whole real frequency axis. The function $e(z)$ is analytical in the upper half ($\xi > 0$) of the complex plane, since both Green's functions and the $\mathbb{T}$-operators are causal functions. The hyperbolic cotangent, on the other hand, introduces singularities along the imaginary axis at the Matsubara frequencies $z = \mathrm{i}\xi_n$, with

$$\xi_n = \frac{2\pi n k_\mathrm{B}T}{\hbar}, \qquad n \in \mathbb{Z} . \tag{2.23}$$

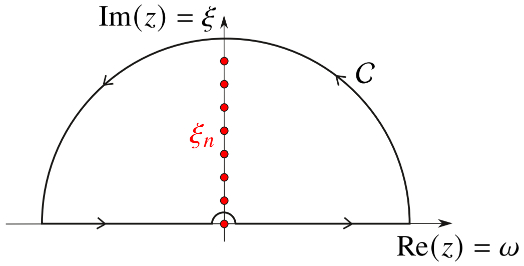

Figure 2.2: Integration contour C in the complex frequency plane. The red circle symbols denote the equidistant single poles of the hyperbolic cotangent $\coth(\hbar z/2k_\mathrm{B}T)$ along the imaginary axis, which define the Matsubara frequencies $\xi_n = 2\pi n k_\mathrm{B}T/\hbar$.

The integral over $f(z) = \coth(\hbar z/2k_\mathrm{B}T)e(z)$ can thus be evaluated by applying the Cauchy residue theorem for a contour C which encloses the singularities at $\mathrm{i}\xi_{n>0}$ as depicted in Fig. 2.2. The poles are all simple and we obtain

$$\oint_C \mathrm{d}z f(z) = 2\pi\mathrm{i}\sum_{n=1}^{\infty}\mathrm{Res}\left(f(z), \mathrm{i}\xi_n\right) = 2\pi\mathrm{i}\frac{2k_\mathrm{B}T}{\hbar}\sum_{n=1}^{\infty} e(\mathrm{i}\xi_n)\,. \tag{2.24}$$

The integral along the semi-circle vanishes due to the high-frequency transparency of most real materials. The pole at $\xi_0 = 0$ is located directly on the contour and thus only contributes with a factor $1/2$ [91]. In summary, the Casimir free energy is given as a sum over Matsubara frequencies as follows

$$\mathcal{F} = k_\mathrm{B}T\sum_{n=0}^{\infty}{}' \operatorname{tr}\log(\mathcal{I} - \mathcal{M}(\mathrm{i}\xi_n))\,, \tag{2.25}$$

where the prime at the sum denotes that the term $n = 0$ is counted with a factor $1/2$.

In the zero-temperature limit ($T = 0$), the hyperbolic cotangent in Eq. (2.22) yields one. There are thus no singularities along the positive imaginary axis and the Casimir energy follows from a Wick rotation of (2.22), leading to

$$\mathcal{E} = \frac{\hbar}{2\pi}\int_0^\infty \mathrm{d}\xi \operatorname{tr}\log\left(\mathcal{I} - \mathcal{M}(\mathrm{i}\xi)\right)\,. \tag{2.26}$$

Our analytical and numerical calculation of the Casimir interactions between two spherical objects will be based on Eqs. (2.25) and (2.26).

2.2 Surface integral approach

Another way to express the force on an object in an electromagnetic field is by examining the electromagnetic stresses. By applying the Maxwell equations (1.1) and (1.2), the force density (2.1) can also be written as

$$\hat{\rho}(\mathbf{r},t)\hat{\mathbf{E}}(\mathbf{r},t) + \hat{\mathbf{j}}(\mathbf{r},t)\times\hat{\mathbf{B}}(\mathbf{r},t) = \nabla_\mathrm{r}\cdot\hat{\mathbb{Z}}(\mathbf{r},t) + \epsilon_0\frac{\partial}{\partial t}\left(\hat{\mathbf{E}}(\mathbf{r},t)\times\hat{\mathbf{B}}(\mathbf{r},t)\right) \tag{2.27}$$

with the Maxwell stress tensor in vacuum [71]

$$\hat{\mathbb{Z}}(\mathbf{r},t) = \epsilon_0\hat{\mathbf{E}}(\mathbf{r},t)\otimes\hat{\mathbf{E}}(\mathbf{r},t) - \epsilon_0\frac{\mathbb{I}}{2}\hat{\mathbf{E}}(\mathbf{r},t)\cdot\hat{\mathbf{E}}(\mathbf{r},t) + \frac{1}{\mu_0}\hat{\mathbf{B}}(\mathbf{r},t)\otimes\hat{\mathbf{B}}(\mathbf{r},t) - \frac{\mathbb{I}}{2\mu_0}\hat{\mathbf{B}}(\mathbf{r},t)\cdot\hat{\mathbf{B}}(\mathbf{r},t)\,, \tag{2.28}$$

where ⊗ denotes the tensor product. We assume stationary conditions, hence, the time-derivative of the momentum density $\hat{\mathbf{E}} \times \hat{\mathbf{B}}$ vanishes. Together with the divergence theorem, the volume integral can be cast to a surface integral

$$\mathbf{F} = \oint_{\partial V} \mathrm{d}^2\mathbf{A} \cdot \langle \hat{\mathbb{Z}}(\mathbf{r}, t) \rangle_{\mathrm{sym}} \tag{2.29}$$

with ∂V defining the boundary of the volume, which encloses the object, as illustrated in Fig. 2.1a. In a medium, the stress tensor is given by [92, 93]

$$\hat{\mathbb{Z}}(\mathbf{r}, t) = \hat{\mathbf{D}}(\mathbf{r}, t) \otimes \hat{\mathbf{E}}(\mathbf{r}, t) - \frac{\mathbb{I}}{2}\hat{\mathbf{D}}(\mathbf{r}, t) \cdot \hat{\mathbf{E}}(\mathbf{r}, t) + \hat{\mathbf{H}}(\mathbf{r}, t) \otimes \hat{\mathbf{B}}(\mathbf{r}, t) - \frac{\mathbb{I}}{2}\hat{\mathbf{H}}(\mathbf{r}, t) \cdot \hat{\mathbf{B}}(\mathbf{r}, t) \,. \tag{2.30}$$

We want to note that there is an ongoing debate about the correct form of the energy-stress tensor in media [94] between the Minkowski and Abraham forms. However, this does not have any effect on the time-averaged force, as both forms result in the same expression.

We will apply the surface-integral approach for the calculation of the optical force on objects trapped by optical tweezers. For classical time-harmonic fields, the averages yield

$$\langle D_i(\mathbf{r}, t) E_j(\mathbf{r}, t) \rangle = \frac{1}{2}\mathrm{Re}\left[D_i(\mathbf{r}, \omega) E_j^*(\mathbf{r}, \omega) \right] \,. \tag{2.31}$$

Furthermore, we assume linear media for our optical force calculation with $\mathbf{D} = \epsilon_0\epsilon\mathbf{E}$ and $\mathbf{B} = \mu_0\mu\mathbf{H}$. The time-averaged force on a body of volume V in an electromagnetic field is thus given by

$$\mathbf{F} = \frac{1}{2}\mathrm{Re} \oint_{\partial V} \mathrm{d}A_j \left[\epsilon_0\epsilon E_i E_j^* + \mu_0\mu H_i H_j^* - \delta_{i,j}\frac{1}{2}\left(\epsilon\epsilon_0 |\mathbf{E}|^2 + \mu\mu_0 |\mathbf{H}|^2 \right) \right] \hat{\mathbf{e}}_i \,, \tag{2.32}$$

where E_i and H_i denote the electromagnetic field components on the boundary ∂V.

3 | Solutions to the Maxwell equations

In the previous Chapter, we introduced the scattering formula for the Casimir free energy between two objects and the optical force expression based on the Maxwell stress tensor. The expressions do not depend on any basis and can, in principle, be applied to any geometry of the objects in the electromagnetic field. This Section will introduce partial-wave bases, which solve the Helmholtz equation. Once we have the solution, we can calculate the matrix elements of the reflection and translation operators, which enter the scattering formula for the Casimir force. We will examine spherical objects both for the dispersion force and optical force, we are considering in this work. An appropriate basis for this geometry is the plane-wave or spherical-wave basis, which we will both discuss in the following Secs. 3.1 and 3.2.

3.1 A plane-wave expansion

In this work, we examine systems that consist of one or two objects. Without loss of generality, we can thus align the objects along the positive or negative z-axis, which allows us to distinguish between waves propagating in the positive and negative z-direction. Furthermore, due to the dispersion relation, the components of the wave vector $\mathbf{K} = (K_x, K_y, K_z)$ are not independent from each other, we thus define

$$\mathbf{K} = (\mathbf{k}, \sigma k_z)\,, \qquad \mathbf{k} = (K_x, K_y)\,, \qquad k_z = \sqrt{n^2\omega^2/c^2 - \mathbf{k}^2}\,, \tag{3.1}$$

where $\mathbf{k}$ is the projection of the wave vector on a plane perpendicular to the propagation direction and $\sigma = \pm$ determines the sign of K_z and thus the propagation direction along the z-direction. We additionally used the dispersion relation with the refractive index of the medium n to express the axial wave vector k_z. The electric and magnetic fields are transverse vector fields, meaning they are perpendicular to the wave vector. Thus, it is convenient to introduce an orthonormal basis in which the fields are expanded. For the polarisation vectors of the electric field, we choose

$$\hat{\epsilon}_{\mathrm{TE}}(\hat{\mathbf{K}}) = \hat{z} \times \hat{\mathbf{K}} = \hat{\phi}_K\,, \qquad \hat{\epsilon}_{\mathrm{TM}}(\hat{\mathbf{K}}) = \hat{\epsilon}_{\mathrm{TE}}(\hat{\mathbf{K}}) \times \hat{\mathbf{K}} = \hat{\theta}_K\,, \tag{3.2}$$

therefore $(\hat{\mathbf{K}}, \hat{\epsilon}_{\mathrm{TM}}, \hat{\epsilon}_{\mathrm{TE}})$ defines a right-handed basis. Note that the hat over the vectors indicates that these are unit vectors, so $\hat{\mathbf{K}} = \mathbf{K}/|\mathbf{K}| = (\sin\theta_K \cos\phi_K, \sin\theta_K \sin\phi_K, \cos\theta_K)$ in spherical coordinates. $\hat{\epsilon}_{\mathrm{TE}}$ defines the transversal electric (TE) polarisation for which the electric field is orthogonal to the plane spanned by the z-axis and the wave vector, called the Fresnel plane (F). Both polarisation vectors can be expressed in terms of the unit vectors of spherical coordinates denoted by $\hat{\phi}_K = (-\sin\phi_K, \cos\phi_K, 0)$ and $\hat{\theta}_K = (\cos\theta_K \cos\phi_K, \cos\theta_K \sin\phi_K, -\sin\theta_K)$.

According to Eq. (1.2), the electric and magnetic fields are orthogonal to each other with $\mathbf{K} \times \mathbf{E} = \omega\mathbf{B}$, which means that the unit vectors for the magnetic field can also be expressed in terms of Eq. (3.2) with

$$\hat{\beta}_p = \hat{\mathbf{K}} \times \hat{\epsilon}_p\,, \tag{3.3}$$

where $p = \mathrm{TE}, \mathrm{TM}$. The unit vector $\hat{\beta}_{\mathrm{TM}} = \hat{\epsilon}_{\mathrm{TE}}$ thus defines the transversal magnetic (TM) polarisation for which the magnetic field is orthogonal to the plane spanned by the z-axis and the wave vector. The expression of the electromagnetic field in a planar wave expansion is thus given by

$$\mathbf{E}(\mathbf{r},t) = \sum_M \left[a_M \boldsymbol{\epsilon}_p \mathrm{e}^{-\mathrm{i}\omega t + \mathrm{i}\mathbf{k}\cdot\boldsymbol{\rho} + \mathrm{i}\sigma k_z z} + c.c.\right] \tag{3.4}$$

with $\boldsymbol{\rho} = (x, y)$ and the multi-index M summing over all field modes $(\omega, \mathbf{k}, p, \sigma)$ according to

$$\sum_M = \sum_{p=\mathrm{TE,TM}} \sum_{\sigma=\pm} \int \frac{\mathrm{d}^2\mathbf{k}}{(2\pi)^2} \int_0^\infty \frac{\mathrm{d}\omega}{2\pi c} \frac{n^2\omega}{ck_z}, \tag{3.5}$$

where we again used the dispersion relation (3.1), to rewrite the integral over the axial wave vector in terms of a frequency integral. The magnetic field can be obtained from the electric field by applying the Maxwell equation (1.2). For a classical field, the expansion coefficients a_M describe the field amplitudes. In Chap. 5, we will derive the field amplitudes for a structured light field, used in an optical tweezer setting. The plane-wave expansion above is also known as angular spectrum decomposition [95]. For a quantum field, the amplitudes are operators which obey the Bose commutation relations [96]

$$\left[a_M, a_{M'}^\dagger\right] = \delta_{M,M'}, \qquad [a_M, a_{M'}] = 0 = \left[a_M^\dagger, a_{M'}^\dagger\right], \tag{3.6}$$

where $\delta_{M,M'} = (2\pi)^3\delta^{(2)}(\mathbf{k}-\mathbf{k}')\delta(k_z - k_z')\delta_{\sigma,\sigma'}$. In the following, we are using the basis independent notation $|\mathbf{k}, p, \sigma\rangle$ for the plane-wave modes such that the spatial representation corresponds with $\langle\mathbf{r}|\mathbf{k}, p, \sigma\rangle \propto \hat{\boldsymbol{\epsilon}}_p(\hat{\mathbf{K}})\mathrm{e}^{\mathrm{i}\mathbf{k}\cdot\boldsymbol{\rho} + \mathrm{i}\sigma k_z z}$. We refrained from adding the frequency dependence to the mode definition since the frequency is conserved during scattering processes in all cases studied in this thesis. Note that the plane-wave basis defines an orthogonal and complete set with the identity given by [97]

$$\mathrm{Id} = \sum_{p=\mathrm{TE,TM}} \sum_{\sigma=\pm} \int \frac{\mathrm{d}^2\mathbf{k}}{(2\pi)^2} |\mathbf{k}, p, \sigma\rangle \langle\mathbf{k}, p, \sigma| . \tag{3.7}$$

3.2 A spherical-wave expansion

Apart from plane waves, solutions to the Helmholtz equation can also be expanded in terms of spherical waves. The electric field is then given by [80]

$$\mathbf{E}(\mathbf{r}) = \sum_{l=1}^{\infty} \sum_{m=-l}^{l} \left[e_{l,m}\mathbf{N}_{l,m}^s(\mathbf{r}) + f_{l,m}\mathbf{M}_{l,m}^s(\mathbf{r})\right], \tag{3.8}$$

where the spherical vector fields $\mathbf{M}_{l,m}^s$ and $\mathbf{N}_{l,m}^s$ respectively define the magnetic (M) and electric (E) modes of the field. They are, in general, defined by [80]

$$\mathbf{M}_{l,m}^s(\mathbf{r}) = z_l(Kr)\mathbf{X}_{l,m}(\hat{\mathbf{r}}), \tag{3.9a}$$

$$\mathbf{N}_{l,m}^s(\mathbf{r}) = \frac{1}{K}\nabla_\mathrm{r} \times \mathbf{M}_{l,m}(\mathbf{r}) = \frac{1}{Kr}\left[\mathrm{i}\sqrt{l(l+1)}z_l(Kr)\mathbf{Z}_{l,m}(\hat{\mathbf{r}}) + \frac{\partial}{\partial r}(rz_l(kr))\mathbf{Y}_{l,m}(\hat{\mathbf{r}})\right]. \tag{3.9b}$$

The indices l and m are associated with the eigenvalues of the angular-momentum operators $\hat{\mathbf{L}}^2$ and $\hat{L}_z$. Charge-neutrality forbids a monopole term, which is why l takes values between 1 and ∞. The radial field dependence $z_l(Kr)$ with $r = |\mathbf{r}|$ is defined by the spherical Bessel functions of order l, which for regular (reg) waves is given by the spherical Bessel functions of the first kind $j_l(Kr)$, while for outgoing (out) waves, we have to consider spherical Hankel functions of the first kind $h_l^{(1)}(Kr)$. The spherical Hankel functions correctly reproduce the large distance behaviour expected for spherical waves far from the origin of the coordinate system with $\lim_{Kr\to\infty} h_l^{(1)}(Kr) = (-1)^{l+1}\mathrm{e}^{\mathrm{i}Kr}/Kr$. We will differentiate between the two cases with the superscript $s = \mathrm{reg}, \mathrm{out}$ in the spherical vector fields. We furthermore introduced the so-called vector spherical harmonics $\mathbf{X}_{l,m}, \mathbf{Y}_{l,m}$ and $\mathbf{Z}_{l,m}$ with $\mathbf{X}_{l,m}(\hat{\mathbf{r}}) \equiv \mathbf{X}_{l,m}(\theta,\varphi)$, where the unit vector in radial direction is given by $\hat{\mathbf{r}} = \mathbf{r}/|\mathbf{r}| = (\sin\theta\cos\varphi, \sin\theta\sin\varphi, \cos\theta)$. According to [98, p.210], they are defined by

$$\mathbf{X}_{l,m}(\hat{\mathbf{r}}) = \frac{-\mathrm{i}(\hat{\mathbf{r}}\times\nabla_{\mathrm{r}})Y_l^m(\hat{\mathbf{r}})}{\sqrt{l(l+1)}}\,, \qquad \mathbf{Y}_{l,m}(\hat{\mathbf{r}}) = \hat{\mathbf{r}}\times\mathbf{X}_{l,m}(\hat{\mathbf{r}})\,, \qquad \mathbf{Z}_{l,m}(\hat{\mathbf{r}}) = \hat{\mathbf{r}}Y_l^m(\hat{\mathbf{r}})\,, \tag{3.10}$$

with the spherical harmonics $Y_l^m(\hat{\mathbf{r}}) \equiv Y_l^m(\theta,\varphi)$ given by

$$Y_l^m(\theta,\varphi) = \sqrt{\frac{(2l+1)}{4\pi}\frac{(l-m)!}{(l+m)!}}P_l^m(\cos\theta)\mathrm{e}^{\mathrm{i}m\varphi} \tag{3.11}$$

and the associated Legendre polynomials $P_l^m(z)$. The vector spherical harmonics are orthonormal on the unit sphere S^2, with e. g. $\int_{S^2}\mathrm{d}\Omega\mathbf{X}_{l,m}\cdot\mathbf{X}_{l',m'} = \delta_{l,l'}\delta_{m,m'}$ and $\int_{S^2}\mathrm{d}\Omega\mathbf{X}_{l,m}\cdot\mathbf{Y}_{l',m'} = 0$. The same relations apply to the combinations of the other vector fields. Note that $\mathbf{Z}_{l,m}$ is a longitudinal vector field. For classical fields, the amplitudes $e_{l,m}$ and $f_{l,m}$ are just expansion coefficients, which one can evaluate by making use of the orthonormality of the vector spherical harmonics as we will see in the next Chapter. For a quantum field they are promoted to operators [99, 100], which obey the canonical commutation relations.

Similar to the plane-wave expansion, we also introduce a basis independent notation for the spherical waves with $|\ell, m, P, s\rangle$, where the spatial representation of the modes given in Eq. (3.8) is determined by $\langle\mathbf{r}|\ell, m, P, s\rangle$. The frequency dependence is implicit again. The multipole basis defines a complete set, where the identity is defined by [97]

$$\mathrm{Id} = \sum_{l=1}^{\infty}\sum_{m=-l}^{l}\sum_{P=\mathrm{E,M}}\sum_{s=\mathrm{reg,out}} |l,m,P,s\rangle\langle l,m,P,s|\;. \tag{3.12}$$

We are going to make use of the respective identities when changing from one representation of the electromagnetic field to the other.

4 | Scattering of electromagnetic waves at a spherical object

The scattering amplitudes of a PEMC sphere, derived in Sec. 4.2 and Sec. 4.3, can be found in the published article [101].

In this Chapter, we will discuss the scattering of electromagnetic waves at a bi-isotropic sphere. We provide explicit expressions for the reflection coefficients in both the spherical- and plane-wave basis. All results are derived for imaginary frequencies, which is relevant for calculating the Casimir free energy, as we discussed in Sec. 2.1.2. In Sec. 4.1, we present the reflection coefficients for a bi-isotropic sphere for incident spherical waves. Furthermore, we also discuss the scattering of planar waves at a spherical object. In this work, we examine various limiting cases of the Casimir interaction, requiring the corresponding asymptotic expansions of the reflection coefficients. We provide asymptotic expansions for large radii in Sec. 4.2, which can be related to the geometrical optics approximation for real frequencies. Furthermore, we also derive expressions in the static limit in Sec. 4.3, which will be particularly important for our study of the Casimir interaction in the high-temperature limit. Within the static limit, we also consider the large-sphere regime.

4.1 Scattering at a bi-isotropic sphere

We consider a spherical object of radius R located in the centre of the coordinate system. The material of the sphere is bi-isotropic, defined by the constitutive equations (1.7), while the surrounding medium is non-chiral with material properties described by permittivity ϵ_m and permeability μ_m. To determine the scattered field, we need to employ appropriate boundary conditions. We assume that there are no free charges and no surface currents. The boundary conditions for the tangential components of the electric and magnetic field thus read [80]

$$[\hat{\mathbf{r}} \times \mathbf{E}_1(\mathbf{r}) = \hat{\mathbf{r}} \times \mathbf{E}_2(\mathbf{r})]_{r=R}\ , \qquad [\hat{\mathbf{r}} \times \mathbf{H}_1(\mathbf{r}) = \hat{\mathbf{r}} \times \mathbf{H}_2(\mathbf{r})]_{r=R}\ , \tag{4.1}$$

where $\hat{\mathbf{r}} = \mathbf{r}/|\mathbf{r}|$ represents the unit vector in radial direction. The indices 1 and 2 account for the fields outside and inside of the sphere. Equivalently, the continuity of the normal components of $\mathbf{D}$ and $\mathbf{B}$ can be considered.

4.1.1 Scattering of a spherical wave at a spherical object

The Mie coefficients are well-known for an isotropic sphere from [80], while analytical solutions for bi-isotropic materials are also available [79, 102] and will be used in the following. Note, however, that the constitutive equations used in Ref. [79] differ from the ones we defined in Eq. (1.7). Furthermore, the results are computed for real frequencies while we provide expressions for imaginary frequencies.

As we discussed earlier, there are two contributions to the field outside an object, the initial incident (inc) field and the scattered (scat) field

$$\mathbf{E}_1(\mathbf{r}) = \mathbf{E}_\mathrm{inc}(\mathbf{r}) + \mathbf{E}_\mathrm{scat}(\mathbf{r})\ . \tag{4.2}$$

The incident field is regular within the sphere. We thus define

$$\mathbf{E}_{\text{inc}}(\mathbf{r}) = \sum_{l,m} \left[e_{l,m}\mathbf{N}^{\text{reg}}_{l,m}(\mathbf{r}) + f_{l,m}\mathbf{M}^{\text{reg}}_{l,m}(\mathbf{r}) \right] , \tag{4.3}$$

where $e_{l,m}$ and $f_{l,m}$ are general expansion coefficients of the electric and magnetic field modes introduced in Sec. 3.2. For real frequencies, the radial dependence of the vector spherical functions is defined by the spherical Bessel function of the first kind, as discussed earlier. For imaginary frequencies $\omega \longrightarrow \mathrm{i}\xi$, the spherical Bessel functions are replaced by the modified Bessel function of the first kind $I_{l+1/2}(x)$

$$j_l(\mathrm{i}x) \rightarrow \mathrm{i}^l \sqrt{\frac{2}{\pi x}} I_{l+1/2}(x) \tag{4.4}$$

with the aspect ratio $x = \mathcal{K}R$, where $\mathcal{K}$ defines the modulus of the wave vector $\mathbf{K}$ in the medium after Wick rotation, which is together with the dispersion relation in the surrounding medium given by

$$\mathcal{K} = \frac{\xi n_{\text{m}}(\mathrm{i}\xi)}{c} . \tag{4.5}$$

Note that the refractive index of the medium is also evaluated at imaginary frequencies. In contrast to the incident field, the scattered field is described by outgoing vector spherical waves, as follows

$$\mathbf{E}_{\text{scat}}(\mathbf{r}) = \sum_{l,m} \left[a_{l,m}\mathbf{N}^{\text{out}}_{l,m}(\mathbf{r}) + b_{l,m}\mathbf{M}^{\text{out}}_{l,m}(\mathbf{r}) \right] . \tag{4.6}$$

For real frequencies, the radial dependence is given by the spherical Hankel functions. For imaginary frequencies, we have to replace them by modified Hankel functions $K_{l+1/2}(x)$

$$h^{(1)}_l(\mathrm{i}x) \longrightarrow -\mathrm{i}^l \frac{2}{\pi} \sqrt{\frac{2}{\pi x}} K_{l+1/2}(x) . \tag{4.7}$$

The Maxwell equation $\nabla \times \mathbf{E} = -\mathrm{i}\omega\mu_{\text{m}}\mu_0\mathbf{H}$ can be used to obtain the respective magnetic fields. As shown in Eq. (1.9), the electromagnetic field within a bi-isotropic medium can be expressed as a superposition of waves with wave numbers $K_{\text{L,R}}$ (1.12). The electric and magnetic field thus yield [79]

$$\mathbf{E}_2(\mathbf{r}) = \sum_{l,m} \left[A_{l,m} \left(\mathbf{M}^{\text{reg,L}}_{l,m}(\mathbf{r}) + \mathbf{N}^{\text{reg,L}}_{l,m}(\mathbf{r}) \right) + B_{l,m} \left(\mathbf{M}^{\text{reg,R}}_{l,m}(\mathbf{r}) - \mathbf{N}^{\text{reg,R}}_{l,m}(\mathbf{r}) \right) \right] , \tag{4.8a}$$

$$\mathbf{H}_2(\mathbf{r}) = a_L \sum_{l,m} \left[A_{l,m} \left(\mathbf{M}^{\text{reg,L}}_{l,m}(\mathbf{r}) + \mathbf{N}^{\text{reg,L}}_{l,m}(\mathbf{r}) \right) + \frac{B_{l,m}}{a_{\text{L}} a_{\text{R}}} \left(\mathbf{M}^{\text{reg,R}}_{l,m}(\mathbf{r}) - \mathbf{N}^{\text{reg,R}}_{l,m}(\mathbf{r}) \right) \right] , \tag{4.8b}$$

where the additional superscripts ’L’ and ’R’ at the spherical vector fields account for wave propagation with the wave numbers $K_{\text{L,R}}$. The coefficients $a_{\text{L,R}}$ are defined in Eq. (1.9). Note that the vector fields $\mathbf{M}_{l,m} \pm \mathbf{N}_{l,m}$ are so-called Beltrami fields [103], which are vector fields that are proportional to their curl. The spherical Bessel functions, which enter the spherical vector fields, are given by

$j_l(\mathrm{i}m_{\mathrm{L,R}}x)$, where $m_{\mathrm{L,R}}$ accounts for the ratio of the refractive index of the sphere and medium (1.10)

$$m_{\mathrm{L,R}} = \frac{n_{\mathrm{L,R}}}{n_{\mathrm{m}}} = \frac{1}{n_{\mathrm{m}}}\sqrt{\epsilon\mu - \frac{(\alpha+\beta)^2}{4}} \pm \mathrm{i}\frac{\beta-\alpha}{2}\,. \tag{4.9}$$

We solve the boundary equation (4.1) by making use of the expansion of the spherical vector fields in terms of vector spherical harmonics (3.9) and their orthonormality along the unit sphere. The electric and magnetic expansion coefficients of the scattered field are then found as linear superposition of the expansion coefficients for the incident field

$$\begin{pmatrix} a_{l,m} \\ b_{l,m} \end{pmatrix} = -\begin{pmatrix} r_l^{(\mathrm{E,E})} & \mathrm{i}r_l^{(\mathrm{E,M})} \\ -\mathrm{i}r_l^{(\mathrm{M,E})} & r_l^{(\mathrm{M,E})} \end{pmatrix} \begin{pmatrix} e_{l,m} \\ f_{l,m} \end{pmatrix}. \tag{4.10}$$

The diagonal entries $r_l^{(P,P)}$ account for the polarisation-conserving Mie reflection coefficients, which are given by

$$r_l^{(\mathrm{E,E})}(x) = C_l(x)\frac{W_l^R(x)A_l^{\mathrm{L}}(x) + W_l^L(x)A_l^R(x)}{W_l^R(x)V_l^{\mathrm{L}}(x) + W_l^L(x)V_l^R(x)}\,, \tag{4.11a}$$

$$r_l^{(\mathrm{M,M})}(x) = C_l(x)\frac{V_l^R(x)B_l^{\mathrm{L}}(x) + V_l^L(x)B_l^R(x)}{W_l^R(x)V_l^{\mathrm{L}}(x) + W_l^L(x)V_l^R(x)}\,, \tag{4.11b}$$

where we adapted the notation from Ref. [80] and introduced the following auxiliary variables

$$\begin{pmatrix} A_l^{\mathrm{L,R}} \\ B_l^{\mathrm{L,R}} \end{pmatrix} = \begin{pmatrix} 1 & -m_\mp \\ m_\mp & -1 \end{pmatrix} \begin{pmatrix} \{I,x\} \\ \{I, m_{\mathrm{L,R}}x\} \end{pmatrix}, \qquad \begin{pmatrix} V_l^{\mathrm{L,R}} \\ W_l^{\mathrm{L,R}} \end{pmatrix} = \begin{pmatrix} 1 & m_\mp \\ m_\mp & 1 \end{pmatrix} \begin{pmatrix} -\{K,x\} \\ \{I, m_{\mathrm{L,R}}x\} \end{pmatrix} \tag{4.12}$$

which we have written in a matrix-vector equation for convenience. $m_\pm$ defines the relative impedance

$$m_\pm = \sqrt{\frac{\epsilon_{\mathrm{m}}\mu}{\epsilon\mu_{\mathrm{m}}}}\left[\sqrt{1 - \frac{(\alpha+\beta)^2}{4\epsilon\mu}} \mp \mathrm{i}\frac{(\alpha+\beta)^2}{4\epsilon\mu}\right]. \tag{4.13}$$

The expressions $\{I,z\}$ and $\{K,z\}$ account for logarithmic derivatives of the modified Bessel functions with

$$\{\mathcal{I},z\} = \frac{\mathcal{I}'_{l+1/2}(z)}{\mathcal{I}_{l+1/2}(z)} + \frac{1}{2z}\,, \tag{4.14}$$

where $\mathcal{I}_{l+1/2}(z)$ either represents the modified Bessel functions of the first kind $I_{l+1/2}(z)$ or the modified Hankel functions $K_{l+1/2}(z)$. The notation was inspired by a similar one in Ref. [104]. The prefactor $C_l(x)$ in Eq. (4.11) accounts for the ratio of the two Bessel functions

$$C_l(x) = (-1)^l\frac{\pi}{2}\frac{I_{l+1/2}(x)}{K_{l+1/2}(x)}\,. \tag{4.15}$$

The reflection coefficients are deliberately only written in ratios of Bessel functions. One reason is that the given form of the reflections coefficient is helpful when examining several limiting cases, such as the large sphere regime or the static limit, as we will see in the following Sections. Furthermore, routines already exist for an efficient calculation of the ratios of Bessel functions (see e.g. Ref. [105]), which is relevant for the numerical computation of the Casimir free energy. Lastly, in this work, we examine the Casimir force on spherical objects and the optical force induced by an external laser field. In the latter case, we need the reflection coefficients for real frequencies. For real frequencies, the modified Bessel functions are replaced by the spherical Bessel functions and the spherical Hankel functions of the first kind, as we discussed above in Eqs. (4.4) and (4.7).

For the polarisation-mixing Mie reflection coefficient $r_l^{(P,\bar{P})}$, we find

$$r_l^{(\mathrm{M,E})} = \mathrm{i}C_l(x)\,[\{I,x\} - \{K,x\}]\,\frac{m_-\{I,m_\mathrm{R}x\} - m_+\{I,m_\mathrm{L}x\}}{W_l^R V_l^\mathrm{L} + W_l^L V_l^R}\,, \tag{4.16a}$$

$$r_l^{(\mathrm{E,M})} = \mathrm{i}C_l(x)\,[\{I,x\} - \{K,x\}]\,\frac{m_-\{I,m_\mathrm{L}x\} - m_+\{I,m_\mathrm{R}x\}}{W_l^R(x)V_l^\mathrm{L}(x) + W_l^L(x)V_l^R(x)}\,. \tag{4.16b}$$

In the isotropic limit, we get $m_\mathrm{L} = m_\mathrm{R}$ and $m_+ = m_-$ and the scattering coefficients reduce to the known Mie expressions [80] for imaginary frequencies with $r_l^{(\mathrm{E,E})} = C_l A_l/V_l$ and $r_l^{(\mathrm{M,M})} = C_l B_l/W_l$ while the polarisation-mixing coefficients yield zero. Furthermore, one also notices that for reciprocal material ($\alpha = -\beta$) the relative impedance $m_\pm$, defined in Eq. (4.13) becomes the same and the reflection coefficients $r_l^{(\mathrm{E,M})}$ and $r_l^{(\mathrm{M,E})}$ only differ by a minus sign.

We are particularly interested in non-reciprocal materials, with the earlier introduced PEMC materials as a special case. According to Eq. (1.6), the parameter $m_\mathrm{L,R}$ is going to infinity in the PEMC limit, while $m_\pm = \mp\mathrm{i}\tan(\theta)$, where θ conveys the transition from perfect electric $\theta = 0$ to perfect magnetic $\theta = \pi/2$ conductor. The polarisation-conserving Mie coefficients thus yield

$$r_l^{(\mathrm{E,E})}(x) = -C_l(x)\left[\cos^2(\theta)\frac{\{I,x\}}{\{K,x\}} + \sin^2\theta\right]\,, \tag{4.17a}$$

$$r_l^{(\mathrm{M,M})}(x) = -C_l(x)\left[\cos^2(\theta) + \sin^2\theta\frac{\{I,x\}}{\{K,x\}}\right]\,. \tag{4.17b}$$

The two polarisation-mixing coefficients become identical, and they are given by

$$r_l^{(\mathrm{M,E})}(x) = r_l^{(\mathrm{E,M})}(x) = -C_l(x)\frac{\sin(2\theta)}{2}\left[\frac{\{I,x\}}{\{K,x\}} - 1\right]\,. \tag{4.18}$$

The Mie coefficients for a PEMC sphere can thus also be obtained from a duality transformation of the Mie coefficients of either one of the two limiting cases $\theta = 0$ or $\theta = \pi/2$, which we will discuss below in more detail.

We conclude by providing the expression for the matrix elements of the reflection operator $\mathcal{R}$ of a bi-isotropic sphere in the multipole basis, which yield

$$\langle l', m', P', s'|\mathcal{R}|l, m, P, s\rangle = -\mathrm{i}^{P'-P} r_l^{(P',P)} \delta_{l,l'}\delta_{m,m'}\delta_{s,\mathrm{reg}}\delta_{s',\mathrm{out}}\,, \tag{4.19}$$

where we identify the polarisation in the exponents of the imaginary unit as 1 (2) for E (M). The expression represents the scattering of an incident P-polarised spherical wave, regular at the origin, into an outgoing P'-polarised spherical wave. The amplitude is given by the Mie reflection coefficients $r_l^{(P',P)}$ which are independent of m. l and m are conserved during the scattering process.

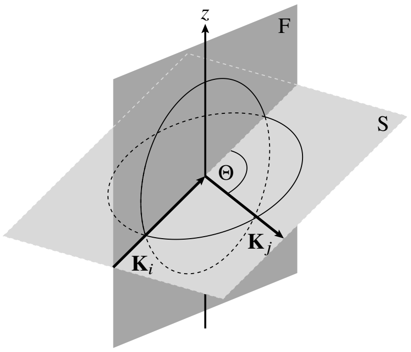

Figure 4.1: Scattering geometry at a sphere. The incident wave vector $\mathbf{K}_i$ and the symmetry axis z define the Fresnel plane (F), while the scattering plane (S) is spanned by the incident and the outgoing wave vector $\mathbf{K}_j$. The scattering angle Θ is defined by $\cos(\Theta) = \hat{\mathbf{K}}_i \cdot \hat{\mathbf{K}}_j$.

4.1.2 Scattering of a plane wave at a spherical object

In this Section, we consider the scattering of a plane wave with a wave vector $\mathbf{K}_i$, as shown in Fig. 4.1 and polarisation p_i, which is scattered at a sphere. The scattered wave is then defined by a wave vector $\mathbf{K}_j$ and a polarisation p_j. The plane spanned by the incident and reflected wave vector is called scattering plane (S). To make use of the results, which we obtained in the previous Section, we perform a basis change from plane waves to spherical waves by introducing the identity (3.12) in the multipole basis as follows

$$\begin{aligned}\langle \mathbf{k}_j, p_j, \pm|\mathcal{R}|\mathbf{k}_i, p_i, \mp\rangle = \sum_{P,P'} \sum_{l,m,l',m'} & \langle \mathbf{k}_j, p_j, \pm|l', m', P', \mathrm{out}\rangle \\ & \times \langle l', m', P', \mathrm{out}|\mathcal{R}|l, m, P, \mathrm{reg}\rangle \, \langle l, m, P, \mathrm{reg}|\mathbf{k}_i, p_i, \mp\rangle \ ,\end{aligned} \tag{4.20}$$

where we already accounted for the fact that the propagation direction changes upon scattering. Due to conservation of the angular momentum numbers (l, m), the reflection matrix elements simplify with the earlier obtained Mie reflections coefficients (4.19) to

$$\langle \mathbf{k}_j, p_j, \pm|\mathcal{R}|\mathbf{k}_i, p_i, \mp\rangle = -\sum_{P,P'} \sum_{l,m} \mathrm{i}^{P'-P} r_l^{(P',P')} \langle \mathbf{k}_j, p_j, \pm|l, m, P', \mathrm{out}\rangle \, \langle l, m, P, \mathrm{reg}|\mathbf{k}_i, p_i, \mp\rangle \ . \tag{4.21}$$

The basis transformation coefficient can be computed by expressing both bases in their respective spatial form. Already Canaguier-Durand *et al.* determined in Ref. [106] the coefficients for a transformation from the spherical to the plane-wave basis. The set of transformation coefficients was completed by Messina *et al.* in Ref. [107]. The transformation coefficient from a spherical wave to a plane wave is given by

$$\langle \mathbf{k}, p, \pm|l, m, P, \mathrm{out}\rangle = 2\pi \frac{\mathrm{i}^{1-p}}{\sqrt{l(l+1)}} \frac{1}{\mathcal{K}_K} \left(\frac{m}{\sin\theta_K}\right)^{\delta_{p,P}} \left(\frac{\partial}{\partial\theta_K}\right)^{1-\delta_{p,P}} \mathrm{Y}_l^m(\hat{\mathbf{K}}) \tag{4.22}$$

with the spherical harmonics in reciprocal space $\mathrm{Y}_l^m(\hat{\mathbf{K}}) \equiv \mathrm{Y}_l^m(\theta_K, \phi_K)$. The coefficient for a transformation from a planar wave to a spherical wave is given by

$$\langle l, m, P, \mathrm{reg}|\mathbf{k}, p, \pm\rangle = -4\pi \frac{\mathrm{i}^{p-1}}{\sqrt{l(l+1)}} \left(\frac{m}{\sin\theta_K}\right)^{\delta_{p,P}} \left(\frac{\partial}{\partial\theta_K}\right)^{1-\delta_{p,P}} \mathrm{Y}_l^{m*}(\hat{\mathbf{K}}) \, . \tag{4.23}$$

We identify the polarisation coefficient p = TE (TM) with 1 (2) and P = E (M) accordingly with 1

(2) as before. An angle addition theorem for spherical harmonics allows us to carry out the sum over m with [98, p. 164]

$$P_l(\cos(\Theta)) = \frac{4\pi}{2l+1} \sum_{m=-l}^{l} \left(Y_l^m(\hat{\mathbf{K}}_i)\right)^* Y_l^m(\hat{\mathbf{K}}_j) \,, \tag{4.24}$$

where the argument of the Legendre polynomials of order l depends on the angle between the incident and the reflected wave vector, illustrated in Fig. 4.1, and for imaginary frequencies defined by

$$\cos\Theta = \hat{\mathbf{K}}_i \cdot \hat{\mathbf{K}}_j = -\frac{1}{\mathcal{K}^2}\left(\mathbf{k}_i \cdot \mathbf{k}_j + \kappa_i \kappa_j\right) \,. \tag{4.25}$$

After introducing the basis transformations coefficients (4.22) and (4.23) into Eq. (4.21) and performing the sum over m with (4.24), we obtain the following expression for the reflection matrix elements in the plane-wave basis

$$\begin{aligned} \langle \mathbf{k}_j, p_j, \pm|\mathcal{R}|\mathbf{k}_i, p_i, \mp\rangle = \frac{2\pi}{\mathcal{K}\kappa_j} \big[& A_{j,i} S_{p_j,p_i}(\Theta) + (-1)^{p_j+p_i} B_{j,i} S_{\bar{p}_j,\bar{p}_i}(\Theta) \\ & - (-1)^{p_j} C_{j,i} S_{\bar{p}_j,p_i}(\Theta) + (-1)^{p_i} D_{j,i} S_{p_j,\bar{p}_i}(\Theta) \big] \,. \end{aligned} \tag{4.26}$$

The bar over a polarisation refers to the other polarisation, i.e. $\bar{p} = \mathrm{TE}$ if $p = \mathrm{TM}$ and vice versa. $S_{p,p'}$ defines the amplitude scattering matrix elements [80] for a bi-isotropic sphere, which are given by

$$S_{p,p'}(\Theta) = \sum_{l=1}^{\infty} \frac{2l+1}{l(l+1)} \left[r_l^{(P,P')} \tau_l(\cos\Theta) + (-1)^{P'-P} r_l^{(\bar{P},\bar{P}')} \pi_l(\cos\Theta) \right] \,, \tag{4.27}$$

where $p = \mathrm{TM(TE)}$ corresponds to $P = \mathrm{E(M)}$. The angular functions $\pi_l(\cos\Theta)$ and $\tau_l(\cos\Theta)$ are defined by [80]

$$\pi_l(z) = P_l'(z) = \frac{P_l^1(z)}{\sqrt{z^2-1}} \,, \qquad \tau_l(z) = -z\pi_l(z) + l(l+1)P_l(z) \,. \tag{4.28}$$

The coefficients $A_{j,i}, B_{j,i}, C_{j,i}$ and $D_{j,i}$ account for the conversion from the scattering plane (S) to the Fresnel plane (F), both illustrated in Fig. 4.1. They are given by [33]

$$A_{j,i} = A(\hat{\mathbf{K}}_j, \hat{\mathbf{K}}_i) = \frac{\mathcal{K}^4 \cos(\phi_{j,i}) - \left[\kappa_i\kappa_j + k_i k_j \cos(\phi_{j,i})\right]\left[k_i k_j + \kappa_i \kappa_j \cos(\phi_{j,i})\right]}{\mathcal{K}^4 - \left[\kappa_i\kappa_j + k_i k_j \cos(\phi_{j,i})\right]^2} \,, \tag{4.29a}$$

$$B_{j,i} = B(\hat{\mathbf{K}}_j, \hat{\mathbf{K}}_i) = -\frac{\mathcal{K}^2 k_i k_j \sin^2(\phi_{j,i})}{\mathcal{K}^4 - \left[\kappa_i\kappa_j + k_i k_j \cos(\phi_{j,i})\right]^2} \,, \tag{4.29b}$$

$$C_{j,i} = C(\hat{\mathbf{K}}_j, \hat{\mathbf{K}}_i) = +\mathcal{K} \sin(\phi_{j,i}) \frac{\kappa_j k_i^2 + \kappa_i k_i k_j \cos(\phi_{j,i})}{\mathcal{K}^4 - \left[\kappa_i\kappa_j + k_i k_j \cos(\phi_{j,i})\right]^2} \,, \tag{4.29c}$$

$$D_{j,i} = D(\hat{\mathbf{K}}_j, \hat{\mathbf{K}}_i) = -\mathcal{K} \sin(\phi_{j,i}) \frac{\kappa_i k_j^2 + \kappa_j k_i k_j \cos(\phi_{j,i})}{\mathcal{K}^4 - \left[\kappa_i\kappa_j + k_i k_j \cos(\phi_{j,i})\right]^2} \,, \tag{4.29d}$$

where $\phi_{j,i} = \phi_{K_j} - \phi_{K_i}$. Note that in the zero-frequency limit ($\mathcal{K} = 0$), expect for $A_{j,i}$, all other polarisation conversion coefficient yield zero and $A_{j,i} = 1$. The same holds for $\mathbf{k}_i = \mathbf{k}_j$. We will employ this simplification on several occasions in this thesis.

We note that in the isotropic limit, the Mie reflection coefficient $r_l^{(\mathrm{E,M})}$ and $r_l^{(\mathrm{M,E})}$ vanish and the reflection matrix elements (4.26) agree with the ones presented in Ref. [33].

4.2 Scattering at a large sphere, the geometrical optics regime

The Casimir interaction between large spheres is of particular interest. We thus analyse the reflection at large bi-isotropic spheres. First, we determine the expression for the reflection coefficients and follow up with the expansion of the scattering amplitudes. The discussion shown in the following is valid for finite frequency, but the zero-frequency limit is discussed in detail in the next Section. The general approach is demonstrated for the PEMC spheres. Results for bi-isotropic spheres are presented in Appendix B.2.

4.2.1 Reflection coefficients for a large sphere

We derive the asymptotic expansion of the Mie coefficients (4.11) and (4.16) by employing the Debye expansion of the modified Bessel functions for $x = \mathcal{K}R \gg 1$. With the expansion of the logarithmic derivatives of the Bessel functions of the first (A.3a) and second kind (A.3b), we find for (4.14)

$$\{I,x\} \approx \sqrt{1+\Lambda^2} + \frac{1}{2x}\frac{\Lambda^2}{1+\Lambda^2}\,, \qquad \{K,x\} \approx -\sqrt{1+\Lambda^2} + \frac{1}{2x}\frac{\Lambda^2}{1+\Lambda^2}\,, \tag{4.30}$$

where we introduced $\Lambda = \lambda/x$ with $\lambda = l + 1/2$. The ratio of the Bessel functions defined in Eq. (4.15) yields together with (A.1)

$$C_l(x) \approx (-1)^l \frac{\mathrm{e}^{\Psi(\Lambda)}}{2}\left[1 + \frac{c(\Lambda)}{x}\right], \qquad c(\Lambda) = \frac{1}{4\sqrt{1+\Lambda^2}} - \frac{5\Lambda^2}{12(1+\Lambda^2)^{3/2}}\,, \tag{4.31}$$

where the argument of the exponential is given by

$$\Psi(\Lambda) = 2x\left[\sqrt{1+\Lambda^2} - \Lambda \operatorname{arcsinh}(\Lambda)\right]\,. \tag{4.32}$$

With the above-introduced expression, we find that the Mie reflection coefficients (4.11) and (4.16), can be cast to the following form

$$r_l^{(P,P')} = (-1)^l \frac{\mathrm{e}^{\Psi}}{2} r_{p,p'}(\Lambda)\left[1 + \frac{\rho_{p,p'}(\Lambda)}{x} + O(x^{-2})\right]\,. \tag{4.33}$$

The coefficient $r_{p,p'}(\Lambda)$ accounts for the leading-order term, while $\rho_{p,p'}(\Lambda)$ presents the leading correction in the $x \gg 1$ expansion. As mentioned above, we are only going to present the expansion for the PEMC spheres here, the corresponding terms for general bi-isotropic materials can be found in Appendix B.2. The leading terms for PEMC spheres are according to Eqs. (4.17) and (4.18) given by

$$r_{\mathrm{TM,TM}} = \cos(2\theta)\,, \qquad r_{\mathrm{TE,TE}} = -\cos(2\theta)\,, \qquad r_{\mathrm{TE,TM}} = r_{\mathrm{TM,TE}} = -\sin(2\theta)\,. \tag{4.34}$$

Recall that the material parameter θ takes values between 0 and $\pi/2$, accounting for a PEC and PMC. The subleading terms in Eq. (4.33) yield

$$\rho_{\mathrm{TM,TM}}(\Lambda) = c(\Lambda) + \frac{\cos^2(\theta)}{\cos(2\theta)}\frac{\Lambda^2}{(1+\Lambda^2)^{3/2}}\,, \qquad \rho_{\mathrm{TE,TE}}(\Lambda) = c(\Lambda) - \frac{\sin^2(\theta)}{\cos(2\theta)}\frac{\Lambda^2}{(1+\Lambda^2)^{3/2}}\,, \tag{4.35a}$$

$$\rho_{\mathrm{TM,TE}}(\Lambda) = \rho_{\mathrm{TE,TM}}(\Lambda) = c(\Lambda) + \frac{1}{2}\frac{\Lambda^2}{(1+\Lambda^2)^{3/2}}\,, \tag{4.35b}$$

where $c(\Lambda)$ (4.31) defines the leading correction of $C_l(x)$. The term appears as a prefactor for all reflection coefficients and thus does not depend on the explicit material properties.

4.2.2 Amplitude scattering matrix for a large sphere

The expansion in Eq. (4.33) is sufficient for calculations in the multipole representation of the reflection operator but not for the plane-wave representation. There, it is necessary to evaluate the sum over angular momenta l of the scattering amplitudes (4.26). The localization principle [108] plays an important role in this expansion. According to this principle, the scattering of a ray with an impact parameter b on the sphere (see Fig. 4.2) is dominated by angular momenta of the order of $\mathcal{K}b$. Given the localization principle, we must account for angular momenta $\lambda = l + 1/2 \lesssim x$. Since the size parameter $x = \mathcal{K}R$ for a fixed frequency $\mathcal{K}$ becomes large for large radii R, we can approximate the sums in Eq. (4.27) by integrals over λ [34]

$$S_{p,p'} = 2\sum_{l=1}^{\infty}(l+1/2)h(l+1/2) \approx 2\int_{1/2}^{\infty}\mathrm{d}\lambda\lambda h(\lambda)\,. \tag{4.36}$$

The summands $h(l+1/2)$ of the amplitudes scattering matrix elements involve the reflection coefficients and the angular functions τ_l and π_l, which we expand according to (A.6) and thus find for the term of the scattering amplitudes the following approximation

$$\begin{aligned} h(l+1/2) &= r_l^{(P,P')}\frac{\tau_l(\cosh(\Theta))}{l(l+1)} + (-1)^{P'-P}r_l^{(\bar{P},\bar{P}')}\frac{\pi_l(\cosh(\Theta))}{l(l+1)} \\ &\approx \frac{(-1)^l \mathrm{e}^{\lambda u}}{\sqrt{2\pi\lambda\sinh(u)}}\left[r_l^{(P,P')} + \frac{1}{\lambda}\left(\frac{(-1)^{P'-P}}{\sinh(u)}r_l^{(\bar{P},\bar{P}')} - \frac{7}{8}\coth(u)r_l^{(P,P')}\right)\right]\,, \end{aligned} \tag{4.37}$$

where u is defined through $\cosh(u) = -\cosh(\Theta)$ and we also employed the convention that the bar above the polarisation parameter defines the "other" polarisation, e. g. if $P = \mathrm{E}$ then $\bar{P} = \mathrm{M}$. Next, we use the expansion of the reflection coefficients $r_l^{(P,P')}$ we derived earlier in Eq. (4.33) and insert it in the above expression. We have to include the leading and sub-leading terms of the expansions for the first term in the brackets, while the leading order is sufficient for the Mie coefficients in the round brackets. Combining the expansions and rewriting the sum over angular momenta as integral as described above leads to the following expression for the amplitudes scattering matrix elements

$$S_{p,p'} \approx -\mathrm{i}^{p'-p}\frac{x^{3/2}}{\sqrt{2\pi\sinh(u)}}\int_{1/x}^{\infty}\mathrm{d}\Lambda g_{p,p'}(\Lambda)\mathrm{e}^{-xf(\Lambda)}\,, \tag{4.38}$$

where we substituted $\Lambda = \lambda/x$. The argument of the exponential combines the exponential scaling

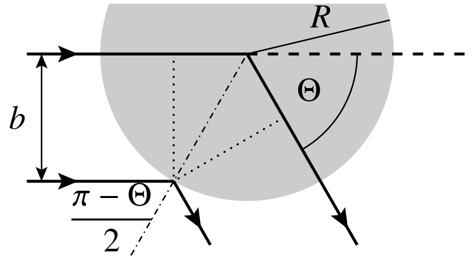

Figure 4.2: Scattering geometry at a sphere of radius R for a scattering angle Θ. The corresponding impact parameter b in ray optics is given by $R\cos(\Theta/2)$. The total path difference between rays reflected at the surface and the centre (denoted by the dotted lines) is given by $2R\sin(\Theta/2)$.

(4.31) of the reflection coefficients and the angular functions (4.37) and yields

$$f(\Lambda) = -\Psi(\Lambda)/x - \Lambda u = -2\sqrt{1+\Lambda^2} + 2\Lambda\operatorname{arcsinh}(\Lambda) - \Lambda u\,. \tag{4.39}$$

The term $g_{p,p'}$ combines all the remaining terms and is given by

$$g_{p,p'}(\Lambda) = \sqrt{\Lambda}r_{p,p'}(\Lambda)\left[1 + \frac{1}{x}\left(\rho_{p,p'}(\Lambda) + \frac{(-1)^{p'-p}}{\mathrm{i}\Lambda\sin(\Theta)}\frac{r_{\bar{p},\bar{p}'}(\Lambda)}{r_{p,p'}(\Lambda)} - \frac{7}{8}\frac{\mathrm{i}\cot(\Theta)}{\Lambda}\right)\right]\,. \tag{4.40}$$

f as a function of Λ has one global minimum, which means that the main contribution to the integral comes from the function around this minimum. The saddle point (sp) is found at [35]

$$\Lambda_{\mathrm{sp}} = \mathrm{i}\cos(\Theta/2) = \mathrm{i}\sin((\pi-\Theta/2))\,. \tag{4.41}$$

We expand f and $g_{p,p'}$ in a Taylor expansion around this minimum with $f(\Lambda) \approx \sum_{n=1}^{4} f_{\mathrm{sp}}^{(n)}(\Lambda-\Lambda_{\mathrm{sp}})^n/n!$, where $f_{\mathrm{sp}}^{(n)}$ denotes the n-th derivative evaluated at the saddle Λ_{sp}. A similar expansion can also be performed for $g_{p,p'}$. The size parameter x is large, we can thus apply the saddle-point approximation discussed in Sec. A.6.2, which leads to the following expression for the scattering amplitude of large bi-isotropic spheres

$$\begin{aligned} S_{p,p'} \approx \frac{x g_{p,p'}(\Lambda_{\mathrm{sp}})\mathrm{e}^{-xf_{\mathrm{sp}}}}{\sqrt{f_{\mathrm{sp}}^{(2)}\sinh(u)}}\Bigg[1 + \frac{1}{2x}\Bigg(&\frac{g_{p,p'}^{(2)}(\Lambda_{\mathrm{sp}})}{g_{p,p'}(\Lambda_{\mathrm{sp}})}\left(f_{\mathrm{sp}}^{(2)}\right)^{-1} - \frac{g_{p,p'}^{(1)}(\Lambda_{\mathrm{sp}})}{g_{p,p'}(\Lambda_{\mathrm{sp}})}f_{\mathrm{sp}}^{(3)}\left(f_{\mathrm{sp}}^{(2)}\right)^{-2} \\ &-\frac{1}{4}f_{\mathrm{sp}}^{(4)}\left(f_{\mathrm{sp}}^{(2)}\right)^{-2} + \frac{5}{12}\left(f_{\mathrm{sp}}^{(3)}\right)^2\left(f_{\mathrm{sp}}^{(2)}\right)^{-3}\Bigg)\Bigg]\,. \end{aligned} \tag{4.42}$$

We note that the leading corrections of the scattering matrix elements consist of two contributions. One part includes the corrections from the leading saddle-point approximation, which are contained in $g_{p,p'}(\Lambda_{\mathrm{sp}})$. The other part arises from the next-to-leading order in the saddle-point approximation. It is thus sufficient for the derivatives of $g_{p,p'}$, appearing in Eq. (4.42), to consider only the leading term $\sqrt{\Lambda}r_{p,p'}(\Lambda)$, since the subleading term would contribute to higher-order corrections. This allows us to express the derivatives of $g_{p,p'}(\Lambda)$ only in terms of derivatives of $r_{p,p'}(\Lambda)$

$$\frac{g_{p,p'}^{(1)}}{g_{p,p'}} = \frac{1}{2\Lambda_{\mathrm{sp}}} + \frac{r_{p,p'}^{(1)}}{r_{p,p'}}\,, \qquad \frac{g_{p,p'}^{(2)}}{g_{p,p'}} = -\frac{1}{4\Lambda_{\mathrm{sp}}^2} + \frac{1}{\Lambda_{\mathrm{sp}}}\frac{r_{p,p'}^{(1)}}{r_{p,p'}} + \frac{r_{p,p'}^{(2)}}{r_{p,p'}}\,, \tag{4.43}$$

where all functions are evaluated at the saddle Λ_{sp}.

After inserting the saddle point (4.41) into (4.42), and performing some basic algebraic transformations, the asymptotic expansion of the scattering amplitudes for large aspect ratio x yields

$$S_{p,p'} = \frac{x}{2} r_{p,p'}(\Lambda_{\mathrm{sp}}) \mathrm{e}^{-2x\sin(\Theta/2)} \left[1 + \frac{s_{p,p'}}{x} + O(x^{-2})\right] \tag{4.44}$$

with the leading corrections given by

$$\begin{aligned} s_{p,p'} = \rho_{p,p'}(\Lambda_{\mathrm{sp}}) &+ \frac{1 - 10\sin^2(\Theta/2)}{12\sin^2(\Theta/2)} - \frac{1}{2\sin(\Theta/2)\cos^2(\Theta/2)} \left(1 - (-1)^{p'-p} \frac{r_{\bar{p},\bar{p}'}}{r_{p,p'}}\right) \\ &- \frac{\mathrm{i}\cos(\Theta/2)}{4\sin(\Theta/2)} \frac{r^{(1)}_{p,p'}}{r_{p,p'}} + \frac{\sin(\Theta/2)}{4} \frac{r^{(2)}_{p,p'}}{r_{p,p'}} . \end{aligned} \tag{4.45}$$

The expression is consistent with the well-known Debye expansion of the scattering amplitudes [104], but for imaginary frequencies. The leading term of (4.44) accounts for the direct reflection term. The terms $r_{p,p'}(\Lambda_{\mathrm{sp}})$ agree with the Fresnel reflection coefficients with an incident angle $(\pi - \Theta)/2$ as illustrated in Fig. 4.2 and calculated for general bi-isotropic spheres in Appendix B.2. The leading correction $s_{p,p'}$ accounts for the diffraction corrections.

As shown earlier, the Fresnel reflection coefficients for PEMC materials are only functions of the material parameter (see Eq. (4.34)). They do not depend on the incident angle of the wave. For the leading correction (4.45), all derivatives of the reflection coefficients thus vanish, and we obtain

$$s^{\mathrm{PEMC}}_{p,p'} = \frac{1 - 2\sin^2(\Theta/2)}{2\sin^3(\Theta/2)} - \frac{\cos^2(\Theta/2)}{\sin^3(\Theta/2)} \begin{cases} \frac{\cos^2(\theta)}{\cos(2\theta)} & p = p' = \mathrm{TM} \\ -\frac{\sin^2(\theta)}{\cos(2\theta)} & p = p' = \mathrm{TE} \\ \frac{1}{2} & p' = \bar{p} \end{cases} . \tag{4.46}$$

It is easy to verify that the terms given above agree with the ones obtained in Ref. [34] for a perfect electric conductor ($\theta = 0$).

In Fig. 4.3, we analyse the validity of the asymptotic expansion for the PEMC sphere. We evaluated the amplitude scattering matrix elements for $\cos(\Theta) = -2$ in Fig. 4.3a and for $\cos(\Theta) = -1$ in Fig. 4.3b as function of the size parameter $x = \mathcal{K}R$. In both cases, the panels on the left depict the scattering amplitudes for $\theta = \pi/4$, while the panels on the right show the scattering amplitudes for a perfect magnetic conductor sphere ($\theta = \pi/2$). A similar analysis for perfect electric conductors can be found in Ref. [109]. It is evident from the left panel of Fig. 4.3a, that the polarisation-conserving and polarisation-changing coefficients show a different scaling behaviour. According to our discussion above, the leading order for the polarisation-conserving coefficients is given by the subleading term in Eq. (4.44) for $\theta = \pi/4$. This term is of order $O(1)$, and the subleading term thus scales with $1/x$, as depicted by the dashed line in the left panel. The polarisation-changing coefficients, on the other hand, are proportional to $1/x^2$ as indicated by the solid line. For a perfect magnetic conductor (right panel of Fig. 4.3a), there are no polarisation-changing coefficients and the polarisation-conserving coefficients scale with $1/x^2$. Fig. 4.3a depicts the results for $\cos(\Theta) = -1$. We see that for $\theta = \pi/4$ (left panel), the polarisation-conserving coefficients vanish, while the next-to-leading order for the polarisation-changing coefficients scales with $1/x^4$, as depicted by the dash-dotted line. For $\theta = \pi/2$ (right panel), the polarisation-changing coefficients yield zero while the polarisation-conserving coefficients also scale with $1/x^4$. The different scaling behaviour of the scattering amplitudes for the material parameters θ will directly translate to the behaviour of the Casimir energy for large sphere

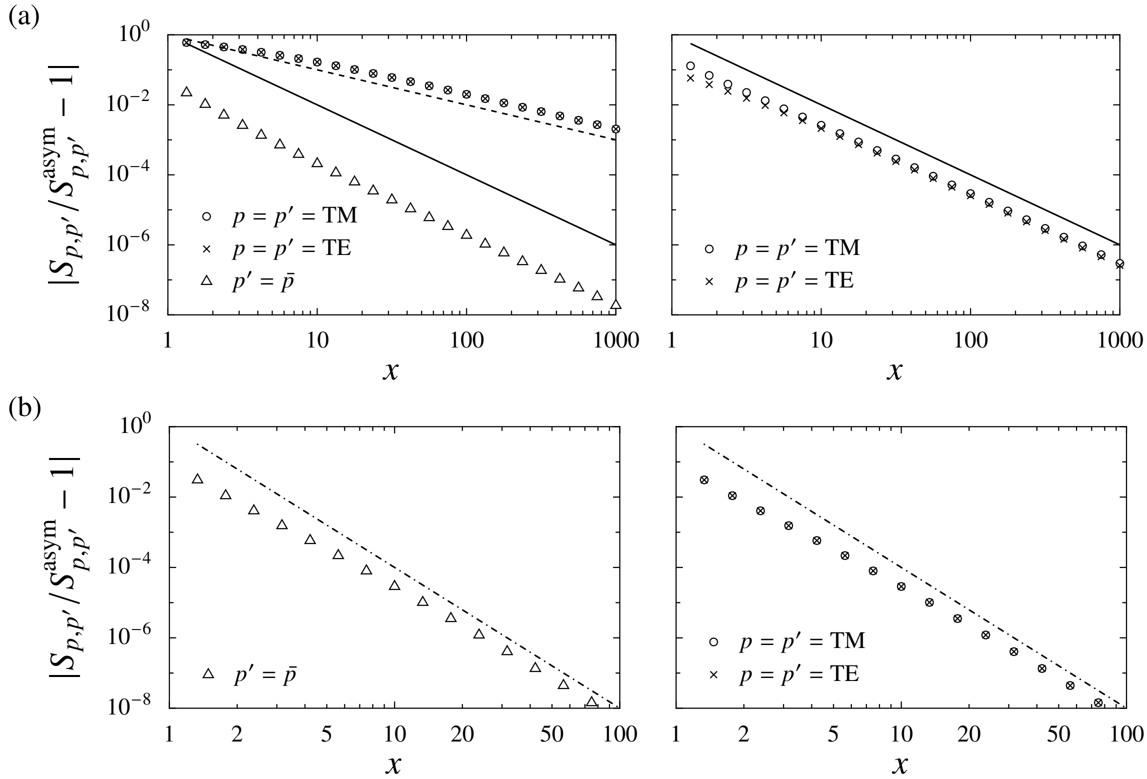

Figure 4.3: Comparison between the scattering amplitudes $S_{p,p'}$ for a PEMC sphere and their asymptotic approximation defined in Eq. (4.44) as function of the aspect ratio x. (a) Relative deviation computed for $\cos(\Theta) = -2$. The left panel shows the results for a PEMC sphere with $\theta = \pi/4$ and the right panel for a PMC sphere ($\theta = \pi/2$). The solid line in both panels indicates a $1/x^2$-scaling, while the dashed line represents a proportionality to $1/x$. (b) Relative deviation computed for $\cos(\Theta) = -2$, where the left and right panels again depict the cases $\theta = \pi/2$ and $\pi/2$. The dash-dotted line indicates a $1/x^4$-scaling.

radii, as we will see later in Chap. 11.

4.3 Low-frequency limit, the Rayleigh regime

This Section will examine the scattering at spherical objects in the limit $x = \mathcal{K}R \to 0$. This limit includes the static case $\mathcal{K} = 0$. The static limit is particularly interesting as it allows for exact calculations of the Casimir interaction, which we will discuss later. Furthermore, the analytical expressions for the reflection coefficients obtained in this Section are also helpful for numerical calculation to avoid instabilities caused by diverging quantities in the low-frequency limit.

4.3.1 Reflection coefficients

We start with the reflection coefficients derived in Sec. 4.1.1 and apply the expansion of the modified Bessel functions for small arguments as presented in Eq. (A.4b). We thus find for the logarithmic derivative of the Bessel functions (4.14), the following expressions

$$\{I, z\} \approx \frac{l+1}{z} + \frac{z}{2}, \qquad \{K, z\} \approx -\frac{l}{z} + \frac{z}{2l-1}. \tag{4.47}$$

Similarly, we apply the expansion for the ratio of the Bessel functions of the first and second kind (4.15), which leads to

$$C_l(x) \approx (-1)^l \frac{[l!]^2}{2(2l+1)[(2l)!]^2}(2x)^{2l+1}. \tag{4.48}$$

The auxiliary functions introduced in Eq. (4.12), thus read

$$A_l^{\mathrm{L,R}} = \frac{l+1}{x}\left[1 - \frac{m_\mp}{m_{\mathrm{L,R}}}\right], \qquad B_l^{\mathrm{L,R}} = \frac{l+1}{x}\left[m_\mp - \frac{1}{m_{\mathrm{L,R}}}\right], \tag{4.49}$$

$$V_l^{\mathrm{L,R}} = \frac{l+1}{x}\left[\frac{m_\mp}{m_{\mathrm{L,R}}} + \frac{l}{l+1}\right], \qquad W_l^{\mathrm{L,R}} = \frac{l+1}{x}\left[\frac{1}{m_{\mathrm{L,R}}} + m_\mp \frac{l}{l+1}\right]. \tag{4.50}$$

Introducing the quantities given above into the four Mie reflection coefficients (4.11) and (4.16), we find a general expression of the form

$$r_l^{(P,P')} = (-1)^l \frac{[l!]^2}{2(2l+1)[(2l)!]^2}\frac{l+1}{l}(2x)^{2l+1}\mathcal{X}_{p,p'}(l) + O\left(x^{2l+2}\right), \tag{4.51}$$

where we again associate the polarisation $p = \mathrm{TM(TE)}$ with $P = \mathrm{E(M)}$. The expansion coefficient $\mathcal{X}_{p,p'}(l)$ accounts for the material properties of the sphere and the surrounding medium. For the polarisation-conserving coefficients, we find

$$\mathcal{X}_{\mathrm{TM,TM}}(l) = \frac{l}{\Delta(l)}\left\{\left[1 - \frac{m_-}{m_{\mathrm{L}}}\right]\left[\frac{1}{m_{\mathrm{R}}} + m_+\frac{l}{l+1}\right] + \left[1 - \frac{m_+}{m_{\mathrm{R}}}\right]\left[\frac{1}{m_{\mathrm{L}}} + m_-\frac{l}{l+1}\right]\right\}, \tag{4.52a}$$

$$\mathcal{X}_{\mathrm{TE,TE}}(l) = \frac{l}{\Delta(l)}\left\{\left[m_- - \frac{1}{m_{\mathrm{L}}}\right]\left[\frac{m_+}{m_{\mathrm{R}}} + \frac{l}{l+1}\right] + \left[m_+ - \frac{1}{m_{\mathrm{R}}}\right]\left[\frac{m_-}{m_{\mathrm{L}}} + \frac{l}{l+1}\right]\right\}, \tag{4.52b}$$

where the function in the denominator is defined as

$$\Delta(l) = (l+1)\left[\frac{1}{m_{\mathrm{L}}} + m_-\frac{l}{l+1}\right]\left[\frac{m_+}{m_{\mathrm{R}}} + \frac{l}{l+1}\right] + \left[\frac{1}{m_{\mathrm{R}}} + m_+\frac{l}{l+1}\right]\left[\frac{m_-}{m_{\mathrm{L}}} + \frac{l}{l+1}\right]. \tag{4.53}$$

The polarisation-mixing coefficients, on the other hand, can be cast to

$$\mathcal{X}_{\mathrm{TM,TE}} = \frac{\mathrm{i}l}{\Delta(l)}\left(\frac{m_-}{m_{\mathrm{L}}} - \frac{m_+}{m_{\mathrm{R}}}\right), \qquad \mathcal{X}_{\mathrm{TE,TM}} = \frac{\mathrm{i}l}{\Delta(l)}\left(\frac{m_-}{m_{\mathrm{R}}} - \frac{m_+}{m_{\mathrm{L}}}\right). \tag{4.54}$$

From Eqs. (4.17) and (4.18), we can obtain the following expression for the expansion coefficients of a PEMC sphere

$$\mathcal{X}_{\mathrm{TM,TM}} = \cos^2(\theta) - \sin^2(\theta)\frac{l}{l+1}, \qquad \mathcal{X}_{\mathrm{TE,TE}} = \sin^2(\theta) - \cos^2(\theta)\frac{l}{l+1}, \tag{4.55a}$$

$$\mathcal{X}_{\mathrm{TM,TE}} = \mathcal{X}_{\mathrm{TE,TM}} = -\sin(\theta)\cos(\theta)\left[1 + \frac{l}{l+1}\right] . \tag{4.55b}$$

We observe that the coefficients are obtained through a duality transformation of the coefficients for a perfect electric conductor [76], which is given by

$$\begin{pmatrix} \mathcal{X}_{\mathrm{TM,TM}} & \mathcal{X}_{\mathrm{TM,TE}} \\ \mathcal{X}_{\mathrm{TE,TM}} & \mathcal{X}_{\mathrm{TE,TE}} \end{pmatrix} = \mathbf{D} \begin{pmatrix} 1 & 0 \\ 0 & -l/(l+1) \end{pmatrix} \mathbf{D}^{-1} , \qquad \mathbf{D} = \begin{pmatrix} \cos(\theta) & \sin(\theta) \\ -\sin(\theta) & \cos(\theta) \end{pmatrix} , \tag{4.56}$$

where $\mathbf{D}^{-1} = \mathbf{D}(-\theta)$. Alternatively, one could also use the coefficients for a perfect magnetic conductor.

For non-magnetic and isotropic media $m_\pm = \sqrt{\epsilon_\mathrm{m}/\epsilon_\mathrm{s}} = 1/m_{\mathrm{L,R}}$, the polarisation mixing and also the magnetic coefficients vanish, while the electric coefficients yield

$$\mathcal{X}_{\mathrm{TM,TM}} = \frac{l(\epsilon_\mathrm{s} - \epsilon_\mathrm{m})}{l\epsilon_\mathrm{s} + (l+1)\epsilon_\mathrm{m}} , \tag{4.57}$$

which is in agreement with the expansion obtained by Ref. [97].

4.3.2 Amplitude scattering matrix elements

Next, we are discussing the amplitude scattering matrix elements for low frequencies. The argument $\cos(\Theta)$ of the angular functions scales like $1/\mathcal{K}^2$ for low frequency, according to Eq. (4.25). We thus employ the large-argument approximation of the angular functions and find together with (A.7)

$$\tau_l(\cos(\Theta)) \approx (-1)^l \frac{(2l)!}{2^l[(l-1)!]^2} \frac{(\mathbf{k}\cdot\mathbf{k}' + kk')^l}{\mathcal{K}^{2l}} , \tag{4.58}$$

while $\pi_l(\cos(\Theta)) \propto \mathcal{K}^2 \tau_l(\cos(\Theta))$ and thus does not contribute to the leading low-frequency asymptotic. Combining all quantities, which enter into the summand of the amplitude scattering matrix elements (4.27), we obtain

$$S_{p,p'} \approx x \sum_{l=1}^{\infty} \mathcal{X}_{p,p'}(l) \frac{y^{2l}}{(2l)!} \tag{4.59}$$

with

$$y = R\sqrt{2\,(\mathbf{k}\cdot\mathbf{k}' + kk')} = 2x\sin(\Theta/2) , \tag{4.60}$$

where we employed that $\cos(\Theta) = 1 - 2\sin^2(\Theta/2)$.

In certain limiting cases, it is possible to carry out the sum over angular momenta analytically, which will be discussed in detail in Chap. 9, when we study the low-frequency contributions to the Casimir interaction. Earlier, we analysed the regime of large sphere radii for finite frequency. Now, we will derive the corresponding expressions for the low-frequency limit. For large radii, y also becomes large. The main contribution to the sum will thus come from large momenta, which allows us, similar to before, to transform the sum over angular momenta into an integral. Furthermore, we approximate the factorial with the Stirling formula $(2l)! \approx \sqrt{4\pi l}(2l)^{2l}\mathrm{e}^{-2l}$ and introduce a scaled variable $\Lambda = 2l/y$. The amplitude scattering matrix elements thus yield [109]

$$S_{p,p'} \approx \frac{x}{\sqrt{2\pi y}} \int_{2/y}^{\infty} \mathrm{d}\Lambda\, \frac{\mathcal{X}_{p,p'}(y\Lambda/2)}{\sqrt{\Lambda}} \mathrm{e}^{-yf(\lambda)} , \tag{4.61}$$

where $f(\Lambda) = \Lambda - \Lambda \log(\Lambda)$. f has a minimum at $\Lambda_{\mathrm{sp}} = 1$ which means, that due to e^{-yf} all other contributions decay exponentially. We can thus employ the saddle-point approximation (see Sec. A.6.2) to evaluate the integral given above, which leads to

$$S_{p,p'} \approx \frac{x}{2} \mathcal{X}_{p,p'}(y/2) \mathrm{e}^{2x \sin(\Theta/2)} . \tag{4.62}$$

It can now easily be shown, that for $y \gg 1$ the expansion coefficients $\mathcal{X}_{p,p'}(y/2)$ agree with the respective Fresnel coefficients for a bi-isotropic plane presented in Sec. B.2

$$r_{p,p'} \approx \lim_{y \to \infty} \mathcal{X}_{p,p'}(y/2) . \tag{4.63}$$

From (4.55), we immediately recover the Fresnel reflection coefficients for a PEMC plane (4.34).

Part II

Trapping spherical particles with a vortex beam

This part of the thesis investigates how chiral or non-chiral microspheres interact with a vortex beam. Specifically, we consider circularly polarised Laguerre-Gaussian beams. We determine an explicit analytical expression for the optical force components on a spherical object.

It is crucial to have an accurate model for studying the behaviour of nano- and micro-sized particles in vortex beams. We thus start in Chap. 5 by modelling the focused laser field for realistic applications. Experimental setups usually include optical aberrations, which, for example, arise from misalignments of the optical components and thus lead to a deterioration of the trapping efficiency. We include such effects in our theory. We solve the scattering problem at the spherical object by computing the multipole expansion of the focused field and applying standard Mie theory. The optical force components are then obtained by integrating the Maxwell stress tensor over a surface which encloses the trapped sphere. We provide explicit expressions for the force components which are then evaluated numerically. We apply our theory in Chap. 6, where we examine the different trapping regimes of a dielectric or chiral sphere in a vortex beam. In Chap. 7, we introduce an *in situ* method which allows us to determine the radius of trapped microspheres with nanometer-precision. The method utilizes our theoretical model to fit experimentally obtained data of spheres trapped by vortex beams.

5 | Mie-Debye theory for optical forces including optical aberrations

Optical trapping of objects involves highly focused laser beams, meaning beams that are focused up to the diffraction limit $\lambda/2\mathrm{NA}$ [110], where λ is the wavelength of the laser beam and NA is the numerical aperture, which defines the opening cone of the focused beam. Focusing with a high NA (NA $>$ 1) is necessary to create a gradient field, which ensures objects are stably trapped. Furthermore, it reduces scattering forces that push the object in the propagation direction of the beam [61]. Early theoretical models applied the paraxial approximation for focused beams [111], where it is assumed that the angle between a ray passing through an imaging system and the optical axis is small. However, this assumption is invalid for high NA objectives. Also, the electromagnetic field within the paraxial models is only transversely polarised to the propagation direction, which also does not reflect reality. The focusing leads to longitudinal polarisation components [112, 113], which is a direct consequence of Heisenberg's uncertainty principle for spatially confined photons.

A more realistic description of the focused beam comes with the vectorial diffraction theory introduced by Stratton and Chu [114]. Within this theory, the field at any observation point (e. g. the focus) is given as a superposition of planar waves propagating from a reference surface towards that point. If the reference surface is spherical, as required for focused beams, the theory is commonly known as the Debye-Wolf diffraction integral [115]. This method can be applied to different input fields that enter the imaging system. Usually, a paraxial beam model is employed at the entrance. In this particular study, we will focus on trapping with a Laguerre-Gaussian field as input. We include primary optical aberrations for a more realistic description of experimental setups.

This Chapter establishes the theoretical foundation for investigating the trapping of spherical objects in vortex beams. Our approach builds on previous results for a Gaussian beam with aberrations [116, 117] and a Laguerre-Gaussian beam without aberrations [118]. The general setup will be introduced in Sec. 5.1. We will use the Debye-Wolf integral representation for the electromagnetic field at the exit of the objective. To account for modulations of the field through the optical system, we will apply the vectorial ray tracing method. We consider the trapping of spherical objects with radii in the range of the beam wavelength. Hence, it is necessary to apply Mie-theory to obtain the scattered field. Based on the results for the incident and scattered field, we derive an expression for the optical force components (see Sec. 5.2).

5.1 Vectorial diffraction and focusing through an interface

Our studied system is shown in Fig. 5.2a. We consider a monochromatic Laguerre-Gaussian beam at the entrance of an imagining system. The beam is focused through an interface into a sample region of refractive index n_w, where the trapped particle is located. In the following, we present an expression for the electromagnetic field in the sample region.

Laguerre-Gaussian (LG) beam modes $\mathrm{LG}_{p,\ell}$ have an azimuthal phase $\exp(\mathrm{i}\ell\phi)$, where the topological charge ℓ defines the orbital angular momentum carried per photon. The wavefront of a vortex beam is helicoidal, with the sign of ℓ determining the handedness of the vortex. The modulus $|\ell|$ defines the number of helices within one wavelength, as illustrated in the bottom panels of Fig. 5.1 for $\ell = 1$ and 2. $\mathrm{LG}_{p,\ell}$ modes have $p + 1$ intensity nodes. In this work, we will only consider the

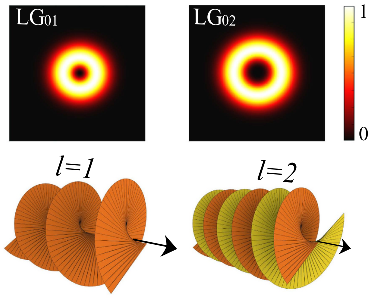

Figure 5.1: Illustration of the Laguerre-Gaussian modes $\mathrm{LG}_{0,\ell}$ for $\ell = 1$ and $\ell = 2$. The top panels present the intensity profiles and the bottom panels show the phase structure of the beams. Taken from Ref. [120].

case $p = 0$, where the transverse intensity profile is ring-shaped (see intensity profiles in Fig. 5.1). The electric field vector for a $\mathrm{LG}_{0,\ell}$ mode, at the entrance of the objective is defined by [119]

$$\mathbf{E}_{\mathrm{inc}}(\mathbf{r}) = E_0 \left(\frac{\sqrt{2}\rho}{w_0} \right)^{|\ell|} \exp\left(-\frac{\rho^2}{w_0^2} \right) \mathrm{e}^{\mathrm{i}\ell\phi} \hat{\varepsilon}_\sigma \,, \tag{5.1}$$

where $\hat{\varepsilon}_\sigma = (\hat{\mathbf{x}} + \mathrm{i}\sigma\hat{\mathbf{y}})/\sqrt{2}$ is the unit vector of a left- ($\sigma = 1$) or right- ($\sigma = -1$) circularly polarised wave $\mathbf{E}_{\mathrm{inc}}(\mathbf{r})\mathrm{e}^{\mathrm{i}K_0 z}$ traveling along the z-direction with wave vector $\mathbf{K}_0 = K_0\hat{z}$. The field amplitude varies with distance $\rho = \sqrt{x^2 + y^2}$ from the centre axis of the beam. w_0 defines the so-called beam-waist. Laguerre-Gaussian beams with $\ell = 0$ describe the standard Gaussian beam, used in most optical tweezer setups. It follows from (5.1), that the ring of highest intensity is defined by $\rho = w_0\sqrt{|\ell|/2}$. Hence, the radius of the ring increases with the topological charge.

The field in the image space of an optical system is described by vectorial diffraction integrals, with the Debye-Wolf integral [115, 121] as the most common representation. At an observation point $\mathbf{r}$ near the focus, the field is determined by a field $\mathbf{E}_{\mathrm{rs}}$ at a Gaussian reference surface (rs) within this approximation. The reference surface is assumed to be far from the observation point [122]. The angular spectrum representation of the electric field in the vicinity of the focus yields [121, 123]

$$\mathbf{E}(\mathbf{r}) = \frac{-\mathrm{i}Kf\mathrm{e}^{\mathrm{i}Kf}}{2\pi} \int_{\Omega_{\mathrm{m}}} \mathrm{d}\Omega \mathbf{E}_{\mathrm{rs}}(\theta, \phi) \mathrm{e}^{\mathrm{i}\mathbf{K}_{\mathrm{w}}\cdot\mathbf{r}} \,, \tag{5.2}$$

where f defines the focal length and $K = n_s K_0$ determines the modulus of the wave vector at the exit of the objective $\mathbf{K} = K\hat{\mathbf{K}}$ with unit vector $\hat{\mathbf{K}} = (\sin(\theta)\cos(\phi), \sin(\theta)\sin(\phi), \cos(\theta))$, as it is illustrated in Fig. 5.2a. The wave vector in the sample region is defined by $\mathbf{K}_{\mathrm{w}} = K_{\mathrm{w}}\hat{\mathbf{K}}_{\mathrm{w}}$, where $\hat{\mathbf{K}}_{\mathrm{w}} = (\sin(\theta_{\mathrm{w}})\cos(\phi_{\mathrm{w}}), \sin(\theta_{\mathrm{w}})\sin(\phi_{\mathrm{w}}), \cos(\theta_{\mathrm{w}}))$ with $K_{\mathrm{w}} = n_{\mathrm{w}}K_0$ and the solid angle Ω_{m} accounts for the numerical aperture of the system. Hence, the electric field at the objective exit is a superposition of plane waves with wave vectors spanning a cone defined by $\phi \in [0, 2\pi]$ and $\theta \in [0, \theta_{\mathrm{m}}]$. In the following, we will specify the value of the maximal polar angle θ_{m}.

5.1.1 Vectorial ray tracing

The electric field at the spherical reference frame can be obtained by tracing the field at the entrance of the objective given by Eq. (5.1) through the optical system to the sample region. The macroscopic size of the optical system justifies the use of geometrical optics to describe the focusing process [124]. The incident field $\mathbf{E}_{\mathrm{inc}}$ is focused by a lens and then transmitted through an interface, which leads to

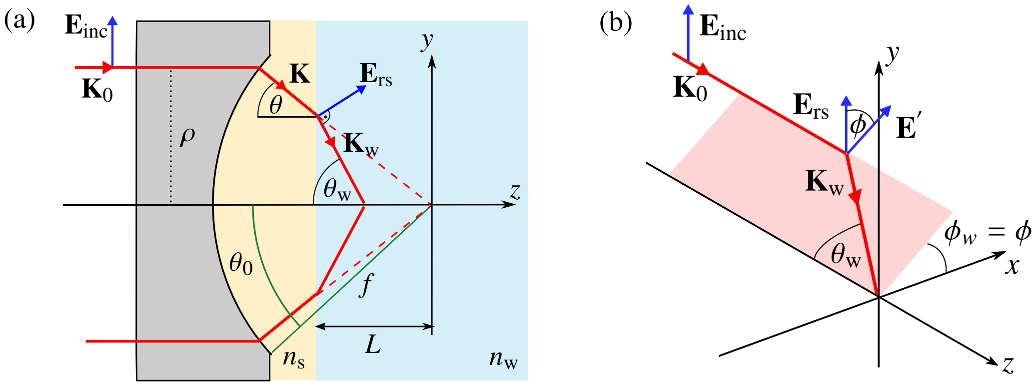

Figure 5.2: Focusing a beam through an interface. Figure (a) depicts an electromagnetic wave travelling along the z-direction with wave vector $\mathbf{K}_0 = K_0\hat{\mathbf{z}}$, which is refracted at an objective into a medium with refractive index n_{s}. The direction of the wave vector $\mathbf{K}$ in the medium at the exit of the objective is defined by the polar angle θ, which takes values from 0 to $\theta_0 = \sin^{-1}(\mathrm{NA}/n_{\mathrm{s}})$, where NA is the numerical aperture of the objective. The optical system is assumed to fulfil the sine condition with $\rho = f\sin(\theta)$, where f is the focal length. The electromagnetic wave with wave vector $\mathbf{K}$ enters a second medium of index n_{w} and is refracted once more with a refraction angle θ_{w}, which defines the direction of the wave vector $\mathbf{K}_{\mathrm{w}}$. $\mathbf{E}_{\mathrm{rs}}$ defines the corresponding electric field vector. Without an interface ($n_{\mathrm{s}} = n_{\mathrm{w}}$) rays focus all in one point, which defines the origin of the coordinate system. The distance of this nominal focus to the interface is denoted as L. Figure (b) represents the transformation of the electric field vector during the focusing as described in Eq. (5.3). After passing the interface, the incident field vector $\mathbf{E}_{\mathrm{inc}}$ transforms into $\mathbf{E}' \propto \mathbb{R}_2(\theta_{\mathrm{w}})\mathbb{R}_3(\phi)\mathbf{E}_{\mathrm{inc}}$ which leads to a polarisation change compared to the initial input field. The corrected vector field is obtained by rotating around the z-axis about $-\phi$: $\mathbf{E}_{\mathrm{rs}} \propto \mathbb{R}_3^{-1}(\phi_{\mathrm{w}})\mathbf{E}'$, where the azimuth angle in the sample region ϕ_{w} is the same as the polar angle ϕ at the exit of the objective.

the following expression for the field $\mathbf{E}_{\mathrm{rs}}$ at the reference surface

$$\mathbf{E}_{\mathrm{rs}} = \mathbb{R}_3^{-1}(\phi_{\mathrm{w}})\mathbb{R}_2(\theta_{\mathrm{w}})\mathrm{e}^{\mathrm{i}\Psi_{\text{g-w}}(\theta)}T(\theta)\mathbb{R}_2^{-1}(\theta)\mathrm{e}^{\mathrm{i}\Psi_{\mathrm{ast}}(\theta,\phi)}A(\theta)\mathbb{R}_2(\theta)\mathbb{R}_3(\phi)\mathbf{E}_{\mathrm{inc}}\,. \tag{5.3}$$

It is important to note that these transformations describe standard setups in optical tweezers experiments, particularly the one we discuss in Chap. 7.

We apply vectorial ray tracing as described in Refs. [125–127] to obtain the electromagnetic field in the sample region. Within this approach, so-called Jones matrices transform the field vectors as they pass through the optical systems. In our case, the ray enters the objective at the azimuthal angle ϕ, where it is refracted by an angle θ into a medium of refractive index n_{s}. This transformation can be described by the first two rotation matrices from the right to the left in Eq. (5.3), which are given by

$$\mathbb{R}_3(\phi) = \begin{pmatrix} \cos(\phi) & \sin(\phi) & 0 \\ -\sin(\phi) & \cos(\phi) & 0 \\ 0 & 0 & 1 \end{pmatrix}, \qquad \mathbb{R}_2(\theta) = \begin{pmatrix} \cos(\theta) & 0 & \sin(\theta) \\ 0 & 1 & 0 \\ -\sin(\theta) & 0 & \cos(\theta) \end{pmatrix}. \tag{5.4}$$

The input beam is focused aplanatically [128], which means that the field intensity is modulated in such a way that $|\mathbf{E}_{\mathrm{rs}}|^2 = \cos(\theta)|\mathbf{E}_{\mathrm{inc}}|^2$, to ensure energy conservation upon transforming from a plane wavefront to a spherical wavefront. We assume that the medium at the entrance and exit of the objective are the same. The electric field amplitude is thus modulated by a factor $A(\theta) = \sqrt{\cos(\theta)}$.

Note also that we are not accounting for the modulation of the field amplitude due to the transmission through the objective. We assume that the Fresnel transmission coefficients [80] are almost one, due to near index matching between the optical system and the medium at the exit.

Misalignment in the optical system can lead to optical aberrations like astigmatism and coma. Here, we are going to take astigmatism into account, which includes the effect of an elongation of the focal spot in a direction perpendicular to the propagation axis, and thus breaking the rotational symmetry of the incident beam [129], through the phase factor $e^{i\Psi_{\text{ast}}(\theta,\phi)}$ introduced in Eq. (5.3). This asymmetry in the field intensity leads to interesting effects, as we will discuss in more detail in Chap. 7. The direction of elongation is defined by an angle ϕ_{ast} measured with respect to the x-axis, and the amplitude A_{ast} describes the amount of elongation. The Zernike polynomials present the phase-shift due to the astigmatism [117]

$$\Psi_{\text{ast}}(\theta,\phi) = 2\pi A_{\text{ast}} \left(\frac{\sin(\theta)}{\sin(\theta_0)}\right)^2 \cos\left[2(\phi_{\text{ast}} - \phi)\right] \ . \tag{5.5}$$

As the light ray passes from the medium with refractive index n_{s} to the medium with n_{w}, it gets refracted. Fresnel transmission coefficients for the transverse electric and magnetic field modes generally account for refraction at an interface. However, we assume that the transmission coefficients are nearly identical due to near-index matching. As a result, we introduce a single modulation amplitude which accounts for the transmission [116, 130]

$$T(\theta) = \frac{2\cos(\theta)}{\cos(\theta) + N\cos(\theta_{\text{w}})}\,, \qquad N = \frac{n_{\text{w}}}{n_{\text{s}}}\,. \tag{5.6}$$

The polar angles θ and θ_{w} are related through Snell's law: $n_{\text{s}}\sin(\theta) = n_{\text{w}}\sin(\theta_{\text{w}})$. When light travels from one medium to another, its phase velocity changes. The phase shift gets larger as the incident angle θ increases, leading to a focus distortion. Consequently, for $n_{\text{s}} > n_{\text{w}}$, the rays intersect on the optical axis at a position between the interface and the nominal focus. The nominal focus is defined by the position of the focus when there is no interface, as depicted by the red dashed lines in Fig. 5.2a. The distance between the nominal focus and the interface is denoted by L. The function that defines the phase shift is called the spherical aberration function [131], which is defined by

$$\Psi_{\text{g-w}}(\theta) = LK_{\text{w}}\cos(\theta_{\text{w}}) - \tilde{L}K\cos(\theta)\,, \tag{5.7}$$

with the distance L between the paraxial focal and the interface measured in the sample region, while $\tilde{L} = L/N$ defines the distance measured in the medium with refractive index n_{s}. We change the direction of the vector field by performing the rotations $\mathbb{R}_2(\theta_{\text{w}})\mathbb{R}_2^{-1}(\theta)$.

In total, the direction of the electric field vector is defined by $\mathbf{E}' \propto \mathbb{R}_2(\theta_{\text{w}})\mathbb{R}_3(\phi)\mathbf{E}_{\text{inc}}$, depicted in Fig. 5.2b. After performing all the transformations we discussed up to this point, the polarisation at the entrance and exit of the objective no longer match. To readjust the polarisation vector, we rotate the electric field around the z-axis about $-\phi_{\text{w}}$, leading to $\mathbf{E}_{\text{rs}} \propto \mathbb{R}_3^{-1}(\phi_{\text{w}})\mathbf{E}'$. Note, also that the azimuthal angle ϕ_{w} of the wave vector $\mathbf{K}_{\text{w}}$ is the same as ϕ for the wave vector $\mathbf{K}$.

5.1.2 Debye-Wolf integral representation of the focused field

Inserting expression (5.3) into the vectorial Debye-Wolf diffraction integral (5.2), we find for the electric field in the sample region

$$\mathbf{E}(\mathbf{r}) = \int_{\Omega_\mathrm{m}} \mathrm{d}\Omega E(\theta,\phi)\mathrm{e}^{\mathrm{i}\mathbf{K}_\mathrm{w}\cdot\mathbf{r}}\mathrm{e}^{\mathrm{i}\mathbf{K}_\mathrm{w}\cdot\mathbf{R}}\hat{\boldsymbol{\epsilon}}_\sigma(\hat{\mathbf{K}}_\mathrm{w})\,, \tag{5.8}$$

where we integrate over the solid angle Ω_m with the maximal polar angle θ_m. The maximal polar angle is usually defined by the NA of the objective with $\sin^{-1}(\mathrm{NA}/n_s)$ as illustrated in Fig. 5.2a. However, for NA $> n_\mathrm{s}$, we instead use the angle θ_m determined by $\sin(\theta_\mathrm{m}) = \min\{N, \mathrm{NA}/n_s\}$. We discard the contribution from the evanescent sector. Evanescent waves decay exponentially and can thus be neglected if the interface is far away from the focus where the sphere is trapped. Furthermore, we also added a phase $\mathrm{e}^{\mathrm{i}\mathbf{K}_\mathrm{w}\cdot\mathbf{R}}$ in Eq. (5.8) which translates the origin of the coordinate system from the focus to the centre of the trapped sphere. The vector $\mathbf{R} = \mathbf{R}(r_R, \varphi_R, \theta_R)$ defines the position of the sphere with respect to the focus. This transformation becomes important when considering the scattering of the focused field at the spherical object. The complex amplitude $E(\theta,\phi)$ is given by

$$E(\theta,\phi) = \frac{-\mathrm{i}E_0 K f \mathrm{e}^{\mathrm{i}Kf}}{2\pi}\sqrt{\cos(\theta)}T(\theta)\left(\sqrt{2}\gamma\sin(\theta)\right)^{|\ell|}\mathrm{e}^{-\gamma^2\sin^2(\theta)}\mathrm{e}^{\mathrm{i}\ell\phi}\mathrm{e}^{\mathrm{i}\Psi_\text{g-w}(\theta)+\mathrm{i}\Psi_\mathrm{ast}(\theta,\phi)}\,, \tag{5.9}$$

where we also applied Abbe's sine condition $\rho = f\sin(\theta)$ [132]. Moreover, we introduced the ratio $\gamma = f/w_0$ of the focal length f and beam waist radius w_0. The polarisation vector in the sample region was obtained by performing the rotations defined in Eq. (5.3) with $\hat{\boldsymbol{\epsilon}}_\sigma = \mathbb{R}_3^{-1}(\phi_\mathrm{w})\mathbb{R}_2(\theta_\mathrm{w})\hat{\boldsymbol{\varepsilon}}_\sigma$, resulting in the following expression

$$\hat{\boldsymbol{\epsilon}}_\sigma(\hat{\mathbf{K}}_\mathrm{w}) = \frac{\mathrm{e}^{\mathrm{i}\sigma\phi_\mathrm{w}}}{\sqrt{2}}\left(\hat{\boldsymbol{\epsilon}}_\mathrm{TM}(\hat{\mathbf{K}}_\mathrm{w}) + \mathrm{i}\sigma\hat{\boldsymbol{\epsilon}}_\mathrm{TE}(\hat{\mathbf{K}}_\mathrm{w})\right)\,, \tag{5.10}$$

where we use the notation $\hat{\boldsymbol{\epsilon}}_\sigma(\hat{\mathbf{K}}_\mathrm{w}) \equiv \hat{\boldsymbol{\epsilon}}_\sigma(\theta_\mathrm{w},\phi_\mathrm{w})$. Additionally, we introduced the unit vectors $\hat{\boldsymbol{\epsilon}}_p$ for TM- and TE-polarised modes defined in Eq. (3.2), which are related to the unit vector in spherical coordinates as follows: $\hat{\boldsymbol{\epsilon}}_\mathrm{TM}(\hat{\mathbf{K}}_\mathrm{w}) = \hat{\boldsymbol{\theta}}_\mathrm{w}$ and $\hat{\boldsymbol{\epsilon}}_\mathrm{TE}(\hat{\mathbf{K}}_\mathrm{w}) = \hat{\boldsymbol{\phi}}_\mathrm{w}$.

5.2 Multipole expansion of the optical force components, the MDSA+ theory

The time-averaged optical force exerted by the focused laser beam can be calculated from the surface integral over the Maxwell stress tensor as discussed in Sec. 2.2. We are interested in the trapping of spherical objects of radius R, which are immersed in a homogeneous, linear and non-magnetic medium. We thus choose a spherical surface of radius $R_> > R$, which encloses the object with the surface area element $\mathrm{d}\mathbf{A} = \hat{\mathbf{r}}R_>^2\mathrm{d}\Omega$, as illustrated in Fig. 5.3. The time-averaged force thus yields

$$\mathbf{F} = \frac{R_>^2}{2}\mathrm{Re}\oint_{S^2}\mathrm{d}\Omega\left[\epsilon_0\epsilon_\mathrm{w}\mathbf{E}^*(\mathbf{E}\cdot\hat{\mathbf{r}}) + \mu_0\mathbf{H}^*(\mathbf{H}\cdot\hat{\mathbf{r}}) - \frac{1}{2}\left(\epsilon_0\epsilon_\mathrm{w}|\mathbf{E}|^2 + \mu_0|\mathbf{H}|^2\right)\hat{\mathbf{r}}\right]_{r=R_>}\,. \tag{5.11}$$

The surface integral is carried out over the unit sphere S^2, and the fields are evaluated at radial distance $r = R_>$, which can be chosen arbitrarily as long as it is larger than the radius of the trapped

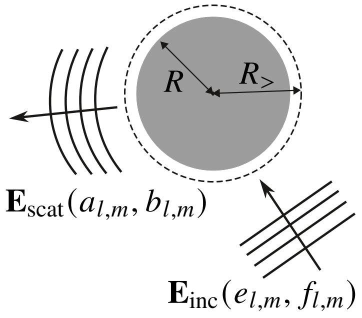

Figure 5.3: Illustration of the scattering at a spherical particle of radius R. An incident field $\mathbf{E}_{\text{inc}}$, defined by the multipole expansion coefficients $e_{l,m}, f_{l,m}$ is scattered into a field $\mathbf{E}_{\text{scat}}$, defined by the coefficients $a_{l,m}, b_{l,m}$. We analyse the momentum transfer through a surface of radius $R_> > R$ surrounding the spherical object.

object. The field outside the scatterer, which enters the Maxwell stress tensor, consists of the incident and scattered field

$$\mathbf{E} = \mathbf{E}_{\text{inc}} + \mathbf{E}_{\text{scat}} \,. \tag{5.12}$$

Terms quadratic in the incident field, which are of the form $E^*_{\text{inc},i}E_{\text{inc},j}$, describe the density flux through the closed surface in the absence of the scatterer and thus do not contribute to the momentum change in lossless media. The terms quadratic in the scattered field, of the form $E^*_{\text{scat},i}E_{\text{scat},j}$, describe the momentum carried away from the object, while the cross-terms $E^*_{\text{scat},i}E_{\text{inc},j}$ and $E^*_{\text{inc},i}E_{\text{scat},j}$ account for the interference between the scattered and incident field and make up for the extinction (ext) part of the force. The optical force can thus be separated into two parts [133]

$$\mathbf{F} = \mathbf{F}_{\text{scat}} + \mathbf{F}_{\text{ext}} \,. \tag{5.13}$$

Due to the spherical symmetry of the scatterer, it is convenient to expand the incident and scattered field in a spherical-wave basis with expansion coefficients $(e_{l,m}, f_{l,m})$ and $(a_{l,}, b_{l,m})$, as introduced in Sec. 4.1.1. The surface integral can be computed analytically by using the definition of the spherical vector fields $\mathbf{N}_{l,m}$ and $\mathbf{M}_{l,m}$ in terms of the vector spherical harmonics $\mathbf{X}_{l,m}$, $\mathbf{Y}_{l,m}$ and $\mathbf{Z}_{l,m}$ defined in Eq. (3.9). The calculation of the surface integral involves quite a lot of algebra by applying various recursion relations for the spherical harmonics. Explicit results for the z-component F_z of the optical force and also for $F_x + \mathrm{i}F_y$ can be found in Refs. [111, 134]. All three force components for spherical scatterer were derived in Refs. [123, 135]. A detailed evaluation of the two separate parts of the force was carried out in detail in Ref. [136]. Due to the different notations used in the mentioned works, we provide the explicit force expression in terms of the coefficients $(a_{l,m}, b_{l,m}, e_{l,m}, f_{l,m})$ in Appendix C.1. Note that the results for the optical force given there are not unique to a spherical scatterer, they apply to any object, where the scattered field can be written in a multipole expansion, and the scatterer itself can be enclosed by a spherical surface.

Hence, with the expressions provided in Appendix C.1, the optical force can be immediately obtained if the multipole expansion coefficients of the incident and scattered field are known. We are thus going to derive the multipole expansion of the incident focused field given in Eq. (5.8) and also derive the scattered field in the following Sections.

5.2.1 Multipole expansion of the focused vortex beam

In general, the multipole expansion of an electromagnetic field can be obtained by using the orthogonality of vector spherical harmonics, as explained in detail in Appendix C.2. We found that the multipole expansion coefficients are given by a surface integral over the Fourier components of the incident electromagnetic field. The Fourier components can be extracted by using the angular spectrum decomposition of the focused field given in Eq. (5.8), which yields

$$\mathbf{E}(\mathbf{K}') = (2\pi)^3 \int_{\Omega_\mathrm{m}} \mathrm{d}\Omega E(\theta,\phi) \mathrm{e}^{\mathrm{i}\mathbf{K}_\mathrm{w}\cdot\mathbf{r}} \mathrm{e}^{\mathrm{i}\mathbf{K}_\mathrm{w}\cdot\mathbf{R}} \hat{\boldsymbol{\epsilon}}_\sigma(\hat{\mathbf{K}}_\mathrm{w}) \delta(\mathbf{K}' - \mathbf{K}_\mathrm{w})\,. \tag{5.14}$$

Introducing the Fourier component in Eq. (C.14), we obtain the following expression for the electric and magnetic multipole expansion coefficients $(e_{l,m}, f_{l,m})$ of the incident beam

$$\left\{ \begin{array}{c} f_{l,m} \\ e_{l,m} \end{array} \right\} = 4\pi \mathrm{i}^l \int_{\Omega_\mathrm{m}} \mathrm{d}\Omega E(\theta,\phi) \mathrm{e}^{\mathrm{i}\mathbf{K}_\mathrm{w}\cdot\mathbf{R}} \mathbf{X}^*_{l,m}(\hat{\mathbf{K}}_\mathrm{w}) \cdot \left\{ \begin{array}{c} \hat{\boldsymbol{\epsilon}}_\sigma(\hat{\mathbf{K}}_\mathrm{w}) \\ \mathrm{i}\hat{\mathbf{K}}_\mathrm{w} \times \hat{\boldsymbol{\epsilon}}_\sigma(\hat{\mathbf{K}}_\mathrm{w}) \end{array} \right\}, \tag{5.15}$$

with vector spherical harmonics in reciprocal space $\mathbf{X}_{l,m}(\hat{\mathbf{K}}_\mathrm{w}) = -\mathrm{i}(\hat{\mathbf{K}}_\mathrm{w} + \nabla_{K_\mathrm{w}}) Y_l^m(\hat{\mathbf{K}}_\mathrm{w})/\sqrt{l(l+1)}$. It is sufficient to compute either the electric or magnetic multipole coefficients since the polarisation vectors (5.10) only differ by a sign $\mathrm{i}\hat{\mathbf{K}}_\mathrm{w} \times \hat{\boldsymbol{\epsilon}}_\sigma = \sigma\hat{\boldsymbol{\epsilon}}_\sigma$. The scalar product of the vector spherical harmonics with the polarisation unit vector $\hat{\boldsymbol{\epsilon}}_p$, $p = \mathrm{TM}, \mathrm{TE}$ is presented in Eqs. (C.15b) and (C.16b) and we thus find

$$\mathbf{X}^*_{l,m}(\hat{\mathbf{K}}_\mathrm{w}) \cdot \hat{\boldsymbol{\epsilon}}_\sigma(\hat{\mathbf{K}}_\mathrm{w}) = \sqrt{\frac{2l+1}{4\pi}} d^l_{m,\sigma}(\theta_\mathrm{w}) \mathrm{e}^{-\mathrm{i}(m-\sigma)\phi_\mathrm{w}}\,, \tag{5.16}$$

where we used [98, Eq. (5) from Sec. 4.17] to introduce the Wigner d-matrix elements $d^l_{m,\sigma}(\theta_\mathrm{w})$. Inserting (5.16) into (5.15) the multipole expansion coefficients yield

$$f_{l,m} = \sigma e_{l,m} = \mathrm{i}^l \sqrt{4\pi(2l+1)} \int_{\Omega_\mathrm{m}} \mathrm{d}\Omega E(\theta,\phi) \mathrm{e}^{\mathrm{i}\mathbf{K}_\mathrm{w}\cdot\mathbf{R}} d^l_{m,\sigma}(\theta_\mathrm{w}) \mathrm{e}^{-\mathrm{i}(m-\sigma-\ell)\phi_\mathrm{w}}\,, \tag{5.17}$$

where $E(\theta,\phi)$ was defined in Eq. (5.9). We simplify the above-given expression by carrying out the integral over the azimuth angle. For this purpose, we introduce the following integral which includes all components in Eq. (5.17) depending on $\phi = \phi_\mathrm{w}$

$$I = \int_0^{2\pi} \mathrm{d}\phi \mathrm{e}^{\mathrm{i}\mathbf{K}_\mathrm{w}\cdot\mathbf{R}} \mathrm{e}^{-\mathrm{i}M\phi} \mathrm{e}^{\mathrm{i}\tilde{A}_\mathrm{ast}\cos(2(\phi_\mathrm{ast}-\phi))} \tag{5.18}$$

with $M = m - \sigma - \ell$ and $\tilde{A}_\mathrm{ast} = 2\pi A_\mathrm{ast}\sin(\theta)/\sin(\theta_0)$, which accounts for the phase introduced by astigmatism (5.5). A similar integral was evaluated in Ref. [137], we present a slightly simplified version of the calculation in Appendix C.3, where we found (C.21)

$$I = 2\pi \mathrm{i}^M \mathrm{e}^{-\mathrm{i}M\varphi_R} \mathrm{e}^{\mathrm{i}K_\mathrm{w} z_R \cos(\theta_\mathrm{w})} g_m^{\sigma,\ell}(\mathbf{R}) \tag{5.19}$$

with the position vector $\mathbf{R}$ expressed in cylindrical coordinates (ρ_R, φ_R, z_R). The coefficient $g_m^{(\sigma,\ell)}(\mathbf{R})$ accounts for the astigmatism and is defined by

$$g_m^{(\sigma,\ell)}(\mathbf{R}) = \sum_{s=-\infty}^{\infty} (-\mathrm{i})^s J_s\left(2\pi A_\mathrm{ast}\frac{\sin^2\theta}{\sin^2\theta_0}\right) J_{2s+m-\sigma-\ell}(K\rho_R\sin\theta) \mathrm{e}^{2\mathrm{i}s(\phi_\mathrm{ast}-\varphi_R)}\,. \tag{5.20}$$

In the absence of astigmatism ($A_{\text{ast}} = 0$), the first Bessel function in the sum yields $J_s(0) = \delta_{s,0}$. Hence, only the $s = 0$ term contributes and the coefficient $g_m^{(\sigma,\ell)}$ reduces to [133]

$$g_m^{(\sigma,\ell)}(\mathbf{R}) = J_{m-\sigma-\ell}(K\rho_R \sin\theta) \,. \tag{5.21}$$

The multipole expansion coefficients of the vortex field (5.8) thus yield

$$f_{l,m} = \sigma e_{l,m} = \mathrm{i}E_0 K f \mathrm{e}^{-\mathrm{i}Kf}\mathrm{i}^l \sqrt{4\pi(2l+1)}\mathrm{e}^{-\mathrm{i}(m-\sigma-\ell)\varphi_R} G_{l,m}^{(\sigma,\ell)} \,, \tag{5.22}$$

where we factored out the integral over the polar angle, which is defined by

$$\begin{aligned} G_{l,m}^{(\sigma,\ell)}(\mathbf{R}) = \left(\sqrt{2}\gamma\right)^{|\ell|} \int_0^{\theta_{\mathrm{m}}} \mathrm{d}\theta \sqrt{\cos(\theta)}\, (\sin(\theta))^{|\ell|+1}\, \mathrm{e}^{-\gamma^2 \sin^2(\theta)} d^l_{m,\sigma}(\theta_{\mathrm{w}}) g_m^{(\sigma,\ell)}(\mathbf{R}) \\ \times \exp\left[\mathrm{i}K_{\mathrm{w}} \cos(\theta) z_R + \mathrm{i}\Psi_{\text{g-w}}(\theta)\right] \,. \end{aligned} \tag{5.23}$$

5.2.2 Multipole expansion of the scattered field

In a lot of optical tweezer setups, the diameter of the trapped objects is much smaller than the wavelength of the beam, it is thus sufficient to obtain the scattered field within the Rayleigh limit [138]. On the other hand, if the particle is much larger, a ray optics approach can be conducted to obtain the optical force [139]. While studying spheres with radii in the range of the wavelength, we need to calculate the scattered field from Mie theory, as discussed in Chap. 4. We consider the scattering at chiral spherical particles, which can be obtained as a limiting case of bi-isotropic media with constitutive equations given by [140]

$$\begin{pmatrix} \mathbf{D} \\ \mathbf{B} \end{pmatrix} = \begin{pmatrix} \epsilon_0\epsilon & \mathrm{i}\kappa/c_0 \\ -\mathrm{i}\kappa/c_0 & \mu_0\mu \end{pmatrix} \begin{pmatrix} \mathbf{E} \\ \mathbf{H} \end{pmatrix} . \tag{5.24}$$

The chirality parameter κ accounts for the circular dichroism, resulting in the material's distinct response to left- and right-circularly polarised fields. Within the Mie theory, the multipole expansion coefficients for a chiral sphere are given by (4.10)

$$a_{l,m} = -a_l e_{l,m} \,, \qquad a_l = r_l^{(\mathrm{E,E})} + \sigma r_l^{(\mathrm{E,M})} \,, \tag{5.25a}$$

$$b_{l,m} = -b_l f_{l,m} \,, \qquad b_l = r_l^{(\mathrm{M,M})} + \sigma r_l^{(\mathrm{M,E})} \,, \tag{5.25b}$$

where the coefficients $r_l^{(P,P')}$ are defined in Eqs. (4.11) and (4.11). Recall that we presented the Mie coefficients for imaginary frequencies. For optical forces, we however need the expressions in real frequencies. The transformation of the reflection coefficients from imaginary to real frequencies is detailed in Sec. 4.1.1.

5.2.3 Optical force exerted by a vortex beam on a spherical object

The trapping force is usually expressed as a force efficiency [141] $\mathbf{Q} = \mathbf{F}/(n_{\mathrm{w}}P/c)$, with the refractive index n_{w} of the medium surrounding the trapped sphere and the speed of light c. P defines the energy flux per unit-time through the objective, which can be computed from the surface integral over the objective entrance over the time-averaged Poynting vector $P = \int \mathrm{d}^2\mathbf{a}\langle\mathbf{S}\rangle$. The energy flux is in propagation direction and for a time-harmonic field we get [71]: $\langle \mathbf{S} \rangle = |\mathbf{E}(\mathbf{r})|^2 \mathbf{K}/2\omega\mu_0$. After introducing the field expression, we obtain the following energy flux

$$P = 2\pi \frac{n|E_0|^2}{c\mu_0} \int_0^{f \sin(\theta_0)} \mathrm{d}\rho\rho \left(\frac{2\rho^2}{w_0^2} \right)^{|\ell|} \exp\left(-\frac{2\rho^2}{w_0^2} \right) T^2(\theta) , \tag{5.26}$$

where $T(\theta)$, defined in Eq. (5.6), accounts for the transmission coefficients through the interface. We use the sine condition $\rho = f \sin(\theta)$ and get $P = (\pi n_s w_0^2 |E_0|^2 / 8c\mu_0) A_\ell$ with A_ℓ given by

$$A_\ell = 8(2\gamma^2)^{|\ell|+1} \int_0^{\sin(\theta_0)} \mathrm{d}t t^{2|\ell|+1} \mathrm{e}^{-2\gamma^2 t^2} \frac{\sqrt{(1-t^2)(N^2-t^2)}}{\left(\sqrt{1-t^2} + \sqrt{N^2-t^2} \right)^2} . \tag{5.27}$$

We express the force in cylindrical coordinates to account for the symmetry of the optical tweezer setup. We write $\mathbf{Q} = Q_\rho \hat{\boldsymbol{\rho}} + Q_\varphi \hat{\boldsymbol{\varphi}} + Q_z \hat{\mathbf{z}}$, with the radial force component Q_ρ, the azimuthal force component Q_φ and the force in the axial direction Q_z. We insert the multipole expansion coefficients of the incident (5.17) and scattered field (5.25) in the force expression presented in Sec. C.1.

The scattering part of the axial force efficiency yields (C.2)

$$\begin{aligned} Q_{\mathrm{scat},z} = -\frac{8\gamma^2}{A_\ell N} \mathrm{Re} \sum_{l=1}^{\infty} \sum_{m=-l}^{l} \Bigg[& \frac{\sqrt{l(l+2)(l-m+1)(l+m+1)}}{l+1} (a_l a_{l+1}^* + b_l b_{l+1}^*) G_{l,m}^{(\sigma,\ell)} G_{l+1,m}^{(\sigma,\ell)*} \\ & + m \frac{2l+1}{l(l+1)} a_l b_l^* \left| G_{l,m}^{(\sigma,\ell)} \right|^2 \Bigg] \end{aligned} \tag{5.28}$$

and the extinction part is given by (C.3)

$$Q_{\mathrm{ext},z} = \frac{4\gamma^2}{A_\ell N} \mathrm{Re} \sum_{l=1}^{\infty} \sum_{m=-l}^{l} (2l+1)(a_l + b_l) G_{l,m}^{(\sigma,\ell)} \left(G_{l,m}^{\prime(\sigma,\ell)} \right)^* . \tag{5.29}$$

The coefficient $G_{l,m}^{\prime(\sigma,\ell)}$ abbreviates a sum of multipole coefficients $G_{l,m}^{(\sigma,\ell)}$ of different degrees, given by

$$G_{l,m}^{\prime(\sigma,\ell)} = \frac{\sqrt{l(l+2)\left[(l+1)^2 - m^2\right]}}{(2l+1)(l+1)} G_{l+1,m}^{(\sigma,\ell)} + \frac{\sqrt{(l^2-m^2)(l^2-1)}}{l(2l+1)} G_{l-1,m}^{(\sigma,\ell)} + \sigma \frac{m}{l(l+1)} G_{l,m}^{(\sigma,\ell)} . \tag{5.30}$$

The transverse force components in cylindrical coordinates can be obtained with (C.8). From Eq. (C.5), we obtain, after some algebraic transformation, the following expression for the scattering part of the transverse force components

$$\begin{aligned}\left\{\begin{array}{c} Q_{\mathrm{scat},\rho} \\ Q_{\mathrm{scat},\varphi} \end{array}\right\} = \frac{4\gamma^2}{A_\ell N}\left\{\begin{array}{c} \mathrm{Im} \\ -\mathrm{Re} \end{array}\right\}\sum_{l=1}^{\infty}\sum_{m=-l}^{l}\Bigg[&\frac{\sqrt{l(l+2)(l+m+1)(l+m+2)}}{l+1}(a_l a_{l+1}^* + b_l b_{l+1}^*) \\ &\times\left(G_{l,m}^{(\sigma,\ell)} G_{l+1,m+1}^{(\sigma,\ell)*} \pm G_{l,-m}^{(\sigma,\ell)} G_{l+1,-m-1}^{(\sigma,\ell)*}\right) \\ &- 2\frac{2l+1}{l(l+1)}\sqrt{(l-m)(l+m+1)}\mathrm{Re}(a_l b_l^*) G_{l,m}^{(\sigma,\ell)} G_{l,m+1}^{(\sigma,\ell)*}\Bigg]\end{aligned} \tag{5.31}$$

while the extinction part according to (C.6) yields

$$\left\{\begin{array}{c} Q_{\mathrm{ext},\rho} \\ Q_{\mathrm{ext},\varphi} \end{array}\right\} = \frac{2\gamma^2}{A_\ell N}\left\{\begin{array}{c} \mathrm{Im} \\ -\mathrm{Re} \end{array}\right\}\sum_{l=1}^{\infty}\sum_{m=-l}^{l}(2l+1)(a_l+b_l)G_{l,m}^{(\sigma,\ell)}\left(G_{l,m+1}^{-,(\sigma,\ell)} \mp G_{l,m-1}^{+,(\sigma,\ell)}\right)^* . \tag{5.32}$$

Note that the upper (lower) sign corresponds to the radial (azimuthal) force component. The coefficients $G_{l,m\mp1}^{\pm,(\sigma,\ell)}$ are functions of $G_{l,m\mp1}^{(\sigma,\ell)}$

$$\begin{aligned}G_{l,m}^{\pm,(\sigma,\ell)} &= \mp\frac{\sqrt{(l\pm m)(l\pm m+1)(l^2-1)}}{l(2l+1)}G_{l-1,m}^{(\sigma,\ell)} + \sigma\frac{\sqrt{(l\mp m)(l\pm m+1)}}{l(l+1)}G_{l,m}^{(\sigma,\ell)} \\ &\pm\frac{\sqrt{(l\mp m)(l\mp m+1)((l+1)^2-1)}}{(l+1)(2l+1)}G_{l+1,m}^{(\sigma,\ell)} .\end{aligned} \tag{5.33}$$

The force expressions (5.28), (5.29) and (5.31), (5.32) constitute the so-called Mie-Debye Spherical Aberration + Astigmatism (MDSA+) theory for spherical objects trapped by a focused, circular-polarised vortex beam. The MDSA+ theory was first derived for dielectric spheres in focused Gaussian beams [129]. If astigmatism is disregarded, $A_{\mathrm{ast}} = 0$, the theory is referred to as Mie-Debye Spherical Aberration (MDSA), which was first discussed in Ref. [116]. If there is also no spherical aberration ($n_{\mathrm{s}} = n_{\mathrm{w}}$), one obtains the Mie-Debye (MD) theory introduced in Ref. [133]. It is worth noting that the force expressions mentioned earlier are quite similar to those used in the MD theory. However, there are a few key differences, such as the multipole expansion coefficients and the normalization function A_ℓ, which take the structure of the light field and the aberrations into account.

We conclude this Chapter with some remarks regarding the numerical evaluation of the force components. First, we note that the expressions for the coefficients $G_{l,m}^{'(\sigma,\ell)}$ and $G_{l,m}^{\pm,(\sigma,\ell)}$ presented in Eqs. (5.30) and (5.33) respectively, agree with recursion relation for the Wigner d-matrix elements $d_{m,\sigma}^{\ell}$, given in Ref. [98, p. 90]. By using these recursion relations, we can obtain the following integral expressions for the coefficients

$$\begin{aligned}G_{l,m}^{'(\sigma,\ell)} = \left(\sqrt{2}\gamma\right)^{|\ell|}\int_0^{\theta_m} &\mathrm{d}\theta\sqrt{\cos(\theta)}\cos(\theta_{\mathrm{w}})\,(\sin(\theta))^{|\ell|+1}\,\mathrm{e}^{-\gamma^2\sin^2(\theta)}d_{m,\sigma}^{l}(\theta_{\mathrm{w}})g_m^{(\sigma,\ell)}(\mathbf{R}) \\ &\times\exp\left[\mathrm{i}K_{\mathrm{w}}\cos(\theta)z_R + \mathrm{i}\Psi_{\mathrm{g\text{-}w}}(\theta)\right]\end{aligned} \tag{5.34}$$

and

$$G_{l,m}^{\pm,(\sigma,\ell)} = \left(\sqrt{2}\gamma\right)^{|\ell|} \int_0^{\theta_m} \mathrm{d}\theta \sqrt{\cos(\theta)} \sin(\theta_\mathrm{w}) \left(\sin(\theta)\right)^{|\ell|+1} \mathrm{e}^{-\gamma^2 \sin^2(\theta)} d^l_{m\pm1,\sigma}(\theta_\mathrm{w}) g_m^{(\sigma,\ell)}(\mathbf{R}) \\ \times \exp\left[\mathrm{i}K_\mathrm{w} \cos(\theta) z_R + \mathrm{i}\Psi_{\text{g-w}}(\theta)\right] . \tag{5.35}$$

Earlier works (see e. g. Refs. [129, 142]) based their calculations on the above given integral expressions. However, this means that for each pair (l, m), three integrals have to be computed numerically to obtain the optical force. In our approach, we only compute the multipole expansion coefficient $G_{l,m}^{(\sigma,\ell)}$ and evaluate the other expansion coefficients from the recursion relations (5.30) and (5.33), which thus saves computation time.

The numerical results shown in the following Chapters were obtained from an implementation of the force expression in Python using the scientific libraries `NumPy` [143], `SciPy` [144] as well as `Numba` [145] for just-in-time compilation.

6 | Trapping chiral and non-chiral particles with vortex beams

In the previous Chapter, we introduced the MDSA+ theory for vortex beams, which allows us to calculate the optical force on a spherical particle. In this Chapter, we will apply our theory to investigate the trapping of spherical objects using a focused Laguerre-Gaussian (LG) beam.

The critical difference between Gaussian and Laguerre-Gaussian beams is that, before being focused by a high numerical aperture objective, a Gaussian beam only carries spin angular momentum associated with the two polarisation states (left- or right-circularly polarised). However, a Laguerre-Gaussian beam also carries orbital angular momentum. During the focusing, spin angular momentum is converted into orbital angular momentum, as discussed in Refs. [67, 146, 147]. The resulting angular momentum carried by the vortex can thus be larger or smaller, depending on the polarisation before focusing. Furthermore, the focusing with a high NA objective leads to a doughnut-shaped intensity profile, where the energy spirals around the optical axis [148]. Depending on the size of the sphere compared to the annular focal spot, there thus exist different trapping regimes [2]. If the particle is way smaller than the radius of the ring of maximal intensity, it orbits around the beam axis [66]. This is a result of the response of the particle to the intensity profile of the beam. The electric field induces a dipole in the polarisable particle $\mathbf{p}_{\mathrm{el}} \propto \mathbf{E}$, which leads to a force $\mathbf{F} = \nabla(\mathbf{p}_{\mathrm{el}} \cdot \mathbf{E}) \propto \nabla|\mathbf{E}|^2$ pointing to the region of highest intensity. The same gradient force also keeps particles trapped along the optical axis for a Gaussian beam, where the region of highest intensity is along the beam axis and not in a ring-shaped area around the axis. In contrast, if the object is large enough, it can also be trapped in the dark spot on the beam axis [149]. Note also that the additional orbital angular momentum carried by the vortex beam increases the transferred momentum to the sphere, allowing it to orbit around the axis if trapped in the ring regime [68].

The enhanced torque and the different trapping regimes in a vortex beam lead to interesting effects, which we will discuss below. Our findings benefit the analysis in Chap. 7, where we use our theory to fit experimental data. First, we analyse in Sec. 6.1 the trapping of dielectric spheres by applying the MD theory without including any aberrations. Then, in Sec. 6.2, we consider trapping particles with a chirooptical response. Finally, we discuss how spherical aberration affects the trapping in Sec. 6.3.

6.1 Dielectric sphere trapped by a vortex beam

If not stated otherwise, we consider the trapping of a polystyrene microsphere of refractive index $n = 1.5694$ [150] in water with refractive index $n_{\mathrm{w}} = 1.3246$ at $T = 19\,^{\circ}\mathrm{C}$ [151]. The beam has a vacuum wave length of $\lambda_0 = 1.064\,\mu\mathrm{m}$ and is left-circularly polarised ($\sigma = 1$). It enters an objective with numerical aperture NA = 1.4 through an entrance port of radius $h = 2.8$ mm. The medium at the exit of the objective has a refractive index $n_{\mathrm{s}} = 1.518$. The beam waist w_0 is in experimental setups with a vortex beam chosen such that optimal filling is ensured [152]. For our theoretical analysis we are using a beam waist of $w_0(|\ell|)$ taken from Ref. [153], which ensures a filling factor of the objective of about 50 % $\left(w_0(|\ell| > 1) \approx 0.5\sqrt{2/|\ell|}\right)$.

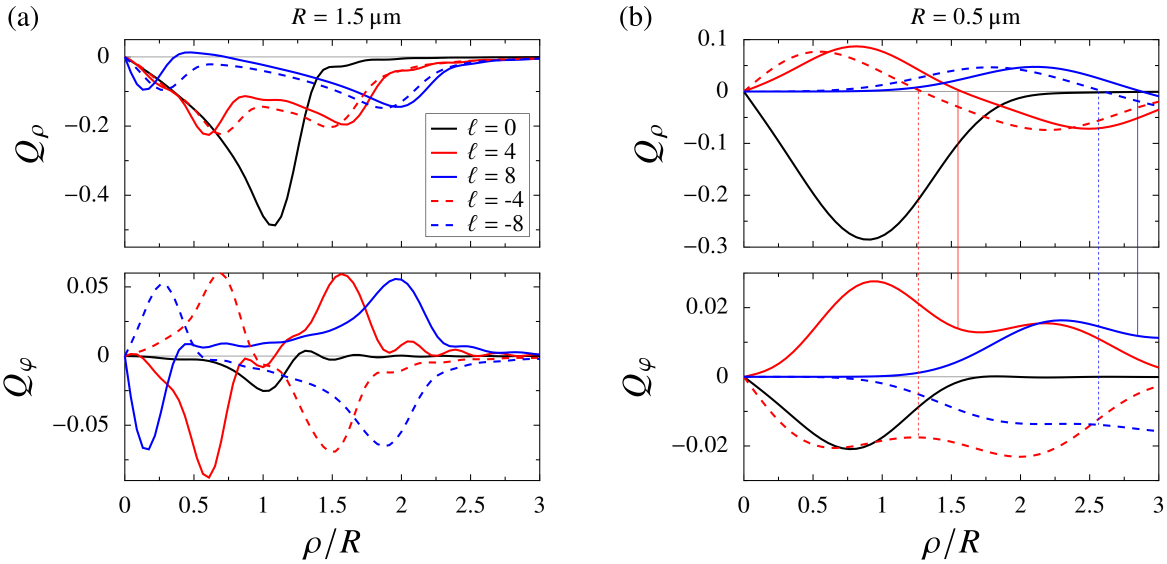

Figure 6.1: Radial and azimuthal force component. Both figures show the radial Q_ρ and azimuthal Q_φ force efficiency as function of the radial displacement ρ for spheres of radii 1.5 µm in (a) and 0.5 µm in (b). The force components for all four cases are calculated at $z = 0$ and for topological charges $\ell = 0, \pm4$, and ±8. Vertical lines, shown in Figure (b), represent the radial off-axis equilibrium positions, defined by $Q_\rho(\rho = \rho_{\mathrm{eq}}) = 0$. The lines in the top Figure connect to corresponding values of the azimuthal force, as shown in the bottom Figure.

6.1.1 On- and off-axis trapping

For a Gaussian beam at the entrance of an objective, there exists one stable on-axis regime ($\rho_{\mathrm{eq}} = 0$). For Laguerre-Gaussian beams, on the other hand, an object can also be trapped on the ring spot [68]. Whether a particle is trapped on-axis or off-axis (on the ring) depends on the size of the object and the topological charge ℓ, which defines the radius of maximum intensity. As can be seen in the top panels of Fig. 6.1, where we show the radial force efficiency Q_ρ as a function of the radial displacement for $z = 0$, calculated from Eqs. (5.31)-(5.32). The radial equilibrium is defined by a vanishing radial force component $Q_\rho(\rho = \rho_{\mathrm{eq}})$. For a sphere with radius $R = 1.5$ µm, as shown in Fig. 6.1a, there is only an on-axis equilibrium for $\ell = 0, 4$. However, for $\ell = 8$, there exist three equilibria, one is located at $\rho_{\mathrm{eq}} = 0$ and the other two at $\rho_{\mathrm{eq}} > 0$. In contrast, for spheres with radius $R = 0.5$ µm (Fig. 6.1b), off-axis equilibria can already be found for $|\ell| = 4$. Where the sphere is trapped in an experimental setting depends on the stability of the equilibrium position. A negative force gradient defines a stable radial equilibrium. For the large sphere shown in Fig. 6.1a, the on-axis equilibrium is stable for all displayed values of ℓ. There is also a stable off-axis equilibrium that corresponds to the ring regime for $\ell = 8$. The topological charge increase causes the equilibrium positions to transition from one stable equilibrium to an unstable equilibrium and a stable periodic orbit [2]. In contrast, for the small sphere depicted in Fig. 6.1a, only for $\ell = 0$ there is a stable on-axis equilibrium. In all other cases, the sphere is trapped in an orbit around the axis. Hence, various trapping regimes exist depending on the topological charge and size of the sphere.

Optical tweezers are three-dimensional traps, therefore a stable equilibrium $\mathbf{R}_{\mathrm{eq}} = \mathbf{R}_{\mathrm{eq}}(\rho_{\mathrm{eq}}, z_{\mathrm{eq}})$ is

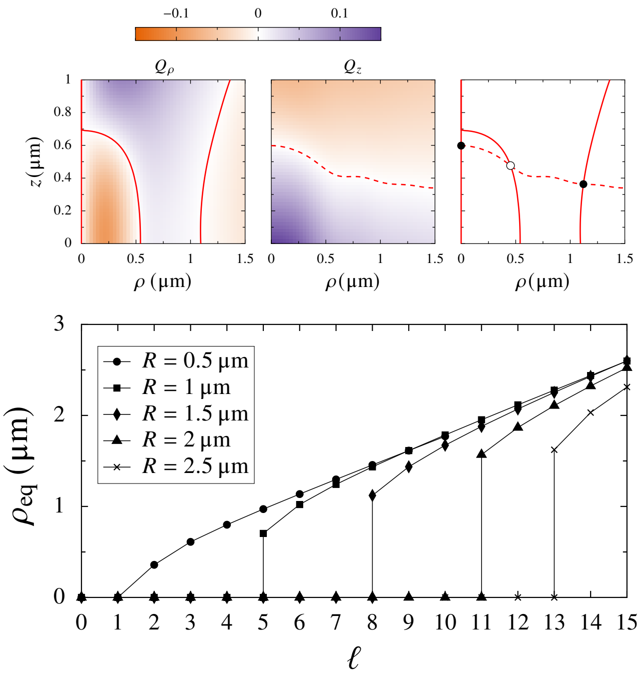

Figure 6.2: On- and off-axis trapping. Top: Equilibrium positions of a microbead with radius 1.5 µm, trapped in a vortex beam with topological charge $\ell = 8$. The first two figures show the radial and axial force fields in the ρz-plane. The solid and dashed lines, respectively, depict the vanishing of the radial and axial force. The last Figure combines the zero-force curves and highlights one unstable (un-filled circle) and the two stable (filled circles) equilibrium positions. **Bottom:** Stable radial equilibrium distance ρ_{eq} as function of the topological charge ℓ for various values of the sphere radius. $\rho_{\mathrm{eq}} = 0$ is an on-axis equilibrium, while $\rho_{\mathrm{eq}} > 0$ indicates trapping in the ring-regime.

defined by the vanishing of both the axial and radial force

$$F_\rho(\mathbf{R}_{\mathrm{eq}}) = 0 = F_z(\mathbf{R}_{\mathrm{eq}}) \quad \text{and} \quad \left.\frac{\partial F_\rho}{\partial \rho}\right|_{\mathrm{eq}}, \left.\frac{\partial F_z}{\partial z}\right|_{\mathrm{eq}} < 0\,. \tag{6.1}$$

The respective derivatives of the force components are negative at the equilibrium to ensure stability. To better understand how the stable equilibrium is evaluated, we have depicted the force fields of a sphere with radius 1.5 µm, displaced in the axial and radial directions in the top panels of Fig. 6.2. The first two figures show the force field of the radial and axial force components, with the curves of vanishing forces depicted as solid and dashed red lines, respectively, for the radial and axial force. The equilibrium positions are defined by the three intersection points of the curves (see third figure). All three equilibria points are stable in axial direction, as the force becomes negative with increasing axial displacement of the sphere from the focus. However, there is one unstable equilibrium in the radial direction, which is represented by the unfilled circle. Small radial deviations from the unstable equilibrium result in a sphere jumping to the on-axis equilibrium or the ring-shaped regime, represented by filled circle symbols. In the bottom panel of Fig. 6.2, we determined the stable radial equilibrium distance ρ_{eq} as function of the topological charge ℓ for various sphere radii R. It is evident from Fig. 6.2 that with increasing radius, higher order beam modes ℓ are necessary to get a sphere trapped in an orbit. Furthermore, stable on- and off-axis equilibria exist for spheres with radii $R \leq 1$µm. The radial equilibrium increases with topological charge [118].

Theoretical studies of this kind offer insights into the position where particles get trapped, depending on their size and the beam mode ℓ used. This is especially useful when trapping in the ring regimes needs to be avoided. We will explore this matter further in the next Chapter.

We now return to Fig. 6.1 to analyse the azimuthal force component Q_φ. In the on-axis regime, there is no force in the azimuthal direction. However, if the object is displaced radially, it experiences

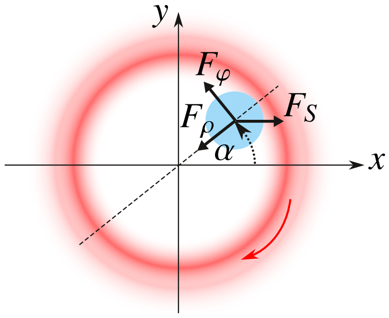

Figure 6.3: Rotation angle α. Schematic illustration of a trapped particle (blue) in a vortex beam, with the ring of highest intensity shown in red. The direction of the torque in the ring regime is shown with a red arrow. If a particle is displaced from the optical axis (coordinate origin), it can experience a torque $\mathbf{F}_\varphi$, which is orientated in the opposite direction to the torque in the ring of highest intensity. If additionally a constant transverse force $\mathbf{F}_\mathrm{S}$ is applied, the particle finds its new equilibrium in a position rotated about an angle α.

a torque as can be seen in the bottom panels of Fig. 6.1, where we depict Q_φ calculated from Eqs. (5.31)-(5.32). It is known that objects trapped in the orbit rotate in the direction defined by the sign of ℓ [68]. We depict the radial equilibrium positions, which define the ring-shaped regime, in Fig. 6.1b, by vertical lines. The lines connect to the respective azimuthal force values in the bottom panel. We confirm that the sign of ℓ matches the sign of Q_φ. For the 1.5 micron sphere, shown in Fig. 6.1a, we however note that in the cases $\ell = \pm 8$, for small displacements from the axis, the particle experiences a torque in the opposite direction to the torque in the ring-shaped regime. This so-called negative optical torque was theoretically analysed in Ref. [57] and experimentally probed in Ref. [142] for an elliptical polarised Gaussian beam. In the next Section, we want to further analyse the torque experienced for small displacements from the optical axis.

6.1.2 Negative optical torque

The negative optical torque can be probed by applying a constant transverse force on the sphere [142]. The motion of a microbead trapped in the medium by a focused beam with a constant force $\mathbf{F}_S = F_S\hat{\mathbf{x}}$ along the positive and negative x-direction can be described by the following set of equations in cylindrical coordinates

$$\begin{aligned} m(\ddot{\rho}_R - \rho_R\dot{\varphi}_R^2) &= F_\rho + F_S\cos(\varphi_R) - \gamma\dot{\rho}_R \\ m(2\dot{\rho}_R\dot{\varphi}_R + \rho_R\ddot{\varphi}_R) &= F_\varphi - F_S\sin(\varphi_R) - \gamma\rho_R\dot{\varphi}_R \\ m\ddot{z}_R &= F_z - \gamma\dot{z}_R\,, \end{aligned} \tag{6.2}$$

with the mass m of the microbead and the Stokes drag coefficient γ of the medium. If the sphere is displaced from the optical axis, it rotates into a new equilibrium, as shown in Fig. 6.3. The equilibrium position $\mathbf{R}_\mathrm{eq} = \mathbf{R}(\rho_R = \rho_\mathrm{eq}, \varphi_R = \alpha, z_R = z_\mathrm{eq})$ is defined by

$$F_z(\mathbf{R}_\mathrm{eq}) = 0\,, \qquad \arctan\left(\frac{F_\varphi(\mathbf{R}_\mathrm{eq})}{|F_\rho(\mathbf{R}_\mathrm{eq})|}\right) = \alpha\,. \tag{6.3}$$

Already, our analysis in Fig. 6.1 suggested that the rotation and thus the rotation angle α changes with the size of the sphere and the topological charge. We thus analysed the rotation angles as a function of the sphere radius in Fig. 6.4. The rotation angles were computed for a fixed displacement $\rho = 0.01$ µm and topological charges $\ell = 0$ and ± 1. It is evident from Fig. 6.4 that a negative optical torque strongly depends on the radius of the sphere and the topological charge of the beam. Notice that it is not always possible to find new equilibrium positions. If the object is too small, it will immediately jump into the ring if displaced. Furthermore, we notice that the rotation angle oscillates

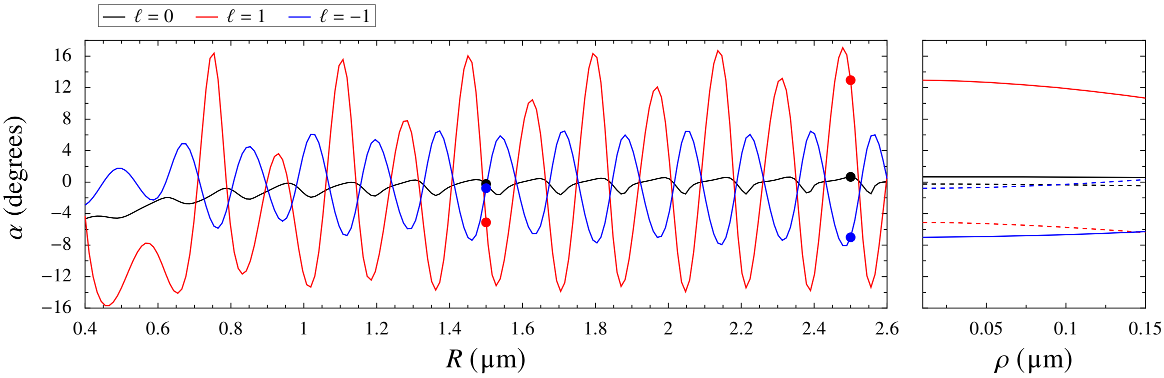

Figure 6.4: Radius dependence of the rotation angle. The left panel presents the rotation angle α as a function of the sphere radius R for vortex beams with $\ell = 0$ and ± 1. The rotation angle is computed for a small displacement of $\rho = 0.01$ µm from the beam axis. The right panel shows the dependence of the rotation angle on the displacement ρ for a sphere of radius 1.5 µm (dotted lines) and for a sphere of radius 2.5 µm (solid lines). We use the same colour convention for the different topological charges as in the left panel, where circle symbols mark the corresponding radii.

for radii larger than the beam wavelength. This corresponds to radii larger than $\lambda_0/n \approx 0.68$ µm for our chosen parameters. Origin of the oscillations is the interference between rays scattered at the front of the sphere (with respect to the propagation direction of the beam) and rays which perform one round-trip within the sphere. Constructive interference appears if the path accumulated during one round-trip within the sphere is a multiple of the wavelength [154]. For a sphere of radius R, the total path within one round-trip is thus $4R$. The distance between two local minima/maxima extracted from Fig. 6.4 yields $\Delta R \approx 0.17$ µm, which agrees with the theoretical expected value of $\lambda_0/4n$. We also remark that the amplitude of the torque for $\ell = -1$ is smaller than for $\ell = 1$, which is related to the chosen polarisation of the incident beam. We used a left-circular polarised beam, which is associated with a spin angular momentum $+\hbar$ and thus partially cancels with the orbital angular momentum $-\hbar$. For $\ell = 1$, on the other hand, the resulting angular momentum is enhanced.

The depicted rotation angles were calculated for a fixed displacement $\rho = 0.01$ µm, we thus also analysed in the left panel of Fig. 6.4 the dependence of the rotation angle against radial displacements. We found that the rotation angle is robust against variations within $\rho < 0.05$ µm. The sphere is immersed in water, causing a Brownian motion. It is thus important to find measurable quantities like the rotation angle that are robust against small spatial variations. The fact that the rotation angle does not depend on ρ for very small displacements was also utilized in a previous study by [142].

6.2 Chiral sphere trapped by a vortex beam

Chirality is generally related to the geometrical structure of an object, where the mirror image is not identical to the original state, regardless of how it is rotated or translated. Chiral objects can be found everywhere in nature, with the DNA being the most prominent example. Characterizing or even selecting objects based on their chirality is of great interest [155, 156]. In a first approximation, chirality can be modeled by a chiroptical parameter κ [156, 157] as introduced in Sec. 5.2.2, which we will employ in the following.

Earlier studies analysed the trapping of chiral particles [158, 159] with a focused Gaussian beam and found that the rotation angle is sensitive to chirality. Recent work also analysed the trapping

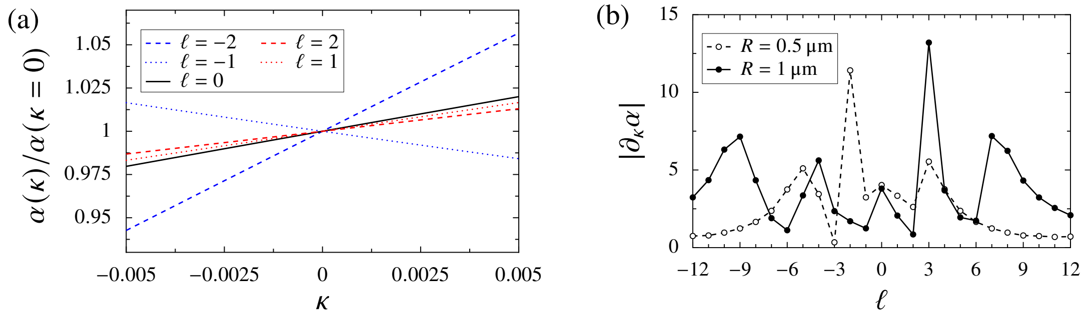

Figure 6.5: Chirality dependence of the rotation angle. Figure (a) presents the rotation angle $\alpha(\kappa)$ as a function of the chirality parameter κ for a sphere of radius $R = 0.5$ μm. The rotation angle is normalized by the angle for zero chirality ($\kappa = 0$) and is calculated for topological charges ranging from $\ell = -2$ to 2. Figure (b) depicts the derivative of α with respect to κ evaluated at $\kappa = 0$ as a function of the topological charge. The derivatives are calculated for spheres of radii $R = 0.5$ μm and 1 μm.

with azimuthally-polarised vortex beams [160]. However, realising an azimuthally-polarised beam is much more difficult (see e.g. for review [161]) than circularly polarised beams, which we are considering in our analysis. The chirality of objects modifies the azimuthal component of the optical force. We computed in Fig. 6.5a the rotation angle α for a sphere of radius $R = 0.5$ μm and chirality parameters ranging from −0.005 to 0.005, the refractive index is the same as before. The rotation angle was normalized by the rotation angle $\alpha(\kappa = 0)$ for zero chirality. We found that depending on the topological charge ℓ, the rotation angle for a chiral particle is either larger or smaller than the rotation angle for a non-chiral sphere. Furthermore, we also found that certain beam modes are more sensitive to chiral objects than others. It is evident from the depicted cases in Fig. 6.5a, that the beam with topological charge $\ell = -2$ is most sensitive to variations in κ, since it shows the strongest variation with κ. This suggests that there is an optimal beam mode ℓ_{opt} to probe chirality. The beam mode that exhibits the highest sensitivity depends on the radius of the sphere. We thus examined in Fig. 6.5b the slope of $\alpha(\kappa)$ at $\kappa = 0$ as function of the topological charge for a sphere of radius $R = 0.5$ μm and $R = 1$ μm. The absolute value of the gradient is largest for $\ell_{\text{opt}} = -2$ and $\ell_{\text{opt}} = 3$, respectively for the two spheres. The studies [158, 159] proposed to use the rotation angle as a probe for chirality. They used a Gaussian beam at the entrance of the objective. However, our result suggests that Laguerre-Gaussian beams are better suited, specifically if the optimal beam mode for a certain sphere size is known.

6.3 Influence of spherical aberrations on optical trapping

In this Section, we will briefly discuss how spherical aberrations influence the trapping in a vortex beam. Spherical aberration occurs due to the refraction of the beam at an interface. As we discussed earlier, spherical aberration is characterized by the distance L between the interface and the paraxial focus, as shown in Figure 5.2a. The parameter L is typically determined theoretically by simulating the experimental procedure, as it is not usually accessible in experiments [116]. The sphere is first placed on the interface, and then displaced by a fixed distance d. Theoretically, this amounts to determining the axial equilibrium position $z_R = z_{\text{eq}}$, where the sphere touches the interface, as shown in Fig. 6.6a. Recall that z_R defines the distance of the sphere centre from the focal spot. Therefore, the distance L_0 from the focus to the interface can be calculated from $L_0 = R - z_{\mathrm{eq}}$, with z_{eq} as solution of

$$Q_z(\rho_R = 0, \phi_R = 0, z_R = z_{\mathrm{eq}}, L = R - z_{\mathrm{eq}}) = 0\,. \tag{6.4}$$

The distance after displacing the sphere is $L = L_0 + d/N$.

In Fig. 6.6b, we analysed the focal distance as function of the topological charge ℓ for a sphere of radius $R = 1.5\,\mu\mathrm{m}$ and found that the focal distance decreases with increasing $|\ell|$. The intensity profile of a vortex beam along the beam axis depends on the topological charge. It can thus lead to additional changes in the focus position on top of the distortion due to the refraction at the interface. Additionally, we analysed in Fig. 6.6c how the rotation angle α changes with increasing distance between the nominal focus position and the interface. We computed rotation angles within the MDSA theory for a sphere of radius $R = 1.5\,\mu\mathrm{m}$ as a function of the topological charge ℓ. The rotation angles were computed for different displacements d. Furthermore, we subtracted the rotation angle α_{MD}, the rotation angle calculated within the MD theory, without spherical aberration. It is evident from Fig. 6.6c that the rotation angles for higher beam modes $|\ell| > 0$ are more sensitive to changes in the distance d. For $\ell = 0$, there are almost no variation with distance d.

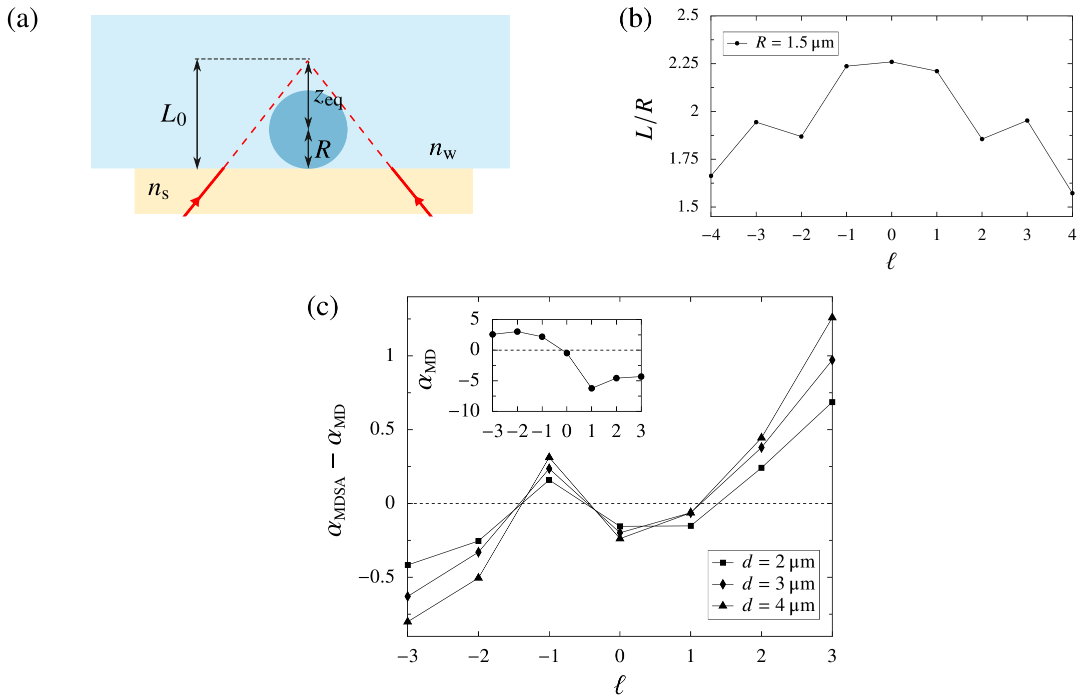

Figure 6.6: Spherical aberration. Figure (a) depicts the paraxial focal distance L_0 for a trapped spherical particle touching the interface. Figure (b) represents the distance L between the paraxial focal and the interface as a function of the topological charge ℓ for a sphere of radius $R = 1.5\,\mu\mathrm{m}$. The distance is calculated from $L = L_0 + d/N$, where $d = 2\,\mu\mathrm{m}$ and $N = n_{\mathrm{w}}/n_{\mathrm{s}}$. L_0 is obtained as solution from Eq. (6.4). Figure (c) presents the difference between the rotation angle calculated within the MDSA theory (α_{MDSA}) and within the MD theory (α_{MD}) as a function of the topological charge ℓ. The rotation angles are computed for a sphere of radius $1.5\,\mu\mathrm{m}$ for various focal distances d. The inset depicts the rotation angles calculated with the MD theory for comparison.

7 | Characterizing microbeads by trapping in a vortex beam

The content discussed in this Chapter can be found in Ref. [153] and, therefore, also contains input from numerous discussions with all authors of the article. The idea of using vortex beams for determining the radius of microbeads was developed by Kainã Diniz and collaborators from UFRJ. The author of this thesis carried out the numerical calculation, as well as parts of the analysis of the experimental data.

In the previous Chapter, we discussed two trapping regimes for particles trapped by a vortex beam. Where the object is trapped depends on the size and the topological charge of the beam. Objects which are large compared to the size of the ring-shaped trap find their stable position on the optical axis. For small displacements from the on-axis regime, the particle experiences a rotation which results from the optical torque. The direction of the torque depends on the size and topological charge and can point in the opposite direction to the angular momentum of the vortex. For higher beam modes ($|\ell| > 0$), we observed that the rotation angle is extremely sensitive to the radius of the sphere. In this Chapter, we will discuss how these results can be practically applied in experiments to determine the size of trapped microspheres. This can be done by measuring the rotation angle for different topological charges ℓ.

Various techniques exist in the literature to identify the size of particles immersed in a liquid, as is the case for the system we are studying. One common approach is dynamic light scattering [162], which, however, cannot determine the size of an individual trapped particle but instead the average size of the dilute mixture of colloids. Another way is to extract the trapped particle from the liquid and measure it with an electron microscope or other imaging systems. This method is also limited in its applicability since the trapped particle is usually used for further measurements. Our proposed *in situ* method provides a solution to this problem. Other approaches apply machine learning to characterize colloids [163–165]. The latter uses a generative model based on the Lorentz-Mie theory to fit holograms of individual particles in a liquid. However, this approach again does not work when considering an individual trapped particle, which is used in further experiments where the knowledge of the size of the bead is needed, like for measuring the stiffness or trapping efficiency of optical tweezers (see e. g. [166]).

The following Section provides a detailed overview of the proposed radius measurement method. We begin in Sec. 7.1 by giving an overview of the experimental setup and also explaining how the rotation angles can be extracted from the experimental data. We apply the theory developed in the previous Chapter to fit the experimental data, as detailed in Sec. 7.2. This allows us to determine the characteristics of the trapped bead. Furthermore, we found that our method also provides information about other quantities of the optical system.

7.1 Experimental setup and analysis of the data

We consider the same setup and parameters as in the previous Section, with a polystyrene sphere trapped by a vortex beam of topological charge ℓ. The bead was trapped, while touching the interface and is then moved upwards by a height $d = (2 \pm 1)\ \mu\text{m}$. We described this procedure in Sec. 6.3,

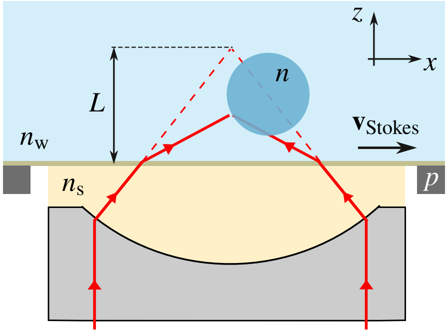

Figure 7.1: Illustration of the experimental setup. A bead of refractive index n is trapped in a laser beam focused through an interface with refractive indices n_s and n_w on either side of the interface. A glass slide at the interface is displaced by a positioning system (p) along the x-direction with a velocity $\mathbf{v}_{\mathrm{Stokes}} = v_{\mathrm{Stokes}}\hat{\mathbf{x}}$, thus leading to a Stokes drag force, which displaces the bead from its equilibrium position.

which allows us to extract the paraxial focal distance L, also shown in Fig. 7.1. The rotation angle is measured by applying a constant force on the sphere, as discussed in Sec. 6.1.2. In the experiment, this is achieved indirectly. A glass slide is placed at the interface (see Fig. 7.1) and moved in a transverse direction. Hence, a Stokes drag force arises, which displaces the trapped particle from its axial equilibrium position. Once the bead is displaced from its on-axis equilibrium, it will rotate to its new equilibrium, as illustrated in Fig. 6.3. The procedure was repeated for several beam modes ℓ for each trapped sphere. We refer to Refs. [142, 153] for readers interested in more details on the experimental setup and technical realization.

In the following, we will discuss how to efficiently extract the rotation angle from a large number of data sets. For each beam mode ℓ, the position of the microsphere is measured over a time $T = 10\,\mathrm{s}$, resulting in 1000 data points, as it is shown for the x- and y-coordinate as a function of the time in the left and top panel of Fig. 7.2. The central panel displays the data points within the xy-plane, resulting in two distinct clusters originating from the displacement in positive and negative x-direction. We use a `scikit-learn` routine, an open-source machine learning software package [167], to identify the two clusters, which are depicted by yellow and blue points in Fig. 7.2. The open circles that lie between the two identified clusters are disregarded in the analysis. They correspond to the measured positions of the spheres during the displacement. Using machine learning software facilitates the data analysis significantly, since it works for a large number of data sets and we do not need to introduce criteria for each individual data set to identify the clusters. Next, we determine the probability histogram distributions with respect to each direction and test whether it is normally distributed. Finally, a 2D Gaussian model of the form

$$f(x, y) = A \exp\left[-a(x - x_i)^2 - b(x - x_i)(y - y_i) - c(y - y_i)^2\right] \tag{7.1}$$

is used to fit each cluster. The Gaussian function is parameterized by the amplitude A, the centre coordinates $\mathbf{r}_i = (x_i, y_i)$ and parameters a, b and c, which characterize the spread in the xy-plane. The centre coordinates of the Gaussian model determine the equilibrium position of the bead. We assume that the equilibrium positions are symmetrically displaced from the optical axis, which allows us to deduce the rotation angle α from the slope of the line connecting the two equilibrium positions with $\tan(\alpha) = (y_2 - y_1)/(x_2 - x_1)$. The error of α was found by propagating the fitting errors of the coordinates. Previous work [142] determined the rotation angle by performing a linear fit of all data points. However, the linear fit is inadequate for a two-dimensional problem since it only minimizes the error in the y-direction. Exchanging x- and y-coordinates and again performing a linear fit reveals that it leads to a different rotation angle, as can be seen by the dashed black lines in the central panel of Fig. 7.2. Our method avoids this ambiguity. Furthermore, we are also able to evaluate the radial

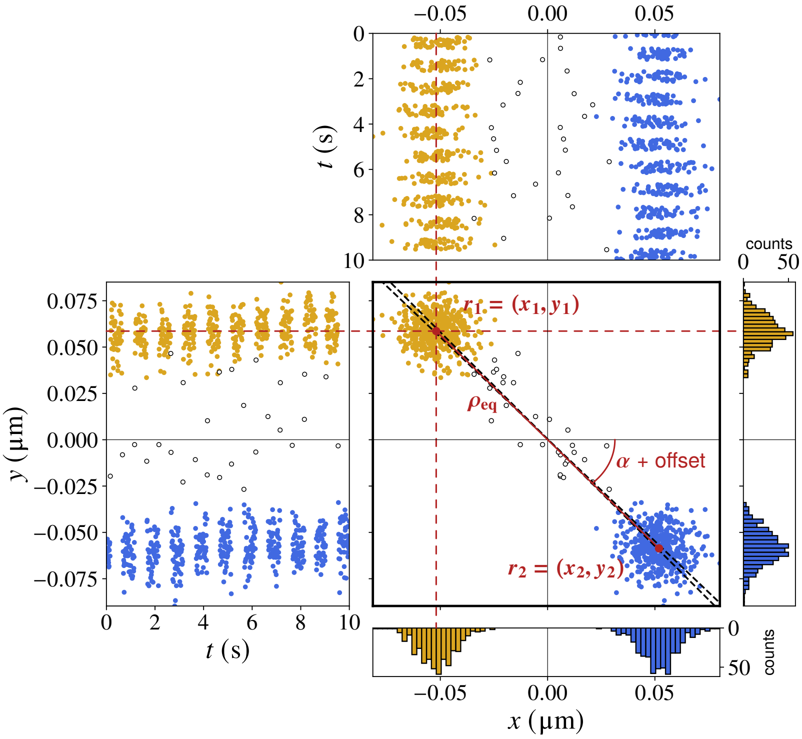

Figure 7.2: Extracting the rotation angle from the experimental data. The x- and y- coordinates of the bead were measured over a period of $T = 10\,s$ as depicted at the top and left panel, respectively. The central panel illustrates the position distribution in the xy-plane with probability histograms for each coordinate as depicted on the right and bottom panels. The yellow and blue coloured data points, corresponding to the two equilibrium positions, were identified with a machine-learning routine. Data points depicted as open circles are disregarded. The histograms indicate that the x- and y-coordinate are normally distributed, which allows for a fit with a 2D Gaussian model to determine the two equilibrium positions $\mathbf{r}_1$ and $\mathbf{r}_2$ of the bead, shown as red dots. We assume that the equilibria are symmetrically displaced from the optical axis. The rotation angle can thus be evaluated from the slope of the line connecting the two equilibria. The whole experimental setup was rotated by an offset angle, which needs to be subtracted to obtain the angle α. Furthermore, we find the radial equilibrium displacement ρ_{eq} from the distance between the two equilibria. The black dashed lines depict the result of a linear fit of the data in x- and y-direction.

equilibrium displacement ρ_{eq} from the distance between the two points with $2\rho_{eq} = |\mathbf{r}_1 - \mathbf{r}_2|$, which is needed for the theoretical evaluation of the rotation angle, as we discussed in connection with Fig. 6.4.

Data sets which fail the normality test, are analysed separately. The clusters in some data sets exhibit an overall drift during the measurement, as it is shown in Fig. 7.3a for the x-coordinate of a certain data set. The corresponding probability distribution (shown at the right panel of Fig. 7.3a) thus exhibits some skewness or even two distinct maxima, which does not allow for a fit with a Gaussian model. We analyse the viability of a data set by identifying each individual cluster in the time series of the x- and y-coordinate and determine the mean values, as well as, the standard deviations (as depicted by the crosses and error bars in Fig. 7.3a). Next, the minimal and maximal mean coordinates are extracted, both indicated by the dashed lines for each equilibrium position (respectively the blue and yellow data points). We furthermore evaluated the mean value of the standard deviations of the individual clusters. If the distance between the minimum and maximum mean is larger than twice

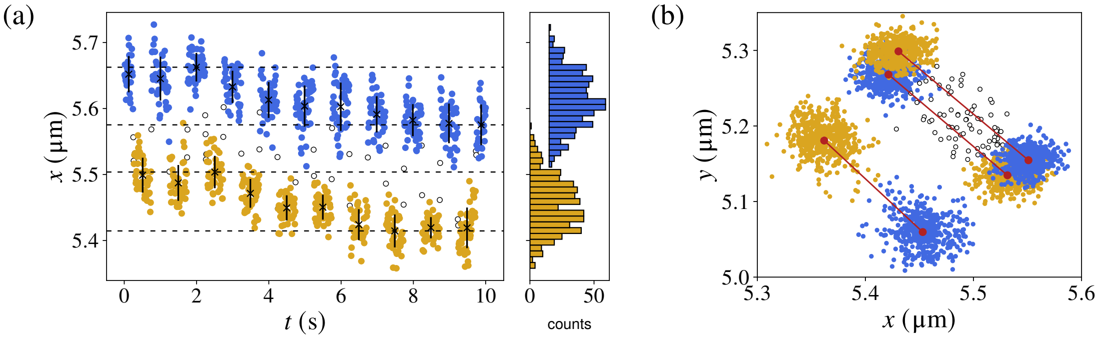

Figure 7.3: Data analysis. (a) The left panel depicts the x-coordinates of the displaced bead as function of the time t, similar to Fig. 7.2 but for a different data set. The crosses present the mean x-coordinate within each cluster, while the dashed lines present the maximum and minimum mean values. For each cluster, we additionally computed the mean standard deviation, which is illustrated by the vertical lines. The right panel depicts the corresponding histogram of the position distribution. We shifted the upper histogram from the zero-axis to avoid an overlap with the lower histogram. (b) Position distribution of the bead in the xy-plane for three rounds of measurement for a particular beam mode. The red dots present the equilibrium position of the bead extracted from the corresponding position distributions.

the mean of the standard deviation, we disregarded the data set.

The measurement for each mode ℓ was repeated several times. The obtained data sets of the individual runs are presented in Fig. 7.3b. It is evident that there is a significant shift in the data, which makes combining data sets for a particular beam mode impossible. Hence, the rotation angle for each individual run had to be determined separately.

7.2 Fitting the experimental data to theory

This Section is devoted to the theoretical analysis of the experimentally obtained data for the rotation angles. First, in Sec. 7.2.1, we present our fitting procedure. In Sec. 7.2.2, we discuss the results for two beads of nominal size (1.50 ± 0.04) µm which are in the following referred to as beads A and B. We follow up with a discussion of beads of nominal size (2.260 ± 0.075) µm, which we refer to as beads C and D in Sec. 7.2.3.

7.2.1 Numerical analysis

The rotation angle α is determined by solving the system (6.3), where we used the radial equilibrium distance ρ_{eq} extracted from the experimental data. The rotation angles show little dependence on ρ for small displacements as we already confirmed in Sec. 6.1.2. We thus use the average displacement of all rounds for one beam mode as input for the numerical calculation of the rotation angle.

We fit the experimental data by minimizing a weighted sum of squared errors between the theoretically and experimentally obtained rotation angles, denoted as χ^2. We sum over all beam modes for which measurements were performed and all rounds of measurement, leading to the following

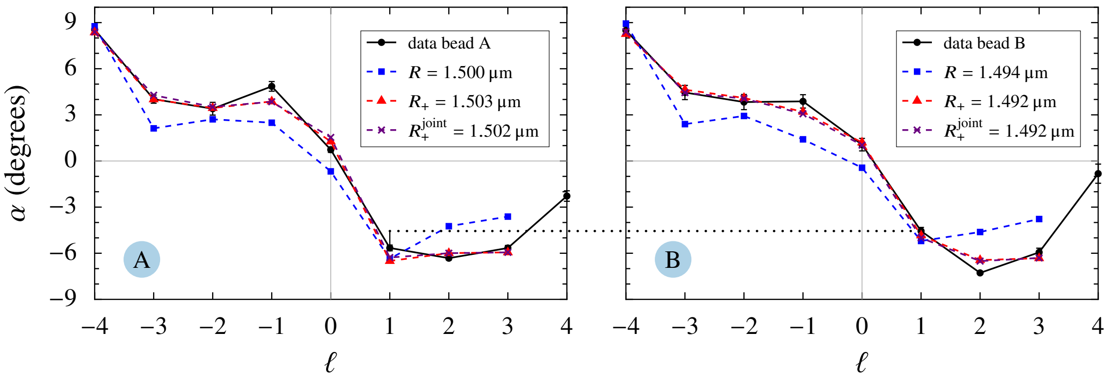

Figure 7.4: Beads with a nominal size of 1.5 microns. The figure represents the experimental and theoretical rotation angles for bead A (left) and bead B (right) as a function of the topological charge ℓ. The circle symbols depict the mean values of the experimentally obtained rotation angles from the several runs of measurement. The error bars depict the standard deviations from the different runs. We fitted the experimental data points by using the MDSA theory (squared symbols) and the MDSA+ theory (triangle symbols). Furthermore, a joint fit with common astigmatism parameters for beads A and B was performed (cross symbols). The corresponding radii found from the fits are shown in the legends. The dotted line connecting the two figures illustrates the difference between the rotation angles for the two beads measured for $\ell = 1$. Similar figures can be found in Ref. [153] but without the results for the joint fit.

definition of the loss function

$$\chi^2 = \frac{1}{N}\sum_{\ell}\frac{1}{M_\ell}\sum_{r}\left(\frac{\alpha(\ell) - \alpha_{\mathrm{exp}}(\ell, r)}{\Delta\alpha_{\mathrm{exp}}(\ell, r)}\right)^2 \tag{7.2}$$

with the experimentally determined rotation angle $\alpha_{\mathrm{exp}}(\ell, r) \pm \Delta\alpha_{\mathrm{exp}}(\ell, r)$ and its uncertainty for the beam mode ℓ from measurement round r. N is the number of beam modes, and M_ℓ is the number of measurement rounds for each beam mode. M_ℓ depends on ℓ, which is a result of the fact that sometimes beads are lost during the measurement process or certain data sets are disregarded, as we discussed in the previous Section. We used the MDSA and MDSA+ theory presented in Sec. 5.2.3 to compute the theoretical rotation angles. The paraxial focal distance L was determined by the approach described in Sec. 6.3 with the experimentally measured displacement $d = (2 \pm 1)$ µm of the bead from the interface.

The minimization of χ^2 is performed with the Minuit class from the `iminuit` package [168], which provides the fitting parameters, their uncertainties and correlations. The computation time, especially for the MDSA+ theory, was quite time-consuming. As a result, we computed the rotation angles for the different beam modes in parallel on several processes.

7.2.2 Beads of nominal size 1.5 microns

For beads A and B of nominal radius 1.5 microns, measurements were performed for $|\ell|$ up to 4 to ensure on-axis trapping. Three to four rounds of measurement were performed for each beam mode ℓ. The averaged rotation angles from the different rounds of measurement are depicted in Fig. 7.4 as circles, with error bars showing the standard deviations. We notice that the two rotation angles for $\ell = 0$ are indistinguishable within their error bars. However, higher beam modes enable a distinction between the two beads, as shown for $\ell = 1$ by the dotted lines in Fig. 7.4. Hence, only

bead	R (µm)	χ^2
A	1.500 ± 0.004	21.7
B	1.494 ± 0.003	26.4

Table 7.1: Parameters from a fit with the MDSA theory. Optimal radii from a fit with the MDSA theory together with the corresponding value of χ^2 for beads A and B of nominal size 1.50 µm.

Laguerre-Gaussian beams of topological charges $|\ell| > 0$ can be used to distinguish trapped beads based on their radius, as already expected from our discussion in connection with Fig. 6.4. The rotation is mostly opposite to the one in the ring regime, which is defined by the sign of ℓ, which we also found for $R = 1.5\,,\mu\text{m}$ in Fig. 6.4. It is also notable that the modulus of the rotation angle for $\ell = 4$ is way smaller than the angle for $\ell = -4$. A theoretical calculation of the rotation angle for the nominal radius using the MDSA theory yields a value of about $-15.7°$, so it is way smaller than what was experimentally found, which is about $-2.7°$ and $-0.8°$, respectively for bead A and B. We suspect that this discrepancy originates from the torque exerted along the ring regime of the beam. For $\ell = 4$, the bead is in the limiting case between the on-axis and ring regime. While there is a stable on-axis equilibrium, the bead also experiences a positive torque from the ring [152]. We thus excluded the rotation angle for $\ell = 4$ from the fit. We chose the nominal radius as the initial value for our fit and restricted the fitting interval of the radius to twice the standard deviation provided by the manufacturer, resulting in an interval ranging from 1.42 to 1.58 µm.

First, we applied the MDSA theory to fit the experimental rotation angles. The fitted data points are depicted as squares in Fig. 7.4 and the optimal radii are shown in Tab. 7.1 together with the value of χ^2 for both bead A and B. Apart from the rotation angle for $\ell = 0$, there is good agreement between theory and experiment. The theoretical and experimental obtained rotation angles for $\ell = 0$ have an opposite sign. This suggests that the MDSA theory is not sufficient to explain the experimental data accurately. According to our discussion from the previous Sections, the rotation angle for $\ell = 0$ is smaller than the rotation angle for higher-order beam modes. The positive rotation angle for $\ell = 0$ and also the relative large rotation angle for $\ell = -1$, originate from additional field asymmetries introduced by effects like astigmatism. We thus also performed a fit with the MDSA+ theory with A_{ast}, ϕ_{ast} and L as additional fitting parameters to account for the optical aberrations of the system. We introduce L as a fitting parameter due to the large uncertainty of the experimentally measured height d. This is also supported by our results from the previous Chapter, where we found in Fig. 6.6c, that rotation angles for higher beam modes are more sensitive to spherical aberration. The results are depicted in Fig. 7.4 by the triangle symbols and the fitted parameter can be found in Tab. 7.2. Including optical aberrations yields an almost perfect fit of the experimental data and thus also correctly reproduces the positive rotation angle in the case $\ell = 0$. Note that $\chi^2 > 1$, so there is no indication for over-fitting.

bead	R (µm)	L (µm)	A_{ast}	ϕ_{ast} (rad)	χ^2
A	1.503 ± 0.007	5.8 ± 0.6	0.245 ± 0.026	0.37 ± 0.14	2.2
B	1.492 ± 0.005	4.7 ± 0.6	0.262 ± 0.024	0.44 ± 0.12	2.3

Table 7.2: Parameters from a fit with the MDSA+ theory. Optimal radius R, paraxial focal distance L and astigmatism parameters A_{ast}, ϕ_{ast} found from a fit with the MDSA+ theory for beads A and B of nominal size 1.5 µm. The corresponding values of χ^2 are shown in the last column.

R_A (µm)	R_B (µm)	L_A (µm)	L_B (µm)	A_ast	ϕ_ast (rad)	$\chi^2_{A,B}$
1.502 ± 0.010	1.492 ± 0.007	5.6 ± 0.8	4.8 ± 0.8	0.254 ± 0.026	0.41 ± 0.14	2.3, 2.4

Table 7.3: Joint fit of two beads with the MDSA+ theory. Parameters from the joint fit of beads A and B with shared values for the astigmatism parameters but separate values for the focal distance L.

We want to highlight that the astigmatism parameters $A_\mathrm{ast}, \phi_\mathrm{ast}$ of beads A and B are well within the error bars of each other. This is expected since these are characteristics of the experimental setup, which are not influenced by the measurement for a particular bead. Taking this into account, we also performed a combined fit for beads A and B with joint parameters for astigmatism, which are depicted by the cross symbols in Fig. 7.4 and the fitting parameter can be found in Tab. 7.3. There is no significant change to the results found from the individual fits. These findings have important implications. First, we can reduce the number of fitting parameters by using joint astigmatism parameters. Based on our findings, only six are necessary instead of eight fitting parameters for the two beads. This also reduces the overall computation time. However, it is important to note that this approach requires the experimental setup to stay the same while performing measurements for different beads. The paraxial distance L is adjusted for every bead, so individual fitting parameters are necessary here. The second conclusion, which we can draw from our joint fit results, is that our method for measuring radii also works to estimate optical aberrations. We will revisit this point later.

The radii from the MDSA and MDSA+ theory are both within each other's error bars. Hence, if only the radius of a trapped sphere is of interest, it is sufficient to apply the MDSA theory for fitting, which drastically reduces the computation time if only one fitting parameter is used instead of four. Furthermore, we also found that, in principle, one round of measurement for each beam mode ℓ is sufficient, as can be seen in Fig. 7.5a. We fitted the data for each round of measurement and compared the radius with the fitted radius of all rounds of measurement. Again, this also reduces the computation time, but also time for performing the experiment and analysing of the data.

Apart from determining the radius, we can also characterize the primary optical aberrations of the system defined by the parameters $A_\mathrm{ast}, \phi_\mathrm{ast}$ and L, as mentioned above. Due to the relatively large number of fitting parameters, there are, however, also cross-correlations, which translates into the uncertainty of the fitted radii within the MDSA+ theory compared to the MDSA theory. As can be seen from the correlation matrices illustrated in Fig. 7.5b, A_ast and L are particularly strongly correlated. Both parameters are responsible for a defocusing, hence an increase of one parameter can be compensated by a reduction of the other which is reflected by the negative correlation value of these two parameters. Variation in ϕ_ast can be reversed by a change in A_ast, as was already discussed in Ref. [117]. The effect of spherical aberration is enhanced with increasing displacement L, however, larger spheres average out these changes in the energy density profile, which explains the positive correlation between L and the bead radius R.

All results presented are performed for a temperature of $T = 19\,^\circ\mathrm{C}$. To account for temperature variations, which specifically affect the refractive index of water, we also repeated the calculations for a temperature of $T = 24\,^\circ\mathrm{C}$ and found no significant changes in the fitted rotation angles within the error bars of the measured angles.

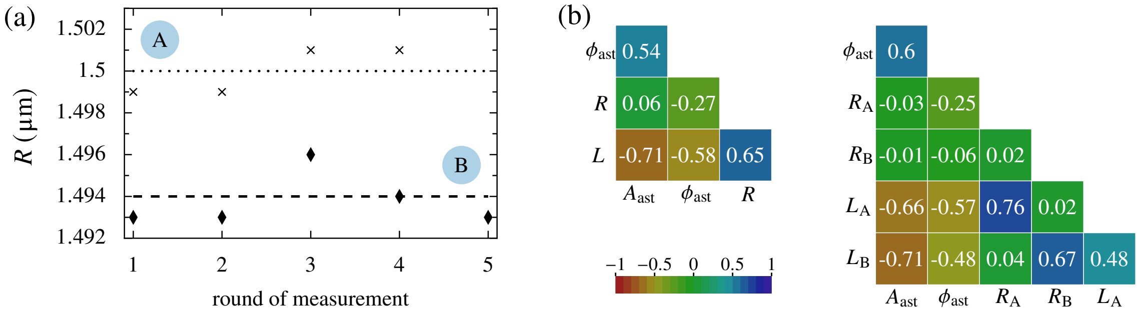

ϕ_{ast}	0.54		
R	0.06	-0.27	
L	-0.71	-0.58	0.65
	A_{ast}	ϕ_{ast}	R

ϕ_{ast}	0.6				
R_{A}	-0.03	-0.25			
R_{B}	-0.01	-0.06	0.02		
L_{A}	-0.66	-0.57	0.76	0.02	
L_{B}	-0.71	-0.48	0.04	0.67	0.48
	A_{ast}	ϕ_{ast}	R_{A}	R_{B}	L_{A}

Figure 7.5: Figure (a) shows the fitted radii for each round of measurement for bead A (cross symbols) and B (diamond symbols). For comparison, we also present the fitted radii shown in Tab. 7.1 as dotted and dashed lines, respectively, for beads A and B. (b) The left panel depicts the correlation matrix for the fitting parameters of bead A in the MDSA+ theory, and the right panel depicts the correlation matrix from the joint fit of beads A and B. Both matrices are symmetric with ones on the diagonal entries, which are not shown. A value of 0 means that the parameters are uncorrelated.

7.2.3 Beads of nominal size 2.26 microns

Next, we discuss the results for beads C and D with a nominal size of 2.26 µm. The larger size of the spheres allows trapping in the on-axis regime for higher beam modes ℓ than for the smaller beads, as we discussed in the previous Chapter in connection with Fig. 6.2. The experiment was performed for $|\ell| \leq 7$ as it is depicted by the black circle symbols in Fig. 7.6. The sign of the rotation angles is opposite to the corresponding sign of the topological charges. This is, again, a consequence of the negative optical torque. However, theoretically stable trapping positions were only found for $|\ell| \leq 6$. As a result, we excluded the rotation angles for $\ell = \pm 7$ from the fitting process. The fit with the MDSA theory was performed within an interval ranging from 2.11 µm to 2.41 µm with the nominal radius as starting point. The results from the fit are depicted as squared symbols in Fig. 7.6, and the fitted radii with their uncertainties can be found in the Tab. 7.4 for both beads C and D. The results obtained from the fitting procedure are in good agreement with the experimental data. To estimate the sensitivity of the procedure, we also computed the rotation angles obtained for the nominal radius, which are represented by open square symbols in Fig. 7.6. As we can see, the rotation angles for $|\ell| = 1, 2, 3$ are opposite to those found in the experiment. Hence, higher beam modes allow the distinction between beads of different sizes. For a Gaussian beam ($\ell = 0$), it is impossible to differentiate between two beads within the experimental error bars. Additionally, we performed a fit with the MDSA+ theory by using the astigmatism parameters we found from the joint fit for beads A and B, again assuming that the optical aberrations of the system did not change during measurement. The fitted values are depicted in Fig. 7.6 as cross symbols and the fitting parameters are given in

bead	R (µm)	χ^2
C	2.339 ± 0.003	40.1
D	2.331 ± 0.003	67.7

Table 7.4: Parameters from a fit with the MDSA theory. Optimal radii from a fit with the MDSA theory together with the corresponding value of χ^2 for beads C and D of nominal size 2.26 µm.

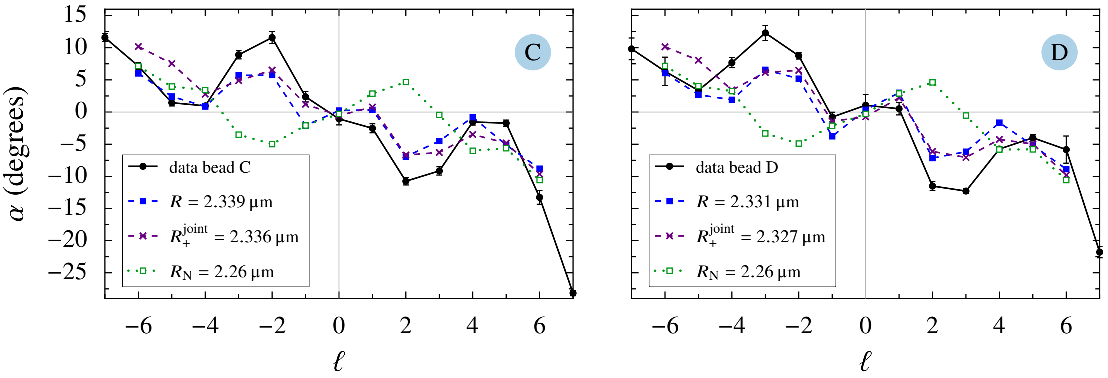

Figure 7.6: Beads with a nominal size of 2.26 microns. The figure represents the rotation angles for beads C (left) and D (right) as function of the topological charge ℓ. Similar to Fig. 7.4, the experimental results are shown as circle symbols. The error bars correspond to the standard deviations of the mean values computed from the several rounds of measuring α. Only for bead D there is one round of measurement for $\ell = 3, 4, 5$. In these case the error bars correspond to the errors of $\alpha_{\text{exp}}(\ell)$. The data points were fitted by using the MDSA theory (filled squared symbols) and the MDSA+ theory (cross symbols) with the astigmatism parameters obtained from the joint fit of beads A and B. For comparison, also the theoretical data points within the MDSA theory for the nominal radius $R_N = 2.26\,\mu m$ are shown (unfilled squares). A similar figure can be found in Ref. [153] but without the result for the joint fit shown here.

Tab. 7.5. Introducing astigmatism shows no significant improvement. Objects in the geometrical optics regime, with $R \gg \lambda$ are less sensitive to field asymmetries introduced by optical aberrations. The asymmetries are averaged out over the sphere. Even if A_{ast} and ϕ_{ast} are used as additional fitting parameters, there is no significant improvement. These results suggest that it is sufficient to apply the MDSA theory to fit the radius of beads in the geometrical optics regime. We observed in Sec. 6.1.2, that the rotation angle is not a unique function of the bead radius. There are oscillations due to interference between waves scattered at the back and front of the sphere. Examining χ^2 as a function of the bead radius R as shown in Fig. 7.7a, we thus also find multiple minima for the loss function. The distance between the minima is close to the expected value of $\lambda_0/4n \approx 0.169\mu m$ as depicted by the arrows in Fig. 7.7a. It is possible to resolve the ambiguity of the fitting radius by analysing the values of χ^2. The radii at ≈ 2.17 microns can be ruled out due to the large value of χ^2 compared to the values of χ^2 for the two other found radii. Additionally, by including astigmatism (dotted lines in Fig. 7.7a), we found no stable trapping position for a beam mode of $\ell = 6$, which also suggests that the radii for ≈ 2.17 microns can be ruled out. The radii found at ≈ 2.5 microns deviate by more than three times the standard deviation of the manufacturer-provided value for the radius and can thus also be neglected. For the smaller beads of nominal radii 1.5 µm, such ambiguities do not appear, as can be seen in Fig. 7.7b. It is evident that the fitted radii, shown by the horizontal lines, define the global minima of χ^2.

bead	R (µm)	L (µm)	A_{ast}	ϕ_{ast} (rad)	χ^2
C	2.336 ± 0.004	4.4 ± 0.78	0.254 (fixed)	0.41 (fixed)	47.1
D	2.327 ± 0.003	4.4 ± 0.47	0.254 (fixed)	0.44 (fixed)	84.7

Table 7.5: Parameters from a fit with the MDSA+ theory. Fit parameters for beads C and D of nominal size 2.26 µm, where the astigmatism parameters are fixed to the values found from the joint fit given in Tab. 7.3.

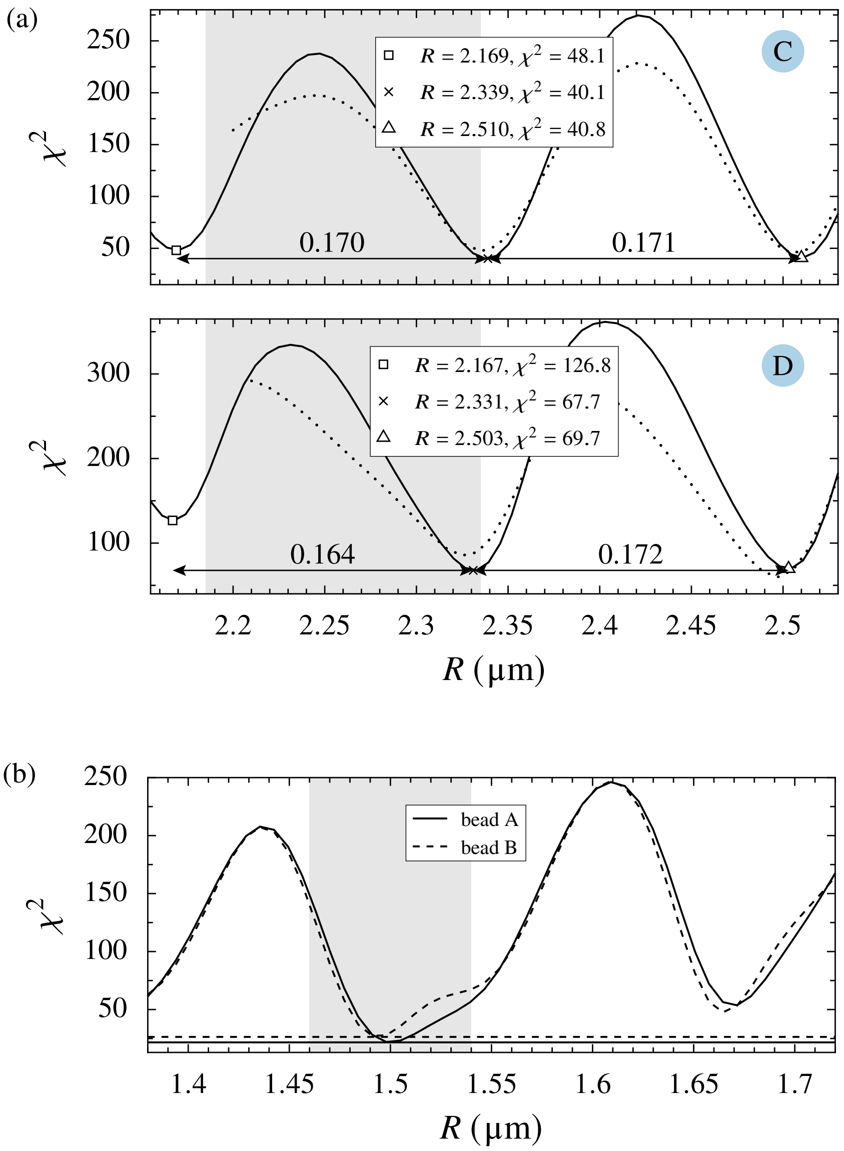

Figure 7.7: (a) Top and bottom panel respectively show χ^2 for bead C and D as function of the radius R. The values of χ^2 were calculated from the MDSA (solid lines) and the MDSA+ (dotted lines) theory. The grey-shaded areas represent the nominal values of the bead with their error bars (2.260 ± 0.075) µm. We determined the minima of χ^2 from the MDSA theory. The found radii and the χ^2 values are presented in the legends. The distance between the minima is depicted by the arrows. Figure (b) presents χ^2 for beads A and B calculated within the MDSA theory. The grey-shaded area accounts for the interval (1.50 ± 0.04) µm. The horizontal lines represent the global minima of χ^2 of beads A and B. Similar Figure in Ref. [142].

Part III

Casimir interaction between spherical objects

In the previous Part of this thesis, we explored the behaviour of spherical objects in a structured light field. If we disregard any external source fields and place the sphere near a second sphere, macroscopic dispersion forces, known as the Casimir force, arise. Compared to optical forces, where a beam with a certain frequency is used, Casimir forces are a broadband phenomenon, which makes them more complicated. Apart from certain limiting cases, fluctuations at every frequency and wave vector contribute to the force.

In this Part of the thesis, we will analyse the Casimir interaction between two spherical objects. The starting point will be the scattering formula, which we introduced in a basis-independent way in Sec. 2.1. In Chap. 8, we use the symmetries of the spherical geometry and present the scattering formula in a plane-wave and spherical-wave description. Chapter 9 provides a comprehensive study of the classical Casimir interaction of Drude spheres in vacuum and dielectric spheres in an electrolyte. In Chap. 10, we study the Casimir interaction between bi-isotropic spheres for arbitrary temperatures but within the limit of small and large distances. We apply our findings in Chap. 11 to an idealized system of perfect electromagnetic conductor spheres, where we study the influence of distance and temperature on the sign of the Casimir force. Our analytical results in the various limiting cases, e. g. short and large distances as well as low and high temperatures, are supported by numerical calculation in the intermediate regimes.

8 | Scattering approach to the sphere-sphere geometry

In this Chapter, we are going to apply the scattering formula to the studied setup of two bi-isotropic spheres. This geometry has two natural basis sets. A common approach to computing the Casimir free energy between two spheres involves using a spherical-wave basis. This basis is adequate for large separations between the spheres, where only a few multipoles are needed. However, for small distances, several thousand multipoles are necessary. It was not long ago that numerical calculations were able to reach the experimental relevant distance scale of $L/R \propto 10^{-3}$ for a sphere-plane setup, where R is the sphere radius and L the surface-to-surface distance [59, 169]. Other approaches with a bi-spherical wave basis were able to reduce the number of relevant multipoles [170]. A more efficient approach follows from a plane-wave description of the scattering formula [33, 171]. As we will see in the following discussions, not only numerical but also analytical calculations become more feasible within the plane-wave basis.

First, we start in Sec. 8.1 by introducing the general geometry under consideration and all relevant parameters used throughout this part of the thesis. Section 8.2 employs the plane-wave basis to describe the scattering process between the two objects. The expressions presented there will be the basis for the calculations in the following Chapters. For large distances between spheres, we use the multipole description of the scattering formula presented in Section 8.3.

8.1 General definitions for the sphere-sphere setup

As discussed in Sec. 2.1, the Casimir free energy at finite temperatures within the scattering approach is given by a functional evaluated at the Matsubara frequencies $\xi_n = 2\pi n k_\mathrm{B}T/\hbar$ (2.25)

$$\mathcal{F} = k_\mathrm{B}T \sum_{n=0}^{\infty}{}' \mathcal{F}(\xi_n)\,, \qquad \mathcal{F}(\xi) = \mathrm{tr}\log(\mathcal{I} - \mathcal{M}(\mathrm{i}\xi)) \tag{8.1}$$

with the round-trip operator $\mathcal{M} = \mathcal{T}_{12}\mathcal{R}_2\mathcal{T}_{21}\mathcal{R}_1$. We study the interaction between two stationary objects, meaning the frequency is conserved during the scattering process. It is thus sufficient to examine each frequency contribution to the free energy separately in the form $\mathcal{F}(\xi)$. Since $\mathrm{tr}\mathcal{M} < 1$ [172], we can expand the logarithm in a Mercator series, and each frequency contribution is given by

$$\mathcal{F}(\xi) = -\sum_{r=1}^{\infty} \frac{\mathrm{tr}\mathcal{M}^r}{r}\,, \tag{8.2}$$

where the dependence of the round-trip operator on the frequency is implicit in the following. The expansion given above has practical advantages, as we will see in the following. However, it also allows for a direct physical interpretation. Each summation index r can be understood as the number of round-trips the electromagnetic field performs between the two objects. A single round-trip ($r = 1$) is, for example, depicted in Fig. 8.1. At first, the electromagnetic field is reflected by sphere 1, then it gets transferred to sphere 2 where it is reflected again and finally returns to sphere 1. Neglecting multiple round-trips between the objects is equivalent to the Born approximation in scattering theory [173]. The expression (8.2) is the foundation for all analytical calculations of the Casimir free energy in this work. The two spheres of radii R_1 and R_2 are centred along the z-axis with a surface-to-surface

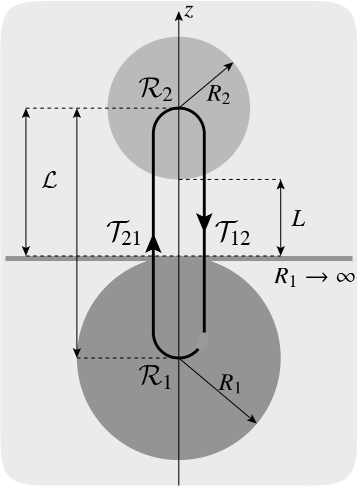

Figure 8.1: Sphere-sphere/plane geometry. Scattering geometry consisting of two spheres of radii R_1 and R_2 or, in the limit $R_1 \to \infty$, a sphere in front of a plane placed along the z-axis with a surface-to-surface distance L. In the sphere-sphere geometry, we also define the centre-to-centre distance with $\mathcal{L} = L + R_1 + R_2$, and for the sphere-plane setup, we will use $\mathcal{L} = L + R_2$. The loop between the sphere centres indicates the round-trip operator $\mathcal{M}$. The round-trip operator accounts for the reverberation of the electromagnetic field between the two spheres. It includes the reflection of the electromagnetic field at sphere 1 with the operator $\mathcal{R}_1$, the translation from sphere 1 to sphere 2 is described by the operator $\mathcal{T}_{21}$, the reflection at sphere 2 with $\mathcal{R}_2$ and finally the translation back to sphere 1 with $\mathcal{T}_{12}$.

distance L. Note that the two spheres form a cavity, where the dominant wavelength scales with the distance. Therefore, the convergence of the round-trip expansion (8.2) is controlled by the ratio of the surface distance to the radius. We thus introduce

$$x = \frac{L}{R_{\text{eff}}}, \qquad R_{\text{eff}} = \frac{R_1 R_2}{R_1 + R_2}, \tag{8.3}$$

where R_{eff} refers to the effective (eff) radius. We remark that the aspect ratio $x = L/R_{\text{eff}}$ should not be confused with the size parameter $\mathcal{K}R$ we used in the first Part of this thesis. Here and in the following x always refers to the above introduced aspect ratio. The sphere-plane geometry is obtained as a limiting case by taking one radius to infinity, as depicted in Fig. 8.1. Instead of using one of the radii as a control parameter to switch between the sphere-sphere and sphere-plane setup, it is more convenient to introduce the following parameter

$$u = \frac{R_{\text{eff}}}{R_1 + R_2} \tag{8.4}$$

which takes values between 0 and 1/4, respectively, accounting for a sphere in front of a plane and two equally sized spheres. We also assume that the spheres are dissimilar and bi-isotropic while the surrounding medium is isotropic.

As explained in Sec. 2.1, the Casimir force can be obtained by taking the negative gradient of the Casimir free energy with respect to the relative position of the objects. For our axial symmetric geometry, the force points along the z-direction. The derivative of the free energy (8.1) with respect to the surface-to-surface distance thus gives the Casimir force

$$F = -\frac{\partial \mathcal{F}}{\partial L} = k_{\text{B}} T \sum_{n=0}^{\infty}{}' \operatorname{tr}\left[(\mathcal{I} - \mathcal{M}(\mathrm{i}\xi_n))^{-1} \partial_L \mathcal{M}(\mathrm{i}\xi_n)\right] . \tag{8.5}$$

8.2 Angular spectrum decomposition of the scattering formula

To compute the Casimir free energy, as given in Eq. (8.2), we need to evaluate the trace of the round-trip operator in a specific basis. In this Section, we are going to employ the plane-wave basis introduced in Sec.3.1. The trace of the r-th fold round-trip matrix yields

$$\mathrm{tr}\mathcal{M}^r = \sum_{p_1=\mathrm{TE,TM}} \int \frac{\mathrm{d}^2\mathbf{k}_1}{(2\pi)^2} \langle \mathbf{k}_1, p_1, - |\, (\mathcal{T}_{12}\mathcal{R}_2\mathcal{T}_{21}\mathcal{R}_1)^r \,| \mathbf{k}_1, p_1, - \rangle\,. \tag{8.6}$$

Recall that the plane-wave basis $|\mathbf{k}, p, \sigma\rangle$ is defined by the transverse wave vector $\mathbf{k}$, the polarisation p and the propagation direction $\sigma = \pm$. Note that sphere 1 only reflects waves travelling in the negative z-direction, which means $\mathcal{R}_1\,|\mathbf{k}, p, +\rangle$ vanishes. The plane-wave basis has the advantage that the translation operator is diagonal within this basis and yields a phase factor $\mathcal{T}_{12}|\mathbf{k}, p, -\rangle = \mathrm{e}^{-\mathrm{i}\sigma k_z \mathcal{L}}|\mathbf{k}, p, -\rangle$, where k_z is the modulus of the z-component of the wave vector

$$k_z = \mathrm{i}\kappa = \mathrm{i}\sqrt{\mathcal{K}^2 + \mathbf{k}^2} \tag{8.7}$$

with the imaginary wave number $\mathcal{K}$ in a medium of refractive index n_m defined in Eq. (4.5) and the axial wave vector κ for imaginary frequencies. The matrix elements of the translation operator in the plane-wave basis are thus given by

$$\langle \mathbf{k}', p', \sigma' | \mathcal{T} | \mathbf{k}, p, \sigma \rangle = \mathrm{e}^{-\kappa\mathcal{L}} \delta_{p',p} \delta_{\sigma',\sigma} \delta(\mathbf{k}' - \mathbf{k})\,. \tag{8.8}$$

We assume a non-chiral medium between the spheres. Hence, there is no mixing of polarisations during the translation process. By using the resolution of the identity in the plane-wave basis, given in Eq. (3.7) and taking advantage of the diagonal nature of the translation operator, the trace reads [33]

$$\begin{aligned} \mathrm{tr}\mathcal{M}^r = \sum_{p_1,\ldots,p_{2r}} \int \frac{\mathrm{d}^2\mathbf{k}_1 \ldots \mathrm{d}^2\mathbf{k}_{2r}}{(2\pi)^{4r}} \prod_{j=1}^{r} & \mathrm{e}^{-\kappa_{2j}\mathcal{L}} \mathrm{e}^{-\kappa_{2j-1}\mathcal{L}} \\ & \times \langle \mathbf{k}_{2j+1}, p_{2j+1}, - | \mathcal{R}_2 | \mathbf{k}_{2j}, p_{2j}, + \rangle \langle \mathbf{k}_{2j}, p_{2j}, + | \mathcal{R}_1 | \mathbf{k}_{2j-1}, p_{2j-1}, - \rangle\,, \end{aligned} \tag{8.9}$$

where the summation indices are cyclic to account for the trace, so e. g. we identify $2r + 1$ with 1. The cyclic character will become relevant on several occasions throughout this work. Note that the matrix elements of the reflection operator are defined in Eq. (4.26).

8.3 Multipole expansion of the scattering formula

In this Section, we provide the trace expression in the multipole basis. The multipole expansion of the scattering formula for the sphere-plane geometry with isotropic objects was already determined in Ref. [174]. Here, we derive the expression for two spheres and also include polarisation mixing.

As a reminder, the multipole basis $|l, m, P, s\rangle$, introduced in Sec. 3.2 is defined by the multipole moments l, m, the polarisation $P = \mathrm{E}, \mathrm{M}$ and $s = \mathrm{reg}, \mathrm{out}$, which distinguishes between regular and outgoing waves with respect to a sphere's centre. The multipole moments l and m are conserved upon scattering at a bi-isotropic sphere. Furthermore, the geometry is invariant under rotations about the symmetry axis, which we have chosen as the z-axis. The round-trip operator thus commutes with the z-component of the angular momentum operator, which means m is also conserved upon translation of the electromagnetic field from one sphere to the other. The round-trip matrix becomes block-diagonal and the trace of the r-fold round-trip matrix yields

$$\mathrm{tr}\mathcal{M}^r = \sum_{m=-\infty}^{\infty} \sum_{l_1=\max(1,|m|)}^{\infty} \sum_{P_1=\mathrm{M,E}} \langle l_1, m, P_1, \mathrm{out}| \left(\mathcal{T}_{12}\mathcal{R}_2\mathcal{T}_{21}\mathcal{R}_1\right)^r |l_1, m, P_1, \mathrm{reg}\rangle \,, \tag{8.10}$$

where we exchanged the summation over m and l to make use of the block-diagonal character. Only incident regular waves $|\mathrm{reg}\rangle$ scatter into outgoing $\langle\mathrm{out}|$ modes at the spheres, so we already carried out the sum over s. After inserting the identity in the spherical-wave basis (3.12) and making use of the Mie coefficients (4.19), we obtain

$$\begin{aligned}\mathrm{tr}\mathcal{M}^r = \sum_{m=-\infty}^{\infty} \sum_{l_1,\dots,l_{2r}} \sum_{P_1,\dots,P_{2r}} \sum_{Q_1,\dots,Q_{2r}} \prod_{j=1}^{2r} \mathrm{i}^{P_{2j}-Q_{2j-1}} \mathrm{i}^{P_{2j-1}-Q_{2j}} r_{l_{2j+1}}^{2;(Q_{2j-1},P_{2j})} r_{l_{2j}}^{1;(Q_{2j},P_{2j-1})} \\ \times \langle l_{2j+1}, m, P_{2j+1}, \mathrm{reg}|\mathcal{T}_{12}|l_{2j}, m, Q_{2j+1}, \mathrm{out}\rangle \langle l_{2j}, m, P_{2j}, \mathrm{reg}|\mathcal{T}_{21}|l_{2j-1}, m, Q_{2j}, \mathrm{out}\rangle \,.\end{aligned} \tag{8.11}$$

We added a superscript $t = 1, 2$ to the Mie coefficients $r_l^{t;(P,P')}$ to distinguish between spheres 1 and 2. The summation indices are cyclic, equivalent to what we discussed for the plane-wave expansion. The multipole moment l and polarisation P are, in general, not conserved while the field propagates from one sphere to the other. To determine the matrix elements of the translation operator in the multipole basis, it is convenient to perform a basis change into the plane-wave basis, where the translation operator is diagonal (8.8)

$$\langle l', m, P', \mathrm{reg}|\mathcal{T}|l, m, P, \mathrm{out}\rangle = \sum_{p=\mathrm{TE,TM}} \int \frac{\mathrm{d}^2\mathbf{k}}{(2\pi)^2} e^{-\kappa\mathcal{L}} \langle l', m, P', \mathrm{reg}|\mathbf{k}, p, \pm\rangle \langle \mathbf{k}, p, \pm|l, m, P, \mathrm{out}\rangle \,. \tag{8.12}$$

The integral given above can be evaluated by using the basis transformation coefficients introduced in Eqs. (4.22) and (4.23), together with the expansion [98]: $e^{-\kappa\mathcal{L}} = \sum_{l=0}^{\infty}(2l+1)\mathrm{i}^l h_l(\mathrm{i}\mathcal{K}\mathcal{L})P_l(\cos(\theta_K))$, where $\kappa = \mathcal{K}\cos(\theta_K)$. The solution is well-known in the literature [175]

$$\langle l', m, P', \mathrm{reg}|\mathcal{T}|l, m, P, \mathrm{out}\rangle = \frac{2(-1)^{m+1}\sqrt{\pi}(\pm\mathrm{i})^{l-l'}}{\pi\sqrt{l(l+1)l'(l'+1)}} \sum_{l''=|l-l'|}^{l+l'} \sqrt{2l''+1}\, k_{l''}(\mathcal{K}\mathcal{L})\, c_{l,l',l'',m}^{P,P'} Y_{-m,m,0}^{l,l',l''} \,. \tag{8.13}$$

We remark that the translation coefficients for imaginary frequencies can also be obtained from a Wick rotation of the coefficients for real frequencies, known for a long time, see e.g. Ref. [176]. The $+(-)$ sign corresponds to a wave travelling in positive (negative) z-direction and $k_l(\mathcal{K}\mathcal{L}) = -(\pi\mathrm{i}^l/2)h_l(\mathrm{i}\mathcal{K}\mathcal{L})$ defines the modified spherical Hankel function. Depending on whether the polarization is conserved or not, the coefficient $c_{l,l',l'',m}^{P,P'}$ yield

$$c_{l,l',l'',m}^{P,P'} = \begin{cases} l(l+1) + l'(l'+1) - l''(l''+1) & P = P' \\ \pm 2m\mathcal{K}\mathcal{L} & P \neq P' \end{cases} \tag{8.14}$$

and $Y_{-m,m,0}^{l,l',l''}$ defines the Gaunt coefficients with two Wigner-3j symbols

$$Y_{-m,m,0}^{l,l',l''} = \sqrt{\frac{(2l+1)(2l'+1)(2l''+1)}{4\pi}} \begin{pmatrix} l & l' & l'' \\ 0 & 0 & 0 \end{pmatrix} \begin{pmatrix} l & l' & l'' \\ -m & m & 0 \end{pmatrix} \,. \tag{8.15}$$

9 Universal Casimir interaction and approximate conformal invariance

The content discussed in this Chapter is published in Refs. [177, 178] and [179] and, therefore, also contains input from discussions with authors of the articles. All analytical calculations performed in Ref. [177], which are presented in Secs. 9.2 and 9.3, have been done by the author of this work. The work presented in Secs. 9.4 and 9.4.3 was done in close collaboration with Benjamin Spreng, who has provided the numerical results for the Casimir interaction between dielectric spheres in an electrolytic solution.

The Casimir interaction is usually known as a quantum effect arising from the vacuum fluctuations of the electromagnetic field. However, at finite temperatures, thermal photons with wavelength $\lambda_T = \hbar c/k_\mathrm{B}T$ also contribute, which can dominate the quantum contribution at high temperatures. This leads to a finite Casimir force between objects even in the classical limit $\hbar \longrightarrow 0$, which, given the definition of the thermal wavelength, is equivalent to $T \longrightarrow \infty$. As a result, the Casimir free energy becomes linear in temperature, yielding a constant Casimir entropy [6].

Within the scattering approach, the high-temperature limit amounts to taking the zero-frequency term of the Matsubara sum. For metallic objects described by the Drude (Dr) model

$$\epsilon_\mathrm{Dr}(\xi) = 1 + \frac{\sigma(\mathrm{i}\xi)}{\epsilon_0\xi}\,, \qquad \sigma(\mathrm{i}\xi) = \frac{\epsilon_0\omega_\mathrm{p}^2}{\xi+\gamma} \tag{9.1}$$

the dielectric function ϵ_Dr diverges in this limit. The reason for the divergence is the finite dc-conductivity $\sigma(0) = \epsilon_0\omega_\mathrm{p}/\gamma$, where ω_p denotes the plasma frequency and γ defines the relaxation frequency. The Casimir free energy thus becomes independent of the dielectric properties of the system and the Casimir entropy is exclusively a function of the geometric properties. Analytical results for the plane-plane [180, 181], the sphere-plane [24], and two equally-sized spheres [25] were obtained successfully in the past. A setup, which we found to be dual to the metallic objects in vacuum, involves dielectric objects in an electrolytic solution. Here, the finite dc-conductivity of the medium is responsible for the high-temperature behaviour. Until recently, the contribution of the Casimir effect in these setups was never considered [27], but experiments [4, 58] confirmed that the Casimir interaction could lead to a long-range force between dielectric objects in a conducting medium.

In this Chapter, we want to study the Casimir interaction for these two types of systems involving two spherical objects. We start in Sec. 9.1 by defining the high-temperature limit and the duality relation between the two systems mentioned above. In the following Sec. 9.2, we determine the high-temperature result for a scalar field between two spheres with Dirichlet boundary conditions. The scalar result is known to be the dominant contribution at short distances for metallic objects in vacuum, and we found that this also holds for dielectric objects in an electrolytic solution. Sec. 9.3 discusses the derivation of the analytical result of the Casimir free energy for two Drude spheres, which was suspected to be impossible to derive within the scattering approach [182]. For the dielectric objects in an electrolyte, we could not derive analytical expressions for the Casimir free energy. However, in Sec. 9.4, we present several limiting results and a semi-analytical approximation formula. We end with a discussion of the importance of our result for biological and colloidal systems.

9.1 Casimir interaction at high-temperatures and duality relation

As we discussed earlier, the Casimir free energy at finite temperatures is given by the sum over Matsubara frequencies (8.1). The Matsubara frequencies scale with the temperature T, hence any contribution at finite frequencies are exponentially suppressed at high temperatures, due to the exponential decay of the translation coefficients $\exp(-\kappa L)$ with $\kappa = \sqrt{\mathcal{K}^2 + \mathbf{k}^2}$, $\mathcal{K} = \xi\sqrt{\epsilon_\mathrm{m}}/c$. The dominant term will thus come from the zero Matsubara frequency $\xi = 0$. In this Section, we are going to compute the zero-frequency terms of the Casimir free energy, which is purely of entropic origin. We introduce the following notation for the thermal Casimir free energy

$$\mathcal{F}_T = -\frac{k_\mathrm{B}T}{2} f\,, \qquad f = \sum_{r=1}^{\infty} f^{(r)}, \qquad f^{(r)} = \frac{\mathrm{tr}\mathcal{M}^r(0)}{r} \tag{9.2}$$

with the dimensionless free energy f and the r-th round-trip term $f^{(r)}$. Note that the Casimir entropy $k_\mathrm{B} f/2$ is constant.

We assume that the dielectric function of the surrounding medium ϵ_m, diverges slower than $1/\xi^2$ in the zero-frequency limit. This assumption is valid in vacuum, where $\epsilon_\mathrm{m}(\xi) = 1$, and also holds for a conducting electrolytic solution which is modelled with a Drude-type dielectric function for the transverse waves [27]. According to Eq. (9.1), the dielectric function scales like $\epsilon_\mathrm{m}(\xi) \propto 1/\xi$ at low frequency. The axial wave vector component in the static limit is therefore given by the modulus of the transverse wave vector $\kappa = |\mathbf{k}| = k$. Based on (8.9), the angular spectrum representation of the round-trip contribution $f^{(r)}$ reads

$$\begin{aligned} f^{(r)} = \frac{1}{r} \sum_{p_1,\dots,p_{2r}} \int \frac{\mathrm{d}^2\mathbf{k}_1 \dots \mathrm{d}^2\mathbf{k}_{2r}}{(2\pi)^{4r}} \prod_{j=1}^{r} \mathrm{e}^{-k_{2j}\mathcal{L}} \mathrm{e}^{-k_{2j-1}\mathcal{L}} \\ \times \langle \mathbf{k}_{2j+1}, p_{2j+1}, -|\mathcal{R}_2|\mathbf{k}_{2j}, p_{2j}, +\rangle \langle \mathbf{k}_{2j}, p_{2j}, +|\mathcal{R}_1|\mathbf{k}_{2j-1}, p_{2j-1}, -\rangle\,. \end{aligned} \tag{9.3}$$

The reflection matrix elements in the plane-wave basis, defined in Eq. (4.26), depend on the polarisation-conversion coefficients $A_{i,j}, B_{i,j}, C_{i,j}$ and $D_{i,j}$ and the scattering amplitudes S_{p_i,p_j}. Apart from $A_{i,j}$, the other three coefficients vanish all at zero frequency, and $A_{i,j}$ simply yields one. Together with the low-frequency expansion of the scattering amplitudes (4.59), the reflection matrix elements yield

$$\langle \mathbf{k}_i, p_i|\mathcal{R}|\mathbf{k}_j, p_j\rangle = \frac{2\pi R}{k_i} \sum_{l=1}^{\infty} \mathcal{X}_{p_i,p_j}(l) \frac{\chi_{i,j}^{2l}}{(2l)!} \tag{9.4}$$

with

$$\chi_{i,j} = 2R\sqrt{k_i k_j} \cos\left(\frac{\varphi_i - \varphi_j}{2}\right)\,. \tag{9.5}$$

Recall that the expansion coefficients $\mathcal{X}_{p_i,p_j}$ account for the materials of the spheres and the surrounding medium (see Eqs. (4.52) and (4.54)). For dielectric spheres of permittivity ϵ_s in a medium with permittivity ϵ_m only the transverse-magnetic modes contribute, hence only $\mathcal{X}_\mathrm{TM,TM}$ is non-zero (see Eq. (4.57)). The coefficients for a Drude sphere in vacuum (Dv) and a dielectric sphere in an electrolyte (de) can both be obtained from the general case of two dielectrics. The former one is a result of taking the limit $\epsilon_\mathrm{s} \to \infty$, while the latter one can be obtained for $\epsilon_\mathrm{m} \to \infty$, as shown in Tab. 9.1. The two cases can thus be seen as dual to each other. The sum over angular momenta in

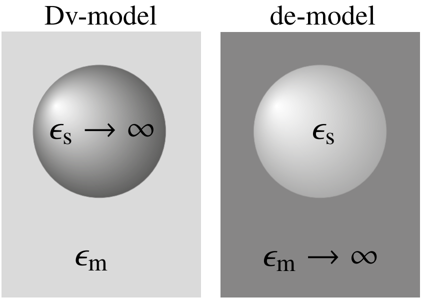

sphere-medium	ϵ_s/ϵ_m	$\mathcal{X}_{\mathrm{TM,TM}}$
dielectric-dielectric	finite	$\frac{l(\epsilon_s-\epsilon_m)}{l\epsilon_s+(l+1)\epsilon_m}$
Drude-vacuum (Dv)	∞	1
dielectric-electrolyte (de)	0	$-\frac{l}{l+1}$

Figure 9.1 & Table 9.1: Illustration of the duality between a Drude sphere in vacuum (Dv) and a dielectric sphere in an electrolyte (de). On the left-hand side of the figure, we depict a metallic sphere with a divergent dielectric function $\epsilon_s \rightarrow \infty$ in the static limit. The medium dielectric constant, which should be finite, is taken as that for vacuum $\epsilon_m = 1$. The figure on the right depicts a dielectric sphere with a finite dielectric constant ϵ_s in an electrolyte with $\epsilon_m \rightarrow \infty$. The table provides the corresponding expansion coefficients $\mathcal{X}_{\mathrm{TM,TM}}$ for the scattering amplitude.

Eq. (9.4) can be carried out in both cases. For the Drude spheres in vacuum, the matrix elements yield

$$\langle \mathbf{k}_i, \mathrm{TM}|\mathcal{R}_{\mathrm{Dv}}|\mathbf{k}_j, \mathrm{TM}\rangle = \frac{2\pi R}{k_i}\left[\cosh(\chi_{i,j}) - 1\right] \tag{9.6}$$

while for a dielectric sphere in an electrolyte, we get

$$\langle \mathbf{k}_i, \mathrm{TM}|\mathcal{R}_{\mathrm{de}}|\mathbf{k}_j, \mathrm{TM}\rangle = -\frac{2\pi R}{k_i}\left[\cosh(\chi_{i,j}) - 2\frac{\sinh(\chi_{i,j})}{\chi_{i,j}} + 2\frac{\cosh(\chi_{i,j}) - 1}{\chi_{i,j}^2}\right]. \tag{9.7}$$

Note that both cases have one term in common, namely $\cosh(\chi) = \sum_{l=0}^{\infty} \chi^{2l}/(2l)!$. This term originates from taking the monopole term $l = 0$ in Eq. (9.4) into account and thus corresponds to the reflection coefficient for a sphere with Dirichlet boundary conditions in a scalar field. The relation between the Casimir interaction for Drude spheres and Dirichlet spheres was already established by [24]. We found that the result for Dirichlet spheres is also applicable to the Casimir interaction between dielectric spheres in an electrolyte.

We thus first derive the Casimir interaction for a scalar field. The results for Drude spheres in vacuum and dielectric spheres in an electrolyte are then obtained by taking the remaining terms in Eqs. (9.6) and (9.7) into account.

9.2 Scalar field between two spheres with Dirichlet boundary conditions

In this Section, we will present the result for the Casimir free energy for a scalar field between Dirichlet boundary conditions using the scattering approach in the plane-wave basis. The result was formerly determined by using bispherical coordinates [24]. Here, we want to show that a plane-wave description can also be applied and that the result is dual to the one presented in Ref. [24]. The formalism introduced in this Section will be helpful for future discussions of the Casimir energy for Drude and dielectric spheres.

9.2.1 Derivation of the Casimir free energy

According to the discussion in the previous Section, the round-trip contribution $f^{(r)}$ to the Casimir free energy for a scalar field (sc) and two spheres with Dirichlet boundary conditions can be expressed as

$$f_{\mathrm{sc}}^{(r)} = \frac{1}{r} \sum_{p_1,\dots,p_{2r}} \int \frac{\mathrm{d}^2\mathbf{k}_1 \dots \mathrm{d}^2\mathbf{k}_{2r}}{(2\pi)^{4r}} \prod_{j=1}^{r} \mathrm{e}^{-k_{2j}\mathcal{L}} \mathrm{e}^{-k_{2j-1}\mathcal{L}} \cosh\left(\chi^{(2)}_{2j,2j+1}\right) \cosh\left(\chi^{(1)}_{2j-1,2j}\right) , \tag{9.8}$$

where the superscript in $\chi^{(n)}$ distinguishes between the two spheres of radii R_n, $n = 1, 2$.

To evaluate the above given multidimensional integral, we note that integrals over consecutive wave vector components are coupled through (9.5). Hence, we first perform a variable transformation to decouple $\chi_{i,j}$. We substitute the polar coordinates (k_i, ϕ_i) with $k_i = u_i^2$, $\phi_i = 2\varphi_i$. The φ_i-integration goes from 0 to π. Due to the symmetry of the cosine function in Eq. (9.5) under shifts by a half period and the fact that the hyperbolic cosine is an even function, we find that the integral over the interval $[\pi, 2\pi]$ yields the same result as the integral over $[0, \pi]$. We can thus expand the integration interval of φ_i to $[0, 2\pi]$ by adding a factor of 1/2. Next, we change from polar coordinates to Cartesian coordinates by substituting $(x_i, y_i) = u_i(\cos\varphi_i, \sin\varphi_i)$. The trace over the round-trip operator yields

$$\begin{aligned} f_{\mathrm{sc}}^{(r)} = \frac{1}{r} \frac{(\rho_1\rho_2)^r}{(2\pi)^{2r}} \int_{-\infty}^{\infty} \mathrm{d}^{2r}\mathbf{x} \int_{-\infty}^{\infty} \mathrm{d}^{2r}\mathbf{y} \prod_{j=1}^{r} & \mathrm{e}^{-\left(x_{2j}^2 + y_{2j}^2\right)} \mathrm{e}^{-\left(x_{2j-1}^2 + y_{2j-1}^2\right)} \\ & \times \left[\mathrm{e}^{\chi^{(2)}_{2j}} + \mathrm{e}^{-\chi^{(2)}_{2j}}\right] \left[\mathrm{e}^{\chi^{(1)}_{2j-1}} + \mathrm{e}^{-\chi^{(1)}_{2j-1}}\right] , \end{aligned} \tag{9.9}$$

where we have rewritten the hyperbolic cosines in terms of exponential functions: $\cosh(\chi) = (\mathrm{e}^{\chi} + \mathrm{e}^{-\chi})/2$. The arguments are defined by

$$\chi_i^{(n)} = 2\rho_n(x_i x_{i+1} + y_i y_{i+1}) , \qquad \rho_n = \frac{R_n}{\mathcal{L}} , \tag{9.10}$$

with aspect ratios ρ_n for $n = 1, 2$. Changing the coordinates decoupled the $4r$-dimensional integral in Eq. (9.8) into a product of two $2r$-dimensional integrals in $\mathbf{x}^t = (x_1, x_2, \dots x_{2r})$ and $\mathbf{y}^t = (y_1, y_2, \dots, y_{2r})$, where t denotes the transposed vector. Each integral is of Gaussian type. After expanding the product in Eq. (9.9), one obtains in total 2^{2r} Gaussian integrals with a bilinear form given by a $2r \times 2r$-dimensional symmetric, semi-definite and cyclic Toepliz matrix

$$\mathbf{M}_2^{\pm} = \begin{pmatrix} 1 & a_1 + a_2 \\ a_1 + a_2 & 1 \end{pmatrix} , \qquad \mathbf{M}_{2r}^{\pm} = \begin{pmatrix} 1 & a_1 & 0 & \dots & 0 & a_{2r} \\ a_1 & 1 & a_2 & & & 0 \\ 0 & a_2 & 1 & \ddots & & \vdots \\ \vdots & & \ddots & \ddots & & 0 \\ 0 & & & & & a_{2r-1} \\ a_{2r} & 0 & \dots & 0 & a_{2r-1} & 1 \end{pmatrix} . \tag{9.11}$$

The off-diagonal elements alternate between $a_{2k-1} = \pm\rho_1$ for all odd indices and $a_{2k} = \pm\rho_2$ for even indices. There are in total 2^{2r} possible sign combinations. However, as we will see later, only the total number of entries with a negative sign is relevant for the result of the integral. We thus introduced a superscript + (−) for even (odd) numbers of off-diagonal elements with a negative sign. As explained in Appendix A.6.3, the result of a multidimensional Gaussian integral is determined by the determinant of the matrix $\mathbf{M}_{2r}^{\pm}$. We will evaluate the determinant in the following.

We can interpret the symmetric band matrix as a Hamiltonian for a tight-binding model with varying hopping elements between adjacent sites. It is well known that the determinant of such matrices can be computed using the transfer matrix method [183]

$$\det \mathbf{M}_{2r}^{\pm} = -\det\left(\mathbf{T} - 1\right) \prod_{n=1}^{2r} a_n \,. \tag{9.12}$$

The transfer matrix $\mathbf{T} = \mathbf{T}_{2r}\mathbf{T}_{2r-1}\dots\mathbf{T}_2\mathbf{T}_1$ results from applying successively transfer matrices $\mathbf{T}_n$ which connect consecutive pairs of components of the eigenvectors of $\mathbf{M}_{2r}^{\pm}$. The one-step transfer matrix is defined by

$$\begin{aligned}\mathbf{T}_n &= \begin{pmatrix} -a_n^{-1} & -a_n^{-1}a_{n-1} \\ 1 & 0 \end{pmatrix} \\ &= \begin{pmatrix} -a_n^{-1} & 0 \\ 0 & 1 \end{pmatrix} \mathbf{A}_{n-1} \begin{pmatrix} 1 & 0 \\ 0 & a_{n-1}^{-1} \end{pmatrix} \quad \text{with} \quad \mathbf{A}_{n-1} = \begin{pmatrix} 1 & -a_{n-1}^2 \\ 1 & 0 \end{pmatrix} .\end{aligned} \tag{9.13}$$

In the second line, we factorized the one-step transfer matrix according to [184] to use the periodicity of the Toepliz matrix. We apply the identity $\det\left(\mathbf{T} - 1\right) = 1 + \det\mathbf{T} - \mathrm{tr}\mathbf{T}$ for symmetric two-dimensional matrices. Determinants are furthermore multiplicative, so the determinant of the transfer matrix is given by the product of the determinants of each one-step transfer matrix: $\det\mathbf{T} = \prod_{n=1}^{2r}\det\mathbf{T}_n$. The entries in the Toeplitz matrix are periodic and cyclic, resulting in a determinant of the transfer matrix equal to one. To proceed with the calculation of $\det\left(\mathbf{T} - 1\right)$, we use that the trace is invariant under permutation, thus leading to

$$\mathrm{tr}\mathbf{T} = \prod_{n=1}^{2r} \mathrm{tr}(\mathbf{A}_1\mathbf{A}_2)^r \,. \tag{9.14}$$

Whenever we multiply two consecutive matrices $\mathbf{A}_n$ and $\mathbf{A}_{n-1}$, the product is always the same due to the periodic alternating entries of the Toepliz matrix. Finally, taking into account that the trace over the r-th power of a matrix is equivalent to sum of the r-th power of the eigenvalues, we find

$$\mathrm{tr}\left(\mathbf{A}_1\mathbf{A}_2\right)^r = \left(y + \sqrt{y^2-1}\right)^r + \left(y - \sqrt{y^2-1}\right)^r = 2T_r(y) \,. \tag{9.15}$$

We introduced the Chebyshev polynomials [185, Chap. 18] $T_r(y)$ of the first kind of order r and argument

$$y = \frac{1 - \rho_1^2 - \rho_2^2}{2\rho_1\rho_2} = \frac{\mathcal{L}^2 - R_1^2 - R_2^2}{2R_1R_2} \,. \tag{9.16}$$

The distance measure y is conformal invariant [186] it remains unchanged if two exterior spheres are mapped to a symmetry, where one sphere is within the other. We also note that y can be expressed in terms of the earlier introduced aspect ratio $x = L/R_{\mathrm{eff}}$ and geometry parameter $u = R_{\mathrm{eff}}/(R_1 + R_2)$

$$y = 1 + x + \frac{u}{2}x^2 \,. \tag{9.17}$$

The above-given definition simplifies the interpretation of y for small ($y \to 1$) and large ($y \to \infty$) distances between the spheres and also the transition from the sphere-sphere to the sphere-plane geometry via the parameter u.

In summary, the determinant of the periodic Toepliz matrix (9.11) yields

$$\det \mathbf{M}_{2r}^{\pm} = 2(\rho_1\rho_2)^r \left(T_r(y) \mp 1\right) . \tag{9.18}$$

Note that the definition above also includes the determinant for a single round-trip, where $T_1(y) = y$ and the determinant yields: $\det \mathbf{M}_2^{\pm} = 1 - \rho_1^2 - \rho_2^2 \mp 2\rho_1\rho_2$.

We can now proceed with the evaluation of the integrals (9.9). We note that half of the 2^{2r} Gaussian integrals are characterized by the bilinear form $\mathbf{M}_{2r}^{+}$, while the other half is represented by $\mathbf{M}_{2r}^{-}$. We thus obtain for the round-trip contribution (9.9)

$$f_{\mathrm{sc}}^{(r)} = \frac{1}{2r}\left(\frac{\rho_1\rho_2}{\pi^2}\right)^r \sum_{\sigma=\pm}\left(\int \mathrm{d}^{2r}\mathbf{x}\mathrm{e}^{-\mathbf{x}^t\mathbf{M}_{2r}^{\sigma}\mathbf{x}}\right)^2 = \frac{(\rho_1\rho_2)^r}{2r}\sum_{\sigma=\pm}\frac{1}{\det \mathbf{M}_{2r}^{\sigma}} . \tag{9.19}$$

We used the result for a multidimensional Gaussian integral defined in Eq. (A.28).

Finally, we insert the result of the determinant (9.18) and perform the sum over the round-trips according to (9.2). The dimensionless Casimir free energy $f_{\mathrm{sc}} = \sum_{r=1}^{\infty} f_{\mathrm{sc}}^{(r)}$ for Dirichlet spheres in a scalar field thus yields

$$f_{\mathrm{sc}} = \sum_{r=1}^{\infty} \frac{1}{2r}\frac{T_r(y)}{T_r^2(y) - 1} = \sum_{r=1}^{\infty} \frac{Z^r}{r}\frac{1 + Z^{2r}}{(1 - Z^{2r})^2} . \tag{9.20}$$

Following the notation introduced in Ref. [24], we defined

$$Z = \exp(-\mu) = y - \sqrt{y^2 - 1}\,, \qquad \mu = \operatorname{arcosh}(y) \tag{9.21}$$

and expressed the Chebyshev polynomials in terms of exponential functions with: $T_r(y) = (Z^{-r} - Z^r)/2$.

We can also write the dimensionless Casimir free energy for a scalar field as

$$f_{\mathrm{sc}} = Z\frac{\mathrm{d}}{\mathrm{d}Z}\sum_{r=1}^{\infty}\frac{1}{r^2}\frac{Z^r}{1 - Z^{2r}} = -\sum_{l=0}^{\infty}(2l + 1)\log\left(1 - Z^{2l+1}\right) . \tag{9.22}$$

The distance measure y is always greater than one, thus $0 < Z < 1$. The last factor in the first sum was thus expanded in a geometrical series. In the next step, we evaluated the round-trip sum with the Mercator series and reproduced the result found in Ref. [24] for the Casimir free energy.

Notably, the reduced Casimir free energy for a scalar field between two spheres with Dirichlet boundary conditions is a function of y, meaning it obeys exact conformal invariance. This property makes this problem analogous to the critical Casimir effect [187, 188].

9.2.2 Convergence and limiting behaviour

In the following, we are going to compare the two representations (9.20) and (9.22) derived above for the Casimir free energy of a scalar field.

For large distances $y > 1$, the multipole expansion turns out to converge much faster than the round-trip expansion, as can be seen in Fig. 9.2a, where we compared the convergence of both sums

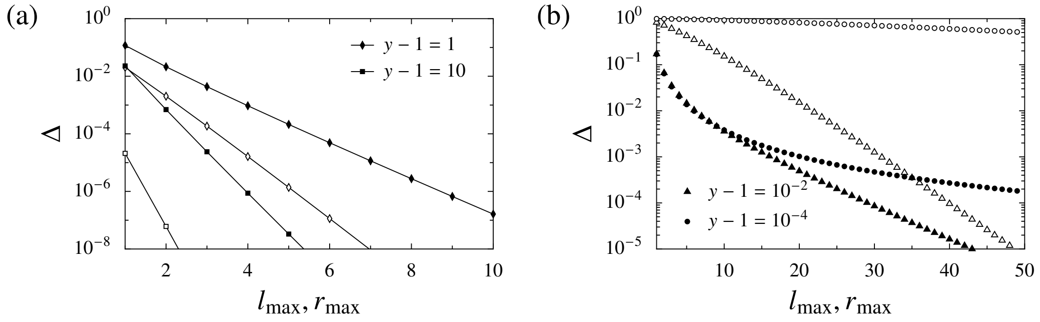

Figure 9.2: Convergence of the scalar Casimir free energy. Both figures show the relative deviation $\Delta = \left|1 - f_{\text{sc}}^{\max}/f_{\text{sc}}^{\text{ref}}\right|$. The free energy $f_{\text{sc}}^{\max}$ is calculated either with the round-trip sum (9.20) (filled symbols) or with the multipole sum (9.22) (un-filled symbols) with the summations respectively performed up to $l_{\max}$ or $r_{\max}$ and $f_{\text{sc}}^{\text{ref}}$ is the numerically exact result for the free energy evaluated for $l_{\text{ref}} \gg l_{\max}$ or $r_{\text{ref}} \gg r_{\max}$. **(a)** Analysis of the convergence for large distances $y > 1$ with a reference result which was calculated for $l_{\max}^{\text{ref}} = 50$. **(b)** Analysis of the convergence for small distances $y - 1 \ll 1$ with a reference result which was computed for $r_{\max}^{\text{ref}} = 1000$.

for $y - 1 = 1$ and 10. The leading order can be extracted from the first term ($l = 0$) in Eq. (9.22) by using $Z = 1/(2y) + O(y^{-3})$. We obtain the following expression for the Casimir free energy at large separations

$$f_{\text{sc}} \approx \frac{1}{2y} \,. \tag{9.23}$$

Of particular interest is the small distance regime $y \longrightarrow 1$, which according to Eq. (9.21) corresponds to $\mu \longrightarrow 0$. The round-trip sum converges much faster in this regime compared to the expansion in bispherical multipoles. Each summand decays with $\mathrm{e}^{-\mu x}/x$ in the r-sum, while each summand in the l-sum scales with $x\mathrm{e}^{-\mu x}$. In Fig. 9.2b, we depicted the convergence of each sum for distances $y-1 = 10^{-2}$ and 10^{-4}. It is evident that even for small round-trip numbers $r < 10$, the approximation of the Casimir free energy is extremely accurate. Later on, we will utilize these findings.

The r-sum simplifies not only the numerical computation for small distances but also the evaluation of the asymptotic expansion of the Casimir free energy. We can express (9.20) in terms of so-called F-series [189], which is a generalization of the Lambert series and defined as

$$\mathcal{L}_q(s, z) = \sum_{k=1}^{\infty} \frac{k^s q^{kz}}{1 - q^k} \,. \tag{9.24}$$

After decomposing the fraction in Eq. (9.20), we find for the total free energy

$$f_{\text{sc}} = Z \frac{\mathrm{d}}{\mathrm{d}Z} \left[\mathcal{L}_Z(-2, 1) - \mathcal{L}_{Z^2}(-2, 1)\right] \,. \tag{9.25}$$

Small distances correspond to $Z = 1 + O(\sqrt{y - 1})$. The expansion of the Lambert series in the limit $Z \longrightarrow 1$ is known [190] and presented in Appendix A.4. After some basic algebraic transformations, which are in detail given in Appendix D.1, we find for the asymptotic expansion of Casimir free energy $\mathcal{F}_{\mathrm{sc}} = -(k_{\mathrm{B}}T/2)f_{\mathrm{sc}}$ for small distances

$$\begin{aligned}\mathcal{F}_{\mathrm{sc}} = \frac{k_{\mathrm{B}}T}{2}\Bigg[&-\frac{\zeta(3)}{2\mu^2} + \frac{1}{12}\log(\mu) + \frac{1}{12} - \log(A) + \frac{1}{6}\log(2) \\ &+\sum_{n=1}^{\infty}\frac{2n+1}{2n}\frac{B_{2n}B_{2n+2}}{(2n+2)!}\left(2^{2n+1}-1\right)\mu^{2n}\Bigg]\,,\end{aligned} \tag{9.26}$$

where we introduced the Apéry constant $\zeta(3) = 1.202\ldots$, the Glaisher's constant $A = 1.28242\ldots$ and the Bernoulli numbers B_k. Instead of μ as an expansion coefficient, it is more natural to use the aspect ratio $x = L/R_{\mathrm{eff}}$. According to Eqs. (9.21) and (9.17) is μ given by $\sqrt{2x} + O(x^{3/2})$ for short distances. The leading term in Eq. (9.26) thus yields $\mathcal{F}_{\mathrm{sc}} \approx 2\pi R_{\mathrm{eff}}\mathcal{F}_{\mathrm{pp}}(L)$ with $\mathcal{F}_{\mathrm{pp}} = -k_{\mathrm{B}}T\zeta(3)/16L$ which corresponds to the proximity-force-approximation result. The divergence of the leading term for $\mu \to 0$ is related to the zero-eigenvalue of the matrix $\mathbf{M}^{\pm}_{2r}$, which originates from the cyclic character of the matrix associated with closed boundary conditions. We furthermore remark that the terms up to the order of μ^4 in Eq. (9.26) are in agreement with the values given in Ref. [24]. Our expansion goes, however, beyond the known results and also provides a simple relation for the expansion coefficients in terms of the Bernoulli numbers.

9.3 Metallic spheres described by the Drude model in vacuum

In this Section, we will derive the Casimir free energy for two Drude spheres in vacuum. First, we will identify the monopole contributions (Secs. 9.3.1 and 9.3.2), which are not present for an electromagnetic field compared to the scalar field. We will present in Sec. 9.3.3 the result for the Casimir free energy for arbitrary radii as well as for geometrical limiting cases like the sphere-plane setup. Finally, we derive in Sec. 9.3.4 an expansion of the free energy for small separations.

9.3.1 Identifying the monopole terms in a scalar field

We insert the reflection coefficients (9.6) for a Drude sphere in vacuum into the round-trip contribution to the thermal Casimir free energy (9.3). After performing the same variable transformation as for the scalar field, the r-th round-trip contribution for the Drude-vacuum-Drude (DvD) model reads

$$\begin{aligned}f^{(r)}_{\mathrm{DvD}} = \frac{1}{r}\frac{(\rho_1\rho_2)^r}{(2\pi)^{2r}}\int \mathrm{d}^{2r}\mathbf{x}\int \mathrm{d}^{2r}\mathbf{y}\prod_{j=1}^{r}&\,\mathrm{e}^{-\left(x^2_{2j}+y^2_{2j}\right)}\mathrm{e}^{-\left(x^2_{2j-1}+y^2_{2j-1}\right)} \\ &\times\left[\mathrm{e}^{\chi^{(2)}_{2j}} + \mathrm{e}^{-\chi^{(2)}_{2j}} - 2\right]\left[\mathrm{e}^{\chi^{(1)}_{2j-1}} + \mathrm{e}^{-\chi^{(1)}_{2j-1}} - 2\right]\,,\end{aligned} \tag{9.27}$$

where $\chi^{(n)}_i$ was defined in Eq. (9.10). As highlighted earlier, the Casimir free energy for two Drude spheres differs from the Casimir free energy for a scalar field only by contributions from the monopole terms. Hence, we need to identify all terms which originate from couplings to monopole modes. These are all terms in Eq. (9.27), which contain at least one factor -2 after expanding the product. We introduce the following definition for the monopole terms

$$\Delta_r = f^{(r)}_{\mathrm{DvD}} - f^{(r)}_{\mathrm{sc}}\,. \tag{9.28}$$

There are in total $3^{2r} - 2^{2r}$ monopole terms, which are all of Gaussian-type. The bilinear form in the exponent can be described by tridiagonal matrices similar to the matrix (9.11) for the scalar case. However, with each factor -2 appearing in the expansion of the product in Eq. (9.27) the corresponding pair of off-diagonal matrix elements vanish, thus breaking the cyclic invariance given in the scalar case. The matrices are thus block-diagonal, where the number of blocks depends on the numbers of -2 factors. Each block matrix is given by a symmetric tridiagonal 2-Toepliz matrix [191] of the form

$$\mathbf{m}_n^{(1/2)} = \begin{pmatrix} 1 & \pm\rho_{1/2} & \cdots & & 0 \\ \pm\rho_{1/2} & 1 & \pm\rho_{2/1} & & \\ \vdots & \pm\rho_{2/1} & 1 & \ddots & \\ & & \ddots & \ddots & \\ 0 & & & & 1 \end{pmatrix} . \tag{9.29}$$

The pairs of off-diagonal matrices alternate between ρ_1 and ρ_2 and come either with a positive or negative sign, similar to what we discussed earlier. Each block matrix is characterized by its size n and the index of the first off-diagonal entry indicated as a superscript with either 1 or 2. For a $2r$-dimensional block matrix with k blocks, we write

$$\mathbf{M}_w = \operatorname{diag}\left(\mathbf{m}_{n_1}^{(s_1)}\mathbf{m}_{n_2}^{(s_2)}\mathbf{m}_{n_3}^{(s_3)}\dots\mathbf{m}_{n_k}^{(s_k)}\right) . \tag{9.30}$$

The index w denotes an element of a set $\Pi_{2r,k}$ containing a multiset of tuples $\{(n_1, s_1), (n_2, s_2), \dots, (n_k, s_k)\}$, where each tuple characterizes the dimension n_i of the block matrix and the index $s_i \in \{1, 2\}$ of the first off-diagonal entry. The sizes of the blocks $n_i \in \{1, 2, \dots 2r\}$ are chosen such that $\sum_{i=1}^{k} n_i = 2r$. Furthermore, we cannot set s_i freely. The value rather depends on the size n_{i-1} and the index s_{i-1} of the previous block in the following way

$$s_i = \begin{cases} s_{i-1} & \text{if} \quad n_{i-1} = 2m - 1,\ m \in \mathbb{N} \\ \overline{s_{i-1}} & \text{if} \quad n_{i-1} = 2m,\ m \in \mathbb{N} \end{cases} \tag{9.31}$$

with $\bar{s} = 2(1)$ if $s = 1(2)$. This means that if the previous block is odd-dimensional, the superscript changes from 2 to 1 or vice versa. We depicted in the left panel of Fig. 9.3 a block matrix $\mathbf{M}_w$ consisting of three blocks. The Gaussian integrals are computed from the determinants of the block-matrices (9.30) which are simply given by the product of the determinants of each individual block. The blocks $\mathbf{m}_n^{(1,2)}$ are submatrices of the earlier introduced matrix $\mathbf{M}_{2r}^{(\pm)}$ given in Eq. (9.11). Hence, a Laplace expansion of the latter one can be expressed in terms of the minors $\det \mathbf{m}_n^{(1,2)}$. We find

$$\det \mathbf{M}_{2r}^{\pm} = \det \mathbf{m}_{2r-1}^{(1)} - \rho_1^2 \det \mathbf{m}_{2r-2}^{(1)} - \rho_2^2 \det \mathbf{m}_{2r-2}^{(2)} \pm 2(\rho_1\rho_2)^r . \tag{9.32}$$

By exchanging the superscripts of the matrices and indices of ρ_n from 1 to 2 and vice versa, we get the same expansion for $\det \mathbf{m}_n^{(2)}$. We expressed the determinant of $\mathbf{M}_{2r}^{\pm}$ in terms of the Chebychev polynomials of the first kind (9.18), which on the other hand are related to Chebychev polynomials of the second kind $U_n(y)$ by the following recursion relation [185, Eq. 18.9.9]: $2T_n(y) = U_n(y) - U_{n-2}(y)$. With the recursion relation and the Laplace expansion given above, in principle, it is possible to get the determinants of the blocks. Alternatively, the determinants can also be found in Ref. [192], where the characteristic polynomials of the blocks were derived. For odd-sized blocks,

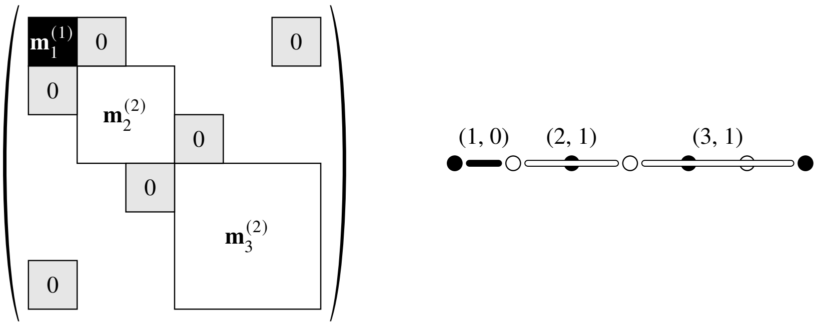

Figure 9.3: Diagrammatic representation. Left: Block matrix $\mathbf{M}_w = \operatorname{diag}\left(\mathbf{m}_1^{(1)}\mathbf{m}_3^{(2)}\mathbf{m}_2^{(1)}\right)$ corresponding to the multiset $w = \{(1,1),(2,2),(3,2)\}$ of the set or partitions $\Pi_{6,2}$ for $r = 3$ round-trips. The block colours illustrate the superscript 1 in black and 2 in white. **Right:** Diagrammatic representation of the block matrix as a chain with $2r + 1 = 7$ alternating between black and white nodes. The colour of the first node depends on the superscript of the first block matrix $\mathbf{m}_1^{(1)}$, which is here chosen to be black. The nodes are equidistantly placed, and the length of lines connecting two nodes represents the dimension of a block matrix. Similar Figure in Ref. [177].

we find

$$\det \mathbf{m}_{2k+1}^{(1,2)} = (\rho_1\rho_2)^k U_k(y) \tag{9.33}$$

and for even-sized matrices

$$\det \mathbf{m}_{2k}^{(1,2)} = (\rho_1\rho_2)^k \left[U_k(y) + \frac{\rho_{2,1}}{\rho_{1,2}} U_{k-1}(y)\right] . \tag{9.34}$$

Note that the determinants of the blocks do not depend on the sign of the off-diagonal matrix elements. After accounting for the multiplicity related to the signs, we thus find for the monopole terms

$$\begin{aligned}\Delta_r &= \frac{1}{r}\frac{(\rho_1\rho_2)^r}{\pi^{2r}}\sum_{k=1}^{2r}(-1)^k \sum_{w\in\Pi_{2r,k}} \left(\int \mathrm{d}^{2r}\mathbf{x}\mathrm{e}^{-\mathbf{x}^t\mathbf{M}_w\mathbf{x}}\right)^2 \\ &= \frac{(\rho_1\rho_2)^r}{r}\sum_{k=1}^{2r}(-1)^k \sum_{w\in\Pi_{2r,k}} \frac{1}{\det \mathbf{M}_w} ,\end{aligned} \tag{9.35}$$

where we applied (A.28) to evaluate the multidimensional Gaussian integral. Note also, that the determinant of the block matrix $\mathbf{M}_w$ is not unique to the given set $w \in \Pi_{2r,k}$. Due to the cyclic character of the determinant, permutations of the block matrices yield the same determinant. In the following, we are identifying all possible partitions $\Pi_{2r,k}$ for a given round-trip number r.

9.3.2 Combinatorial structure of the round-trip partitions

We introduce a diagrammatic representation for the block matrix to analyse all compositions $w \in \Pi_{2r,k}$. For r round-trips, we consider a directed graph of $2r + 1$ equally spaced bi-coloured nodes. The colour of the nodes alternates between black and white, while the first and last nodes are always identical. Each node represents one of the two spheres. Without loss of generality, the black-coloured nodes represent sphere 1, and the white nodes represent sphere 2. The blocks $\mathbf{m}_n^{(1,2)}$ themselves are presented by coloured lines connecting the nodes, where the colour again refers to the node where the line starts. The relation between a block matrix and a graph is illustrated in Fig. 9.3 for the 6-dimensional block matrix $\mathbf{M}_w = \mathrm{diag}(\mathbf{m}_1^{(1)}\mathbf{m}_3^{(2)}\mathbf{m}_2^{(1)})$ consisting of 3 blocks. The corresponding diagram consists of 7 nodes and 3 lines. An edge between two adjacent nodes represents a block of size $n = 1$. Within the scattering picture, it can be seen as half a round-trip, starting at one sphere and ending at the other. An edge of size $n = 2$ is the shortest line connecting two nodes of the same colour. In the scattering picture, it thus illustrates one round-trip. Hence, a single round-trip can be represented in two ways: either by two lines of opposite colours or one edge connecting two nodes of the same colour. As the round-trip number increases, the number of possible partitions also grows. Note, furthermore, that odd-dimensional matrices are always presented by lines connecting two nodes of opposite colours. On the other hand, even-dimensional matrices are presented by lines connecting nodes of the same colour. Whenever there is an edge with an odd length, the following line will change its colour. This directly relates to the condition introduced earlier in Eq. (9.31), where the values of the tuples (n_i, s_i) in the multiset w depend on the values of the preceding tuple (n_{i-1}, s_{i-1}).

The connection between colour and dimension of neighbouring lines can be accounted for via a recursive description, which we present in the following. First, we abbreviate the inverse determinants of the block by

$$d_n^{(s)} = \frac{1}{\det \mathbf{m}_n^{(s)}} \,. \tag{9.36}$$

We consider r round-trips, which corresponds to a chain of length $2r$. The chain can either start with a white node or a black node. We thus introduce two sets of partitions, which we denote as $h_{2r}^{(s)}$ with $s \in \{1, 2\}$. All possible partitions can be expressed by the following recursion relation

$$h_{2r}^{(s)}(t) = t d_{2r}^{(s)} - t \sum_{n=1}^{r-1} d_{2n}^{(s)} h_{2r-2n}^{(s)}(t) - t \sum_{n=1}^{r} d_{2n-1}^{(s)} h_{2r-2n+1}^{(\bar{s})}(t) \tag{9.37}$$

which we depicted explanatory in Fig. 9.4a for graphs starting and ending with a black node. The first term $d_{2r}^{(s)}$ accounts for a single edge of maximal length $2r$ connecting the first and last node of the same colour. The other two terms account for graphs with more than one edge. There are two possibilities to consider: On the one hand, if the first edge has an even length, as given by the second term in Eq. (9.37), the following edge will begin with a node of the same colour as the first one. On the other hand, if the first edge has an odd length, then the second edge will begin with a node of the opposite colour, which is indicated by the bar above s, in the last term of Eq. (9.37).

The auxiliary variable t counts the total number of lines. Each new edge comes with a factor t, hence if we want to determine all partitions consisting of k lines, we take the k-th derivative of Eq. (9.37) with respect to t and set $t = 0$. The relative minus sign between the first term and the other two terms is due to the fact that each new block contributes a minus sign leading to a factor $(-1)^k$ in Eq. (9.35). We similarly derive a recursion relation for graphs which start and end with nodes of different colours, given by

$$h_{2r-1}^{(s)}(t) = t d_{2r-1}^{(s)} - t \sum_{n=1}^{r-2} d_{2n}^{(s)} h_{2r-2n-1}^{(s)}(t) - t \sum_{n=1}^{r-2} d_{2n-1}^{(s)} h_{2r-2n}^{(\bar{s})}(t) \tag{9.38}$$

and illustrated in Fig. 9.4b. The first term represents a graph with one edge of length $2r - 1$, and the

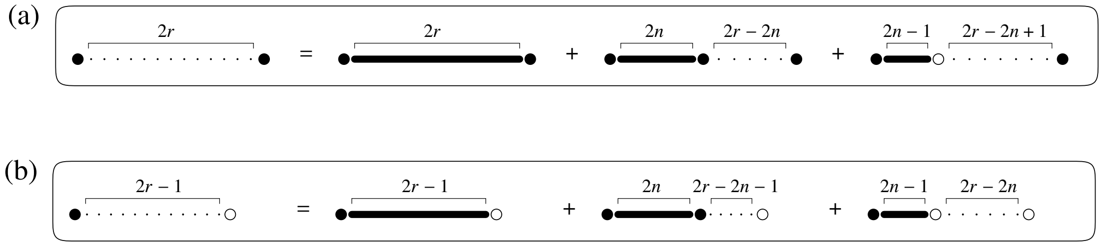

Figure 9.4: Recursion relation. Illustration of the possible partitions between two nodes of the same colour (a) and of opposite colours (b). Figure (a) depicts the recursion relations given in Eq. (9.37) for $s = 1$ and Figure (b) depicts the recursion relations given in Eq. (9.38) for $s = 1$.

two remaining terms account for partitions into at least to edges.

Before we proceed with the evaluation of the monopole terms Δ_r, we want to highlight that the recursion relations given above are reminiscent of the Laplace expansions of appropriately chosen matrices. We found that the recursion relations are related to lower Hessenberg matrices

$$\mathbf{H}_n^{(s)}\left(\left\{d_i^{(s)}\right\}_{i=1,\dots,n};\left\{d_j^{(\bar{s})}\right\}_{j=1,\dots,n-1}\right)=\begin{pmatrix} d_1^{(s)} & 1 & & & & 0 \\ d_2^{(s)} & d_1^{(\bar{s})} & 1 & & & \\ d_3^{(s)} & d_2^{(\bar{s})} & d_1^{(s)} & 1 & & \\ \vdots & \vdots & \vdots & \vdots & & 1 \\ d_n^{(s)} & d_{n-1}^{(\bar{s})} & d_{n-2}^{(s)} & d_{n-3}^{(\bar{s})} & \cdots & d_1^{(\bar{s})} \end{pmatrix} \tag{9.39}$$

by [193]

$$h_n^{(s)}(t=1)=(-1)^{n+1}\det\mathbf{H}_n^{(s)}\,. \tag{9.40}$$

If we disregard the colour of the nodes, thus assuming $d_n^{(1)} = d_n^{(2)} = d_n$, the problem reduces to finding integer partitions. A partition of n elements into k non-empty subsets can be described by the so-called partial ordinary (o) Bell polynomials [194, 195]

$$B_{n,k}^{\mathrm{o}}(d_1,d_2,\dots,d_n)=\sum_{m_i}\frac{k!}{m_1!m_2!\cdots m_n!}d_1^{m_1}d_2^{m_2}\cdots d_n^{m_n}\quad\text{with}\quad\sum_{i=1}^{n}m_i=k,\ \sum_{i=1}^{n}im_i=n\,. \tag{9.41}$$

The ordinary Bell polynomials are commutative. The pre-factor $k!/(m_1!m_2!\cdots m_n!)$ of each monomial considers all possible permutations of the factors in the monomial. Summing over all possible partitions, one obtains the complete ordinary Bell polynomials B_n^{o}, which are directly linked to the determinant of the above-introduced Hessenberg matrix [195]

$$B_n^{\mathrm{o}}(\{d_i\})=\sum_{k=1}^{n}B_{n,k}^{\mathrm{o}}(\{d_i\})=\det\mathbf{H}_n(\{d_i\})\,. \tag{9.42}$$

In our case, however, not all realizations of partitions are possible which is why we have to take care of the multiplicity of each partition separately.

So far, we have considered open-chain diagrams with the starting point chosen at a specific node.

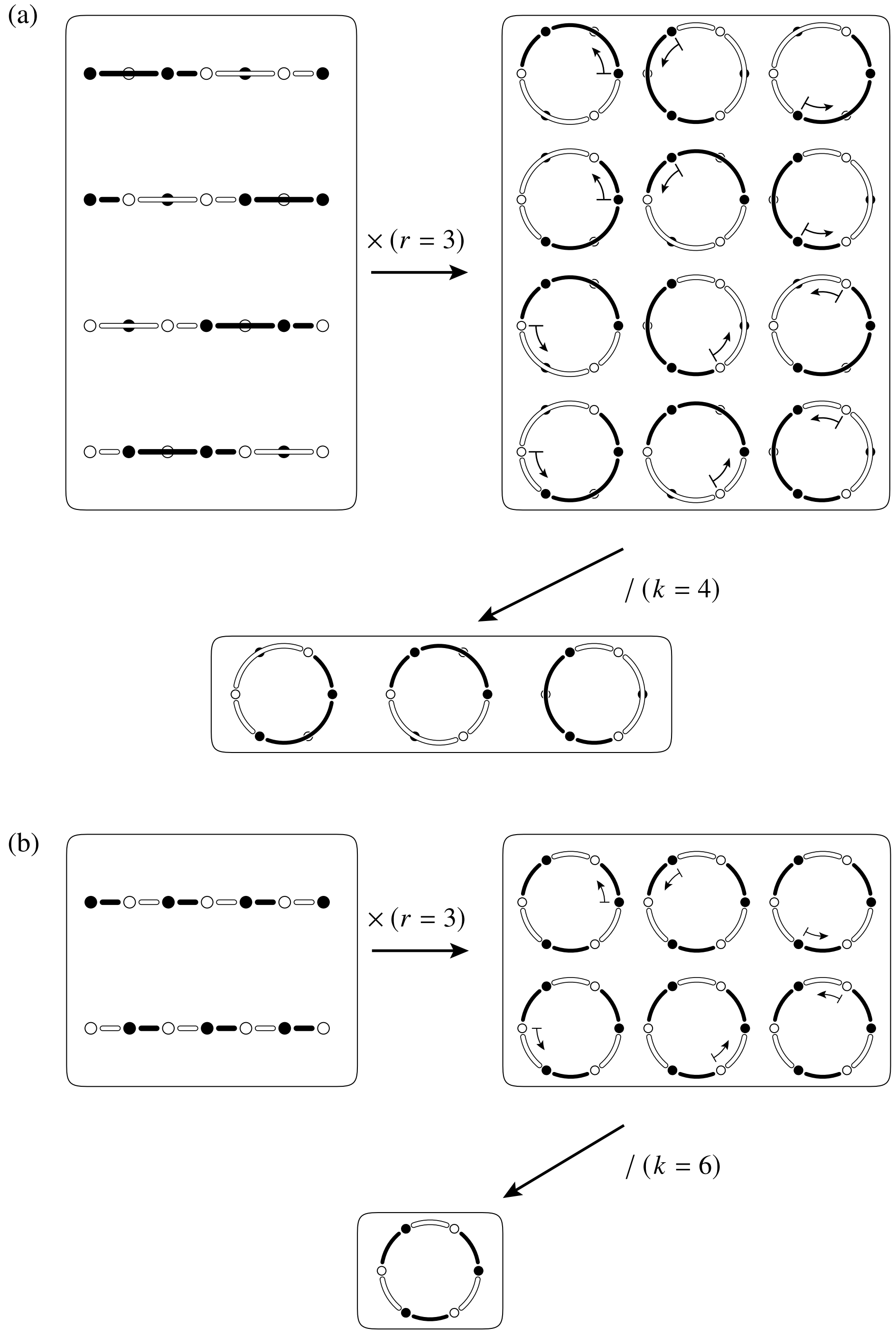

Figure 9.5: Multiplicity of the round-trip partitions. The first panel in Figure (a) illustrates the partition $w = \{(2,1),(1,1),(2,2),(1,1)\}$ of $\Pi_{6,4}$ and all its non-equal permutations from top to bottom. There are four graphs in total. The second panel on the right depicts the partitions in a closed-loop graph. Each partition can start from one of the three nodes in a closed-loop graph, as it is highlighted by the arrows. In total, there are only three distinct closed loop graphs which present the partition of the three round-trips into four blocks. A similar figure can be found in Ref. [177]. Figure (b) illustrates the partition of three round-trips into six blocks which corresponds with the multiset $w = \{(1,1),(1,2),(1,1),(1,2),(1,1),(1,2)\} \in \Pi_{6,6}$. There are only two non-equal partitions as depicted in the first panel. In a closed-loop representation, there is only one unique graph for the partition.

However, the starting point can, in principle, be at every node within the chain, no node is set apart from the others. Hence, rather than an open chain, we consider closed chain diagrams in the following. Every configuration thus has r different nodes as starting points, as it is depicted in Fig. 9.5a and 9.5b for a chain of length $2r = 6$ with 4 and 6 edges, respectively. To account for this multiplicity, we are introducing a factor r to $h_{2r}^{(s)}$. In our recursive description of the possible partitions we, however, already include all non-equal circular permutations of the blocks. Hence, to avoid any double counting, we have to remove the k cyclic permutation of a partition in k blocks, as illustrated with the third panel in Fig. 9.5a and 9.5b. We can extract the partitions in k blocks from $h_{2r}^{(s)}(t)$ by taking the k-th derivative with respect to t as we discussed earlier, which allows us to modify the multiplicity. We thus find for monopole contributions (9.35)

$$\Delta_r = -\frac{(\rho_1\rho_2)^r}{r}\sum_{k=1}^{\infty}\frac{1}{k}\left[\frac{\mathrm{d}^k}{\mathrm{d}t^k}\left(h_{2r}^{(1)}(t)+h_{2r}^{(2)}(t)\right)\right]_{t=0}, \tag{9.43}$$

where the factor r/k adjusts the multiplicity as described above. We further remark that the overall negative sign arises from the fact that according to (9.35), odd numbers of blocks come with a negative sign. The functions $h_{2r}^{(s)}(t)$ are polynomials in t, where the lowest order is linear in t. Hence, we can express the sum over the derivatives also in terms of an integral

$$\Delta_r = -(\rho_1\rho_2)^r\int_0^1 \mathrm{d}t\,\frac{h_{2r}^{(1)}(t)+h_{2r}^{(2)}(t)}{t}\,. \tag{9.44}$$

The full result for the monopole contributions is given after taking the sum over the round-trips, which will be discussed in detail in the next Section.

9.3.3 Casimir free energy for general radii and limiting cases

In this Section, we proceed with the evaluation of the earlier derived monopole terms. The aim is to derive the full result for the Casimir free energy of two Drude spheres in vacuum. We define the contribution from all monopole terms as Δ, which according to Eq. (9.2) is given by the round-trip sum over Δ_r

$$\Delta = f_{\mathrm{DvD}} - f_{\mathrm{sc}} = \sum_{r=1}^{\infty}\frac{\Delta_r}{r}. \tag{9.45}$$

We introduce the following generating function for the partitions $h_{2r}^{(s)}(t)$, which enters the monopole term (9.44)

$$\begin{aligned} H^{(s)}(x;t) &= \sum_{n=1}^{\infty} h_n^{(1,2)}(t)x^n \\ &= \sum_{r=1}^{\infty} h_{2r}^{(s)}(t)x^{2r} + \sum_{r=1}^{\infty} h_{2r-1}^{(1,2)}(t)x^{2r-1} = H_{\mathrm{e}}^{(s)}(x;t) + H_{\mathrm{o}}^{(s)}(x;t)\,, \end{aligned} \tag{9.46}$$

where we separated the sums with even (e) and odd (o) powers in the auxiliary variable x. Hence, the exponent of x counts the number of round-trips. After introducing (9.44) into (9.45), we obtain together with the generating functions, the following expression for the monopole contributions

$$\Delta = -\int_0^1 \mathrm{d}t \frac{H_\mathrm{e}^{(1)}(\sqrt{\rho_1\rho_2};t) + H_\mathrm{e}^{(2)}(\sqrt{\rho_1\rho_2};t)}{t} . \tag{9.47}$$

To proceed with the evaluation of the monopole term, we introduce generating functions for the inverse determinants of individual blocks $d_n^{(s)}$ defined in Eq. (9.36)

$$D^{(s)}(x) = \sum_{n=1}^{\infty} d_n^{(s)} x^n = D_\mathrm{e}^{(s)}(x) + D_\mathrm{o}^{(s)}(x) , \tag{9.48}$$

where we performed the same decomposition in an even and odd part as in Eq. (9.46). The generating functions $H_\mathrm{e}^{(1,2)}$ are determined by summing over the recurrence relations (9.37) and (9.38), respectively for the even and odd partitions, and they yield

$$H_\mathrm{e}^{(s)}(t) = tD_\mathrm{e}^{(s)} - tD_\mathrm{e}^{(s)} H_\mathrm{e}^{(s)}(t) - tD_\mathrm{o}^{(s)} H_\mathrm{o}^{(\bar{s})}(t) , \tag{9.49a}$$

$$H_\mathrm{o}^{(s)}(t) = tD_\mathrm{o}^{(s)} - tD_\mathrm{e}^{(s)} H_\mathrm{o}^{(s)}(t) - tD_\mathrm{o}^{(s)} H_\mathrm{e}^{(\bar{s})}(t) , \tag{9.49b}$$

where we omitted the x-dependence for convenience. We solve the set of equations for the even function $H_\mathrm{e}^{(s)}$ both for $s = 1$ and $s = 2$ and get

$$H_\mathrm{e}^{(1)} + H_\mathrm{e}^{(2)} = t\frac{D_\mathrm{e}^{(1)} + D_\mathrm{e}^{(2)} + tD_\mathrm{e}^{(1)}D_\mathrm{e}^{(2)} - tD_\mathrm{o}^{(1)}D_\mathrm{o}^{(2)}}{\left(1 + tD_\mathrm{e}^{(1)}\right)\left(1 + tD_\mathrm{e}^{(2)}\right) - t^2 D_\mathrm{o}^{(1)}D_\mathrm{o}^{(2)}} . \tag{9.50}$$

Noting that the numerator equals the derivative with respect to t of the denominator, it is straightforward to evaluate the integral in Eq. (9.47), and we find

$$\Delta = -\log\left[\left(1 + D_\mathrm{e}^{(1)}\right)\left(1 + D_\mathrm{e}^{(2)}\right) - D_\mathrm{o}^{(1)}D_\mathrm{o}^{(2)}\right] . \tag{9.51}$$

The sums $D_\mathrm{e}^{(s)}$ and $D_\mathrm{o}^{(s)}$ over the inverse determinants (9.36) yield together with (9.34) and (9.33)

$$D_\mathrm{e}^{(1)}(\sqrt{\rho_1\rho_2}) = \sum_{n=1}^{\infty} \frac{1}{U_n(y) + \alpha_+ U_{n-1}(y)} , \tag{9.52a}$$

$$D_\mathrm{e}^{(2)}(\sqrt{\rho_1\rho_2}) = \sum_{n=1}^{\infty} \frac{1}{U_n(y) + \alpha_- U_{n-1}(y)} , \tag{9.52b}$$

$$D_\mathrm{o}^{(1)}(\sqrt{\rho_1\rho_2}) = D_\mathrm{o}^{(2)}(\sqrt{\rho_1\rho_2}) = \sqrt{\rho_1\rho_2}\sum_{n=0}^{\infty} \frac{1}{U_n(y)} . \tag{9.52c}$$

Recall that the Chebyshev polynomials of the second kind $U_n(y)$ are functions of the conformal distance scale y, which we defined in Eq. (9.16). Additionally, we introduced the parameter $\alpha_\pm$, which accounts for the ratio of the sphere radii

$$\alpha_+ = \frac{1}{\alpha_-} = \frac{R_2}{R_1} = \frac{1 - 2u \pm \sqrt{1 - 4u}}{2u} . \tag{9.53}$$

As a reminder the parameter u, defined in Eq. (8.4), takes values between 0 and $1/4$, respectively accounting for the sphere-plane geometry and two equally-sized spheres.

By expanding the logarithm, we can convince ourselves that all partitions of round-trips are contained in Eq. (9.51). We, therefore, first factorize the argument of the logarithm and then apply the Mercator series

$$\begin{aligned}\Delta &= -\log\left(1+D_\mathrm{e}^{(1)}\right) - \log\left(1+D_\mathrm{e}^{(2)}\right) - \log\left(1+D_\mathrm{o}^{(1)}D_\mathrm{o}^{(2)}\left(1+D_\mathrm{e}^{(1)}\right)^{-1}\left(1+D_\mathrm{e}^{(2)}\right)^{-1}\right)\\ &= -\left\{\sum_{k=1}^{\infty}\frac{(-1)^k}{k}\left[\left(D_\mathrm{e}^{(1)}\right)^k+\left(D_\mathrm{e}^{(2)}\right)^k\right]+\sum_{n=1}^{\infty}\frac{1}{n}\left[\sum_{l=0}^{\infty}\left(-D_\mathrm{e}^{(1)}\right)^l D_\mathrm{o}^{(1)}\sum_{m=0}^{\infty}\left(-D_\mathrm{e}^{(2)}\right)^m D_\mathrm{o}^{(2)}\right]^n\right\}.\end{aligned} \tag{9.54}$$

The first sum accounts for arbitrary repetitions of full round-trips starting either on sphere 1 or on sphere 2 as represented by $D_\mathrm{e}^{(1)}$ or $D_\mathrm{e}^{(2)}$, respectively. Expressions containing both $D_\mathrm{e}^{(1)}$ and $D_\mathrm{e}^{(2)}$ can only arise if half round-trips represented by $D_\mathrm{o}^{(1)}$ and $D_\mathrm{o}^{(2)}$ occur as it is the case in the second term. It can be clearly seen that half a round-trip induces a change between full round-trips starting on sphere 1 and on sphere 2. The number of factors (-1) correctly reflects the number of blocks in the matrices $\mathbf{M}_w$.

Notably, Fosco *et al.* [196], showed that the difference between the Casimir free energy of objects made of Drude metals and the Casimir free energy for a scalar field with Dirichlet boundary conditions is related to the capacitance matrix $\mathbf{C}$ of the arrangement of conductors. For the special case of two conductors, Ref. [196] found

$$\Delta = -\log\left[\det(\mathbf{C})T^2\right]\,. \tag{9.55}$$

Note that we adopt the choice of units of [196], where their quantity ΔF equals $T\Delta/2$. Even though this was not mentioned in Ref. [196], the capacitance matrix elements of two conducting spheres of arbitrary radii were already known to Maxwell [197]. Following the more modern notation in Ref. [198], the capacitance coefficients can be expressed as

$$c_{11} = R_1\left[1+D_\mathrm{e}^{(1)}(\sqrt{\rho_1\rho_2})\right]\,, \tag{9.56a}$$

$$c_{22} = R_2\left[1+D_\mathrm{e}^{(2)}(\sqrt{\rho_1\rho_2})\right]\,, \tag{9.56b}$$

$$c_{12} = c_{21} = -\sqrt{R_1R_2}D_\mathrm{o}^{(1,2)}(\sqrt{\rho_1\rho_2})\,. \tag{9.56c}$$

Comparing these coefficients and (9.55) with our result (9.51) connects the capacitance coefficients to the scattering of electromagnetic waves in the static limit. It thus highlights the connection between our round-trip description and the method of image charges used by Maxwell [197] to obtain the capacitance coefficients. We remark that the general result (9.55) and our result (9.51) differ by a factor $R_1R_2T^2$ in the logarithm. This factor is irrelevant to the Casimir force. However, it affects the Casimir entropy. The term arises from the Casimir self energies of the spheres at an infinite distance [6, 199]. These contributions are excluded in the scattering approach, as discussed in connection with Eq. (2.18), but they are included in Ref. [196]. For our result in Eq. (9.51), the entropy in the high-temperature limit becomes a constant, as expected [6].

Similar to the scalar result, we are going to express the Casimir free energy in terms of the parameter $Z = \exp(-\mu)$ with $\mu = \mathrm{arcosh}(y)$ as introduced in Eq. (9.21). The Chebyshev polynomials of the second kind are given by [185, Eq. 18.5.2] $U_n(y) = (Z^{-(n+1)} - Z^{n+1})/(Z^{-1} - Z)$. The series

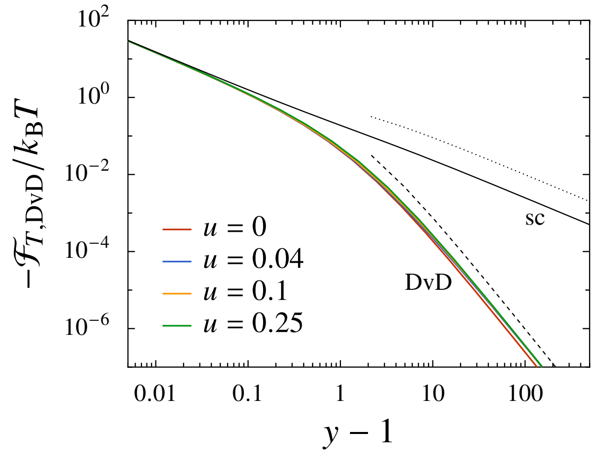

Figure 9.6: Casimir free energy for two Drude spheres in vacuum. Negative free energy in units of $k_\mathrm{B}T$ as a function of the conformal invariant distance scale $y - 1$ for geometry parameters ranging from $u = 0$ for the sphere-plane setup to $u = 0.25$ for two equally-sized spheres. For comparison, also the dimensionless free energy for Dirichlet spheres in a scalar field is shown (solid black line). The dotted and dashed lines represent the scaling at large distances for the scalar result ($\propto 1/y$) and the Drude case ($\propto 1/y^3$), respectively.

presented in Eq. (9.52a)-(9.52c) are thus given by

$$D_\mathrm{e}^{(1,2)} = (1 - g_\pm^2) \sum_{n=1}^{\infty} \frac{Z^n}{1 - g_\pm^2 Z^{2n}}\,, \qquad D_\mathrm{o}^{(1,2)} = \sqrt{(1 - g_+^2)(1 - g_-^2)} \sum_{n=1}^{\infty} \frac{Z^n}{1 - Z^{2n}}\,, \tag{9.57}$$

where we introduced the following function

$$g_\pm = g_\pm(Z) = \left(\frac{Z^2 + \alpha_\pm Z}{1 + \alpha_\pm Z}\right)^{1/2}. \tag{9.58}$$

Note that g_+ and g_- are related by $g_+ g_- = Z$. The parameter $Z = y - \sqrt{y^2 - 1}$ is always smaller or equal to one, hence also $g_\pm < 1$, which allows us to expand the summand in $D_\mathrm{e,\,o}^{(1,2)}$ in a geometrical series and perform a similar resummation as in the scalar case. The high-temperature limit of the Casimir free energy for two Drude spheres in vacuum $\mathcal{F}_{T,\mathrm{DvD}} = -(k_\mathrm{B}T/2) f_\mathrm{DvD}$ with $f_\mathrm{DvD} = f_\mathrm{sc} + \Delta$ thus yields

$$\begin{aligned}\mathcal{F}_{T,\mathrm{DvD}} = \frac{k_\mathrm{B}T}{2} \Bigg\{ &\sum_{l=0}^{\infty} (2l + 1) \log(1 - Z^{2l+1}) \\ &+ \log\Bigg[\left(1 + \frac{1 - g_+^2}{g_+} \sum_{l=0}^{\infty} \frac{(Z g_+)^{2\ell+1}}{1 - Z^{2\ell+1}}\right)\left(1 + \frac{1 - g_-^2}{g_-} \sum_{l=0}^{\infty} \frac{(Z g_-)^{2\ell+1}}{1 - Z^{2\ell+1}}\right) \\ &- \frac{(1 - g_+^2)(1 - g_-^2)}{g_+ g_-} \left(\sum_{l=0}^{\infty} \frac{Z^{2l+1}}{1 - Z^{2l+1}}\right)^2\Bigg]\Bigg\}\,. \end{aligned} \tag{9.59}$$

We remark that the explicit dependence of Δ on u via $\alpha_\pm$ breaks the conformal invariance found for the scalar case.

In Fig. 9.6, we depict the negative free energy as function of $y - 1$ for different geometrical parameters u ranging from $u = 0$ for the sphere-plane geometry to $u = 1/4$ for two equally-sized spheres. The free energy is a monotonically decreasing function of the distance, which for short distances $y - 1 \ll 1$ converges towards the scalar result, depicted as a black line. Furthermore, we note that the u-dependence is very weak. The variation remains in a rather thin band between the two limiting cases $u = 0$ and $1/4$ but increases for larger distances, where the deviation from the scalar result is largest. An asymptotic expansion for large distances $Z \approx 1/(2y)$ reveals the different scaling for the sphere-sphere and sphere-plane geometry, with

$$f_{\mathrm{DvD}}(u \neq 0) \approx \frac{3}{4y^3}\,, \qquad f_{\mathrm{DvD}}(u = 0) \approx \frac{1}{2y^3}\,. \tag{9.60}$$

Recall that the scalar result only decreases with $1/y$ according to Eq. (9.23). The almost conformal invariance was also used in Ref. [25] for evaluating the Casimir free energy for two equally-sized spheres by applying the transformation optics approach.

The Casimir free energy for two spheres of the same radii can easily be obtained from Eq. (9.59) by using $g_+ = g_- = \sqrt{Z} =: Y$, which leads to the following expression for the monopole term

$$\begin{aligned}\Delta^{u=0} &= -\left[\log\left(1 + D_{\mathrm{e}} + D_{\mathrm{o}}\right) + \log\left(1 + D_{\mathrm{e}} - D_{\mathrm{o}}\right)\right] \\ &= -\left[\log\left(1 - \sum_{l=1}^{\infty} \frac{(1-Y^2)(1-Y^{2l})Y^{2l+1}}{1 - Y^{2l+1}}\right) + \log\left(1 + \sum_{l=1}^{\infty} \frac{(1-Y^2)(1-Y^{2l})Y^{2l+1}}{1 + Y^{2l+1}}\right)\right. \\ &\qquad \left. - \log(1 - Y^2)\right]\,.\end{aligned} \tag{9.61}$$

Similar to Z also the parameter Y can be expressed in terms of the aspect ratio $\delta = L/2R$ of the system with $Y = 1 + \delta - \sqrt{\delta(2+\delta)}$. The other limit, where expressions for the classical Casimir free energy are already known, is the sphere-plane geometry. By setting $u = 0$, we get $g_+ = Z$ and $g_- = 1$. The contribution from the sums $D^{(2)}_{\mathrm{e,\,o}}$ given in Eq. (9.52) thus vanishes and what remains of the monopole term yields

$$\Delta^{u=0} = -\log\left(1 + D^{(1)}_{\mathrm{e}}\right) = -\log\left[1 + (1 - Z^2)\sum_{l=0}^{\infty} \frac{Z^{4l+1}}{1 - Z^{2l+1}}\right]\,, \tag{9.62}$$

where the dependence on the aspect ratio $\epsilon = L/R$ is given by $Z = 1 + \epsilon - \sqrt{\epsilon(2+\epsilon)}$. Agreement with the result obtained in Ref. [24] can be found after a resummation, which is carried out in Appendix D.3 for interested readers.

9.3.4 Expansion for short separations

Typical distances-ranges in experiments probing the Casimir interaction between two metallic spheres [19] are about $L \approx 30\,\mathrm{nm} - 4\,\mu\mathrm{m}$ with effective radii of about $R_{\mathrm{eff}} = 13\,\mu\mathrm{m} - 46\,\mu\mathrm{m}$ leading to aspect ratios smaller than $x \lessapprox 10^{-3}$. We already know from the results shown in Fig. 9.6, that the dominant contribution at small distances comes from the scalar expression. Here, we want to analyse the leading corrections by performing a small distance expansion of (9.59). We already determined the short-distance expansion for the scalar term in Sec. 9.2.2. In the following, we are thus deriving the expansion of the monopole term Δ. Similar to the scalar case, we are going to expand (9.59) by using the Lambert series. Therefore, we introduce the following notation for the functions $g_\pm$ (9.58)

$$g_+ = Z^{1/2+\nu(\mu)} \quad \text{with } \nu(\mu) = \frac{1}{2} - \frac{1}{2\mu}\left[\log(1 + \alpha_+ \mathrm{e}^{\mu}) - \log(1 + \alpha_+ \mathrm{e}^{-\mu})\right]\,, \tag{9.63}$$

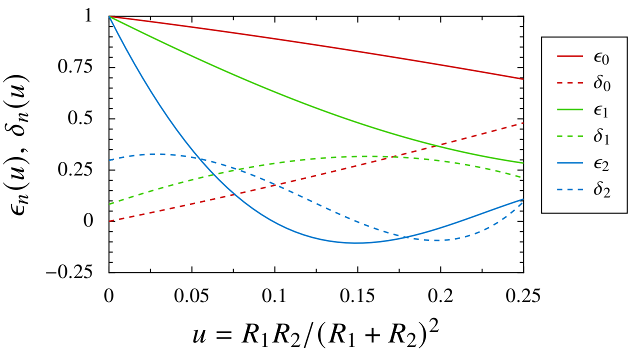

Figure 9.7: Coefficients of the short distance expansion. First three expansion coefficients ϵ_n and δ_n as defined in Eqs. (D.34a)–(D.36b) as function of the geometry parameter u. The explicit results for the limiting cases $u = 0$ and $1/4$ can be found in Tab. 9.2.

where we used the identity $x = \exp(\log(x))$ and $g_- = Z^{1/2-\nu}$. Furthermore, we define

$$J(c) = \frac{1 - Z^{2(c-1)}}{Z^{c-1}} \tag{9.64}$$

to account for the prefactors in Eq. (9.59) with $c = 3/2 \pm \nu$. We abbreviate the sum by using the Lambert series defined in Eq. (9.24)

$$I(c) = \sum_{l=0}^{\infty} \frac{Z^{c(2l+1)}}{1 - Z^{2l+1}} = \mathcal{L}_Z(0,c) - \mathcal{L}_{Z^2}(0,c)\,. \tag{9.65}$$

The monopole term, given by the second half of Eq. (9.59), takes thus the following form

$$\begin{aligned} \Delta = -\log\big\{&[1 + J(3/2-\nu)\, I(3/2-\nu)]\,[1 + J(3/2+\nu)\, I(3/2+\nu)] \\ &- J(3/2-\nu)\, J(3/2+\nu)\, I^2(1)\big\}\,. \end{aligned} \tag{9.66}$$

The expansion of each individual term into a power series of μ is quite technical. For details on the calculation we refer to Appendix D.2, where we found (D.33)

$$\Delta = -\log\left[\sum_{n=0}^{2} \frac{\epsilon_n(u)(\gamma_1 - \log\mu) + \delta_n(u)}{(2n+1)!}\mu^{2n} + O(\mu^6)\right], \tag{9.67}$$

with $\gamma_1 = \gamma + \log 2$ and the Euler-Mascheroni constant $\gamma = 0.577\ldots$. The expansion coefficients $\epsilon_n(u)$ and $\delta_n(u)$ are functions of u, they are defined in Eqs. (D.34a) to (D.36b) and depicted in Fig. 9.7. For the limiting cases $u = 0$ and $1/4$, the explicit values can be found in Tab. 9.2. All coefficients fulfil the relation: $-1 \le \epsilon_n, \delta_n \le 1$. Furthermore, we see that $\epsilon_n \le \epsilon_{n-1}$, which we can use to expand the logarithm in a power series in μ

$$\begin{aligned} \Delta = -\Bigg\{&\log\left[\epsilon_0(\gamma_1 - \log\mu) + \delta_0\right] + \frac{1}{6}\frac{\epsilon_1(\gamma_1 - \log\mu) + \delta_1}{\epsilon_0(\gamma_1 - \log\mu) + \delta_0}\mu^2 \\ &+ \frac{1}{360}\left[\frac{3\left[\epsilon_2(\gamma_1 - \log\mu) + \delta_2\right]}{\epsilon_0(\gamma_1 - \log\mu) + \delta_0} - \frac{5\left[\epsilon_1(\gamma_1 - \log\mu) + \delta_1\right]^2}{\left[\epsilon_0(\gamma_1 - \log\mu) + \delta_0\right]^2}\right]\mu^4 + O(\mu^6)\Bigg\}\,. \end{aligned} \tag{9.68}$$

It is worth noting that the monopole term does not lead to an algebraic divergence, unlike the scalar result (9.26). In the interpretation of a tight-binding model, this is related to the fact that for the monopole contributions, the bilinear form $\mathbf{M}_w$ describes open boundary conditions that cannot give

u	0	1/4
ϵ_0	1	$\log(2)$
δ_0	0	$\log^2(2)$
ϵ_1	1	$\frac{1}{2}\left(\log(2)-\frac{1}{8}\right)$
δ_1	1/12	$\frac{1}{2}\left(\log^2(2)-\frac{1}{12}\log(2)\right)$
ϵ_2	1	$\frac{1}{3}\left(\log(2)-\frac{47}{128}\right)$
δ_2	107/360	$\frac{1}{3}\left(\log^2(2)-\frac{83}{320}\log(2)-\frac{5}{384}\right)$

Table 9.2: Expansion coefficients $\epsilon_n(u)$ and $\delta_n(u)$ defined in Eqs. (D.34a)–(D.36b) in the limit of the sphere-plane geometry $u = 0$ and of equally-sized spheres $u = 1/4$.

rise to zero-eigenvalues.

Emig&Bimonte determined in Ref. [24] a small distance expansion for the sphere-plane geometry of the form

$$\Delta^{u=0} = -\left[\log(\gamma_1 - \log\mu) + \frac{1}{6}\frac{-\gamma_2 + \log\mu}{-\gamma_1 + \log\mu}\mu^2 - \frac{1}{180}\frac{\gamma_3 - \gamma_4\log\mu + \log^2\mu}{(-\gamma_1 + \log\mu)^2}\mu^4 + O(\mu^6)\right], \quad (9.69)$$

where the expansion coefficients γ_i were evaluated numerically. Upon comparing their expression with our result (9.68) for $u = 0$, we are able to find analytical expressions for the expansion coefficients

$$\gamma_1 = \gamma + \log(2), \quad (9.70a)$$

$$\gamma_2 = \gamma_1 + \frac{1}{12}, \quad (9.70b)$$

$$\gamma_3 = \frac{1}{2}\left(5\gamma_2^2 - 3\gamma_1^2 - \frac{107}{120}\gamma_1\right), \quad (9.70c)$$

$$\gamma_4 = 5\gamma_2 - 3\gamma_1 - \frac{107}{240}. \quad (9.70d)$$

9.4 Dielectric spheres in an electrolytic solution

In this Section, we consider the other setup, where the high-temperature limit leads to a universal expression for the dimensionless Casimir free energy, namely dielectric objects in an electrolytic solution. In this setup, the dielectric function of the medium diverges due to a finite dc-conductivity of the medium. Hence, the Casimir interaction no longer depends on the explicit material properties in the high-temperature limit for a sphere with finite static dielectric function. The dimensionless Casimir free energy becomes a universal function of the geometrical parameters.

In Sec. 9.4.1, we will first introduce the explicit expression for the round-trip contribution to the Casimir free energy, which we then evaluate in the single-round-trip approximation. In Sec. 9.4.2, we discuss the duality between the previous setup of Drude spheres in vacuum and the dielectric spheres in an electrolyte. Furthermore, we provide a semi-analytical approximation, allowing for a simple calculation of the Casimir free energy for all distances. The distance range, where the high-temperature result is valid, is much larger for dielectrics in an electrolyte compared to Drude spheres in a vacuum. This has consequences for experiments and potential relevance for biophysical and colloidal systems, which we will discuss in Sec. 9.4.3.

9.4.1 Explicit expression and round-trip approximation

We introduced the reflection matrix element for a dielectric sphere in an electrolyte in Eq. (9.7). However, the given expression is impractical for analytical calculations due to the $\chi_{i,j}$-term in the denominators. We can circumvent the problem by rewriting the expansion coefficients $\mathcal{X}_{\mathrm{TM,TM}}(l) = -l/(l+1)$ of the scattering amplitude. We introduce the following integral representation: $\mathcal{X}_{\mathrm{TM,TM}}(l) = -\int_0^1 \mathrm{d}t(1-2t^{2l+1})$. After inserting the coefficients $\mathcal{X}_{\mathrm{TM,TM}}$ into Eq. (9.4) for the matrix elements of the reflection operator and performing the sum over angular momenta, we arrive at

$$\langle \mathbf{k}_i, \mathrm{TM}|\mathcal{R}_{\mathrm{de}}|\mathbf{k}_j, \mathrm{TM}\rangle = -\frac{2\pi R}{k_i}\int_0^1 \mathrm{d}t \left[\cosh(\chi_{i,j}) - 2t\cosh(t\chi_{i,j})\right] \tag{9.71}$$

with $\chi_{i,j}$ defined in Eq. (9.5). We insert the reflection matrix elements given above into the trace expression (9.3) and perform the same variable transformation to Cartesian coordinates as in Sec. 9.2. Furthermore, we exchange the order of the t-integral with the integrals associated with the transverse wave vectors. We thus find for the r-th round-trip contribution of the free energy for a dielectric-electrolyte-dielectric (ded) setup

$$\begin{aligned} f^{(r)}_{\mathrm{ded}} = \frac{1}{r}\frac{(\rho_1\rho_2)^r}{\pi^{2r}} \int_0^1 \mathrm{d}^{2r}\mathbf{t} \int \mathrm{d}^{2r}\mathbf{x} \int \mathrm{d}^{2r}\mathbf{y} \prod_{j=1}^{r} \mathrm{e}^{-\left(x_{2j}^2+y_{2j}^2\right)}\mathrm{e}^{-\left(x_{2j-1}^2+y_{2j-1}^2\right)} \\ \times \left[\cosh(\chi^{(2)}_{2j}) - 2t_{2j}\cosh(t_{2j}\chi^{(2)}_{2j})\right]\left[\cosh(\chi^{(1)}_{2j-1}) - 2t_{2j-1}\cosh(t_{2j-1}\chi^{(1)}_{2j-1})\right] , \end{aligned} \tag{9.72}$$

where $\mathbf{t}^t = (t_1, t_2, \dots, t_{2r})$ with cyclic indices $2r+1 \equiv 1$. The argument $\chi_j^{(1/2)}$ of the hyperbolic cosines is defined in Eq. (9.10). The $2r$-dimensional integrals over $\mathbf{x}$ and $\mathbf{y}$ are again of Gaussian-type with the bilinear form given by a symmetric and cyclic Toepliz matrix

$$\mathbf{M}^{\pm}_{2r}(\mathbf{t}) = \begin{pmatrix} 1 & \pm t_1\rho_1 & 0 & \dots & 0 & \pm t_{2r}\rho_2 \\ \pm t_1\rho_1 & 1 & \pm t_2\rho_2 & & & 0 \\ 0 & \pm t_2\rho_2 & 1 & \ddots & & \vdots \\ \vdots & & \ddots & \ddots & & 0 \\ 0 & & & & & \pm t_{2r-1}\rho_1 \\ \pm t_{2r}\rho_2 & 0 & \dots & 0 & \pm t_{2r-1}\rho_1 & 1 \end{pmatrix} . \tag{9.73}$$

The off-diagonal elements depend on the auxiliary variable t_i. Similar to the previous cases, the matrix can be associated with a tight-binding model. For the scalar case, the hopping matrix elements between adjacent sites varied periodically between two values, but here, the hopping matrix elements are generically non-periodic. By applying the transfer-matrix approach introduced for the scalar case in Sec. 9.2, specifically in Eqs. (9.12)-(9.13), we find for the determinant of the matrix $\mathbf{M}^{(\pm)}_{2r}(\mathbf{t})$

$$\det \mathbf{M}^{\pm}_{2r}(\mathbf{t}) = \mathrm{tr}\left[\begin{pmatrix} 1 & -(t_1\rho_1)^2 \\ 1 & 0 \end{pmatrix} \cdots \begin{pmatrix} 1 & -(t_{2r}\rho_2)^2 \\ 1 & 0 \end{pmatrix}\right] \pm 2(\rho_1\rho_2)^r \prod_{i=1}^{2r} t_i . \tag{9.74}$$

Note that while all sign combinations are possible in the matrix (9.73), the determinant depends only on the total number of off-diagonal entries with a negative sign. We observed this dependence already in our discussion of the Casimir interaction for a scalar field.

To proceed with the evaluation of the round-trip contribution (9.72), we rewrite the first hyperbolic cosine in the brackets with the help of the δ-function as $\cosh(z) = 2\int_0^1 \mathrm{d}t\,t\cosh(tz)\delta(t-1)$. Furthermore, we applied the convention that the integral yields a factor $1/2$ if the δ-function is located on the boundary of the integration interval. Formally, the integration over $\mathbf{x}$ and $\mathbf{y}$ can be carried out with the result for multi-dimensional Gaussian integral presented in Eq. (A.28)

$$f^{(r)}_{\mathrm{ded}} = \frac{(4\rho_1\rho_2)^r}{2r}\sum_{\sigma=\pm1}\int_0^1 \mathrm{d}^{2r}\mathbf{t}\,\frac{\prod_{i=1}^{2r} t_i\,[\delta(t_i-1)-1]}{\det\mathbf{M}^{\sigma}_r(\mathbf{t})}\,. \tag{9.75}$$

Recall that the terms without a t_i-dependence contribute to the scalar result, which is included in the round-trip term for dielectric spheres in an electrolyte, as we established at the beginning of this Chapter. Similar to the previously discussed DvD-model, the round-trip term will be of the form $f^{(r)}_{\mathrm{ded}} = f^{(r)}_{\mathrm{sc}} + \ldots$. Due to the non-periodic nature of the matrix $\mathbf{M}^{\pm}_{2r}(\mathbf{t})$, it is, however, challenging to find a closed analytical expression for the determinant and additionally evaluate the t_i-integrals.

It is feasible to perform the integrals in the single-round-trip approximation, where the value of r is equal to 1. For $r = 1$, the determinant of the bilinear form yields

$$\det\mathbf{M}^{\pm}_2(\mathbf{t}) = \det\begin{pmatrix} 1 & t_1\rho_1 \pm t_2\rho_2 \\ t_1\rho_1 \pm t_2\rho_2 & 1 \end{pmatrix} = 1 - (t_1\rho_1 \pm t_2\rho_2)^2\,. \tag{9.76}$$

After substituting the result for the determinant into Eq. (9.75) and performing the product in the integrand, we obtain

$$f^{(1)}_{\mathrm{ded}} = f^{(1)}_{\mathrm{sc}} + 2\sum_{\sigma=\pm1}\int_0^1 \mathrm{d}^2\mathbf{t}\,\frac{t_1t_2}{z-(t_1\sqrt{\alpha_-}+\sigma t_2\sqrt{\alpha_+})^2}\,[1-\delta(t_1-1)-\delta(t_2-1)]\,, \tag{9.77}$$

where we separated the scalar contribution $f^{(1)}_{\mathrm{sc}}$ and used the same geometrical parameters $\alpha_\pm$ as for the DvD-model, which are defined in Eq. (9.53). Furthermore, we introduced the parameter z, which is given by

$$z = \frac{1}{\rho_1\rho_2} = 2y + \alpha_+ + \alpha_-\,. \tag{9.78}$$

We decompose the fraction in the integrand of Eq. (9.77), into two partial fractions and carry out the t_1, t_2 integrals. After some algebraic transformations, we find the single-round-trip term of the Casimir free energy for two dielectric spheres in an electrolyte

$$f^{(1)}_{\mathrm{ded}}(y,u) = f^{(1)}_{\mathrm{sc}}(y) + \frac{z}{6}\log\left[\frac{z^2(y^2-1)}{(yz+1/2)^2}\right] + \frac{1}{6\sqrt{z}}\sum_{\sigma=\pm}\frac{1}{\alpha_\sigma^{3/2}}\log\left[\frac{2y^2+\alpha_\sigma y-1+\sqrt{\alpha_\sigma z}}{2y^2+\alpha_\sigma y-1-\sqrt{\alpha_\sigma z}}\right]\,. \tag{9.79}$$

The single-round-trip expression for a scalar field is given by

$$f^{(1)}_{\mathrm{sc}}(y) = \frac{y}{2(y^2-1)} \tag{9.80}$$

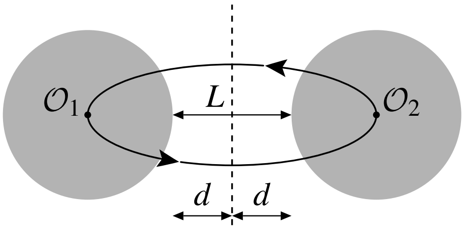

Figure 9.8: A single round-trip between two equally-sized spheres with a distance L can be interpreted as two round-trips performed between a sphere and a plane in a distance $d = L/2$.

which can either be extracted from Eq. (9.20) or by setting $t_1 = 1 = t_2$ in the expression for the determinant in Eq. (9.76). Note that the dependence on u via $\alpha_\pm$, breaks the conformal invariance similar to what we also observed for the DvD-model.

In the remainder of this Section, we analyse the geometrical limiting cases of the single-round-trip expression and the validity of the round-trip approximation. For two equally-sized spheres ($u = 1/4$), the single-round-trip result simplifies with $\alpha_+ = \alpha_- = 1$ to

$$\begin{aligned} f^{(1)}_{\text{ded}}(y, u = 1/4) = f^{(1)}_{\text{sc}}(y) + \frac{y+1}{3} \log\left[\frac{(y^2-1)(y+1)^2}{(y+1/2)^4}\right] \\ + \frac{1}{3\sqrt{2(y+1)}} \log\left[\frac{2y - 1 + \sqrt{2/(y+1)}}{2y - 1 - \sqrt{2/(y+1)}}\right] . \end{aligned} \tag{9.81}$$

In the plane-sphere geometry ($u = 0$), on the other hand, α_+ goes to infinity thus leading to a non-vanishing contribution of the $\sigma = +$ term in Eq. (9.79). By summarizing the remaining terms, we find

$$f^{(1)}_{\text{ded}}(y, u = 0) = f^{(1)}_{\text{sc}}(y) + \frac{y}{2} \log\left(\frac{y^2-1}{y^2}\right) . \tag{9.82}$$

The setup with two spheres of equal radius R is symmetric with respect to a plane perpendicular to the z-axis, as shown in Fig. 9.8. The distance L between the two sphere surfaces can be interpreted as twice the distance d between a sphere and a plane. We can thus transform the single-round-trip expression for two equally-sized spheres into the double-round-trip result for the sphere-plane geometry. Wirzba already recognized this connection in Ref. [200] for the Casimir interaction in a scalar field with Dirichlet and Neumann boundary conditions on the spheres. We found that by a simple replacement of y in Eq. (9.81) with $2y^2 - 1$, we obtain the double-round-trip expression for the sphere-plane setup

$$f^{(2)}_{\text{ded}}(y, u = 0) = \frac{1}{16} \frac{2y^2 - 1}{y^2(y^2-1)} + \frac{y^2}{3} \log\left(\frac{y^6(y^2-1)}{(y^2-1/4)^4}\right) + \frac{1}{12y} \log\left(\frac{4y^3 - 3y + 1}{4y^3 - 3y - 1}\right) , \tag{9.83}$$

where $y = 1 + d/R$ for the sphere-plane geometry.

Our discussion of the Casimir interaction between Dirichlet spheres showed that small round-trip numbers are sufficient to describe the Casimir free energy for two spheres far apart (see Fig. 9.2a). Upon expanding the hyperbolic cosines for small arguments ($\chi^{(n)} \propto R_n/\mathcal{L}$) in Eq. (9.72), we see that the round-trip contribution scales with $f^{(r)} \propto (R_1 R_2/\mathcal{L})^{3r}$. The single-round-trip term is thus the dominant term for large distances. Based on these findings, we propose the following round-trip

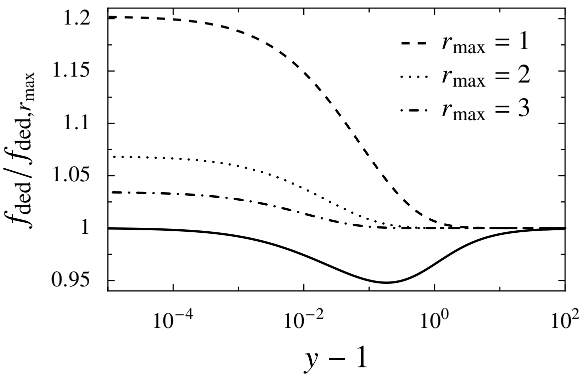

Figure 9.9: Round-trip approximation for the sphere-plane geometry. Ratio between the exact Casimir free energy $f_{\rm ded}$ and the round-trip approximation $f_{{\rm ded},r_{\max}}$ as defined in Eq. (9.84). For increasing numbers of round-trips $r_{\max}$, the accuracy of the approximation increases over the whole domain of distances between the sphere and the plane. Additionally, the exact result is compared to an approximation, shown as a solid line, which includes the result for a scalar field and the round-trip terms up to $r = 3$ as defined in Eq. (9.85).

approximation for the dimensionless Casimir free energy

$$f_{{\rm ded},r_{\max}} = \sum_{r=1}^{r_{\max}} f_{\rm ded}^{(r)}\,, \tag{9.84}$$

where $r_{\max} \to \infty$ corresponds to the exact result (9.2). Fig. 9.9 presents a comparison of the round-trip approximation for $r_{\max} = 1$ (dashed line) and $r_{\max} = 2$ (dotted line) with the exact result for the sphere-plane geometry. The ratio goes to one for large distances, which shows that low round-trip numbers are sufficient for large distances. Furthermore, we find that the error at short distances can be reduced by more than a factor of two if the double round-trip is included in the approximation compared to only taking the single-round-trip term (9.82) into account.

In order to obtain an even better description for small separations, one could think of replacing the round-trip expansion of the scalar field contribution by its exact expression as given in Eq. (9.20). However, the scalar contribution up to three round-trips contains contributions of order of $(R_1R_2/\mathcal{L})^3$ even though the single round-trip $f_{\rm ded}^{(1)}$ yields already the correct large-distance limit. In other words, the terms $f_{\rm ded}^{(r)}$ needs to be taken into account for up to three round-trips so that no contribution with $(R_1R_2/\mathcal{L})^3$ for large $\mathcal{L}$ appears. Only then can one expect to reproduce the small- and large-distance limit for the ded-model correctly. We thus end up with the following approximation for the dimensionless free energy

$$f_{\rm ded}^{\rm approx} \approx f_{\rm sc} + \sum_{r=1}^{3}\left(f_{\rm ded}^{(r)} - f_{\rm sc}^{(r)}\right)\,. \tag{9.85}$$

Note that we have to remove the scalar parts $f_{\rm sc}^{(r)}$ from the round-trip expression $f_{\rm ded}^{(r)}$, since they are already included in $f_{\rm sc} = \sum_{r=1}^{\infty} f_{\rm sc}^{(r)}$. The approximation formula given above is based on the fact that analytical results for three round-trips are available. We already introduced the single- and double-round-trip expressions for the sphere-plane geometry, respectively, in Eq. (9.82) and (9.83). We were also able to find a result for three round-trips. The calculation is quite technical, we thus refer readers interested in details to Appendix E. The final result for $f_{\rm ded}^{(3)} = {\rm tr}\mathcal{M}_{\rm ded}^3/r$ can be found in Eq. (E.18). We used this result to plot the round-trip approximation for $r_{\max} = 3$, presented in Fig. 9.9 by the dash-dotted line and also to compute the approximation introduced in Eq. (9.85), which is depicted by the solid line in Fig. 9.9. As expected, the short- and large-distance behaviour is correctly captured by our introduced approximation formula. It only deviates for intermediate distances $y - 1 \approx 0.1$.

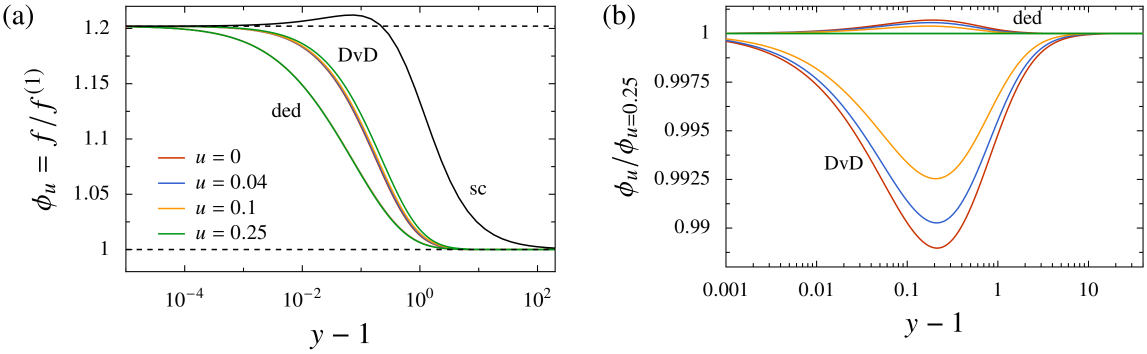

Figure 9.10: Approximation of the full Casimir free energy. (a) Ratio ϕ of the full free energy f with respect to the single-round-trip result $f^{(1)}$ as function of the distance $y-1$. The ratio is depicted for various geometry parameters u. The ratio goes to one for large distances $y-1 \gg 1$ and approaches the Apéry constant $\zeta(3)$ for small distances $y-1 \ll 1$. The ratio ϕ_u only weakly dependence on u for intermediate distance $y-1 \approx 0.1$ as can be seen in Figure (b), where we compared the ratio ϕ_u with $\phi_{u=0.25}$. Both adapted from [178].

In summary, we obtained the single-round-trip approximation of the Casimir free energy between two dielectric spheres in an electrolyte. We found that the approximation correctly captures the behaviour of the Casimir free energy at large distances. For the sphere-plane geometry, we improved the model by introducing higher round-trip numbers. However, a formula for any sphere size and distance range would be of interest for practical applications. The following Section will introduce an approximation that fulfils these conditions.

9.4.2 Duality between the ded- and DvD-model and approximate conformal invariance

As discussed in the context of Fig. 9.9, the single-round-trip result yields the correct result for large distances. We are thus comparing the total free energy with the respective single-round-trip expressions by defining

$$\phi_u(y) = \frac{f(y,u)}{f^{(1)}(y,u)} \,. \tag{9.86}$$

The results are shown in Fig. 9.10a, where we also included the ratio for the Drude-vacuum-Drude (DvD) setup. The single round-trip result can be calculated from Eq. (9.27) for $r = 1$ and yields

$$f^{(1)}_{\mathrm{DvD}}(y,u) = f^{(1)}_{\mathrm{sc}}(y) + \frac{1}{z} - \sum_{\sigma=\pm} \frac{1}{2y+\alpha_\sigma} \,. \tag{9.87}$$

The ratios were in both cases computed for $u = 0, 0.04, 0.1$ and 0.25 to capture the variation from the sphere-plane geometry to two equally-sized spheres. We found that for both models and for all depicted values of u, the ratio goes to one in the limit of large distances $y \gg 1$, meaning that the single-round-trip expression dominates the full result. In contrast, for short distances $y \to 1$, the ded-model and DvD-model approach the same constant, which is determined by the divergent part of the scalar result, which for comparison is also depicted in Fig. 9.10a. Remarkably, already the single-round-trip results reproduce this divergence for small separations with $f^{(1)}_{\mathrm{sc}} = 1/(4(y-1)) + O(1)$,

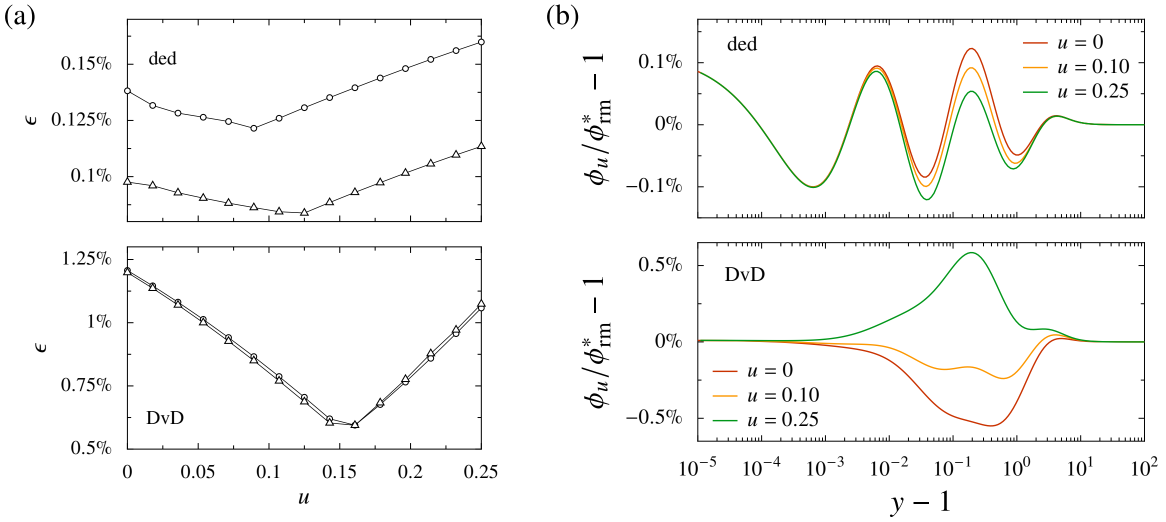

Figure 9.11: Error of the rational model. (a) Maximal relative error of the rational model defined in Eq. (9.89) for $n = 2$ and $n = 4$, as a function of u. For each u, the maximal error of the rational model over the whole parameter space (y, u) was computed for both the ded-model (top figure) and the DvD-model (bottom figure). The maximal error is minimized for a $u^*_{\mathrm{ded}} \approx 0.1$ and $u^*_{\mathrm{DvD}} \approx 0.15$. (b) Relative deviation between the ratio ϕ_u as given in Eq. (9.86) and the rational model calculated for u^*: $\phi^*_{\mathrm{rm}} = \phi_{\mathrm{rm}}(u^*)$. The ratios were computed for $u = 0, 0.1$ and 0.25.

thus leading to

$$f \approx \sum_{r=1}^{\infty} \frac{f^{(1)}}{r^3} \approx \frac{\zeta(3)}{4(y-1)} \quad \text{for} \quad y \to 1\,, \tag{9.88}$$

which we also obtained in Sec. 9.2.2. The constant approached by ϕ_u is given by the Apéry's constant $\zeta(3) = \sum_{r=1}^{\infty} 1/r^3 = 1.202\ldots$. Both for the Drude spheres in vacuum and for the dielectrics, the ratio decreases monotonically from $\zeta(3)$ to one as the distance increases. Remarkably, for both cases the ratios ϕ_u very weakly depend on the geometry parameter u. This is a result of the definition of the parameter $y = 1 + x + ux^2/2$, which already captures parts of the u-dependence. The u-dependence is particularly weak for the ded-model as we found by analysing the ratio between ϕ_u and $\phi_{u=1/4}$ in Fig. 9.10b. Curves with ratios below 1 correspond to the DvD-model, while those with ratios above 1 correspond to the ded-model. The green curve stays at a ratio of 1 as it represents the u-independent case. Again, the small deviations of $\phi_u/\phi_{u=1/4}$ from 1 show a weak breaking of conformal invariance.

The ϕ_u-curves for the ded- and DvD-model are monotonic, thus allowing for an approximation with a rational model (rm) of the form [179]

$$\phi_{\mathrm{rm}}(y) = \prod_{k=1}^{n} \frac{\mathrm{e}^{y-1} + \mu_k - 1}{\mathrm{e}^{y-1} + \nu_k - 1}\,. \tag{9.89}$$

In this model, the exponential term e^{y-1} becomes dominant for large distances, and as a result, $\phi_{\mathrm{rm}}(y \to \infty)$ approaches one. On the other hand, for short distances, the ratio is determined by the model parameters μ_k and ν_k with $\phi_{\mathrm{rm}}(y \to 1) \to \prod_k \mu_k/\nu_k$. To obtain the model parameters, we

		ded-model				DvD-model			
	k	1	2	3	4	1	2	3	4
$n = 2$	ν_k	0.004618	0.09639			0.011495	0.19868		
	μ_k	0.004415	0.08397			0.011359	0.16728		
$n = 4$	ν_k	0.000889	0.02990	0.02991	0.08200	0.031645	0.08542	0.08542	0.16187
	μ_k	0.000878	0.02132	0.05374	0.05394	0.029993	0.10121	0.10122	0.10122

Table 9.3: Fitting parameters of the rational model. Expansion coefficients ν_k, μ_k of the rational model (9.89) for $n = 2$, with a maximal deviation of $\epsilon_{\text{ded}} = 1.2 \times 10^{-3}$ and $\epsilon_{\text{DvD}} = 5.9 \times 10^{-3}$, respectively for the ded-model and the DvD-model and for $n = 4$ with a maximal deviation of $\epsilon_{\text{ded}} = 0.9 \times 10^{-3}$ and $\epsilon_{\text{DvD}} = 5.7 \times 10^{-3}$.

need to minimize the relative deviation of ϕ_{rm} from ϕ_u for a fixed value of u according to

$$\epsilon = \min_{\mu_k,\nu_k} \left\{ \left| \frac{\phi_u(y)}{\phi_{\text{rm}}(y)} - 1 \right| \right\} . \tag{9.90}$$

Due to the weak u-dependence, it is possible to fit the numerical data for a specific u^*, such that the relative deviation for all the other u values is minimized. We thus determined the rational model in Fig. 9.11a for each u and computed the maximal deviation over the whole parameter space (y, u). For a rational model with $n = 2$ (presented by the circle symbols in Fig. 9.11a), we found that the optimal fitting parameters are obtained for $u^* \approx 0.1$ and $u^* \approx 0.15$, respectively for the ded-model and the DvD-model. The corresponding fitting coefficients μ_k, ν_k are given in Tab. 9.3. Remarkably, the maximal deviation obtained with the rational model is as low as 0.12 % (ded) and 0.59 % (DvD) over the whole parameter space. Fig. 9.11b depicts the deviation of ϕ_u from the rational model ϕ^*_{rm} which is calculated for u^*. The deviations were computed as functions of the distance scale $y - 1$ for $u = 0$, 0.1 and 0.25 and show that the largest discrepancy arises at intermediate distances for the two limiting cases $u = 0$ and 0.25. We repeated the procedure for a rational model with four fitting parameters ($n = 4$). The maximal deviations as functions of u are depicted as triangle symbols in Fig. 9.11a and the fitting parameters, for which the deviation is minimized, are also given in Tab. 9.3. We found that the fit is slightly improved.

In conclusion, combining the single-round-trip result (9.79) or (9.87) for the ded- or DvD-model together with the respective rational model ϕ^*_{rm} in the following form

$$f(y, u) = f^{(1)}(y, u)\phi^*_{\text{rm}}(y) , \tag{9.91}$$

provides an extremely good approximation of the universal Casimir free energy between two arbitrary-sized spheres. The formula allows for an easy calculation of the Casimir free energy over the whole distance range without the need to perform extensive numerical calculations.

In the next Section, we will discuss the relevance of our results in practical applications.

9.4.3 Relevance for colloidal and biophysical systems

Colloidal and biological systems involve dielectric objects immersed in an electrolytic solution like salted water. Up to recently, it was assumed that long-range interactions are completely screened in these scenarios. It was theoretically shown in Ref. [27] and experimentally verified in Ref. [4] that

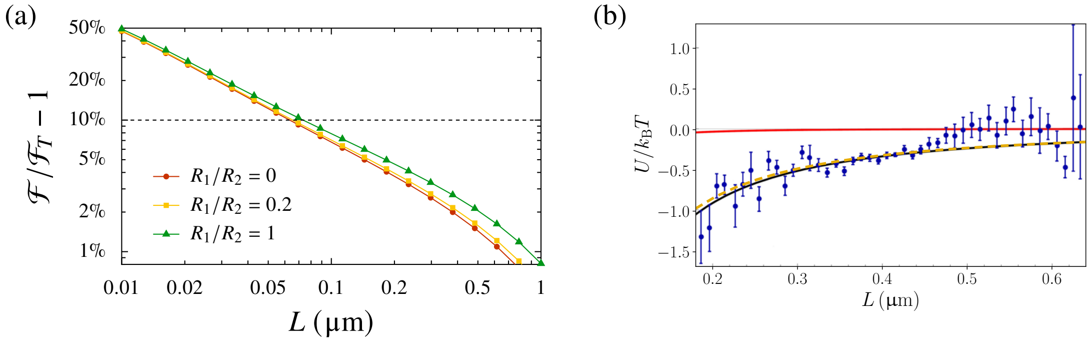

Figure 9.12: Comparison with experimental results. (a) Ratio $\mathcal{F}/\mathcal{F}_T - 1$ with the full free energy $\mathcal{F}$ given in Eq. (2.25) and the high-temperature result $\mathcal{F}_T$ (9.2) as function of the surface-to-surface distance L. The free energies were calculated for a setup of two silica spheres in water at $T = 296\,\mathrm{K}$ as discussed in Ref. [4] with radius $R_1 = 2.35\,\mu\mathrm{m}$ and $u = 0.14$ (bright yellow). The ratio was also calculated for $u = 0$ (red) and $u = 0.25$ (green) with the same value for R_1. The dashed line indicates the threshold, where the relative deviation between the full free energy and the high-temperature result is only 10%. The figure is taken from [178]. (b) Interaction free energy U between two silica spheres of radii $R_1 = 2.35\,\mu\mathrm{m}$ and $R_2 = 11.74\,\mu\mathrm{m}$ as function of the distance L. The figure was taken from [4]. Shown are the experimental points and the theoretical values of the Casimir free energy ($U \equiv \mathcal{F}$). The zero-frequency term is excluded in the red curve, while the black curve takes thermal contributions into account. The dashed yellow curve was added to the figure and depicts the result obtained from the approximation (9.91) for dielectric spheres in an electrolyte.

the behaviour at long distances (above the Debye screening length) is dominated by non-screened interaction due to the low-frequency transverse magnetic thermal fluctuations.

We compared in Fig. 9.12a the full Casimir free energy for two dielectric spheres in salted water with the high-temperature contribution to the Casimir interaction. The curves show that the zero-frequency mode provides the dominant contribution at distances as small as 0.1 µm. The distance is thus way smaller than the one for metallic spheres in vacuum, where the zero-frequency modes only become the dominant part for distances of the order of the thermal wavelength $\lambda_T = \hbar c/k_B T$, which at room temperature corresponds to distances of about 8 µm [106]. This makes the universal expression (9.91), we derived earlier for dielectric objects applicable for a much larger distance range then it is the case for Drude spheres. In addition, the high-temperature contribution to the Casimir free energy thus becomes accessible in experiments. A recent experiment [4] probed the Casimir interaction for two silica spheres of radii 2.35 µm and 11.74 µm in salted water. They probed the Casimir force by trapping the smaller sphere in optical tweezers, which, as we already mentioned in Part II of this thesis, allows for an extremely sensitive force measurement. Agreement between experiment and theory could only be found by including the zero-frequency modes, as shown by the black curve in Fig. 9.12b. If the zero-frequency contributions are disregarded, as shown by the red curve in Fig. 9.12b, agreement with the experimental results becomes worse. We also added the result obtained from our approximation formula (9.91) for the specific setup. The dashed yellow line in Fig. 9.12b was obtained with the above-given values for the radii and the fitting parameters given in Tab. 9.3. This shows that our simple approximation formula correctly captures the full numerical result at distances $L \gtrapprox 0.1\,\mu\mathrm{m}$. Additionally, the comparison with the experiment shows that the accuracy of the approximation formula is sufficient for practical proposes.

The Casimir interaction has relevance for biophysical and colloidal science, if it is of the order of $k_B T$, since the immersion in water imposes a Brownian motion to the spheres. We computed the

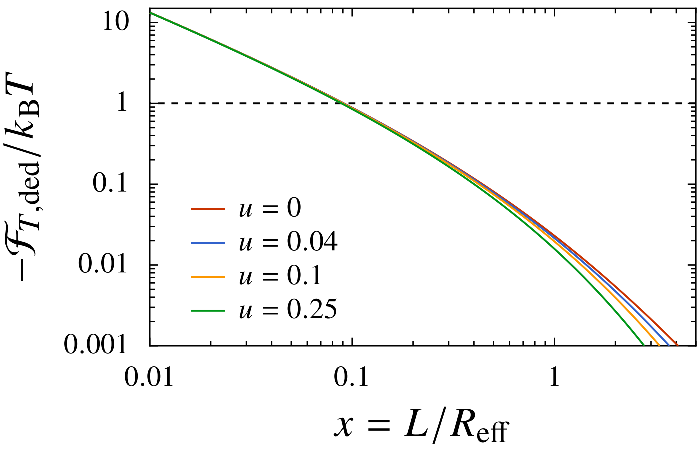

Figure 9.13: Universal Casimir free energy for two dielectric spheres in an electrolyte. Negative Casimir free energy for the ded-model in units of $k_\mathrm{B}T$ as function of the aspect ratio $x = L/R_\mathrm{eff}$. The Casimir energy was calculated for the same values of u as in Fig 9.10a. The dashed line corresponds to a free energy of order $k_\mathrm{B}T$. Adapted from Ref. [179].

universal Casimir free energy for the ded-model as a function of the aspect ratio $x = L/R_\mathrm{eff}$ and found that for distances L of the order of or smaller than one-tenth of the effective radius R_eff, the Casimir interaction is of the order of $k_\mathrm{B}T$, which makes it thus relevant for such scenarios.

Recently the study of the Casimir interaction between dielectric objects in an electrolytic solution was extended to cylindrical geometries [28, 201], which for example, serve as a model for filaments in a cell. The Casimir interaction becomes even more important for these geometries since the interaction increases with the length of the cylinders. Compared to the sphere-sphere geometry, no analytical results for the single-round-trip result between cylinders or even just a cylinder and plane were found.

10 | Casimir interaction between bi-isotropic spheres in vacuum

Parts of this Chapter, which refer to results for bi-isotropic spheres are published in Ref. [101] and thus also contain input from the authors of the article.

In the previous Chapter, we discussed the Casimir interaction between two metallic spheres in vacuum and two dielectric spheres in an electrolyte. The spheres in both cases consist of the same material, which, according to [39], always leads to an attractive Casimir force between the objects. However, a repulsive Casimir force can also appear if we consider two spheres of dissimilar materials and additionally allow for polarisation mixing. This Chapter provides general expressions for the Casimir interaction between two bi-isotropic spheres, which allow for the mixing of polarisations upon scattering as we discussed in Chap. 4.

Most Casimir experiments are performed with two objects in close vicinity to each other to be able to detect a Casimir signal. At close distances, the Casimir force between two smooth but arbitrarily shaped objects can be evaluated from the so-called proximity force approximation (PFA) [202]. The method is based on a local approximation of the surfaces by infinitesimal small parallel surface elements, as schematically illustrated in Fig. 10.1 for two spheres of radii R_1 and R_2. The local plane-plane (pp) interactions are evaluated by the Casimir-Lifshitz formula [13, 14]

$$\mathcal{F}_{\text{pp}}(l) = k_{\text{B}}T\sum_{n=0}^{\infty}{}' \sum_{p=\text{TE,TM}} \int_{\mathcal{K}}^{\infty} \frac{\mathrm{d}\kappa}{2\pi}\kappa \log\left(1 - r_p^{(1)} r_p^{(2)} e^{-2\kappa l}\right) \tag{10.1}$$

for two planes within a distance l, with Fresnel reflection coefficients $r_p \equiv r_{p,p}$. To obtain the PFA result, we integrate over all local distances. In the sphere-sphere setup, the integration goes from the surface-to-surface distance L to ∞. PFA assumes that the Casimir force is additive, which is generally not valid for fluctuation-induced forces. The validity of these approximations is thus limited [31, 203, 204]. A recent study for dielectric spheres [33] showed that the PFA result follows from a large-sphere approximation of the general scattering formula for two spheres, with $\mathcal{F}_{\text{PFA}} = 2\pi R_{\text{eff}} \int_L^{\infty} \mathrm{d}l \mathcal{F}_{\text{pp}}(l)$. The TE and TM modes contribute separably to the Casimir interaction between dielectric spheres in the PFA regime. We want to analyse whether the PFA result can still be obtained from an asymptotic expansion of the scattering approach if we consider polarisation-mixing materials instead. Within our study, we also include the leading corrections in the asymptotic expansion of the Casimir free energy to determine the next-to-leading order in a large-radii approximation. This extends previous calculations for perfect electric reflectors [34, 35] and dielectric spheres [109].

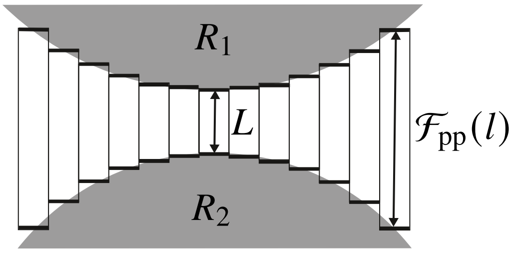

Figure 10.1: Illustration of the proximity force approximation (PFA) for the Casimir free energy between two spherical objects of effective radius $R_{\text{eff}} = R_1R_2/(R_1 + R_2)$. The sphere surfaces are approximated by parallel planar surface elements in a distance l with an interaction energy of $\mathcal{F}_{\text{pp}}(l)$. Within the PFA, the total Casimir free energy $\mathcal{F}_{\text{PFA}}$ is obtained by integrating from the minimal distance L to infinity: $\mathcal{F}_{\text{PFA}} = 2\pi R_{\text{eff}} \int_L^{\infty} \mathcal{F}_{\text{pp}}(l) dl$.

Apart from the small distance limit, we are also interested in the Casimir interaction between two bi-isotropic spheres that are far apart. This gives insight into the change of the Casimir force with distance and allows us to analyse whether effects, like a repulsive Casimir force found for small distances, persist even at large separations.

In Secs. 10.1 and 10.2, we derive the leading and subleading term of the Casimir free energy for two bi-isotropic spheres with large radii. Our calculation follows the one presented in Refs. [33, 109] and has been adapted for bi-isotropic materials where necessary. Additionally, in Sec. 10.3, we discuss the Casimir interaction between bi-isotropic spheres in the large-distance limit.

10.1 Large radii approximation, the leading saddle-point approximation

In this Section, we are going to evaluate the Casimir free energy between two bi-isotropic spheres with radii R_1, R_2 much larger, than the surface-to-surface distance L. For this purpose, we are applying the expansion of the scattering amplitudes for large radii, which according to our previous discussion in Sec. 4.2.2 is given by

$$S_{p_j,p_i}(\Theta) = \frac{R\mathcal{K}}{2} \mathrm{e}^{2R\mathcal{K}\sin(\Theta/2)} \tilde{r}_{p_j,p_i}(\Theta)\,. \tag{10.2}$$

By applying Eq. (4.25), we can express the argument of the exponential function in terms of the in- and out-going wave vector components like: $2\mathcal{K}\sin(\Theta/2) = \sqrt{2\left(\mathcal{K}^2 + \kappa_i\kappa_j + \mathbf{k}_i \cdot \mathbf{k}_j\right)}$. The coefficient $\tilde{r}_{p_j,p_i}$ accounts for the leading and subleading term in the large-sphere expansion at finite frequency, which according to Eq. (4.44) is given by

$$\tilde{r}_{p_j,p_i}(\Theta) = r_{p_j,p_i}\left(\frac{\pi - \Theta}{2}\right)\left[1 + \frac{s_{p_j,p_i}(\Theta)}{R\mathcal{K}} + O(R^{-2})\right]\,. \tag{10.3}$$

Recall that the leading term represents the geometrical optics limit with r_{p_j,p_i} being the Fresnel reflection coefficients for a bi-isotropic plane and an incident angle of $(\pi - \Theta)/2$, where Θ stands for the scattering angle defined between the in- and out-going wave vector. The leading corrections, denoted by s_{p_j,p_i} take diffraction correction at the sphere into account. Note that for vanishing-frequency, the leading term of the scattering amplitude is identical to the one given above, as we have seen in Eq. (4.59). We are going to use the plane-wave representation of the free energy within the scattering approach (8.9) to derive the large-sphere approximation. We thus need the reflection matrix elements in the plane-wave basis (4.26), which, with the representation of the scattering amplitude given above, can be written as

$$\langle \mathbf{k}_j, p_j, \pm|\mathcal{R}|\mathbf{k}_i, p_i, \mp\rangle = \frac{\pi R}{\kappa_j} \mathrm{e}^{2R\mathcal{K}\sin(\Theta/2)} \rho_{p_j,p_i}\,, \tag{10.4}$$

where we introduce $\rho_{p_j,p_i} = \rho_{p_j,p_i}(\mathbf{k}_j, \mathbf{k}_i)$ with

$$\rho_{p_j,p_i} = A_{j,i}\tilde{r}_{p_j,p_i} + (-1)^{p_j+p_i} B_{j,i}\tilde{r}_{\bar{p}_j,\bar{p}_i} - (-1)^{p_j} C_{j,i}\tilde{r}_{\bar{p}_j,p_i} + (-1)^{p_i} D_{j,i}\tilde{r}_{p_j,\bar{p}_i}\,. \tag{10.5}$$

Inserting the reflection matrix elements (10.4) into the trace expression (8.9), we get

$$\mathrm{tr}\mathcal{M}^r = \left(\frac{R_1R_2}{16\pi^2}\right)^r \int \mathrm{d}^{2r}\mathbf{k}\, g(\mathbf{k}_1,\dots,\mathbf{k}_{2r})\mathrm{e}^{-f(\mathbf{k}_1,\dots,\mathbf{k}_{2r})}\,. \tag{10.6}$$

The function f in the exponential accounts for all terms which scale with the sphere radii, which includes the part from the translation matrix elements in the plane-wave basis as well as the part from the large sphere expansion of the scattering matrix elements (10.2). In total, the argument of the exponential is defined by

$$f(\mathbf{k}_1,\dots,\mathbf{k}_{2r}) = \sum_{j=1}^{r}(R_1\eta_{2j}+R_2\eta_{2j-1})\,,\qquad \eta_i = \kappa_i+\kappa_{i+1}-\left[2\left(\mathcal{K}^2+\kappa_i\kappa_{i+1}+\mathbf{k}_i\cdot\mathbf{k}_{i+1}\right)\right]^{1/2}\,. \tag{10.7}$$

We recall that the summation indices are cyclic and make use of the identification $i \equiv 2r+i$. The function $g(\mathbf{k}_1,\dots,\mathbf{k}_{2r})$ accounts for all the remaining terms and is defined by

$$g(\mathbf{k}_1,\dots,\mathbf{k}_{2r}) = \sum_{p_1,\dots,p_{2r}}\prod_{j=1}^{r}\frac{\mathrm{e}^{-(\kappa_{2j}+\kappa_{2j-1})L}}{\kappa_{2j}\kappa_{2j-1}}\rho^{(1)}_{p_{2j+1},p_{2j}}\rho^{(2)}_{p_{2j},p_{2j-1}}\,. \tag{10.8}$$

We note that the trace expression (10.6) is identical to the one for dielectric spheres derived in Ref. [33]. The main difference is the definition of the function g, more precisely the coefficients $\rho_{p,p'}$, which compared to the earlier analysis now also includes polarisation-mixing reflection coefficients $r_{\mathrm{TM,TE}}$ and $r_{\mathrm{TE,TM}}$.

10.1.1 Leading-order saddle-point approximation

One or both radii R_1 and R_2 are considered large, so there exists a point where $|\mathrm{e}^{-f}|$ is largest and decays exponentially away from this saddle-point. The saddle is defined at the point where the gradient of f vanishes. We find that $\partial_{k_{i\alpha}}f=0$, $\alpha=x,y$ is equivalent to $k_{i,\alpha}=k_{i+1,\alpha}$. The saddle points $\mathbf{k}_{\mathrm{sp}}$, given by

$$\mathbf{k}_1=\mathbf{k}_2=\ldots=\mathbf{k}_{2r}\equiv\mathbf{k}_{\mathrm{sp}}\,, \tag{10.9}$$

thus define a two-dimensional manifold. To gain a better understanding of the saddle point, we depicted the function $f=f(\mathbf{k}_1,\mathbf{k}_2)$ for $r=1$ in Fig. 10.2. The left panel shows the projection of f for $k_{1,y}=0=k_{2,y}$, where the saddle is defined by the line $k_{1,x}=k_{2,x}$. The right panel shows the projection for $k_{2,x}=0=k_{2,y}$, where the saddle point is defined by a single-point ($k_{1,x}=0=k_{1,y}$).

The dominant contribution for large sphere radii, thus, comes from the leading-order (LO) saddle-point approximation of the trace expression (10.6). In the first part of this thesis, we used the one-dimensional saddle-point approximation multiple times. Now, we will apply it to a multidimensional integral. The procedure is similar to the one-dimensional case, we discussed in Appendix A.6.2. First, we expand f and g in a Taylor series around the saddle to obtain the leading contribution of (10.6) for large radii. At the saddle point $\mathbf{k}_i=\mathbf{k}_j=\mathbf{k}_{\mathrm{sp}}$, the polarisation-conversion coefficients $B_{j,i}, C_{j,i}$ and $D_{j,i}$ all vanish while the coefficient $A_{j,i}$ yields one. The coefficients $\rho_{p,p'}$ defined in Eq. (10.5), thus correspond with the leading expansion coefficient of the scattering amplitudes:

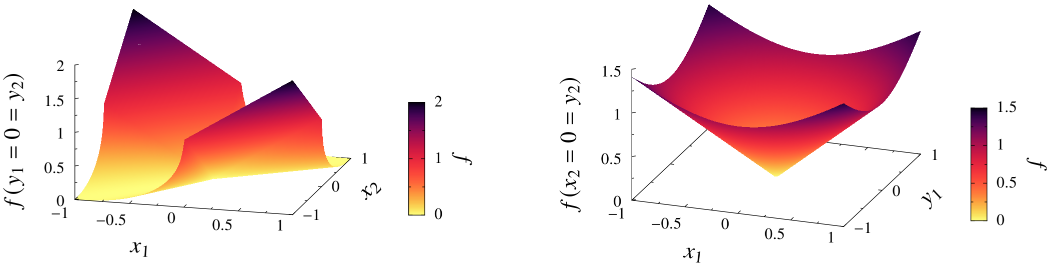

Figure 10.2: Illustration of the function f defined in Eq. (10.7) for a single round-trip ($r = 1$) in the zero-frequency limit ($\mathcal{K} = 0$), which yields $f(\mathbf{k}_1, \mathbf{k}_2) = (R_1 + R_2)\left[k_1 + k_2 + \sqrt{2(k_1 k_2 + \mathbf{k}_1 \cdot \mathbf{k}_2)}\right]$. We depict f as function of the scaled variables $x_i = (R_1 + R_2)k_{i,x}$ and $y_i = (R_1 + R_2)k_{i,y}$. The left panel shows f as function of x_1 and x_2 for fixed $y_1 = 0 = y_2$ with f being minimal along $x_1 = x_2$. The right panel shows f as function of x_1 and y_1 with $x_2 = 0 = y_2$, where f is minimal for $x_1 = 0 = y_1$.

$\rho_{p,p'}\big|_{\mathrm{sp}} = \tilde{r}_{p,p'}\big|_{\mathrm{sp}}$. The function g at the saddle point is thus given by

$$g_{\mathrm{sp}} := g(\mathbf{k}_i = \mathbf{k}_{\mathrm{sp}}) = \frac{\mathrm{e}^{-2r\kappa_{\mathrm{sp}}L}}{\kappa_{\mathrm{sp}}^{2r}} \sum_{p_1,\dots,p_{2r}} \prod_{j=1}^{r} \tilde{r}^{(1)}_{p_{2j+1},p_{2j}}\Big|_{\mathrm{sp}} \tilde{r}^{(2)}_{p_{2j},p_{2j-1}}\Big|_{\mathrm{sp}} . \tag{10.10}$$

For convenience, we will omit the index 'sp' at the reflection coefficients in the following. f vanishes along the saddle point, with the first non-vanishing contribution given by

$$\begin{aligned} f &\approx \frac{1}{2} \sum_{\alpha,\beta=x,y} \sum_{i,j=1}^{2r} \left(\frac{\partial^2 f}{\partial k_{i,\alpha} \partial k_{j,\beta}}\right)_{\mathrm{sp}} (k_{i,\alpha} - k_{\mathrm{sp},\alpha})(k_{j,\beta} - k_{\mathrm{sp},\beta}) \\ &\approx \frac{1}{2} \sum_{\alpha=x,y} \sum_{i,j=1}^{2r} H_{i,j}(k_{i,\alpha} - k_{\mathrm{sp},\alpha})(k_{j,\alpha} - k_{\mathrm{sp},\alpha}) . \end{aligned} \tag{10.11}$$

At the saddle point, only second derivatives of f with respect to the same component $\alpha = \beta$ yield a non-vanishing contribution. This fact is also evident from the projections of f displayed in the right panel of Fig. 10.2. Furthermore, we introduced the Hessian $H_{i,j}$. The Hessian is a cyclic and periodic Toepliz matrix with entries

$$H_{i,j} = \frac{1}{2\kappa_{\mathrm{sp}}} \left[(R_1 + R_2)\bar{\delta}_{i,j} - R_{2-(i+1)\mathrm{mod}2}\bar{\delta}_{i+1,j} - R_{2-i\mathrm{mod}2}\bar{\delta}_{i,j+1}\right] . \tag{10.12}$$

$\bar{\delta}_{i,j}$ denotes the Kronecker delta symbol, where the equality of the indices is taken modulo $2r$ to account for the cyclic character of the summation indices. The cyclic character of the Hessian gives, however, rise to a zero-eigenvalue. As the Hessian matrix is not positive definite, we cannot use the Gaussian integral A.6.3, as we did, to determine the one-dimensional saddle-point approximation (Sec. A.6.2). We perform a discrete Fourier transformation of the transverse wave vector components to single-out the zero-eigenvalue, which is defined by

$$k_{j,\alpha} = \sum_{n=0}^{2r-1} w^{jn} v_{n,\alpha} , \qquad w = \frac{\exp\left(\frac{2\pi\mathrm{i}}{2r}\right)}{\sqrt{2r}} . \tag{10.13}$$

The discrete Fourier transform is a unitary transformation with $\sum_{m=0}^{2r-1} w^{km} w^{-mn} = \delta_{k,n}$. The saddle point in the new coordinates is defined by $v_{1,\alpha} = 0 = v_{2,\alpha} = v_{3,\alpha} = \ldots = v_{2r-1,\alpha}$. The eigendirection $\mathbf{v}_{2r} = \mathbf{v}_0$ to the zero-eigenvalue thus corresponds with the saddle. We can thus write

$$\mathbf{k}_{\mathrm{sp}} = \frac{\mathbf{v}_0}{\sqrt{2r}} \,. \tag{10.14}$$

The Fourier transformation of f yields

$$f \approx \frac{1}{2} \sum_{\alpha=x,y} \sum_{m,n=0}^{2r-1} \tilde{M}_{m,n} v_{m,\alpha} v_{n,\alpha} \,, \tag{10.15}$$

where $\tilde{M}_{m,n}$ define the matrix elements of the Fourier transformed Hessian $H_{i,j}$, which are given by

$$\begin{aligned} \tilde{M}_{m,n} &= \frac{1}{2r} \sum_{i,j=0}^{2r-1} w^{-im} w^{-jm} H_{i,j} \\ &= \frac{1}{\kappa_{\mathrm{sp}}} \left[(R_1 + R_2) \sin^2\left(\frac{\pi m}{2r}\right) \bar{\delta}_{m,-n} - \mathrm{i}(R_1 - R_2) \sin\left(\frac{\pi m}{2r}\right) \cos\left(\frac{\pi m}{2r}\right) \bar{\delta}_{m,-n\pm r} \right] \,. \end{aligned} \tag{10.16}$$

The entries $\tilde{M}_{0,n} = 0 = \tilde{M}_{m,0}$, associated with the zero-eigenvalue of the Hessian, do not contribute to f. We are thus able to separate the integral over $\mathbf{v}_0$ from the remaining integrals over $\mathbf{v}^t = (\mathbf{v}_1, \ldots \mathbf{v}_{2r-1})$. The leading-order (LO) saddle-point approximation of the trace over the r-th round-trip operator thus yields

$$[\mathrm{tr}\mathcal{M}^r]_{\mathrm{LO}} = \left(\frac{R_1 R_2}{16\pi^2}\right)^r \int \mathrm{d}^2\mathbf{v}_0 g_{\mathrm{sp}} \prod_{\alpha=x,y} \int \mathrm{d}^{2r-1}\mathbf{v}_\alpha \exp\left(-\frac{1}{2}\mathbf{v}_\alpha^t \mathbf{M} \mathbf{v}_\alpha\right) \,. \tag{10.17}$$

The matrix $\mathbf{M}$ with entries $\tilde{M}_{m,n}$, $m, n = 1, \ldots 2r-1$, is positive definite and a block matrix of the form

$$\mathbf{M} = \begin{pmatrix} \mathbf{B} & & \mathbf{C} \\ & M_{r,r} & \\ \mathbf{D} & & \mathbf{B}^* \end{pmatrix} , \tag{10.18}$$

with $M_{r,r} = (R_1 + R_2)\kappa_{\mathrm{sp}}^{-1}$ and each block $\mathbf{B}$, $\mathbf{C}$ and $\mathbf{D}$ is a $(r-1)$-dimensional anti-diagonal matrix with entries, which according to Eq. (10.16), are given by

$$B_{m,n} = -\mathrm{i}(R_1 - R_2)\kappa_{\mathrm{sp}}^{-1} \sin\left(\frac{\pi m}{2r}\right) \cos\left(\frac{\pi m}{2r}\right) \delta_{m,r-n} \,, \tag{10.19a}$$

$$C_{m,n} = (R_1 + R_2)\kappa_{\mathrm{sp}}^{-1} \sin^2\left(\frac{\pi m}{2r}\right) \delta_{m,r-n} \,, \quad D_{m,n} = (R_1 + R_2)\kappa_{\mathrm{sp}}^{-1} \cos^2\left(\frac{\pi m}{2r}\right) \delta_{m,r-n} \,. \tag{10.19b}$$

The integral over $\mathbf{v}_\alpha^t = (v_{1,\alpha}, v_{2,\alpha}, \ldots v_{2r-1,\alpha})$ is of Gaussian-type and can directly be evaluated with (A.28). By performing a Laplace expansion with respect to the r-th row or column, we find the determinant $\det(\mathbf{M}) = (-1)^{r-1} M_{r,r} \det(\mathbf{B}\mathbf{B}^* - \mathbf{C}\mathbf{D})$. The products of the anti-diagonal matrices

B, **C** and **D** are diagonal and the determinant is thus given by the product of the entries yielding

$$\begin{aligned}\det\mathbf{M} &= (R_1+R_2)\kappa_{\mathrm{sp}}^{-2r+1}(-1)^{r-1}\prod_{m=1}^{r-1}\sin^2\left(\frac{\pi m}{2r}\right)\cos^2\left(\frac{\pi m}{2r}\right)\left[(R_1-R_2)^2-(R_1+R_2)^2\right]\\ &= (R_1+R_2)\kappa_{\mathrm{sp}}^{-2r+1}(R_1R_2)^{r-1}\prod_{m=1}^{r-1}\sin^2\left(\frac{\pi m}{r}\right),\end{aligned} \tag{10.20}$$

where in the second line we used the trigonometric relation $\sin(2x) = 2\sin(x)\cos(x)$. We apply the identity [205] $\prod_{m=1}^{r-1}\sin(\pi m/r) = r2^{1-r}$ and thus obtain

$$\det\mathbf{M} = \frac{r^2 4^{1-r}\kappa_{\mathrm{sp}}^{-2r+1}}{R_{\mathrm{eff}}}(R_1R_2)^r\,. \tag{10.21}$$

With the above-given expression for the determinant, we find for the leading-order saddle-point approximation (10.17), the following expression

$$[\mathrm{tr}\mathcal{M}^r]_{\mathrm{LO}} = \frac{\pi R_{\mathrm{eff}}}{r}\int\frac{\mathrm{d}^2\mathbf{k}_{\mathrm{sp}}}{(2\pi)^2}\kappa_{\mathrm{sp}}^{2r-1}g_{\mathrm{sp}}\,, \tag{10.22}$$

where we also replaced the integral over $\mathbf{v}_0$ with $\mathbf{k}_{\mathrm{sp}}$ according to Eq. (10.14). Note that the expression above is equivalent to the one for dielectric spheres in Ref. [33]. The key difference is the function g_{sp} given in Eq. (10.10), which accounts for the polarisation-mixing.

In the next Section, we are going to evaluate the expression above and show that it agrees in leading order with the proximity force approximation for bi-isotropic spheres. We will also derive the correction to PFA within the leading saddle-point approximation which arise from the subleading term of the scattering amplitudes $s_{p,p'}$ which account for the diffraction corrections.

10.1.2 Proximity force approximation in the presence of polarisation mixing

For dielectric spheres, there is no polarisation-mixing upon scattering. The function g_{sp} in Eq. (10.10) can directly be evaluated to $g_{\mathrm{sp}} = \left(\mathrm{e}^{-2r\kappa_{\mathrm{sp}}L}/\kappa_{\mathrm{sp}}^{2r}\right)\sum_{p=\mathrm{TE,TM}}\left(\tilde{r}^{(1)}_{p,p}\tilde{r}^{(2)}_{p,p}\right)^r$. The TE- and TM-modes separately contribute to the Casimir interaction. For bi-isotropic spheres, on the other hand, we have to take all polarisation combinations during the r round-trips into account. This means four possible contributions for a single round-trip, as schematically shown in Fig. 10.3. Fig. 10.3a depicts an incoming TM-polarised wave on sphere 1 which is either reflected into a TM- or TE-polarised mode and Fig. 10.3b illustrates an incoming TE-polarised wave on sphere 1. Consequently, for r round-trips, there are 4^r possible sequences of reflection combination between the two spheres. The problem of finding all possible combinations is similar to our discussion for the zero-frequency case, where we had to find all partitions of the r round-trips. There, we found that an evaluation of the Casimir free energy is simpler when performing the sum over all round-trips and then introducing a recursive description of the various combinations. The reflection coefficients are all evaluated at the saddle point, so we are only working with eight different reflection coefficients, four for each sphere. Hence, finding all possible combinations of the eight coefficients is more straightforward than the partition problem, we solved for the Drude spheres. In this case, the number of 'building blocks' increased with increasing round-trip numbers.

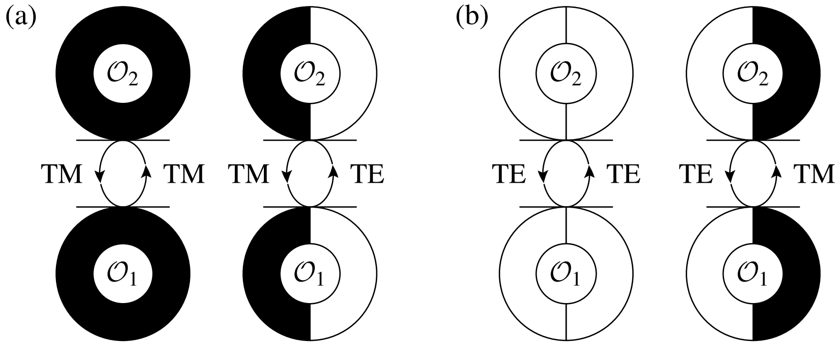

Figure 10.3: Illustration of the four possible polarisation combinations within one round-trip. Figure (a) and (b) respectively depict the scattering channels $A^{\mathrm{TM,TM}}$ and $A^{\mathrm{TE,TE}}$ defined in Eq. (10.27), where on the one hand incoming TM-modes are reflected at sphere 1 and on the other hand TE-modes are reflected at sphere 1. In both cases, the polarisation of the wave reflected from sphere 2 is either transverse-electric or -magnetic.

After carrying out the summation over all round-trips with (10.22), the leading-order frequency contribution of the Casimir free energy yields

$$\mathcal{F}_{\mathrm{LO}}(\xi) = -\pi R_{\mathrm{eff}} \int \frac{\mathrm{d}^2\mathbf{k}_{\mathrm{sp}}}{(2\pi)^2\kappa_{\mathrm{sp}}} \mathcal{P}_2(\mathbf{k}_{\mathrm{sp}}) \,, \tag{10.23}$$

where we introduced the function $\mathcal{P}_2(\mathbf{k}_{\mathrm{sp}})$, which accounts for all polarisation combinations and is defined by

$$\mathcal{P}_n(\mathbf{k}_{\mathrm{sp}}) = \sum_{r=1}^{\infty} \frac{\mathrm{e}^{-2r\kappa_{\mathrm{sp}}L}}{r^n} \sum_{p_1,\dots,p_{2r}} \prod_{j=1}^{r} \tilde{r}^{(1)}_{p_{2j+1},p_{2j}} \tilde{r}^{(2)}_{p_{2j},p_{2j-1}} \,. \tag{10.24}$$

The subscript n refers to the power of the round-trip index r, which is two in the case discussed above. The importance of the function $\mathcal{P}_n$ will become evident in the remainder of this Section.

Not all combinations of reflection coefficients are realized. There are some restrictions. For r round-trips, the mode of polarisation p_1 incident on sphere 2 must match the polarisation p_{2r+1} reflected from sphere 1, as it is illustrated for one round-trip in Fig. 10.3. This condition mathematically arises from the trace expression. We thus introduce functions $h_r^{p',p}$, which account for all polarisation sequences, where the polarisation p is incident on sphere 2 and p' is the polarisation of the reflected wave from sphere 1. The polarisation does not change during the translation from one sphere to the other, since we assume that the medium in which the spheres are immersed is not optically active. The polarisation contribution (10.24) then becomes

$$\mathcal{P}_2 = \int_0^1 \frac{\mathrm{d}t_2}{t_2} \int_0^{t_2} \frac{\mathrm{d}t_1}{t_1} \sum_{r=1}^{\infty} t_1^r \left(h_r^{\mathrm{TM,TM}} + h_r^{\mathrm{TE,TE}} \right) \,, \tag{10.25}$$

where we have rewritten the factor $1/r^2$ in terms of integrals over auxiliary variables t_1 and t_2. The possible polarisation sequences described by $h_r^{p',p}$ can be build up by successively performing single round-trips between the two spheres. Hence, after one round-trip, there are $r-1$ round-trips left, which can be accounted for in the following recursive relation

$$h_r^{p',p} = A^{p',\mathrm{TM}} h_{r-1}^{\mathrm{TM},p} + A^{p',\mathrm{TE}} h_{r-1}^{\mathrm{TE},p} \,. \tag{10.26}$$

$A^{p',p'} = h_1^{p',p}$ defines one round-trip, where a p-polarised wave incoming on sphere 2 can either be reflected into a TM- or TE-polarised wave. The wave reflected from sphere 1 is p'-polarised, thus leading to the following definition

$$A^{p',p} = \left(\tilde{r}^{(1)}_{p',\mathrm{TM}} \tilde{r}^{(2)}_{\mathrm{TM},p} + \tilde{r}^{(1)}_{p',\mathrm{TE}} \tilde{r}^{(2)}_{\mathrm{TE},p}\right) \mathrm{e}^{-2\kappa_{\mathrm{sp}} L} \,. \tag{10.27}$$

Note that Fig. 10.3a and 10.3b respectively illustrate the cases $A^{\mathrm{TM},\mathrm{TM}}$ and $A^{\mathrm{TE},\mathrm{TE}}$. Similar to the discussion for the Drude spheres in Sec. 9.3, we introduce generating functions for the polarisation sequences defined by

$$H^{p',p}(t) = \sum_{r=1}^{\infty} t^r h_r^{p',p} \tag{10.28}$$

which, together with the recursion relations given in Eq. (10.26), yield

$$H^{p',p}(t) = tA^{p',p} + t\left[A^{p',\mathrm{TM}} H^{\mathrm{TM},p}(t) + A^{p',\mathrm{TE}} H^{\mathrm{TE},p}(t)\right] \,. \tag{10.29}$$

We thus obtain for the auxiliary functions $\mathcal{P}_2$, defined in Eq. (10.25)

$$\mathcal{P}_2 = \int_0^1 \frac{\mathrm{d}t_2}{t_2} \int_0^{t_2} \frac{\mathrm{d}t_1}{t_1} \left[H^{\mathrm{TM},\mathrm{TM}}(t_1) + H^{\mathrm{TE},\mathrm{TE}}(t_1)\right] \,. \tag{10.30}$$

Solving (10.29) for $H^{\mathrm{TM},\mathrm{TM}}$ and $H^{\mathrm{TE},\mathrm{TE}}$ leads to

$$H^{\mathrm{TM},\mathrm{TM}}(t) + H^{\mathrm{TE},\mathrm{TE}}(t) = t\frac{A^{\mathrm{TM},\mathrm{TM}} + A^{\mathrm{TE},\mathrm{TE}} - 2tA^{\mathrm{TM},\mathrm{TM}}A^{\mathrm{TE},\mathrm{TE}} + 2tA^{\mathrm{TM},\mathrm{TE}}A^{\mathrm{TE},\mathrm{TM}}}{(1-tA^{\mathrm{TM},\mathrm{TM}})(1-tA^{\mathrm{TE},\mathrm{TE}}) - t^2 A^{\mathrm{TM},\mathrm{TE}}A^{\mathrm{TE},\mathrm{TM}}} \,. \tag{10.31}$$

The nominator is the derivative with respect to t of the denominator, hence the integral over t_1 in Eq. (10.30) yields

$$\mathcal{P}_2 = -\int_0^1 \frac{\mathrm{d}t}{t} \log\det(\mathbb{I} - t\mathbf{A}) \,, \qquad \mathbf{A} = \begin{pmatrix} A^{\mathrm{TM},\mathrm{TM}} & A^{\mathrm{TM},\mathrm{TE}} \\ A^{\mathrm{TE},\mathrm{TM}} & A^{\mathrm{TE},\mathrm{TE}} \end{pmatrix} \,, \tag{10.32}$$

where we set $t_2 = t$ for convenience. The elements of the matrix $\mathbf{A}$ are defined in Eq. (10.27). Recall that the coefficient $\tilde{r}_{p,p'} = r_{p,p'}\left(1 - s_{p,p'}/R\mathcal{K}\right)$ contains the leading term $r_{p,p'}$ and also the subleading term $s_{p,p'}$ of the large sphere approximation. We can thus expand $\mathbf{A}$ for large radii as $\mathbf{A} \approx \mathbf{A}_0 + \mathbf{A}_1/\mathcal{K}$. The matrix $\mathbf{A}_0$ accounts for the round-trip matrix in the plane-wave basis between two bi-isotropic planes separated by a distance L

$$\mathbf{A}_0 = \mathbf{R}_1\mathbf{R}_2\mathrm{e}^{-2\kappa_{\mathrm{sp}} L} \tag{10.33}$$

with the corresponding reflection matrices at each plane defined by

$$\mathbf{R}_i = \begin{pmatrix} r^{(i)}_{\mathrm{TM},\mathrm{TM}} & r^{(i)}_{\mathrm{TM},\mathrm{TE}} \\ r^{(i)}_{\mathrm{TE},\mathrm{TM}} & r^{(i)}_{\mathrm{TE},\mathrm{TE}} \end{pmatrix} \,. \tag{10.34}$$

The components of $\mathbf{A}_1$ take the subleading terms of the reflection matrix into account, which also include diffraction at the sphere. They are given by

$$A_1^{p',p} = \sum_{q=\mathrm{TM},\mathrm{TE}} r^{(1)}_{p',q} r^{(2)}_{q,p} \left(\frac{s^{(1)}_{p',q}}{R_1} + \frac{s^{(2)}_{q,p}}{R_2} \right) \mathrm{e}^{-2\kappa_{\mathrm{sp}} L} \,. \tag{10.35}$$

Furthermore, we approximate the determinant in (10.32) by using $\det(\mathbb{I} - \epsilon \mathbf{X}) = 1 - \epsilon \mathrm{tr} \mathbf{X}$ for small ϵ. Additionally, we expand the logarithm in a Mercator series, leading to

$$\log\det(\mathbb{I} - t\mathbf{A}) \approx \log\det\left(\mathbb{I} - t\mathbf{A}_0\right) + \frac{1}{\mathcal{K}} \mathrm{tr}\left[(\mathbb{I} - t\mathbf{A}_0)^{-1} t\mathbf{A}_1\right] \,. \tag{10.36}$$

Based on this separation, we can write the leading saddle-point approximation of the Casimir free energy as

$$\mathcal{F}_{\mathrm{LO}}(\xi) \approx \mathcal{F}_{\mathrm{PFA}}(\xi) + \mathcal{F}_{\mathrm{diff}}(\xi) \,. \tag{10.37}$$

By substituting $t = \exp(-2\kappa_{\mathrm{sp}}(l - L))$ in Eq. (10.32), we immediately find that the leading order agrees with the PFA result of the Casimir free energy for two bi-isotropic spheres

$$\mathcal{F}_{\mathrm{PFA}}(\xi) = 2\pi R_{\mathrm{eff}} \int_L^\infty \mathrm{d}l \int \frac{\mathrm{d}^2 \mathbf{k}_{\mathrm{sp}}}{(2\pi)^2} \log\det(\mathbb{I} - \mathbf{R}_1 \mathbf{R}_2 \mathrm{e}^{-2\kappa_{\mathrm{sp}} l}) \,. \tag{10.38}$$

More specifically, this holds for any material of the sphere as long as the large-sphere approximation of the scattering amplitudes can be written in the form presented in Eq. (10.2). At the beginning of this Chapter, we introduced the Lifshitz formula for dielectric objects, which depends on the Fresnel reflection coefficients. For bi-isotropic materials, we have to replace the coefficients with reflection matrices, as shown above. The integral over l can be evaluated by diagonalizing the round-trip matrix $\mathbf{A}_0$, where the eigenvalues for the 2×2-matrix can be expressed in terms of its trace and determinant

$$\lambda_{1,2} = \frac{1}{2}\left[\mathrm{tr}\mathbf{A}_0 \pm \sqrt{\mathrm{tr}^2 \mathbf{A}_0 - 4 \det \mathbf{A}_0}\right] \,. \tag{10.39}$$

The PFA expression is thus given in terms of the dilogarithm $\mathrm{Li}_2(\lambda_{1,2})$

$$\mathcal{F}_{\mathrm{PFA}}(\xi) = \pi R_{\mathrm{eff}} \int \frac{\mathrm{d}^2 \mathbf{k}_{\mathrm{sp}}}{(2\pi)^2 \kappa_{\mathrm{sp}}} \left[\mathrm{Li}_2(\lambda_1) + \mathrm{Li}_2(\lambda_2)\right] \,. \tag{10.40}$$

Note that the round-trip matrix $\mathbf{A}_0$ is diagonal if there is no mixing of polarisations and the entries are given by

$$\phi_{\mathrm{TM}} \equiv \lambda_1 = r^{(1)}_{\mathrm{TM,TM}} r^{(2)}_{\mathrm{TM,TM}} \mathrm{e}^{-2\kappa_{\mathrm{sp}} L}, \qquad \phi_{\mathrm{TE}} \equiv \lambda_2 = r^{(1)}_{\mathrm{TE,TE}} r^{(2)}_{\mathrm{TE,TE}} \mathrm{e}^{-2\kappa_{\mathrm{sp}} L}, \tag{10.41}$$

where we adopted the notation from Ref. [33].

To summarize, we have shown that also for polarisation-mixing spheres, the PFA result arises from an asymptotic expansion of the scattering formula for large radii. Next, we want to discuss the leading corrections $\mathcal{F}_{\mathrm{diff}}$, which arise from the diffraction coefficients. The leading corrections originate from the next order of the expansion of $\mathbf{A}$, as defined in Eq. (10.36), which with the coefficients (10.33) and (10.35) yields

$$\mathrm{tr}\left[(\mathbb{I} - t\mathbf{A}_0)^{-1} t\mathbf{A}_1\right] = \frac{\alpha_0 t + \alpha_1 t^2}{(1 - t\lambda_1)(1 - t\lambda_2)} \,. \tag{10.42}$$

The expansion coefficients α_0, α_1 are defined by

$$\alpha_0 = \mathrm{tr}\mathbf{A}_1 = A_1^{\mathrm{TM,TM}} + A_1^{\mathrm{TE,TE}} \,, \tag{10.43a}$$

$$\alpha_1 = -A_0^{\mathrm{TM,TM}} A_1^{\mathrm{TE,TE}} - A_0^{\mathrm{TE,TE}} A_1^{\mathrm{TM,TM}} + A_0^{\mathrm{TM,TE}} A_1^{\mathrm{TE,TM}} + A_0^{\mathrm{TE,TM}} A_1^{\mathrm{TM,TE}} \,. \tag{10.43b}$$

The leading diffraction corrections are thus given by

$$\mathcal{F}_{\mathrm{diff}}(\xi) = -2\pi \frac{R_{\mathrm{eff}}}{\mathcal{K}} \int_L^\infty \mathrm{d}l \int \frac{\mathrm{d}^2\mathbf{k}_{\mathrm{sp}}}{(2\pi)^2} \frac{\left(\alpha_0 + \alpha_1 \mathrm{e}^{-2\kappa_{\mathrm{sp}}(l-L)}\right) \mathrm{e}^{-2\kappa_{\mathrm{sp}}(l-L)}}{\left(1 - \lambda_1 \mathrm{e}^{-2\kappa_{\mathrm{sp}}(l-L)}\right)\left(1 - \lambda_2 \mathrm{e}^{-2\kappa_{\mathrm{sp}}(l-L)}\right)} \,. \tag{10.44}$$

After evaluating the integral over l, we arrive at (A.12)

$$\mathcal{F}_{\mathrm{diff}}(\xi) = \frac{\pi R_{\mathrm{eff}}}{\mathcal{K}} \int \frac{\mathrm{d}^2\mathbf{k}_{\mathrm{sp}}}{(2\pi)^2 \kappa_{\mathrm{sp}}} \left\{ \frac{\alpha_0\lambda_1 + \alpha_1}{\lambda_1(\lambda_1 - \lambda_2)} \log(1 - \lambda_1) + \frac{\alpha_0\lambda_2 + \alpha_1}{\lambda_2(\lambda_2 - \lambda_1)} \log(1 - \lambda_2) \right\} . \tag{10.45}$$

Considering dielectric spheres, we can recover the diffraction corrections obtained in Eq. (6.38) of Ref. [109], where the pre-factors of the logarithm reduce to

$$\frac{\alpha_0\lambda_1 + \alpha_1}{\lambda_1(\lambda_1 - \lambda_2)} = \phi_{\mathrm{TM}} \left(\frac{s^{(1)}_{\mathrm{TM,TM}}}{R_1} + \frac{s^{(2)}_{\mathrm{TM,TM}}}{R_2} \right), \qquad \frac{\alpha_0\lambda_2 + \alpha_1}{\lambda_2(\lambda_2 - \lambda_2)} = \phi_{\mathrm{TE}} \left(\frac{s^{(1)}_{\mathrm{TE,TE}}}{R_1} + \frac{s^{(2)}_{\mathrm{TE,TE}}}{R_2} \right) \tag{10.46}$$

with $\phi_{\mathrm{TM(TE)}}$ defined in Eq. (10.41).

10.2 The subleading saddle-point approximation

In the previous Section, we utilized two approximations. We restricted ourselves to the first two leading terms in the reflection coefficients and, in addition evaluated the leading term of the saddle-point approximation. As a consequence, corrections arise from two sources. We already computed with (10.45) the PFA correction from the subleading term of the reflection coefficients. For the second contribution, we remain within the geometrical optics, i. e. we only keep the leading-order terms of the reflection coefficients, but go one order further in the saddle-point approximation. In this Section, we are going to derive the next-to-leading-order in the saddle-point approximation.

In the previous Section, we only considered the first non-vanishing contribution of g and f along the saddle $v_{i,\alpha} = 0$ with $i = 1, \ldots 2r - 1$ and $\alpha = x, y$. Here, we include the next orders. Similar to the one-dimensional saddle-point approximation discussed in Appendix A.6.2, we expand the function g up to the second order

$$g = g_{\mathrm{sp}} + g_i^\alpha v_{i,\alpha} + \frac{1}{2} g_{ij}^{\alpha\beta} v_{i,\alpha} v_{j,\beta} + O\left((v_i^\alpha)^3\right) . \tag{10.47}$$

We employed the summation convention, which is that we sum over repeated indices. The derivatives of g are evaluated at the saddle and abbreviated by

$$g_i^\alpha = \left.\frac{\partial g}{\partial v_{i,\alpha}}\right|_{\mathrm{sp}}, \qquad g_{ij}^{\alpha\beta} = \left.\frac{\partial^2 g}{\partial v_{i,\alpha} v_{j,\beta}}\right|_{\mathrm{sp}} \tag{10.48}$$

with equivalent expressions for higher-order derivatives. The function f is Taylor expanded up to the fourth order

$$f = -\frac{1}{2}\mathbf{v}_\alpha^t \mathbf{M} \mathbf{v}_\alpha + \frac{1}{6} f_{ijk}^{\alpha\beta\gamma} v_{i,\alpha} v_{j,\beta} v_{k,\gamma} + \frac{1}{24} f_{ijkl}^{\alpha\beta\gamma\delta} v_{i,\alpha} v_{j,\beta} v_{k,\gamma} v_{l,\delta} + O\left((v_i^\alpha)^5\right) \tag{10.49}$$

with the same convention for the derivatives as introduced above. When computing the product $g \exp(-f)$ in Eq. (10.6), we approximate the exponential of the subleading terms by $\exp(-x) \approx (1 - x + x^2/2)$ and thus find

$$\begin{aligned} g\mathrm{e}^{-f} \approx \exp\left(-\frac{1}{2}\mathbf{v}_\alpha^t \mathbf{M} \mathbf{v}_\alpha\right) \Bigg[& g_{\mathrm{sp}} + \frac{1}{2} g_{ij}^{\alpha\beta} v_{i,\alpha} v_{j,\beta} - \frac{1}{24}\left(g_{\mathrm{sp}} f_{ijkl}^{\alpha\beta\gamma\delta} - 4 g_i^\alpha f_{jkl}^{\beta\gamma\delta}\right) v_{i,\alpha} v_{j,\beta} v_{k,\gamma} v_{l,\delta} \\ & + \frac{1}{72} g_{\mathrm{sp}} f_{ijk}^{\alpha\beta\gamma} f_{lmn}^{\delta\epsilon\eta} v_{i,\alpha} v_{j,\beta} v_{k,\gamma} v_{l,\delta} v_{m,\epsilon} v_{n,\eta} \Bigg] . \end{aligned} \tag{10.50}$$

Note that we disregard any odd powers of $v_{i,\alpha}$, since they vanish when performing the integral. The 2-, 4- and 6-point correlation functions (see definition in Eq. (A.29)) can conveniently be computed by applying Wick theorem according to (A.28). Note also that the 2-point correlation function $\langle v_i^\alpha v_j^\beta \rangle$ only yields a non-vanishing contribution if the indices α and β are the same. In summary, we thus find for the trace of the r-th round-trip operator

$$\begin{aligned} \mathrm{tr}\mathcal{M}^r \approx \frac{\pi R_{\mathrm{eff}}}{r} \int \frac{\mathrm{d}^2\mathbf{k}_{\mathrm{sp}}}{(2\pi)^2} \kappa_{\mathrm{sp}}^{2r-1} \Bigg[& g_{\mathrm{sp}} + \frac{1}{2} g_{ij}^{\alpha\alpha} M_{i,j}^{-1} - \frac{1}{8}\left(g_{\mathrm{sp}} f_{ijkl}^{\alpha\alpha\beta\beta} - 4 g_i^\alpha f_{jkl}^{\alpha\beta\beta}\right) M_{i,j}^{-1} M_{k,l}^{-1} \\ & + \frac{1}{24} g_{\mathrm{sp}} \left(3 f_{ijk}^{\alpha\alpha\beta} f_{lmn}^{\beta\gamma\gamma} M_{i,j}^{-1} M_{k,l}^{-1} M_{m,n}^{-1} + 2 f_{ijk}^{\alpha\beta\gamma} f_{lmn}^{\alpha\beta\gamma} M_{i,l}^{-1} M_{j,m}^{-1} M_{m,n}^{-1}\right) \Bigg] , \end{aligned} \tag{10.51}$$

where we also accounted for the fact that the order in which derivatives are taken is not relevant, e.g. $f_{ijk}^{\alpha\alpha\beta} = f_{jki}^{\alpha\beta\alpha} = f_{ikj}^{\alpha\beta\alpha} \ldots$, and thus leads to the multiplicative factors. $M_{i,j}^{-1}$ defines the elements of the inverse of the matrix $\mathbf{M}$. The matrix $\mathbf{M}$ is a block matrix (10.18) and its inverse is also a block matrix with

$$\mathbf{M}^{-1} = \begin{pmatrix} \tilde{\mathbf{B}} & & \tilde{\mathbf{C}} \\ & 1/M_{r,r} & \\ \tilde{\mathbf{D}} & & \tilde{\mathbf{B}}^* \end{pmatrix} \tag{10.52}$$

with anti-diagonal blocks $\tilde{\mathbf{B}}$, $\tilde{\mathbf{C}}$ and $\tilde{\mathbf{D}}$, whose entries are given by

$$\begin{aligned} \tilde{B}_{m,n} &= -\frac{\mathrm{i}\kappa_{\mathrm{sp}}(R_1 - R_2)}{4R_{\mathrm{eff}}(R_1 + R_2)} \frac{1}{\sin\left(\frac{\pi m}{2r}\right)\cos\left(\frac{\pi m}{2r}\right)} \delta_{m,r-n} , \\ \tilde{C}_{m,n} &= \frac{\kappa_{\mathrm{sp}}}{4R_{\mathrm{eff}}} \frac{1}{\sin^2\left(\frac{\pi m}{2r}\right)} \delta_{m,r-n} , \quad \tilde{D}_{m,n} = \frac{\kappa_{\mathrm{sp}}}{4R_{\mathrm{eff}}} \frac{1}{\cos^2\left(\frac{\pi m}{2r}\right)} \delta_{m,r-n} . \end{aligned} \tag{10.53}$$

For convenience, we introduced the effective radius $R_{\mathrm{eff}} = R_1 R_2/(R_1 + R_2)$. The first term in Eq. (10.51) accounts for the leading saddle-point approximation, which we computed in the previous

Section, and the remaining terms are all contributing to the next-to-leading-order corrections, which we are going to evaluate in the following. The derivatives are taken with respect to the Fourier transformed components $v_{i,\alpha}$, the functions f and g, however depend on the wave vector components $k_{n,\alpha}$, hence, we apply the chain rule to evaluate the various derivatives. The second term in Eq. (10.51) is, for example, given by

$$g_i^{\alpha} M_{i,j}^{-1} = \sum_{i=1}^{2r-1} M_{i,j}^{-1} \sum_{n=0}^{2r-1} \left(\frac{\partial g}{\partial k_{n,\alpha}} \right)_{\mathrm{sp}} w^{ni} \tag{10.54}$$

with the Fourier components w^{ni} introduced in Eq. (10.13). The function g is symmetric in the wave vector components, which means that a single derivative evaluated at the saddle point does not depend explicitly on the index n. The sum above, thus, only goes over the Fourier components w^{ni}, which due to the orthogonality of the discrete Fourier transformation yields zero. For the same reasoning also the expression $f_{ijk}^{\alpha\alpha\beta} M_{ij}^{-1}$ vanishes. The only terms which contribute to the next-to-leading-order (NTLO) of the saddle-point approximation are

$$\begin{aligned} [\mathrm{tr}\mathcal{M}^r]_{\mathrm{NTLO}} = \frac{\pi R_{\mathrm{eff}}}{2r} \int \frac{\mathrm{d}^2\mathbf{k}_{\mathrm{sp}}}{(2\pi)^2} \kappa_{\mathrm{sp}}^{2r-1} \Bigg[& g_{ij}^{\alpha\alpha} M_{i,j}^{-1} - \frac{1}{4} g_{\mathrm{sp}} f_{ijkl}^{\alpha\alpha\beta\beta} M_{i,j}^{-1} M_{k,l}^{-1} \\ & + \frac{1}{6} g_{\mathrm{sp}} f_{ijk}^{\alpha\beta\gamma} f_{lmn}^{\alpha\beta\gamma} M_{i,l}^{-1} M_{j,m}^{-1} M_{m,n}^{-1} \Bigg] . \end{aligned} \tag{10.55}$$

Each of the expressions above involves incomplete Fourier transforms of the inverse matrix $\mathbf{M}^{-1}$. According to Ref. [109], the elements are given by a symmetric function, defined as

$$d_{\pm}(m-n) = \sum_{i,j=1}^{2r-1} w^{im} w^{jn} M_{i,j}^{-1} = \frac{\kappa_{\mathrm{sp}}}{2r} \left[\frac{(-1)^{m-n}}{R_1+R_2} \pm d_2(m-n) \frac{R_1-R_2}{R_1 R_2} + \frac{d_3(m-n)}{4R_{\mathrm{eff}}} \right] , \tag{10.56}$$

where the auxiliary functions $d_{2,3}(k)$ are defined by

$$d_2(k) = \begin{cases} r-k & \text{for } k \text{ odd} \\ 0 & \text{else} \end{cases} , \qquad d_3(k) = \frac{1}{3}\left(4r^2 - 12kr + 6k^2 - 1\right) - (-1)^k . \tag{10.57}$$

Of particular importance are the diagonal entries, which are given by

$$d(0) = \frac{\kappa_{\mathrm{sp}}}{6rR_{\mathrm{eff}}}(r^2 + 3u - 1) , \tag{10.58}$$

where we introduced the geometry parameter $u = R_{\mathrm{eff}}/(R_1 + R_2)$. Before we proceed with the evaluation of Eq. (10.55), we note that we can use several results already derived for the dielectric spheres. The expressions involving derivatives with respect to f do not depend on the material of the sphere. A detailed discussion in Ref. [109] showed that they are proportional to $d(0)$ and given by

$$-\frac{1}{4} f_{ijkl}^{\alpha\alpha\beta\beta} M_{ij}^{-1} M_{kl}^{-1} + \frac{1}{6} f_{ijk}^{\alpha\beta\gamma} f_{lmn}^{\alpha\beta\gamma} M_{il}^{-1} M_{jm}^{-1} M_{kn}^{-1} = \frac{2\mathcal{K}^2}{\kappa_{\mathrm{sp}}^4}(2r-1) d(0) . \tag{10.59}$$

The function g also consists of two parts (10.8), where only the functions $\rho_{p,p'}^{(t)}$ explicitly take the bi-isotropy of the spherical particles into account. The remaining part, which includes the translation coefficient, is the same as for dielectric objects. We thus separate the derivatives of g_{ij} into two contributions

$$g_{ij} = g_{ij}^{(a)} + g_{ij}^{(b)} , \tag{10.60}$$

where we omitted the superscript '$\alpha\alpha$' for convenience. The first part indicated by the superscript (a) accounts for the derivatives which do not depend on the character of the spheres and given by

$$g_{ij}^{(a)} = \left(\prod_{j=1}^{r} \frac{\mathrm{e}^{-(\kappa_{2j}+\kappa_{2j-1})L}}{\kappa_{2j}\kappa_{2j-1}} \right)_{ij} \sum_{p_1,\dots,p_{2r}} \prod_{j=1}^{r} r^{(1)}_{p_{2j+1},p_{2j}} r^{(2)}_{p_{2j},p_{2j-1}} . \tag{10.61}$$

It was found in Ref. [109], that this expression is proportional to g evaluated at the saddle

$$g_{ij}^{(a)} M_{i,j}^{-1} = -g_{\mathrm{sp}} \frac{2r \left[L\kappa_{\mathrm{sp}}(\kappa_{\mathrm{sp}}^2 + \mathcal{K}^2) + 2\mathcal{K}^2 \right]}{\kappa_{\mathrm{sp}}^4} d(0) . \tag{10.62}$$

The second part, with the superscript (b) accounts for derivatives of $\rho^{(t)}_{p,p'} = \rho^{(t)}_{p,p'}(\mathbf{k},\mathbf{k}')$

$$g_{ij}^{(b)} = \frac{\mathrm{e}^{-2r\kappa_{\mathrm{sp}}L}}{\kappa_{\mathrm{sp}}^{2r}} \left(\sum_{p_1,\dots,p_{2r}} \prod_{j=1}^{r} \rho^{(1)}_{p_{2j+1},p_{2j}} \rho^{(2)}_{p_{2j},p_{2j-1}} \right)_{ij} . \tag{10.63}$$

Single derivatives at either one of the parts of g evaluated at the saddle point vanish due to the symmetry character, which we discussed earlier. The distinction between the two different parts of the next-to-leading-order corrections, allows us to write

$$[\mathrm{tr}\mathcal{M}^r]_{\mathrm{NTLO}} = [\mathrm{tr}\mathcal{M}^r]^{(i)}_{\mathrm{NTLO}} + [\mathrm{tr}\mathcal{M}^r]^{(ii)}_{\mathrm{NTLO}} , \tag{10.64}$$

where the part denoted with the superscript (i) accounts for the terms which do not depend on the material of the sphere and is together with (10.59) and (10.62) given by

$$[\mathrm{tr}\mathcal{M}^r]^{(i)}_{\mathrm{NTLO}} = -\frac{\pi}{6r^2} \int \frac{\mathrm{d}^2\mathbf{k}_{\mathrm{sp}}}{(2\pi)^2} \kappa_{\mathrm{sp}}^{2r-4} g_{\mathrm{sp}} \left[rL\kappa_{\mathrm{sp}}(\kappa_{\mathrm{sp}}^2 + \mathcal{K}^2) + \mathcal{K}^2 \right] (r^2 + 3u - 1) . \tag{10.65}$$

The corresponding contribution to the free energy follows by summing over all round-trips r, which allows us to evaluate different polarisation combinations in g_{sp} by introducing the same generating functions as in the previous Section. We thus find that the NTLO contribution of the Casimir free energy yields

$$\mathcal{F}^{(i)}_{\mathrm{NTLO}}(\xi) = \frac{\pi}{6} \int \frac{\mathrm{d}^2\mathbf{k}_{\mathrm{sp}}}{(2\pi)^2} \frac{1}{\kappa_{\mathrm{sp}}^4} \left\{ L\kappa_{\mathrm{sp}}(\kappa_{\mathrm{sp}}^2 + \mathcal{K}^2) \left[\mathcal{P}_0 + (3u-1)\mathcal{P}_2 \right] + \mathcal{K}^2 \left[\mathcal{P}_1 + (3u-1)\mathcal{P}_3 \right] \right\} , \tag{10.66}$$

where $\mathcal{P}_n$ account for the earlier introduced generating functions, which is given by

$$\mathcal{P}_n = \mathrm{Li}_n(\lambda_1) + \mathrm{Li}_n(\lambda_2) , \tag{10.67}$$

with the eigenvalues $\lambda_{1,2}$ of the round-trip matrix in the geometrical optics limit, defined in Eq. (10.39)

For dielectric spheres, the result above agrees with Eq. (6.62) of Ref. [109].

Part (ii) of Eq. (10.64) accounts for $g_{ij}^{(b)}$ and is thus given by

$$[\mathrm{tr}\mathcal{M}^r]^{(ii)}_{\mathrm{NTLO}} = \frac{\pi R_{\mathrm{eff}}}{2r} \int \frac{\mathrm{d}^2\mathbf{k}_{\mathrm{sp}}}{(2\pi)^2} \kappa_{\mathrm{sp}}^{2r-1} g_{ij}^{(b)} M^{-1}_{i,j} \,. \tag{10.68}$$

Together with (10.63) and the Fourier transformed matrix elements (10.56), we can express $g_{ij}^{(b)} M^{-1}_{i,j}$ as follows

$$\begin{aligned} g_{ij}^{(b)} M^{-1}_{i,j} &= \frac{\mathrm{e}^{-2r\kappa_{\mathrm{sp}}L}}{\kappa_{\mathrm{sp}}^{2r}} \sum_{p_1,\dots,p_{2r}} \sum_{i,j=1}^{2r-1} M^{-1}_{ij} \sum_{\alpha=x,y} \frac{\partial^2}{\partial v_{i,\alpha} \partial v_{j,\alpha}} \left(\prod_{j=1}^{r} \rho^{(1)}_{p_{2j+1},p_{2j}} \rho^{(2)}_{p_{2j},p_{2j-1}} \right) \\ &= \frac{\mathrm{e}^{-2r\kappa_{\mathrm{sp}}L}}{\kappa_{\mathrm{sp}}^{2r}} \sum_{p_1,\dots,p_{2r}} \sum_{m,n=0}^{2r-1} d_\sigma(m-n) \sum_{\alpha=x,y} \frac{\partial^2}{\partial k_{m,\alpha} \partial k_{n,\alpha}} \left(\prod_{j=1}^{r} \rho^{(1)}_{p_{2j+1},p_{2j}} \rho^{(2)}_{p_{2j},p_{2j-1}} \right) . \end{aligned} \tag{10.69}$$

The evaluation of the above-given expression is quite technical. We thus only outline the general approach in the following. We refer to Appendix F for details on the calculation. We can identify two distinct contributions in the sum provided above, which are denoted by I and J in the following and thus lead to $g_{ij}^{(b)} M^{-1}_{i,j} = I + J$. In Fig. 10.4, we illustrated the two cases for $r = 4$ round-trips.

Case I accounts for all derivatives of the form $\partial^2_{k_i}$, $\partial^2_{k_{i+1}}$ and $\partial^2_{k_{i+1},k_i}$ which are taken with respect to either $\rho^{(1)}_{p,p'}$ or $\rho^{(2)}_{p,p'}$. We can always take both derivatives within the first round-trip, depicted by the two arrows at the top of the diagrams in the left panel of Fig. 10.4. The cyclic character of the summation indices in Eq. (10.69) makes this possible. We then employ a recursive description to account for all polarisation combinations during the r round-trips, where we only have to keep in mind that the incoming wave in the first round-trip and the outgoing wave in the r-th round-trip match. We illustrated this in Fig. 10.4 by separating each circle into two halves, each presenting the polarisation of the incoming and outgoing wave. The colours of the first and last circles must match. As depicted by the black-coloured halves. The discussion of case I is detailed in Sec. F.3 and the contributions to the free energy are given in Eqs. (F.28), (F.38) and (F.40).

The other contribution J involves single derivatives ∂_{k_i} and ∂_{k_j} taken at any point during the r round-trips. Without loss of generality, one derivative is always taken within the first round-trip ($r = 1$), as it is depicted by the arrow at the top of each diagram in the right panel of Fig. 10.4. Again, this is a consequence of the cyclic character of the indices. The second derivative is taken at any other point during the r-round-trips. The derivative can be taken at the same sphere as the first derivative or at the sphere with the other label. Therefore, there are four possible scenarios, as depicted in the right panel of Fig. 10.4. We illustrate the cases where the second derivative is taken within the second round-trip. The two diagrams at the top illustrate the cases where the first derivative is taken at sphere 1 and the second derivative at sphere 1 or sphere 2. The two possibilities are denoted by $J^{(1,1)}$ and $J^{(1,2)}$. We adopted the notation used in Ref. [109], to facilitate the comparison with results obtained for dielectric spheres. Correspondingly, the two diagrams at the bottom of the right panel in Fig. 10.4 represents the case, where the first derivative is taken at sphere 2 while the second one at sphere 1 ($J^{(2,1)}$) or again at sphere 2 ($J^{(2,2)}$). The contribution to the free energy from the case $J^{(2,1)}$ is discussed in Sec. F.4.1, with results given in Eqs. (F.74) and (F.80). Case $J^{(2,2)}$ can be found in Sec. F.4.2 with the final results given in Eqs. (F.91) and (F.93).

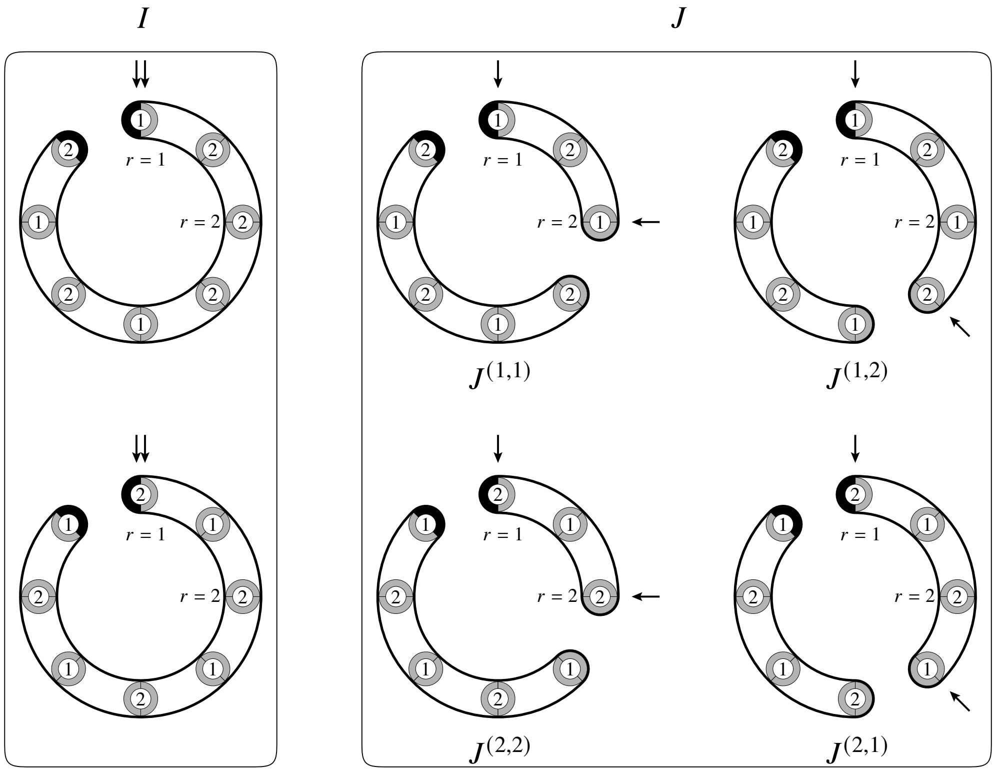

Figure 10.4: Schematic illustration of terms arising in Eq. (10.69) for $r = 4$ round-trips. We start the first round-trip at the top at sphere 1 (2) and continue clockwise. Each sphere is separated into two halves to depict the possible polarisation-mixing, as already done in Fig. 10.3. We assume the incoming wave at sphere 1 (2) at the top to be TM-polarised (black-coloured half). Respectively, the polarisation of the outgoing wave at sphere 2 (1) in the fourth round-trip also has to be TM-polarised (black-coloured half). All kinds of polarisation combinations are possible between the starting and ending points. **Left panel:** Representation of case I, where both derivatives are taken at a single sphere, either at sphere 1 or sphere 2. **Right panel**: Illustration of case J, where the derivatives are taken at different points during the round-trips. We distinguish between four cases, with the first derivatives taken at sphere 1 and the second derivatives either at sphere 1 or 2, respectively denoted by $J^{(1,1)}$ and $J^{(1,2)}$. Similarly, the first derivative can be taken at sphere 2 and the second one either at sphere 2 again or at sphere 1. The two cases are denoted by $J^{(2,2)}$ and $J^{(2,1)}$.

10.3 Large-distance limit, the dipole approximation

In the previous Section, we considered the Casimir interaction for distances smaller than the sphere radii. In this Section, we are going to examine the opposite case, where the sphere radii are small compared to the surface-to-surface separation, and specifically $L \gg R_1$, R_2. Each matrix element of the round-trip matrix scales with $\exp(-2\kappa\mathcal{L})$ from the translation coefficients, hence, for large distances, each round-trip adds an exponential decay, which is why it is usually sufficient to consider only the single-round-trip approximation of the Casimir free energy with $\mathcal{F}(\xi) \approx -\mathrm{tr}\mathcal{M}(\xi)$, according to Eq. (8.2).

Additionally, we assume that the sphere radii are small enough to apply the Rayleigh limit. According to our discussion in Sec. 4.3, the reflection coefficients scale with $(\mathcal{K}R)^{2l+1}$ for small radii. Hence, the dominant contribution arises from the dipolar polarisabilities. Instead of using the plane-wave description for the scattering formula, we are now utilizing the multipole expansion, which we introduced in Sec. 8.3. Combining both the single-round-trip and the dipolar approximation, the Casimir free energy can, according to Eq. (8.10), be written as

$$\mathcal{F}(\xi) \approx -\sum_{m=-1}^{1} \sum_{P=\mathrm{E,M}} M_{P,P}^{(1,m)} \,, \qquad M_{P,P'}^{(1,m)} = \langle 1, m, P | \mathcal{T}_{12} \mathcal{R}_2 \mathcal{T}_{21} \mathcal{R}_1 | 1, m, P \rangle \,, \tag{10.70}$$

where we introduced the matrix elements $M_{P,P'}^{(1,m)}$ of the round-trip matrix in the dipole limit $l = 1$. From the discussion in Sec. 4.3, we obtain the following expression for the Mie reflection coefficients in the dipole limit

$$\langle 1, m, P' | \mathcal{R} | 1, m, P \rangle \approx -\tilde{\xi}^3 \left(\frac{R}{\mathcal{L}} \right)^3 \alpha_{P',P} \,. \tag{10.71}$$

We introduced the reduced frequency $\tilde{\xi} = \mathcal{K}\mathcal{L}$ and the dimensionless polarisability $\alpha_{P',P}$, which according to Eq. (4.51) is given by

$$\alpha_{P',P} = -\mathrm{i}^{P-P'} \frac{2}{3} X_{p',p}(l = 1) \,. \tag{10.72}$$

Recall that we identify $P = \mathrm{E(M)}$ with $p = \mathrm{TM(TE)}$ in the subscripts. For instance, using (4.55) for a PEMC sphere yields the following polarisabilities

$$\alpha_{\mathrm{E,E}} = -\frac{1}{2} \left(\frac{1}{3} + \cos(\theta) \right) , \qquad \alpha_{\mathrm{M,M}} = -\frac{1}{2} \left(\frac{1}{3} - \cos(\theta) \right) , \qquad \alpha_{\mathrm{E,M}} = -\alpha_{\mathrm{M,E}} = \mathrm{i} \frac{\sin(\theta)}{2} \,. \tag{10.73}$$

In the following, we will derive the Casimir free energy for two dipoles and a dipole in front of a plane, which respectively constitutes the large-distance limits of the sphere-sphere and sphere-plane geometry.

10.3.1 Interaction between two dipoles

We start by discussing the interaction between two bi-isotropic dipoles. For the evaluation of the round-trip matrix elements in Eq. (10.70), we employ the translations coefficients introduced in

Eq. (8.13). In the dipolar limit, the polarisation-conserving coefficients yield

$$\langle 1, m, P|\mathcal{T}|1, m, P\rangle = \frac{\mathrm{e}^{-\tilde{\xi}}}{2\tilde{\xi}^3} \begin{cases} 2(1+\tilde{\xi}) & \text{for } m = 0 \\ -(1+\tilde{\xi}+\tilde{\xi}^2) & \text{for } m = \pm 1 \end{cases} \tag{10.74}$$

while we obtain for the polarisation-changing coefficients

$$\langle 1, m, P|\mathcal{T}|1, m, \bar{P}\rangle = \pm \frac{\mathrm{e}^{-\tilde{\xi}}}{2\tilde{\xi}^3}(1+\tilde{\xi}) \quad \text{for } m = \pm 1\,. \tag{10.75}$$

Note that for $m = 0$ the polarisation-changing translation coefficients vanish.

Inserting the reflection and translation coefficients into Eq. (10.70), we find for the diagonal matrix elements of the round-trip matrix

$$M^{(1,0)}_{\mathrm{E,E}} = 9\left(\frac{R_1 R_2}{\mathcal{L}^2}\right)^3 \left(\alpha^{(1)}_{\mathrm{E,E}}\alpha^{(2)}_{\mathrm{E,E}} + \alpha^{(1)}_{\mathrm{E,M}}\alpha^{(2)}_{\mathrm{M,E}}\right)(1+\tilde{\xi})^2 \mathrm{e}^{-2\tilde{\xi}}\,. \tag{10.76}$$

For $m = \pm 1$, on the other hand, the matrix elements are given by

$$\begin{aligned} M^{(1,\pm 1)}_{\mathrm{E,E}} = \frac{9}{4}\left(\frac{R_1 R_2}{\mathcal{L}^2}\right)^3 \Big[&\left(\alpha^{(1)}_{\mathrm{E,E}}\alpha^{(2)}_{\mathrm{E,E}} + \alpha^{(1)}_{\mathrm{E,M}}\alpha^{(2)}_{\mathrm{M,E}}\right)(1+\tilde{\xi}+\tilde{\xi}^2)^2 \\ &- \left(\alpha^{(1)}_{\mathrm{E,E}}\alpha^{(2)}_{\mathrm{M,M}} + \alpha^{(1)}_{\mathrm{E,M}}\alpha^{(2)}_{\mathrm{E,M}}\right)(\tilde{\xi}+\tilde{\xi}^2)^2 \\ &\pm \left(\alpha^{(1)}_{\mathrm{E,E}}\alpha^{(2)}_{\mathrm{E,M}} + \alpha^{(1)}_{\mathrm{E,M}}\alpha^{(2)}_{\mathrm{M,M}}\right)(\tilde{\xi}+\tilde{\xi}^2)(1+\tilde{\xi}+\tilde{\xi}^2) \\ &\mp \left(\alpha^{(1)}_{\mathrm{E,E}}\alpha^{(2)}_{\mathrm{M,E}} + \alpha^{(1)}_{\mathrm{E,M}}\alpha^{(2)}_{\mathrm{E,E}}\right)(\tilde{\xi}+\tilde{\xi}^2)(1+\tilde{\xi}+\tilde{\xi}^2)\Big]\mathrm{e}^{-2\tilde{\xi}}\,, \end{aligned} \tag{10.77}$$

where the first term accounts for the channels, where the polarisation in both directions is conserved, while for the other three terms, in at least one propagation direction, the polarisation is changing.

The matrix elements for the magnetic modes $M^{(1,m)}_{\mathrm{M,M}}$ are obtained by replacing E with M and vice versa in the respective expressions for $m = 0$ and $m = \pm 1$. We concentrate on the case where the coefficients $\alpha_{P,P'}$ are not frequency dependent. We can thus directly carry out the sum over Matsubara frequencies for the Casimir free energy $\mathcal{F} = k_\mathrm{B}T\sum_{n=0}^{\prime\infty}\mathcal{F}(\xi_n)$. The Matsubara sum involves expressions of the form $\sum_{n=0}^{\prime\infty} n^s \mathrm{e}^{-2\nu n}$, with the dimensionless temperature ν given by

$$\nu = \frac{2\pi\mathcal{L}}{\lambda_T} \tag{10.78}$$

with the thermal wave length $\lambda_T = \hbar c/k_\mathrm{B}T$. The Matsubara sum can be evaluated by taking derivatives with respect to n, we can thus write $\sum_{n=0}^{\prime\infty} n^s \mathrm{e}^{-2\nu n} = \delta_{s,0}/2 + (-1)^s \partial_{2\nu}(\mathrm{e}^{2\nu}-1)^{-1}$. Within the dipole-dipole (dip) limit, the Casimir free energy yields

$$\begin{aligned} \mathcal{F}_{\text{dip-dip}} = -\frac{9\hbar c}{2\pi\mathcal{L}}\left(\frac{R_1 R_2}{\mathcal{L}^2}\right)^3 \Bigg\{ &\left[\alpha^{(1)}_{\mathrm{E,E}}\alpha^{(2)}_{\mathrm{E,E}} + \alpha^{(1)}_{\mathrm{E,M}}\alpha^{(2)}_{\mathrm{M,E}} + \alpha^{(1)}_{\mathrm{M,M}}\alpha^{(2)}_{\mathrm{M,M}} + \alpha^{(1)}_{\mathrm{M,E}}\alpha^{(2)}_{\mathrm{E,M}}\right]\frac{f_{P\leftrightarrow P}(\nu)}{5} \\ - &\left[\alpha^{(1)}_{\mathrm{E,E}}\alpha^{(2)}_{\mathrm{M,M}} + \alpha^{(1)}_{\mathrm{E,M}}\alpha^{(2)}_{\mathrm{E,M}} + \alpha^{(1)}_{\mathrm{M,M}}\alpha^{(2)}_{\mathrm{E,E}} + \alpha^{(1)}_{\mathrm{M,E}}\alpha^{(2)}_{\mathrm{M,E}}\right]\frac{f_{P\leftrightarrow\bar{P}}(\nu)}{4}\Bigg\}\,, \end{aligned} \tag{10.79}$$

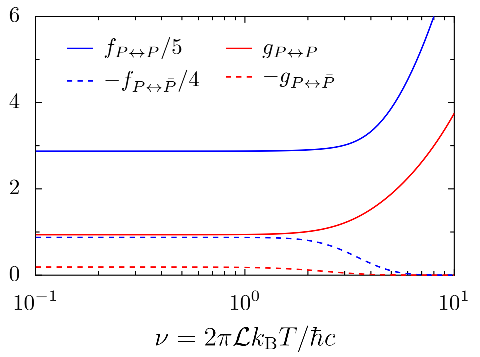

Figure 10.5: Temperature dependence of the polarisation-conserving ($P \leftrightarrow P$) and polarisation-changing scattering channels ($P \leftrightarrow \bar{P}$). The contributions are shown for both the dipole-dipole ($f(\nu)$) and dipole-plane ($g(\nu)$) geometry as function of the dimensionless temperature ν.

where the function $f_{P\leftrightarrow P}(\nu)$ accounts for the polarisation-conserving channels upon translation and is defined as

$$f_{P\leftrightarrow P}(\nu) = \frac{5}{8}\left[6g(\nu)\cosh(\nu) + 6g^2(\nu) + 5g^3(\nu)\cosh(\nu) + g^4(\nu)(1+2\cosh^2(\nu)) \right. \\ \left. + g^5(\nu)\cosh(\nu)(2+\cosh^2(\nu))\right] , \tag{10.80}$$

where we adapted the notation from [206], with

$$g(\nu) = \frac{\nu}{\sinh(\nu)} . \tag{10.81}$$

Correspondingly, the function $f_{P\leftrightarrow \bar{P}}(\nu)$ results from the channels, where the polarisation changes during translation and is defined by

$$f_{P\leftrightarrow \bar{P}}(\nu) = \frac{1}{2}\left[g^3(\nu)\cosh(\nu) + g^4(\nu)(1+2\cosh^2(\nu)) + g^5(\nu)\cosh(\nu)(2+\cosh^2(\nu))\right] . \tag{10.82}$$

First we remark that $f_{P\leftrightarrow P}$ and $f_{P\leftrightarrow \bar{P}}$ both can also be obtained by combining Eqs. (42)-(46) in Ref. [206]. Both functions are positive for all temperatures and $f_{P\leftrightarrow P}(\nu) > f_{P\leftrightarrow \bar{P}}(\nu)$ for all ν as can be seen in Fig. 10.5. The polarisation-conserving channel monotonically increases with temperature from $f_{P\leftrightarrow P}(\nu=0)/5 = 23/8$ in the quantum regime to $f_{P\leftrightarrow P}(\nu\to\infty)/5 = 6/8\nu$ in the classical limit. In contrast, the polarisation-mixing channel monotonically decreases from $f_{P\leftrightarrow \bar{P}}(\nu=0)/4 = 7/8$ to zero in the high-temperature limit. If the cross-polarisabilities vanish $\alpha_{P,\bar{P}} = 0$, the zero-temperature limit of (10.79) reproduces the well-known result from Ref. [207] for the van-der-Waals interaction between two polarisable systems.

10.3.2 Dipole interacting with a planar surface

Next, we determine the Casimir free energy for a dipole and plane. Without loss of generality, we assume that the operator $\mathcal{R}_1$ accounts for the spherical object, while $\mathcal{R}_2$ describes a planar surface. Introducing the reflection coefficients (10.71) for the dipole in Eq. (10.70), the elements of the round-trip matrix read

$$M^{(1,m)}_{P,P} = -\tilde{\xi}^3\left(\frac{R}{\mathcal{L}}\right)^3 \sum_{P'=\mathrm{E,M}} U^{(1,m)}_{P,P'}\alpha^{(1)}_{P',P} , \qquad U^{(1,m)}_{P,P'} = \langle 1,m,P|\mathcal{T}_{12}\mathcal{R}_2\mathcal{T}_{21}|1,m,P'\rangle , \tag{10.83}$$

where we introduced $U^{(1,m)}_{P,P'}$, which account for the matrix elements of the translation operators and the reflection operator at the plane. Instead of using the spherical-wave basis, it is more convenient to derive the matrix elements in the plane-wave basis. Making use of the diagonality of the translations coefficients (8.8), we obtain

$$U^{(1,m)}_{P,P'} = \sum_{p_1,p_2=\mathrm{TE},\mathrm{TM}} \int \frac{\mathrm{d}^2\mathbf{k}}{(2\pi)^2} \mathrm{e}^{-2\kappa\mathcal{L}} r^{(2)}_{p_1,p_2} \langle 1,m,P|\mathbf{k},p_2,+\rangle \langle \mathbf{k},p_1,-|1,m,P'\rangle \tag{10.84}$$

with the Fresnel reflection coefficients $r^{(2)}_{p',p}$ for a bi-isotropic plane (see Eq. (B.11)). We assume that the Fresnel coefficients are constants, as it is the case for the reflection coefficient for a PEMC plane in Eq. (4.34). We can then directly evaluate the integral given above by using the basis conversion coefficients defined in Eqs. (4.22) and (4.23). We exemplify the calculation for $U^{(1,0)}_{\mathrm{E},\mathrm{E}}$. For $m = 0$ and $P = \mathrm{E} = P'$, the sum over p_1 and p_2 only yields a contribution for $p_1 = \mathrm{TM} = p_2$ and the polarisation-changing coefficient yield $\langle 1,0,\mathrm{E}|\mathbf{k},\mathrm{TM},+\rangle = \mathrm{i}\sqrt{6\pi}\sin\theta_K$ and $\langle \mathbf{k},\mathrm{TM},-|1,0,\mathrm{E}\rangle = \mathrm{i}\sqrt{3\pi/2}\sin\theta_K/\kappa\mathcal{K}$. Making use of $\sin(\theta_K) = -\mathrm{i}k/\mathcal{K}$ for imaginary frequencies the integral over the transverse wave vector yields

$$U^{(1,0)}_{\mathrm{E},\mathrm{E}} = \frac{3}{2} r^{(2)}_{\mathrm{TM},\mathrm{TM}} \int_{\mathcal{K}}^{\infty} \frac{\mathrm{d}\kappa}{\mathcal{K}} \left[\frac{\kappa^2}{\mathcal{K}^2} - 1\right] \mathrm{e}^{-2\kappa\mathcal{L}}\,, \tag{10.85}$$

where we transformed the integral into polar coordinates and substituted the transverse wave vector with the axial wave vector component $\kappa = \sqrt{\mathcal{K}^2 + \mathbf{k}^2}$. A similar expression can also be obtained for $U^{(1,0)}_{\mathrm{E},\mathrm{M}}$ and we find

$$U^{(1,0)}_{\mathrm{E},\mathrm{E}} = \frac{3}{2}(I_2(\tilde{\xi})) - I_0(\tilde{\xi}))r^{(2)}_{\mathrm{TM},\mathrm{TM}}\,, \qquad U^{(1,0)}_{\mathrm{E},\mathrm{M}} = \mathrm{i}\frac{3}{2}(I_2(\tilde{\xi})) - I_0(\tilde{\xi}))r^{(2)}_{\mathrm{TM},\mathrm{TE}} \tag{10.86}$$

with the following integral

$$I_n(\tilde{\xi}) = \int_1^{\infty} x^n \mathrm{e}^{-2\tilde{\xi}x}\mathrm{d}x = (-1)^n \left(\frac{d^n}{dz^n}\frac{\mathrm{e}^{-z}}{z}\right)_{z=2\tilde{\xi}}\,. \tag{10.87}$$

The coefficients $U_{\mathrm{M},\mathrm{M}}$ and $U_{\mathrm{M},\mathrm{E}}$ can be respectively obtained by replacing the Fresnel reflection coefficient $r_{\mathrm{TM},\mathrm{TM}}$ with $r_{\mathrm{TE},\mathrm{TE}}$ and $r_{\mathrm{TM},\mathrm{TE}}$ with $-r_{\mathrm{TM},\mathrm{TE}}$. Similar calculations can be performed for $m = \pm 1$, yielding

$$U^{(1,\pm1)}_{\mathrm{E},\mathrm{E}} = \frac{3}{4}\left[I_2 r^{(2)}_{\mathrm{TM},\mathrm{TM}} \mp \mathrm{i}I_1(r^{(2)}_{\mathrm{TM},\mathrm{TE}} + r^{(2)}_{\mathrm{TE},\mathrm{TM}}) - I_0 r^{(2)}_{\mathrm{TE},\mathrm{TE}}\right], \tag{10.88a}$$

$$U^{(1,\pm1)}_{\mathrm{E},\mathrm{M}} = \frac{3}{4}\left[\mp I_1 r^{(2)}_{\mathrm{TM},\mathrm{TM}} + \mathrm{i}I_0 r^{(2)}_{\mathrm{TE},\mathrm{TM}} + \mathrm{i}I_2 r^{(2)}_{\mathrm{TM},\mathrm{TE}} \pm I_1 r^{(2)}_{\mathrm{TE},\mathrm{TE}}\right]. \tag{10.88b}$$

After introducing the coefficients $U^{(1,m)}_{P,P'}$ into Eq. (10.83) and summing over the Matsubara frequencies, as we did before for the dipole-dipole limit, we find for the Casimir free energy between a dipole and plane

$$\begin{aligned}\mathcal{F}_{\text{dip-plane}} = -\frac{\hbar c}{2\pi\mathcal{L}}\left(\frac{R}{\mathcal{L}}\right)^3 \Bigg\{ &- \left[\alpha^{(1)}_{\mathrm{E,E}} r^{(2)}_{\mathrm{TM,TM}} + \alpha^{(1)}_{\mathrm{M,M}} r^{(2)}_{\mathrm{TE,TE}} + \mathrm{i}\alpha^{(1)}_{\mathrm{M,E}} r^{(2)}_{\mathrm{TM,TE}} - \mathrm{i}\alpha^{(1)}_{\mathrm{E,M}} r^{(2)}_{\mathrm{TE,TM}}\right] g_{P\leftrightarrow P}(\nu) \\ &+ \left[\alpha^{(1)}_{\mathrm{E,E}} r^{(2)}_{\mathrm{TE,TE}} + \alpha^{(1)}_{\mathrm{M,M}} r^{(2)}_{\mathrm{TM,TM}} - \mathrm{i}\alpha^{(1)}_{\mathrm{M,E}} r^{(2)}_{\mathrm{TE,TM}} + \mathrm{i}\alpha^{(1)}_{\mathrm{E,M}} r^{(2)}_{\mathrm{TM,TE}}\right] g_{P\leftrightarrow \bar{P}}(\nu) \Bigg\} .\end{aligned} \tag{10.89}$$

The coefficients $g_{P\leftrightarrow P}(\nu)$ and $g_{P\leftrightarrow \bar{P}}(\nu)$ are respectively describing the polarisation-conserving and -mixing channels. They are defined by

$$g_{P\leftrightarrow P}(\nu) = \frac{3}{16}\left[2g(\nu)\cosh(\nu) + 2g^2(\nu) + g^3(\nu)\cosh(\nu)\right] , \tag{10.90a}$$

$$g_{P\leftrightarrow \bar{P}}(\nu) = \frac{3}{16} g^3(\nu)\cosh(\nu) . \tag{10.90b}$$

The functions behave in the same way as their counterparts in the dipole-dipole limit (see Fig. 10.5), with the zero-temperature limit given by $g_{P\leftrightarrow P}(\nu = 0) = 15/16$ and $g_{P\leftrightarrow \bar{P}}(\nu = 0) = 3/16$ while the polarisation-conserving channel yields $3\nu/8$ for high temperatures, and the mixing channel goes to zero.

The different temperature dependence of the scattering channels suggests that, in some instances, the interaction changes with temperature, which we will examine in the next Chapter for the case of perfect electromagnetic conductors in detail.

11 | Application to perfect electromagnetic conductor spheres

Most of the results presented in this Chapter can be found in Refs. [101, 208] and thus also contains input from authors of these articles.

After providing general expressions for the scattering formalism of two spherical objects, we have studied several model systems in various limiting cases in the previous Chapters 9 and 10. From high-temperature results to small- and large-distance expansions of the Casimir free energy. In this Chapter, we apply our findings to a particular system of bi-isotropic objects, namely two perfect electromagnetic conductor (PEMC) spheres in a vacuum. The lossless and frequency-independent boundary conditions of PEMCs are characterized by a duality angle θ, defined in Eq. (1.6). The parameter tunes the electromagnetic response of the object from a perfect electric (PEC) to a perfect magnetic (PMC) conductor by taking values between 0 and $\pi/2$. This idealized model allows us to disentangle the interplay between geometry, boundary conditions and temperature. Already Rode *et al.* have shown in Ref. [56] that the Casimir interaction between two PEMC planes at zero temperature only depends on the difference between the duality angles

$$\delta = |\theta_1 - \theta_2| \,. \tag{11.1}$$

The Casimir interaction changes its sign as a function of δ from attraction to repulsion, as illustrated in the left panel in Fig. 11.1. The force thus vanishes at a certain δ_{crit}. In this Chapter, we want to discuss whether this dependence of the Casimir force on δ still holds for spherical objects and whether δ_{crit} changes for spherical objects at finite temperature. We thus analyse the Casimir interaction in the whole parameter range of different temperatures and distances between the spheres. A schematic of the Chapter outline can be found in the right panel of Fig. 11.1. We provide explicit analytical results for several limiting cases based on the expressions derived in the previous Chapters. For intermediate distance- and temperature-ranges, we resort to numerical calculations. Our numerical calculations are based on an extension of the numerical approach introduced in Ref. [171] to bi-isotropic spheres.

We start in Sec. 11.1 with the short distance limit, which is equivalent to the PFA, and we derive temperature corrections to the quantum vacuum energy derived in Ref. [56]. Going beyond the PFA gives insights into how the curvature of the spheres affects the sign of the Casimir force. By increasing the distance even further, we end up in the dipole-dipole or dipole-plane regime (Sec. 11.2), where we again discuss the Casimir interaction for arbitrary temperatures. Of particular interest will be the high-temperature limit, discussed in Sec. 11.3, where we introduce an approximation formula for the whole distance range. In Sec. 11.4, we show that a sum rule found by Rode *et al.* in Ref. [56] for two planes is no longer valid when considering the Casimir interaction between spherical objects. We summarize our findings in Sec. 11.5, where we analyse the existence of stable equilibrium positions of the spheres and how changing the temperature affects the equilibrium.

11.1 Short-distance asymptotics, the PFA regime

In this Section, we are going to discuss the Casimir interaction between two PEMC spheres at short distances compared to the radii of the spheres. Earlier, we derived an expression for the Casimir free

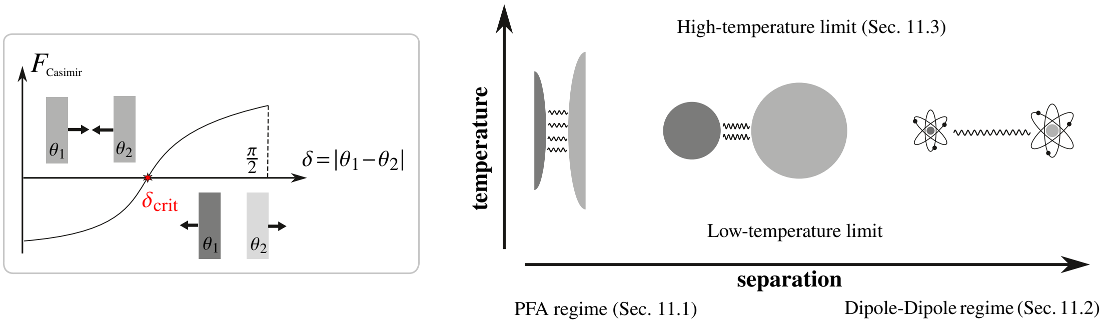

Figure 11.1: Left panel: Schematic illustration of the Casimir force between two PEMC planes characterized by the parameters $\theta_1, \theta_2 \in [0, \pi/2]$, as function of the difference $\delta = |\theta_1 - \theta_2|$. While δ increases from 0 to $\pi/2$, the force transitions from attraction to repulsion. The force vanishes at δ_{crit}. **Right panel:** Overview of the limiting cases for the Casimir interaction between two PEMC spheres, which we discuss in the Sections of this Chapter. We start in Sec. 11.1 with the short-distance limit, where low- and high-temperature results are presented. In Sec. 11.2, we analyse the opposite side of the distance spectrum by considering small spheres at large separations. High-temperature results over the whole distance range are discussed in Sec. 11.3.

energy for arbitrary bi-isotropic spheres (10.40), in terms of the eigenvalues of the round-trip matrix for two planar objects. Together with the Fresnel reflection coefficients for PEMC planes (4.34), are the eigenvalues of the round-trip matrix (10.39) given by

$$\lambda_{1/2} = \exp(\pm 2\mathrm{i}\delta)\exp(-2\kappa L)\,. \tag{11.2}$$

The eigenvalues only depend on the difference between the PEMC parameters θ_1 and θ_2 via δ introduced above in Eq. (11.1), as it was already expected from the result for two PEMC planes in Ref. [56]. Inserting the eigenvalues in the PFA expression (10.40) and transforming the integral over the transverse wave vector into an integral over the axial wave component with $\kappa = \sqrt{\xi^2/c^2 + k^2}$, we obtain

$$\begin{aligned} \mathcal{F}_{\text{PFA}}(\xi) &= -R_{\text{eff}}\text{Re}\int_{\xi/c}^{\infty} \mathrm{d}\kappa \sum_{r=1}^{\infty} \frac{1}{r^2} \mathrm{e}^{2\mathrm{i}\delta r}\mathrm{e}^{-2\kappa L r} \\ &= -\frac{1}{2x}\text{Re}\sum_{r=1}^{\infty}\frac{1}{r^3}\mathrm{e}^{2\mathrm{i}\delta r}\mathrm{e}^{-2\xi L r/c}\,. \end{aligned} \tag{11.3}$$

Note that we omitted the index 'sp' for the integral along the saddle in Eq. (10.40). We carried out the integral in the second step and introduced the aspect ratio $x = L/R_{\text{eff}}$. The expression above constitutes the frequency contribution to the Casimir free energy. It allows us to calculate the Casimir interaction at any temperature.

At zero temperature, the Casimir energy is given by an integral over imaginary frequencies (2.26) $\mathcal{E}_{\text{PFA}} = (\hbar/2\pi)\int_0^\infty \mathrm{d}\xi\mathcal{F}(\xi)$, which yields

$$\mathcal{E}_{\text{PFA}} = -\frac{\hbar c}{8\pi x L}\text{Re}\text{Li}_4(\mathrm{e}^{2\mathrm{i}\delta}) = -\frac{\hbar c}{720\pi L x}\left[\pi^4 - 30\delta^2(\pi-\delta)^2\right]\,. \tag{11.4}$$

We simplified the real part of the polylogarithm $\text{Li}_4(\mathrm{e}^{2\mathrm{i}\delta})$ by means of the Jonquiere inversion formula [185, Eq. 25.12.13]

$$\text{Li}_n(\mathrm{e}^{2\pi\mathrm{i}x}) + (-1)^n\text{Li}_n(\mathrm{e}^{2\pi\mathrm{i}x}) = -(2\pi\mathrm{i})^n B_n(z)/n!\,, \tag{11.5}$$

with the Bernoulli polynomials $B_n(z)$ of order n. We could thus reproduce the result obtained by [56] for two PEMC planes at zero temperature. For $\delta = 0$ the expression agrees with the well-known result obtained by Casimir [5] $\mathcal{E}_{\text{PFA}} = -\hbar c\pi R_{\text{eff}}/720L^2$. Note also, that the Casimir energy for two perfect electric conductors agrees with the sum of the Casimir energy for a scalar field confined between two planes with Dirichlet and Neumann boundary conditions. For $\delta = \pi/2$, on the other hand, we obtain the result by Boyer [43] for a PEC and PMC plane, with $\mathcal{E}_{\text{PFA}} = 7\hbar c\pi R_{\text{eff}}/5760L^2$. This result is equivalent to the one for a scalar field between two planes, one with Neumann and the other plane with Dirichlet boundary conditions and vice versa. The transition from Dirichlet to Neumann boundary conditions can be parameterized by so-called quasi-periodic boundaries [209], which lead to the same result as (11.4). Earlier works found that the PFA result and the leading corrections for an electromagnetic field between perfect reflectors correspond to expressions for scalar fields [210]. We will later also show that this still holds for PEMCs at finite temperatures.

The Casimir energy and due to $F_{\text{PFA}} = -\partial_L\mathcal{E}_{\text{PFA}} = 2\mathcal{E}_{\text{PFA}}/L$ also the Casimir force, changes its sign at a critical angle δ_{crit}, which can be computed analytically and is given by

$$\delta_{\text{crit}}^{T=0} = \left(1 - \sqrt{1 - \sqrt{\frac{2}{15}}}\right)\frac{\pi}{2} = 0.961\ldots\frac{\pi}{4}\,. \tag{11.6}$$

Here and in the following, it is convenient to express critical angles in units of the central angle $\pi/4$. The force thus changes its sign at δ_{crit} and is attractive for systems with $\delta < \delta_{\text{crit}}$ while being repulsive for $\delta > \delta_{\text{crit}}$. In the following, we are going to determine the temperature and distance corrections to the PFA result (11.4) and analyse how δ_{crit} changes when we increase the temperature or the separation between the spheres.

11.1.1 Temperature corrections to the zero-temperature result

The Casimir free energy at finite temperatures follows from the sum over the Matsubara frequencies (8.1) and yields together with (11.3)

$$\mathcal{F}_{\text{PFA}} = -\frac{k_{\text{B}}T}{2x}\text{Re}{\sum_{n=0}^{\infty}}'\sum_{r=1}^{\infty}\frac{1}{r^3}\mathrm{e}^{2\mathrm{i}\delta r}\mathrm{e}^{-2\tau nr}\,, \tag{11.7}$$

where we introduced the dimensionless temperature $\tau = 2\pi L/\lambda_T$. We are interested in the low-temperature corrections to (11.4) and thus analyse the expression above in the regime $L \ll \lambda_T \ll R_{\text{eff}}$. The convergence of (11.7) is either ensured by the oscillatory function or the exponentially decaying function, depending on $\delta > \tau$ or $\delta < \tau$. We are particularly interested in the temperature dependence of δ_{crit}, so we will focus on the case where $\delta > \tau$. We employ the Mellin transform for exponential functions [185, Eq. 8.6.11] $\exp(z) = \int_{c-\mathrm{i}\infty}^{c+\mathrm{i}\infty}\Gamma(s)z^{-s}ds/(2\pi\mathrm{i})$ to extract the leading temperature corrections. After carrying out the Matsubara and round-trip sum, we obtain

$$\mathcal{F}_{\text{PFA}} = -\frac{k_{\text{B}}T}{4x}\left[\text{Re}\left[\text{Li}_3(\mathrm{e}^{2\mathrm{i}\delta})\right] + 2\int_{c-\mathrm{i}\infty}^{c+\mathrm{i}\infty}\frac{\mathrm{d}s}{2\pi\mathrm{i}}\Gamma(s)\zeta(s)\text{Re}\left[\text{Li}_{s+3}(\mathrm{e}^{2\mathrm{i}\delta})\right](4\tau)^{-s}\right]. \tag{11.8}$$

The integration contour in the complex s-plane is chosen such that c is larger than one. For $\delta > 0$, the integrand has a single pole at $s = 1$ arising from the Riemann zeta function $\zeta(s)$. Additionally,

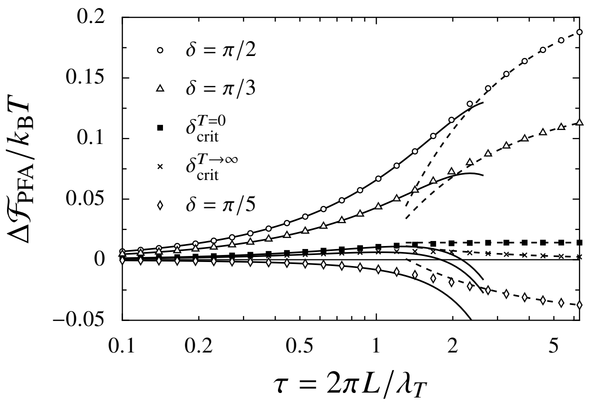

Figure 11.2: Low-temperature expansion of the PFA result. Temperature corrections to the zero-temperature result of the Casimir free energy in units of $k_{\mathrm{B}}T$ for various values of δ, including the critical angles in the low-temperature (filled squares) and high-temperature (crosses) limit, respectively defined in Eqs. (11.6) and (11.11). The solid lines represent the low-temperature expansion given in Eq. (11.9), while the dashed lines depict the difference between the high-temperature result (11.10) and the zero-temperature Casimir energy. Adapted from [208].

there are single poles at $s = 0$ and at all negative odd integers $s = -2n - 1$, $n = 0, 1, 2, \ldots$ which originate from the gamma function $\Gamma(s)$. We will discuss this case in more detail later. We carry out the integral by applying the Cauchy theorem and evaluating the residues at the respective poles. Note that the zero-temperature result (11.4) arises from the pole at $s = 1$, while the others contribute to the low-temperature corrections. We find for the first two leading terms

$$\Delta\mathcal{F}_{\mathrm{PFA}} = \mathcal{F}_{\mathrm{PFA}} - \mathcal{E}_{\mathrm{PFA}} \approx -\frac{\hbar c R_{\mathrm{eff}}}{720\pi L^2}\left[5\left(\pi^2 - 6\delta(\pi-\delta)\right)\tau^2 + \tau^4 + O(\tau^6)\right], \tag{11.9}$$

where we again applied the Jonquiere's relation (11.5) to express the dilogarithm $\mathrm{Li}_2(\mathrm{e}^{2\mathrm{i}\delta})$ arising from the $s = -1$ pole as a polynomial in δ. The limit $\delta = \pi/2$ agrees with the low-temperature expansion performed in Ref. [210]. We compared the asymptotic expansion with numerical calculations in Fig. 11.2 of the free energy in the low-temperature regime. We analysed several values of δ including the critical value (11.6), which is depicted with filled symbols compared to the other values of δ. It is evident from Fig. 11.2 that with decreasing temperature $\tau < 1$, the numerical results converge towards the expansion (11.9), which is depicted by solid lines.

The non-vanishing and positive temperature corrections for $\delta^{T=0}_{\mathrm{cri}}$ indicate that the critical angle decreases with temperature, which is corroborated by analysing the high-temperature limit of the Casimir free energy. The high-temperature result is obtained by taking the zero-frequency ($n = 0$) term in Eq. (11.3), yielding

$$\mathcal{F}_{T,\mathrm{PFA}} = -\frac{k_{\mathrm{B}}T}{4x}\mathrm{Re}\left[\mathrm{Li}_3(\mathrm{e}^{2\mathrm{i}\delta})\right] . \tag{11.10}$$

It implies that the Casimir force vanishes at a critical value

$$\delta^{T\to\infty}_{\mathrm{crit}} = 0.923\ldots\frac{\pi}{4} < \delta^{T=0}_{\mathrm{crit}} , \tag{11.11}$$

which we determined numerically. The high-temperature result is also depicted in Fig. 11.2 with dashed lines. The numerical results converge towards the high-temperature results for $\tau > 2$.

A clearer picture of temperature- and material-dependence of the Casimir force can be obtained from Fig. 11.3, where we analyse the Casimir force for two PEMC spheres relative to the result for two PEC ($\delta = 0$) spheres. The Casimir interaction between two PEC spheres is always attractive. Hence, a negative value of the force ratio accounts for a repulsive force, as shown by the orange-shaded area in Fig. 11.3 and a positive value corresponds to an attractive force (purple-shaded area). The

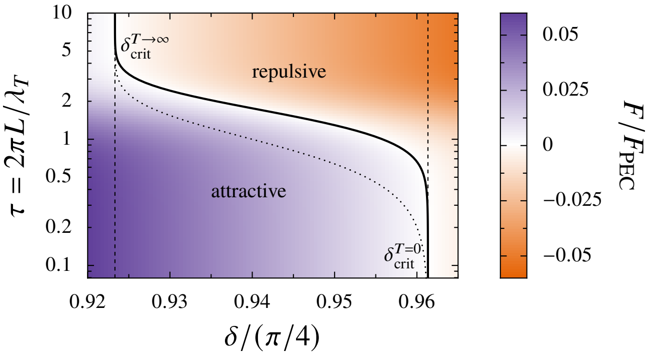

Figure 11.3: PFA result for two PEMC spheres. Casimir force as a function of the duality parameter δ and the dimensionless temperature τ, normalized by the Casimir force for two perfect electric conductors. Negative values correspond to a repulsive force and positive values to an attractive force. The solid line depicts δ_{crit}, which defines the vanishing of the force. The dotted line represents the vanishing Casimir energy. The asymptotic values for low and high temperatures are shown as dashed lines.

line separating the two regions defines δ_{crit}. For comparison, we also added the curve where the Casimir energy vanishes, presented by a dotted line in Fig. 11.3. We see that δ_{crit} as a function of the temperature decreases monotonically from the zero-temperature result (11.6) to the high-temperature limit (11.11). Hence, if we consider a system with a δ-value between the two limiting cases, for example, $\delta = 0.94\pi/4$, we can observe a sign change of the Casimir force with temperature.

Next, we want to briefly discuss the low-temperature expansion for $\delta < \tau$, thus also including the case $\delta = 0$. For this purpose, we express the PFA result (11.7) in terms of the Lambert series, which yields

$$\mathcal{F}_{\text{PFA}} = -\frac{k_{\text{B}}T}{4x}\text{Re}\left[\text{Li}_3(e^{2i\delta}) + 2\mathcal{L}_{\exp(-2\tau)}\left(-3, 1 + i\frac{\delta}{\tau}\right)\right] . \tag{11.12}$$

We apply the asymptotic expression of the Lambert series for $\tau \ll 1$ given in Sec. A.4 and expand the result in terms of $\delta/\tau < 1$, which yields

$$\Delta\mathcal{F}_{\text{PFA}} \approx -\frac{\hbar c}{\pi L x}\left[\delta^2\left(\log(4\pi) + 2\log(\delta/\tau) - 4 + \frac{\pi^2}{72}\right)\tau + \frac{1}{144}\left(\pi^2 + 6\delta^2\right)\tau^2 - \frac{\zeta(3)}{8\pi}\tau^3\right] . \tag{11.13}$$

In the limit $\delta = 0$, we can reproduce the low-temperature corrections found by Ref. [210]. Compared to the previous results for $\delta > \tau$, the subleading term for $\delta = 0$ is of the order of τ^3 compared to τ^4. One also notices that compared to before, there are logarithmic corrections $\log(\delta/\tau)$. These logarithmic corrections were also observed in a study of the Casimir interaction for a scalar field [211].

11.1.2 Beyond PFA, distance corrections to the zero-temperature result

We observed in the previous Section that δ_{crit} changes with temperature. More specifically, the critical angle in the small-distance regime decreases with temperature. Next, we analyse how the spherical geometry affects the Casimir force in comparison to planar surfaces. For this purpose, we are applying the PFA correction formulas we derived in the previous Chapter for bi-isotropic spheres. Corrections to the PFA result involve two contributions, the diffraction and geometrical corrections

$$\Delta\mathcal{E} = \mathcal{E} - \mathcal{E}_{\text{PFA}} \approx \mathcal{E}_{\text{diff}} + \mathcal{E}_{\text{geo}} . \tag{11.14}$$

The diffraction corrections arise from the leading correction of the scattering amplitudes in the large-sphere approximation. We determined the asymptotic expansion of the scattering amplitudes for a PEMC sphere in Eq. (4.46). Inserting these expressions into (10.43), we find for the expansion coefficients α_0 and α_1, the following expressions

$$\alpha_0 = -\cos(2\delta)\alpha_1\,, \qquad \alpha_1 = \frac{\xi}{cR_{\text{eff}}\kappa}\,. \tag{11.15}$$

Together with the earlier introduced eigenvalues (11.2), we insert the expansion coefficients α_0 and α_1 into Eq. (10.45) to obtain the frequency contribution $\mathcal{F}_{\text{diff}}(\xi)$. After carrying out the integral over imaginary frequencies, the diffraction correction to the Casimir energy $\mathcal{E}_{\text{PFA}}$ yields

$$\mathcal{E}_{\text{diff}} = -\frac{\hbar}{4}\text{Re}\int_0^\infty \frac{\mathrm{d}\xi}{2\pi}\int_{\xi/c}^\infty \frac{\mathrm{d}\kappa}{\kappa}\log(1-\mathrm{e}^{2\mathrm{i}\delta-2\kappa L})\,, \tag{11.16}$$

where we performed the same variable transformation from the transverse wave vector k to the axial component κ, as earlier for the evaluation of the PFA result. The integral is carried out, and the result can be expressed in terms of polylogarithms of the second order: $\mathcal{E}_{\text{diff}} = (\hbar c/16\pi L)\text{Re}\text{Li}_2(\mathrm{e}^{2\mathrm{i}\delta})$. Together with the Jonquiere inversion formula (11.5), the diffraction correction for two PEMC spheres are given by

$$\mathcal{E}_{\text{diff}} = \mathcal{E}_{\text{PFA}}\beta_{\text{diff}}x\,, \qquad \beta_{\text{diff}} = -15\frac{\pi^2 - 6\delta(\pi-\delta)}{\pi^4 - 30\delta^2(\pi-\delta)^2}\,, \tag{11.17}$$

where we factored out the PFA result and used $x = L/R_{\text{eff}}$. For $\delta = 0$, we reproduce $\beta_{\text{diff}} = -15/\pi^2$ found in Ref. [34] and for the other limiting case $\delta = \pi/2$, we obtain $\beta_{\text{diff}} = 4/7\pi^2$.

The geometrical corrections follow from the next-to-leading-order (NTLO) correction of the saddle-point approximation of the Casimir free energy, as discussed in detail in Sec. 10.2. We identified two contributions to the geometrical corrections

$$\mathcal{F}_{\text{geo}}(\xi) = \mathcal{F}^{(i)}_{\text{NTLO}}(\xi) + \mathcal{F}^{(ii)}_{\text{NTLO}}(\xi) \tag{11.18}$$

with $\mathcal{F}^{(i)}_{\text{NTLO}}(\xi)$ defined in Eq. (10.66), which is fully determined by the eigenvalues $\lambda_{1,2}$ of the round-trip matrix between PEMC plates. The evaluation of the second term is much more evolved, as shown in Appendix F. In the case of PEMC spheres, the contribution simplifies, however, significantly. In fact it can be shown that $\mathcal{F}^{(ii)}_{\text{NTLO}}(\xi) = 0$, as discussed in Sec. F.5.

The geometrical corrections thus only come from the term $\mathcal{F}^{(i)}_{\text{NTLO}}(\xi)$. After inserting the eigenvalues $\lambda_{1,2}$ into (10.66) and performing the integral over imaginary frequencies, we thus find for the geometrical corrections to the Casimir energy in the short-distance limit

$$\begin{aligned}\mathcal{E}_{\text{geo}} = \frac{\hbar}{6}\text{Re}\int_0^\infty \frac{\mathrm{d}\xi}{2\pi}\int_{\xi/c}^\infty \frac{\mathrm{d}\kappa}{\kappa}\Bigg\{ & L\kappa\left(1+\frac{\xi^2}{c^2\kappa^2}\right)\Big[\text{Li}_0(\mathrm{e}^{2\mathrm{i}\delta-2\kappa L}) + (3u-1)\text{Li}_2(\mathrm{e}^{2\mathrm{i}\delta-2\kappa L})\Big] \\ & + \frac{\xi^2}{c^2\kappa^2}\Big[-\log(1-\mathrm{e}^{2\mathrm{i}\delta-2\kappa L}) + (3u-1)\text{Li}_3(\mathrm{e}^{2\mathrm{i}\delta-2\kappa L})\Big]\Bigg\}\end{aligned} \tag{11.19}$$

with $u = R_{\text{eff}}/(R_1+R_2)$. The integral over the axial wave component and the frequency can be carried out if one introduces the series expansion of the polylogarithms (A.8). We then find, after

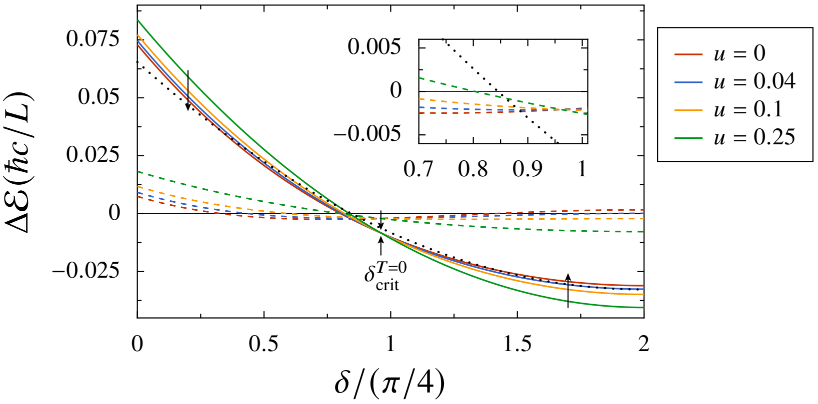

Figure 11.4: Corrections to the PFA result. Lowest-order corrections of the Casimir energy for small distances as a function of the system parameter δ, for various values of u (see Eq. (11.21)). The PFA result vanishes at $\delta_{\mathrm{crit}}^{T=0}$, which makes $\Delta\mathcal{E}$, the leading-order term of the Casimir energy. The lowest-order corrections have two contributions: $\Delta\mathcal{E} = \mathcal{E}_{\mathrm{diff}} + \mathcal{E}_{\mathrm{geo}}$. The diffraction correction is shown as a dotted line, and the geometrical corrections are depicted as dashed lines for the respective u-values. Inset: Zoom to the behaviour at $\delta \approx 0.85\pi/4$, where the diffraction correction changes its sign. Similar figure in Ref. [101].

some algebraic transformations, the following result for the geometrical corrections to the PFA result

$$\mathcal{E}_{\mathrm{geo}} = \mathcal{E}_{\mathrm{PFA}}\beta_{\mathrm{geo}}x, \qquad \beta_{\mathrm{geo}} = \frac{1}{3} - u + \frac{\beta_{\mathrm{diff}}}{3}, \tag{11.20}$$

where we again factored out the PFA result and introduced the expression β_{diff} given above in Eq. (11.17). Note that the geometrical corrections depend on u, indicating that curvature corrections become more important with increasing distance between the sphere.

The small distance expansion of the Casimir energy for two PEMC spheres is thus, in total, given by $\mathcal{E} = \mathcal{E}_{\mathrm{PFA}}\,[1 + \beta x + o(x)]$, where $\beta = \beta_{\mathrm{diff}} + \beta_{\mathrm{geo}}$. Our result is consistent with the limiting cases for $\delta = 0$, which can be found in Ref. [34, 212] and $\delta = \pi/2$ [213]. The term $o(x)$ accounts for PFA corrections, which decay faster than linear. Recent studies on the limiting case of perfect electric reflectors suggest that the next-to-next-to-leading-order correction follows a fractional power-law behaviour with $o(x) \propto x^{3/2}$ [101, 109]. In total, the leading corrections $\Delta\mathcal{E} \approx \mathcal{E}_{\mathrm{PFA}}\beta x$ are given by

$$\Delta\mathcal{E} \approx \frac{\hbar c}{720\pi L}\left[20(\pi^2 - 6\delta(\pi-\delta)) - \frac{1-3u}{3}\left(\pi^4 - 30\delta^2(\pi-\delta)^2\right)\right]. \tag{11.21}$$

The PFA corrections as function of δ are depicted in Fig. 11.4 for u ranging from 0 to 1/4. The corrections are most significant for the case of two equally sized spheres, as expected since this geometry deviates the most from the plane-plane geometry. At $\delta_{\mathrm{crit}}^{T=0}$, we find that the PFA corrections yield a finite contribution, which is the same for all values of u. As a consequence, the corrections $\Delta\mathcal{E}$ then become the leading contribution to the Casimir energy between two PEMC spheres and instead of a L^{-2}-power law, the Casimir energy scales with L^{-1}. This confirms our observation from Sec. 4.2, where we observed different scaling behaviour of the scattering amplitudes with sphere radius for different values of $\theta_{1,2}$. Furthermore, we depicted the diffraction (dotted line) and geometrical (dashed lines) corrections separately in Fig. 11.4. The majority of the PFA correction comes from the diffraction contribution, which remains constant for all values of u. Only at the transition point, where $\mathcal{E}_{\mathrm{diff}}$ changes its sign (shown in the inset) are geometrical corrections the primary contribution.

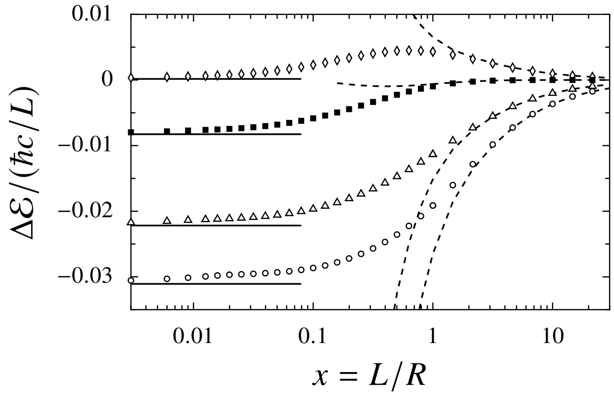

Figure 11.5: Casimir energy in the plane-sphere geometry. PFA corrections for the Casimir energy of a sphere and plane as a function of the aspect ratio x. The Casimir energy is presented for the same δ-values as in Fig. 11.2. In the small-distance regime $x \ll 1$, the corrections converge towards the result presented in Eq. (11.21), which is depicted by the solid lines. For large-distances $x \gg 1$, the corrections converge towards the dipole-plane result found in Eq. (11.28). Adapted from [208].

The validity of the PFA corrections is analysed in Fig. 11.5, where we compare the analytical result with a numerical calculation of the Casimir energy as a function of x. We calculated the PFA correction for the same values of δ as in Fig. 11.2. As expected, for $x \ll 1$, the Casimir energy converges towards (11.21), which is depicted by the solid lines. As we have already seen in Fig. 11.4, the PFA corrections do not vanish for the critical angle found in the PFA regime, which means that δ_{crit} changes with increasing distance between the spheres. Additionally, we tested the validity of our numerical results by examining the Casimir energy in the large-distance regime. It is evident from Fig. 11.5, that the numerical results converge towards the dipole-plane limit, which is represented by the dashed lines. We will analyse this limit in more detail in the following Section.

11.2 Long-range asymptotics, the dipole regime

This Section aims to study the behaviour of the Casimir interaction between two PEMC spheres that are far apart. We want to determine whether the temperature dependence of δ_{crit} found for short distances extends to the long-distance regime. In Sec. 10.3 we introduced the expression for the Casimir interaction between two dipoles or a dipole in front of a plane for bi-isotropic objects, here we will apply these results to the PEMCs. First, we will discuss the result for two dipoles (Sec. 11.2.1) and follow with a discussion of the dipole-plane setup in Sec. 11.2.2.

11.2.1 Dipole-dipole regime

We consider two PEMC spheres with radii R_1, R_2 which are much smaller than the distance L between the spheres. Inserting polarisabilities $\alpha_{P,P'}$ for a PEMC sphere, given in Eq. (10.73) into the dipole-dipole result for the Casimir free energy (10.79), we obtain

$$\mathcal{F}_{\text{dip-dip}} = -\frac{\hbar c}{2\pi\mathcal{L}}\left(\frac{R_1R_2}{\mathcal{L}^2}\right)^3\left[\cos^2(\delta)\left(f_{P\leftrightarrow P}(\nu)+f_{P\leftrightarrow\bar{P}}(\nu)\right)-\sin^2(\delta)\left(\frac{4}{5}f_{P\leftrightarrow P}(\nu)+\frac{5}{4}f_{P\leftrightarrow\bar{P}}(\nu)\right)\right], \tag{11.22}$$

where $f_{P\leftrightarrow P}$ and $f_{P\leftrightarrow\bar{P}}$ are defined in Eqs. (10.80)-(10.82) and account for the polarisation-conserving and -changing channels upon translation of the electromagnetic field between the two spheres. They are functions of the effective temperature $\nu = 2\pi\mathcal{L}/\lambda_T$, which should not be confused with $\tau = 2\pi L/\lambda_T$ introduced in the previous Section. In the zero-temperature limit $\nu \to 0$, the channel functions are in leading order given by the numerical factor 115/8 and 7/2, respectively and the

Casimir energy thus yields

$$\mathcal{E}_{\text{dip-dip}} = -\frac{\hbar c}{16\pi\mathcal{L}}\left(\frac{R_1R_2}{\mathcal{L}^2}\right)^3 [8 + 135\cos(2\delta)] \ . \tag{11.23}$$

We thus reproduce known results for $\delta = 0, \pi/2$ computed in Refs. [214] and [43], respectively. Earlier, we found that the critical angle changes if we go beyond the PFA limit to larger distances. We can now determine the upper bound of δ_{crit} at zero-temperature. Since the Casimir force is given by $F_{\text{dip-dip}} = 7\mathcal{E}_{\text{dip-dip}}/\mathcal{L}$, we can immediately determine the critical angle from the energy expression above

$$\delta_{\text{crit}}^{T=0} = \frac{\pi}{4} + \frac{1}{2}\arcsin\left(\frac{8}{135}\right) = 1.037\ldots\frac{\pi}{4} \ . \tag{11.24}$$

At high temperatures $\nu \longrightarrow \infty$, there is no contribution from the polarisation-changing channel $f_{P\leftrightarrow\bar{P}} = 0$ and the polarisation-conserving channel yields $f_{P\leftrightarrow P} \approx 30\nu/8$ in leading order. The free energy thus reduces to

$$\mathcal{F}_{T,\text{dip-dip}} = -\frac{2k_{\text{B}}T}{8}\left(\frac{R_1R_2}{\mathcal{L}^2}\right)^3 [1 + 9\cos(2\delta)] \ . \tag{11.25}$$

For $\delta = 0$, the result is in agreement with results obtained in Ref. [206] for perfect electric conductors. We can directly determine the critical angle in this limit since the force is proportional to energy with $F_{\text{dip-dip}} = 6\mathcal{F}_{\text{dip-dip}}/\mathcal{L}$

$$\delta_{\text{crit}}^{T\to\infty} = \frac{\pi}{4} + \frac{1}{2}\arcsin\left(\frac{1}{9}\right) = 1.070\ldots\frac{\pi}{4} \ . \tag{11.26}$$

We depicted the Casimir force F, normalized by the perfect reflector result F_{PEC}, as function of δ and the effective temperature ν in Fig. 11.6 with the same conventions as in Fig. 11.3. The zero-force curve is represented by a solid line which separates the attractive force region above the curve from the repulsive force region below it. The critical angle increases monotonically with temperature. For low and high temperatures, the curve converges towards the two limiting results we determined above, which are presented as dashed lines in Fig. 11.3. The Casimir energy shows a similar behaviour (dotted line). Hence, for systems with δ between the two limiting cases $\delta_{\text{crit}}^{T=0}$ and $\delta_{\text{crit}}^{T\to\infty}$, the force transitions from repulsion to attraction upon increasing the temperature. This behaviour is contrary to what we observed in the short-distance regime. One explanation might be that due to the vanishing of the polarisation-mixing channels at higher temperatures ($f_{P\leftrightarrow\bar{P}}(\nu \longrightarrow \infty) \longrightarrow 0$), the magneto-electric effect responsible for the repulsion reduces.

11.2.2 Dipole-plane regime

Next, we are going to examine the case where a dipole is in front of a planar surface. We use the results derived in Eq. (10.89), together with the polarisibilities (10.73) and Fresnel reflection coefficients (4.34) for PEMCs and obtain

$$\mathcal{F}_{\text{dip-plane}} = -\frac{\hbar c}{2\pi\mathcal{L}}\left(\frac{R}{\mathcal{L}}\right)^3 \cos(2\delta)\left[g_{P\leftrightarrow P}(\nu) + g_{P\leftrightarrow\bar{P}}(\nu)\right] \ . \tag{11.27}$$

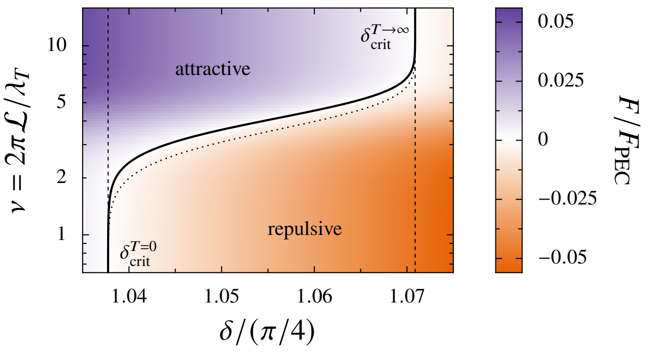

Figure 11.6: Dipole-dipole result for two PEMC spheres. Casimir force F normalized by F_{PEC} calculated for various values of δ and the effective temperature ν, similar to Fig. 11.3. The solid line depicts the parameter values where the force vanishes and the dotted line where the free energy is zero. For low and high temperatures, the curve converges towards the respective limiting values of the critical angle (11.24) and (11.26).

The functions $g_{P\leftrightarrow P}$ and $g_{P\leftrightarrow \bar{P}}$ arise from the polarisation-conserving and -changing channels during translation of the electromagnetic field between the dipole and plane. They are defined in Eqs. (10.90a)-(10.90b). In the zero-temperature limit, they are given by $15/16$ and $3/16$, respectively, which leads to the following expression for the Casimir energy

$$\mathcal{E}_{\text{dip-plane}} = -\frac{9\hbar c}{16\pi\mathcal{L}}\left(\frac{R}{\mathcal{L}}\right)^3 \cos(2\delta)\,. \tag{11.28}$$

A comparison with the full numerical results, depicted in Fig. 11.5, showed qualitative good agreement for aspect ratios $x = L/R > 1$. At high temperatures, the polarisation-changing contribution vanishes and the polarisation-conserving channel $g_{P\leftrightarrow P}$ yields $3\nu/8$.

Note that the Casimir force changes its sign at $\delta_{\text{crit}} = \pi/4$ for all temperatures, hence, compared to the dipole-dipole result (11.22) there is no change of the critical angle with increasing temperature. The temperature dependence only comes into play if we take higher-order corrections to the dipole-plane limit into account. These corrections arise from higher round-trip numbers, as we will see in the following Section.

11.3 High-temperature limit

An explicit analytical expression for the Casimir energy can usually only be derived within the limits of small or large distances between the objects, as shown in the previous two Sections. The Casimir force at intermediate distances is, in most cases, calculated numerically. In this Section, we employ our findings from Chap. 9 and derive a semi-analytical expression for the Casimir free energy based on the single-round-trip result for two PEMC spheres.

In the high-temperature limit, the scattering amplitude matrix of a PEMC matrix follows from a duality transformation (4.56) of the scattering matrix of a PEC or PMC sphere: $\mathbf{S}_{\text{PEMC}} = \mathbf{D}\mathbf{S}_{\text{PEC}}\mathbf{D}^{-1} = \mathbf{D}^{-1}\mathbf{S}_{\text{PMC}}\mathbf{D}$. The reflection matrix elements (9.4) of a PEMC sphere in the plane-wave basis can thus be written as

$$\langle \mathbf{k}_i, p, \pm|\mathcal{R}_{\text{PEMC}}|\mathbf{k}_j, p', \pm\rangle = \frac{2\pi R}{k_i}\left(\mathbf{D}(\theta)\mathbf{S}_{\text{PEC}}\mathbf{D}(-\theta)\right)_{p,p'}\,. \tag{11.29}$$

The scattering matrices for a PEC or PMC sphere are diagonal and can be related to the scattering matrices, we discussed earlier for a Drude sphere in vacuum $S^{\text{PEC}}_{\text{TM,TM}} = S^{\text{Dv}}_{\text{TM,TM}} = \cosh(\chi_{i,j}) - 1$ or a dielectric sphere in an electrolyte $S^{\text{PEC}}_{\text{TE,TE}} = S^{\text{de}}_{\text{TM,TM}} = -\int_0^1 \mathrm{d}t\,\left[\cosh(\chi_{i,j}) - 2t\cosh(t\chi_{i,j})\right]$ with $\chi_{i,j}$ defined in Eq. (9.5). After inserting the matrix elements into Eq. (9.3) for the single round-trip, we obtain

$$\mathrm{tr}\mathcal{M} = \cos^2(\delta)\mathrm{tr}\mathcal{M}_{\mathrm{PEC-PEC}} - \sin^2(\delta)\mathrm{tr}\mathcal{M}_{\mathrm{PEC-PMC}}\,. \tag{11.30}$$

By using the known connection between the scattering amplitudes, we can easily express the trace expression for two identical electric reflectors in terms of the trace expression for the ded- and DvD-model

$$\mathrm{tr}\mathcal{M}_{\mathrm{PEC-PEC}} = \mathrm{tr}\mathcal{M}_{\mathrm{DvD}} + \mathrm{tr}\mathcal{M}_{\mathrm{ded}}\,. \tag{11.31}$$

Together with the single-round-trip result for the ded-model derived in Eq. (9.79) and the DvD-model presented in Eq. (9.87), we obtain the following expression for the single-round-trip term of two perfect electric conductors

$$\begin{aligned}\mathrm{tr}\mathcal{M}_{\mathrm{PEC-PEC}} = {} & \frac{y}{y^2-1} + \frac{1}{z} + \frac{z}{6}\log\left(\frac{z^2(y^2-1)}{(yz+1/2)^2}\right) \\ & - \sum_{\sigma=\pm}\left[\frac{1}{2y+\alpha_\sigma} - \frac{1}{6\sqrt{z}}\frac{1}{\alpha_\sigma^{3/2}}\log\left(\frac{2y^2+\alpha_\sigma y-1+\sqrt{\alpha_\sigma z}}{2y^2+\alpha_\sigma y-1-\sqrt{\alpha_\sigma z}}\right)\right].\end{aligned} \tag{11.32}$$

Recall that $y = 1+x+ux^2/2$ introduced in Eq. (9.17), $\alpha_\pm$ accounts for the ratio of the sphere radii and is defined in Eq. (9.53) and $z = 2y+\alpha_+ +\alpha_-$ (9.78). For the case of mixed boundaries, so one sphere is a perfect electric conductor, while the other sphere is a perfect magnetic conductor, the trace over the round-trip operator yields

$$\begin{aligned}\mathrm{tr}\mathcal{M}_{\mathrm{PEC-PMC}} = {} & \frac{\rho_1\rho_2}{\pi^2}\int_0^1 \mathrm{d}^2\boldsymbol{t}\int_{-\infty}^{\infty}\mathrm{d}^2\mathbf{x}\int_{-\infty}^{\infty}\mathrm{d}^2\mathbf{y}\mathrm{e}^{-(x_1^2+x_2^2)}\mathrm{e}^{-(y_1^2+y_2^2)} \\ & \times\Big[\left(\cosh(\chi_1^{(1)})-1\right)\left(\cosh(\chi_2^{(2)})-2t_2\cosh(t_2\chi_2^{(2)})\right) \\ & \quad + \left(\cosh(\chi_1^{(1)})-2t_1\cosh(t_1\chi_1^{(1)})\right)\left(\cosh(\chi_2^{(2)})-1\right)\Big].\end{aligned} \tag{11.33}$$

We performed the same variable transformation as in Sec 9.2.1, where the arguments of the hyperbolic cosines according to Eq. (9.10) are given by $\chi_1^{(1)} = 2\rho_1(x_1x_2+y_1y_2)$ and $\chi_2^{(2)} = 2\rho_2(x_1x_2+y_1y_2)$. After rewriting the hyperbolic cosines as exponential functions, we can apply the results for two-dimensional Gaussian integrals. In summary, we find

$$\begin{aligned}\mathrm{tr}\mathcal{M}_{\mathrm{PEC-PMC}} = {} & \frac{y}{y^2-1} + \frac{z-2y}{2}\log\left(\frac{z^2(y^2-1)}{(yz+1/2)^2}\right) \\ & - \sum_{\sigma=\pm}\left[\frac{1}{2y+\alpha_\sigma} - \frac{1}{2\sqrt{z}}\frac{1}{\alpha_\sigma^{3/2}}\log\left(\frac{2y^2+\alpha_\sigma y-1+\sqrt{\alpha_\sigma z}}{2y^2+\alpha_\sigma y-1-\sqrt{\alpha_\sigma z}}\right)\right].\end{aligned} \tag{11.34}$$

The single-round-rip expressions simplify significantly for the sphere-plane geometry ($u = 0$). As we discussed earlier, for the dielectrics in an electrolyte, α_- becomes zero in this limit while α_+ goes to infinity. The terms for $\sigma = +$ in Eqs. (11.32) and (11.34), thus vanish, and the remaining terms in both cases summarize to

$$\mathrm{tr}\mathcal{M}^{u=0}_{\mathrm{PEC-PEC}} = \mathrm{tr}\mathcal{M}^{u=0}_{\mathrm{PEC-PMC}} = \frac{y}{y^2-1} - \frac{1}{2y} + \frac{y}{2}\log\left(\frac{y^2-1}{y^2}\right). \tag{11.35}$$

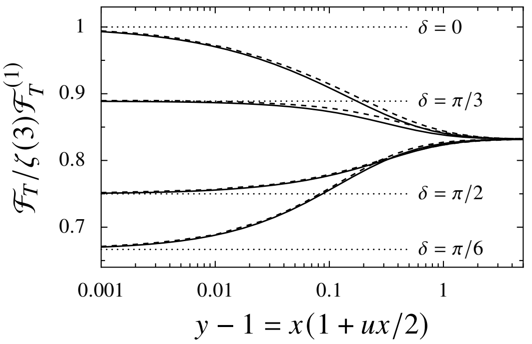

δ	ν_1	ν_2	μ_1	μ_2
0	0.01148	0.18511	0.01103	0.16069
$\pi/6$	0.00020	0.07213	0.08928	0.00021
$\pi/3$	0.17655	0.25447	0.20505	0.20505
$\pi/2$	0.00468	0.21056	0.23221	0.00471

Figure 11.7 & Table 11.1: High-temperature result for two PEMC spheres. Ratio of the high-temperature free energy $\mathcal{F}_T$ and the single-round-trip result $\mathcal{F}_T^{(1)} = -(k_\mathrm{B}T/2)\mathrm{tr}\mathcal{M}$ scaled by the Apéry constant $\zeta(3) = 1.202\ldots$. The ratio is shown for $u = 0$ (solid lines) and for $u = 1/4$ (dashed lines) for $\delta = 0$, $\pi/6$, $\pi/3$ and $\pi/2$. For small distances $y - 1 \ll 1$, the ratio converges towards the PFA result depicted by the dotted lines with values 1, 2/3, 8/9 and 3/4 respectively for the different δ-values. The table presents the expansion coefficients for the rational model (11.37), with maximal relative deviations over the y, u parameter space given by: $\Delta \times 10^3 = 4.6,\ 5.1,\ 5.0,\ 1.9$ respectively for the four δ-values. Adapted from [208].

Hence, we see that the repulsive magneto-electric term (11.34) and the attractive term (11.32) become identical in the sphere-plane limit, which already Pirozhenko *et al.* [215] observed when they studied the dipole-plane expansion of the Casimir free energy for the $\delta = 0$ and $\pi/2$ limits. This also explains the critical angle $\delta_\mathrm{crit} = \pi/4$ found in the dipole-plane limit we discussed in the previous Section.

Upon comparing the single-round-trip expression $\mathcal{F}_T^{(1)} = -(k_\mathrm{B}T/2)\mathrm{tr}\mathcal{M}$ with the full free energy $\mathcal{F}_T$ (see Fig. 11.7) we find that the single-round-trip result becomes exact for large distances $y - 1 \gg 1$, while it only deviates by a numerical factor for small distances $y - 1 \approx x \ll 1$, depicted by the dotted lines in Fig. 11.7. For small distances the contribution from (11.32) and (11.34) become identical: $\mathrm{tr}\mathcal{M}_\mathrm{PEC-PEC} = \mathrm{tr}\mathcal{M}_\mathrm{PEC-PMC} \approx 1/2(y-1) \approx 1/2x$. The ratio with the PFA result (11.10) yields

$$\frac{\mathcal{F}_T}{\mathcal{F}_T^{(1)}} = \frac{\mathrm{Re}\mathrm{Li}_3(\mathrm{e}^{2\mathrm{i}\delta})}{\cos(2\delta)} \quad \text{for} \quad y \to 1\,. \tag{11.36}$$

As shown in Fig. 11.7, the ratio is a monotonic function in y and has a weak dependence on u. It is possible to capture the monotonic behaviour with a rational model, similar to our previous discussion for the ded- and DvD-setup

$$\phi_\delta = \prod_{k=1}^{n} \frac{\mathrm{e}^{y-1} - 1 + \nu_k(\delta)}{\mathrm{e}^{y-1} - 1 + \mu_k(\delta)}\,, \tag{11.37}$$

where the fitting parameters ν_k and μ_k now depend on δ. We fitted the data for $u = 0.25$ and $u = 0$ such that the maximal deviation over the distance range y and over u is minimized. The obtained fitting parameters are presented in Tab. 11.1. Hence, combining the single-round-trip expression (11.30) with the rational model (11.37) provides a good approximation for the full free energy.

Note that for the special case of $u = 0$ and $\delta = \pi/4$ the single round-trip does not contribute. Then, the next order in the round-trip expansion needs to be considered. The double-round-trip expression for the sphere-plane setup is given by

$$\mathrm{tr}\mathcal{M}_{u=0}^2 = \cos^2(2\delta)\mathrm{tr}\mathcal{M}_\mathrm{PEC-PEC}^2 - \sin^2(2\delta)\mathrm{tr}\mathcal{M}_\mathrm{PEC-PMC}^2\,. \tag{11.38}$$

We already observed in Sec. 9.4.1, that the double-round-trip contributions for the sphere-plane setup can be derived from the respective single-round-trip expressions for two equally sized spheres by replacing y with $2y^2 - 1$, which leads to

$$\begin{aligned}\mathrm{tr}\mathcal{M}^2_{\text{PEC}-\text{PEC}} &= \frac{2y^2-1}{4y^2(y^2-1)} + \frac{1}{4y^2} + \frac{2y^2}{3}\log\left(\frac{y^6(y^2-1)}{(y^2-1/4)^4}\right) - \frac{2}{4y^2-1} + \frac{1}{6y}\log\left(\frac{4y^3-3y+1}{4y^3-3y-1}\right)\\ \mathrm{tr}\mathcal{M}^2_{\text{PEC}-\text{PMC}} &= \frac{2y^2-1}{4y^2(y^2-1)} + \log\left(\frac{y^6(y^2-1)}{(y^2-1/4)^4}\right) - \frac{2}{4y^2-1} + \frac{1}{2y}\log\left(\frac{4y^3-3y+1}{4y^3-3y-1}\right),\end{aligned} \tag{11.39}$$

where $y = 1 + d/R$ with the surface-to-surface distance d between sphere and plane.

11.4 A sum rule for PEMC objects

In this Section, we are going to examine a certain characteristic of the system of two PEMC objects. Rode *et al.* [56] observed, that the Casimir force between two PEMC plates at zero temperature obeys a sum rule, where the integral $\int_0^\pi \mathrm{d}\delta F(\delta)$ over the system parameter δ yields zero. A more recent work involving the study of the Casimir interaction between a PEMC plate and a Weyl semi-metal also found that this sum rule holds [216]. Here, we will show that this is, in general, no longer true for spherical objects.

In the PFA limit (11.3), we find that independent of the temperature, the integral over δ is proportional to $\int_0^{\pi/2} \mathrm{d}\delta \cos(2\delta r) = \sin(\pi r)/2r$ which is zero for integer numbers r of round-trips. Hence, the sum rule holds in the PFA regime for all temperatures. However, if we go beyond the PFA limit and look, for example, at the large-distance result for two spheres (11.22), where the integral over the force $F_{\text{dip-dip}} = -\partial_L \mathcal{F}_{\text{dip-dip}}$ yields

$$\begin{aligned}\int_0^{\pi/2} \mathrm{d}\delta F_{\text{dip-dip}}(\delta) = -\frac{\hbar c}{32\mathcal{L}^2}\left(\frac{R_1 R_2}{\mathcal{L}^2}\right)^3 \big[&18g(\nu)\cosh(\nu) + 18g(\nu)^2 + 14g(\nu)^3\cosh(\nu)\\ &+ 2g(\nu)^4\left(2\cosh^2(\nu)+1\right)\big]\end{aligned} \tag{11.40}$$

with $g(\nu) = \nu/\sinh(\nu)$. The integral is non-zero for all temperatures. To examine how the sum rule changes with distance, we thus examine the integral over the Casimir force in the high-temperature limit for various distances, as it is depicted in Fig. 11.8. We determined the integral over the dimensionless thermal Casimir force

$$\mathcal{I} = \frac{\mathcal{L}}{k_\mathrm{B}T}\int_0^\pi \mathrm{d}\delta F_T(\delta) \tag{11.41}$$

for $u = 0.01, 0.05$ and 0.25 scaled by the factor y^3 which for large distances behaves like $(ux^2/2)^3 \approx (L^2/2R_1R_2)^3$ and thus accounts for the scaling of the dimensionless Casimir force in the large distance limit (depicted by the dotted line in Fig. 11.8). In contrast to the sphere-sphere geometry, the sphere-plane ($u = 0$) geometry fulfils the sum-rule also for large distances, as it is depicted in the upper panel of Fig. 11.8. However, the sum rule no longer holds for intermediate distances. The discrepancy can only be explained if higher round-trip orders are taken into account. As we have seen from the discussion in the previous Section, the single-round-trip result scales with $\cos(2\delta)$ and thus vanishes if we perform the integral over δ, which is not the case for the double-round-trip

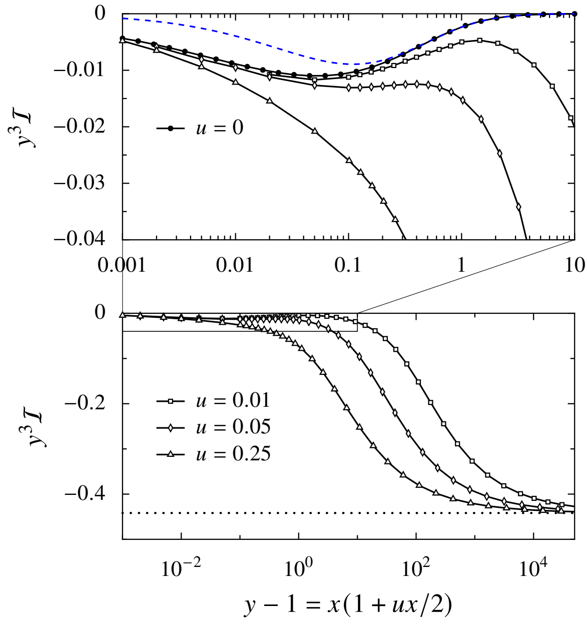

Figure 11.8: Sum rule in the high-temperature limit. Integral of the dimensionless Casimir force given in Eq. (11.41) scaled by the distance ratio y^3. The lower panel depicts the integral for $u = 0.01$ (squared symbols), $u = 0.05$ (diamond symbols) and $u = 0.25$ (triangle symbols), which for large distances $y - 1 \gg 1$ converge towards the dipole-dipole result $-9\pi/64$, presented by the dotted lines. The boxed region for $y - 1 < 10$ is zoomed out in the upper panel, which additionally shows the result for $u = 0$ (filled circle symbols). The integral converges towards zero for small and large distances. The violation of the sum rule at intermediate distances can only be explained when taking at least double round-trips (blue dashed line) into account. Adapted from [208].

term (11.38). The dashed line in the upper panel of Fig. 11.8, depicts the double-round-trip result. As expected, it converges towards the numerical results (filled circles) for large distances, where the double-round-trip approximation $\mathcal{F}_T/k_\mathrm{B}T \approx -\mathrm{tr}\mathcal{M} - \mathrm{tr}\mathcal{M}^2/2$ is exact.

11.5 Switching the sign between PEMC spheres

In the previous Sections, we examined the Casimir interaction for small and large distances and low and high temperatures. We found that the critical angle δ_crit changes as a function of the system parameters. In the following, we utilize these findings to examine the range of δ where an equilibrium position exists and how it changes with temperature and radius variations of one of the spheres. While stable equilibrium positions were ruled out for reciprocal objects in vacuum [40], they are possible for non-reciprocal materials [7], as we observe here.

In Fig. 11.9, we depict the zero-force curves in the $x\delta$-plane for the sphere-plane geometry (solid lines) and two equally sized spheres (dashed lines). The zero-force curves separate the domains, where the force changes its sign as a function of x and δ. The force is always repulsive above a curve and attractive below. We examined the zero- (blue curves) and high-temperature (red curves) limits for both geometries. Finite-temperature results can be found between these two limiting cases in the yellow-shaded area. The curves for geometries with $0 < u < 1/4$ lie between the $u = 0$ and $1/4$ limit, which is explanatory presented for the zero-temperature curves by the blue-shaded area. The zero-force curves increase monotonically with distance for all mentioned cases and converge towards the critical angles we computed earlier for small and long distances, which are depicted as dash-dotted lines. While discussing the PFA corrections in Sec. 11.1.2, we observed that the curvature effects become more important as the distance between the objects increases. With the result in Fig. 11.9, we can now confirm that the variation in the critical angle is smaller for a sphere in front of a plane compared to two equally sized spheres.

Instead of the effect of geometrical variation, we are more interested in how the temperature changes

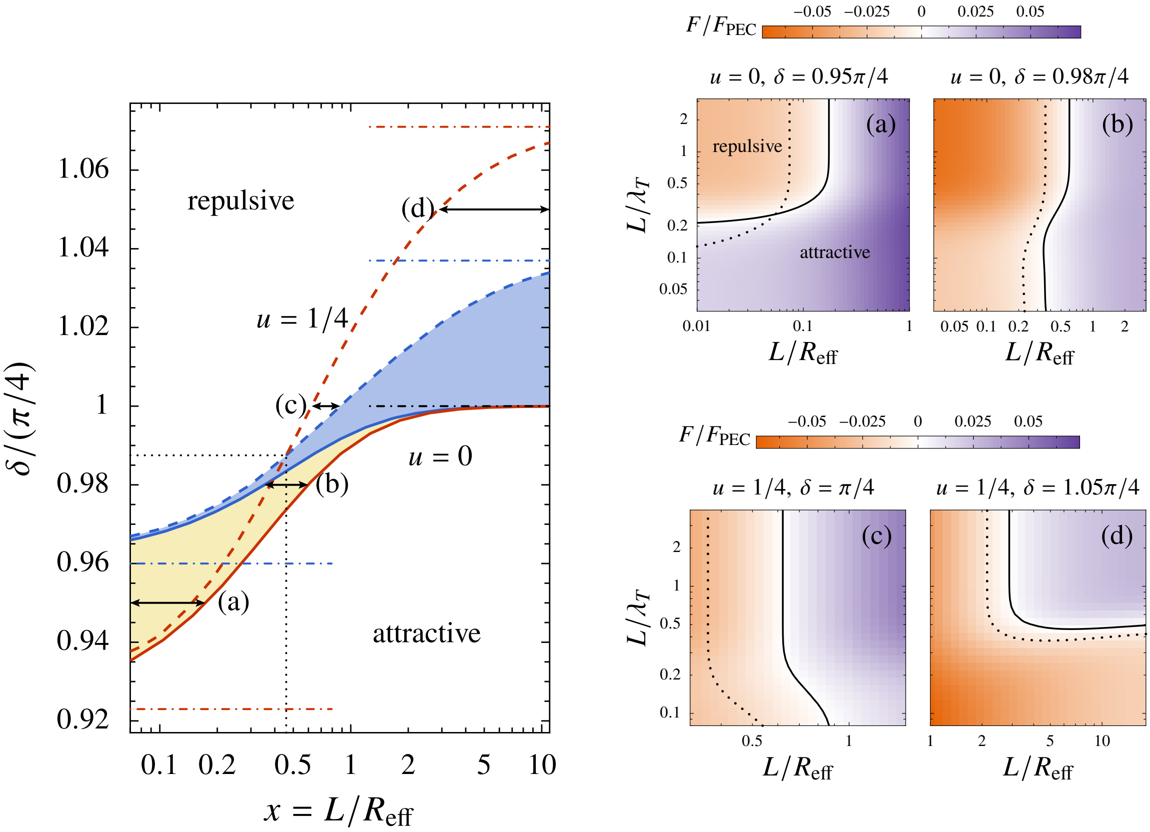

Figure 11.9: Left Panel: Curves of vanishing Casimir force as a function of the aspect ratio $x = L/R_\mathrm{eff}$ and the duality parameter δ in units of $\pi/4$. The zero-force curves are shown for the sphere-plane geometry ($u = 0$) as solid lines and two equally-sized spheres ($u = 1/4$) depicted as dashed lines. Blue-coloured curves present the zero-temperature result, while the red curves for each geometry represent the high-temperature limit. In each of the four cases, the Casimir force is attractive for values of x and δ, which lay below the curve and repulsive for values above the curve. The yellow-shaded area between the zero- and high-temperature limit of the sphere-plane geometry depicts the area where the zero-force curve for intermediate temperatures are located. Zero-force curves at zero temperature for geometries with $0 < u < 1/4$ can be found in the blue-shaded area. Dash-dotted lines depict the critical angles δ_crit in the small- and large distances limit, which we determined in Sec. 11.1 and Sec. 11.2. For the sphere-sphere geometry, we found that the zero-force curves intersect at a point which is highlighted by the black dotted lines. The arrows marked with (a)-(d) present parameter ranges which are analysed in the right panel. **Right Panel:** 2D-force plots as function of the distance L/R_eff and temperature L/λ_T scaled by the force for two perfect reflectors. The force fields are shown for different values of u and δ. Figures (a) and (b) depict the Casimir force between a PEMC sphere and plane, while Figures (c) and (d) present the results for two equally sized spheres. The solid lines present the zero-force curves and the dotted lines define where the Casimir energy is vanishing. Similar figures can be found in Ref. [208].

the equilibrium positions. Variations in temperature are more relevant for experimental setups since the temperature can serve as an external control parameter, while geometrical and material parameters are usually fixed. Therefore, u and δ have set values in the following.

We start with the sphere-plane geometry. According to Fig. 11.9 the equilibrium distance grows with increasing temperature if $0.96\pi/4 \lessapprox \delta < \pi/4$. There is no equilibrium for δ larger than $\pi/4$ and for $0.92\pi/4 \lessapprox \delta \lessapprox 0.96\pi/4$, the force vanishes only at a finite temperature. To further analyse the temperature dependence, we computed the force map for fixed values of δ, as can be seen in Fig. 11.9 (a) and (b) for $\delta = 0.95\pi/4$ and $0.98\pi/4$, with each value as representative of the two just mentioned regimes. The Casimir force was calculated for various temperatures and distances and is normalized by the Casimir force for two perfect electric conductors ($\delta = 0$). The zero-force curve is depicted as a black line, and we also show the curve where the energy vanishes as a dotted line. We can observe from (a) that repulsion only occurs for distances $L < 0.3R_{\text{eff}}$ and for $L > 0.2\lambda_T$. At room temperature, this would correspond to distances $L \approx 1.5$ µm and effective radii of about $R_{\text{eff}} \approx 5$ µm, which can be reached in experiments [217]. On the contrary, for $\delta = 0.98\pi/4$ depicted in (b) the force is repulsive for all temperatures in the small-distance regime. There is only a narrow band around $L \approx 0.5R_{\text{eff}}$, where the zero-force curve is pushed to the right for increasing temperature, meaning that for fixed sphere radii, the equilibrium distance increases with temperature.

Next, we want to analyse how increasing the temperature modifies the equilibrium distance between two equally-sized spheres ($u = 1/4$). As shown in Fig. 11.9, there exists a critical angle ($\approx 0.99\pi/4$), where the zero-temperature and high-temperature curves intersect. This equilibrium point is stable against temperature changes. For values of δ below this angle, the sphere-sphere geometry behaves similarly to the sphere-plane geometry discussed earlier, where increasing the temperature pushes the equilibrium distance to higher values. The behaviour changes for values of δ above this angle but below $\delta \approx 1.04\pi/4$ where an increase in temperature results in a smaller equilibrium distance. The force vanishes only at a certain temperature in the range $1.04\pi/4 \lessapprox \delta \lessapprox 1.07\pi/4$ range. We again analyse force fields for certain δ-values to analyse the temperature dependence further. We choose a system with $\delta = \pi/4$ and one with $\delta = 1.05\pi/4$, respectively depicted in Fig. 11.9 (c) and (d). Compared to (b) is, the distance range of repulsion in (c) larger, and raising the temperature causes the equilibrium distance to move towards smaller values. Contrarily, for $\delta = 1.05\pi/4$ repulsion occurs only for $L > 0.5\lambda_T$ and $L > 3R_{\text{eff}}$. At room temperature, this would lead to a distance of about 3.8 µm and an effective radius of about 1.8 µm.

12 | Conclusions and Outlook

This thesis gave insights into forces acting on spherical objects in both the quantum and classical regimes. Specifically, we examined how particular spheres behave when subjected to a structured light field and studied the Casimir force between two spherical objects.

The scattering of electromagnetic fields at spherical objects forms the basis for discussing the optical and dispersion forces. In the first part of this thesis, we thus solved the scattering problem for a bi-isotropic sphere. Bi-isotropic materials introduce cross-polarisabilities, which lead to the mixing of transverse electric and magnetic field modes when scattered at an object. Additionally, we obtained analytical expressions for the reflection coefficients in various limiting cases, such as the geometrical optics regime and the static limit.

Optical trapping with a vortex beam

One of the most prominent applications of optical forces is the trapping of objects in a focused beam. A number of factors affect the trapping, such as the type of the structured field, the geometry of the trapped particle, and its material. Thus, an accurate model is needed to capture the complex interplay between these factors.

We studied a focused Laguerre-Gaussian beam by applying the Debye-Wolf integral representation. This model goes beyond the paraxial approximation and accurately captures the strongly focused light beam used in most applications of optical tweezers. Optical setups often introduce aberrations, which may impact the trapping efficiency. We thus incorporated aberrations in our theory by using the method of vectorial ray tracing. Specifically, we considered spherical aberration caused by the transfer of the light beam through an interface. Furthermore, we accounted for astigmatism, which typically arises from a misalignment in the optical setup. We computed the multipole expansion from the angular spectrum representation of the focused beam and derived the scattered field by applying Mie theory for a chiral sphere. The spherical symmetry of the trapped object allows for analytic calculations of the optical force components. We thus obtained the MDSA+ theory for chiral objects trapped by a vortex beam. Our obtained force expression extended previous results [129]. The force components are presented in a multipole expansion, which we evaluated numerically. Our implementation allowed for an efficient and fast calculation of the optical force.

We applied the MDSA+ theory to study the trapping of chiral and dielectric objects in vortex beams with topological charge ℓ. We observed different trapping regimes depending on the sphere size and the topological charge. If the spherical object is much smaller than the ring of maximal intensity, the object is trapped in the annular spot. In the opposite case, where the sphere is larger than the ring, it can be trapped along the optical axis. Within the ring regime, the particles exhibit a torque, which is orientated in the same direction as defined by the sign of the topological charge. On-axis trapped particles displaced from their equilibrium position, on the other hand, experience a negative torque. This torque is highly sensitive to the size of the trapped sphere and relatively robust against small radial displacements from the optical axis.

One important application of optical tweezers is the enantioselection of particles. Many biological structures are chiral and can, in the first step, be modelled by a spherical object with a chiral response. We investigated how the torque on a sphere is influenced by chirality and discovered that certain beam modes are more affected by the chiral nature of the trapped particle than others.

Furthermore, we discussed how spherical aberration influences vortex beams of different topological charges. We also examined the influence of spherical aberrations on the trapping.

Finally, we applied our theory to fit an experimentally measured torque. The torque is accessed by measuring the rotation angle of a trapped bead that is displaced from its on-axis equilibrium by a constant force. Our theoretical analysis indicates that the trapped bead's characteristics can be determined by its rotation angle. We thus proposed a method that allows us to determine the size of the bead from the measured rotation angles. For this method to work, it is necessary to determine the rotation angle with a high accuracy from the experimental data. Compared to earlier studies [142], we thus proposed a new scheme to extract the rotation angle based on a two-dimensional Gaussian fit of the spatial distribution of the bead. We fitted the rotation angles with the MDSA+ theory, where the radius of the bead was used as a free parameter. The proposed method allows for an *in situ* measurement of the radius of a trapped bead, with a high accuracy. Additionally, we found that the method is relatively robust against optical aberrations, specifically for spheres in the geometrical optics limit.

Our findings suggest that further research is possible. In our discussions above, we assumed that the refractive index of the bead is known. Our method could also serve as a probe for the refractive index of a trapped bead if the radius of the particle is known but not the refractive index. Additionally, beads trapped by a vortex beam could potentially be utilized to probe the optical aberrations of the system. Furthermore, we found that higher-order vortex beams are more sensitive to a chiral optical response. Future studies might involve specific applications of vortex beams to select particles based on their chiral polarisabilities.

Casimir interaction

In the third part of this thesis, we studied the Casimir interaction between spherical objects. The Casimir interaction is generally considered a quantum effect arising from the fluctuations of the electromagnetic vacuum. However, at high temperatures, thermal fluctuations can make the dominant contribution, making the Casimir force purely classical.

We began by analysing the classical limit of the Casimir interaction, specifically with the well-studied system of Drude spheres in vacuum. One unique property of this system is that the Casimir interaction in the high-temperature limit becomes a universal function of the geometrical parameters. The finite DC-conductivity of the spheres causes the static dielectric function to diverge, making the system independent of any material properties. Earlier work questioned whether an analytical derivation of the Casimir free energy for this system is feasible. However, we were able to derive an analytical expression by using a bi-coloured partition scheme for the scattering process between the spheres. Additionally, we introduced a diagrammatic representation for the scattering process to account for multiplicities arising from a cyclic invariance. We established a relation between electrostatics and Casimir physics by relating our result for the Drude sphere to the capacitance matrix elements of two spherical conductors. With the exact expression for the Casimir free energy available, we also computed an analytical expansion in the small-distance regime.

Two dielectric spheres in an electrolytic solution exhibit similar behaviour to the Drude spheres in vacuum. The universality of the Drude setup in the static limit originates from the divergence of the dielectric function of the spheres. In contrast, for the dielectric spheres in an electrolyte, the dielectric function of the surrounding medium diverges for vanishing frequency. The two setups can thus be seen as dual to each other. Based on the methods introduced for the Drude case, we developed a semi-analytical expression for the Casimir interaction between the dielectric objects. We found a formula applicable to all distances between objects, which enables simple calculations without extensive numerical computations. The main difference between the Drude- and dielectric-setup is the minimal distance over which the universal contribution dominates. In the case of Drude spheres, this distance is essentially the thermal wavelength of about $\simeq 8\,\mu\mathrm{m}$ at room temperature, while a much smaller distance $\sim 100\,\mathrm{nm}$ is found in the case of dielectric spheres. Thus, the universal Casimir free energy of the dielectrics in an electrolyte covers a much broader distance range. Our result for dielectric objects in an electrolyte also has relevance for colloidal and biological systems. We found that the Casimir interaction is of the order of $k_\mathrm{B}T$ in the range where the universal interaction provides the dominant contribution to the Casimir interaction. Recent studies already extended our finding to another simple setup relevant to biological systems of cylinders [28]. Future research might also look into more realistic geometries. While our semi-analytical approach to the Casimir free energy is sufficient for most realistic applications, determining a full analytical result for the two dielectric spheres in an electrolyte is also still of interest.

The last two Chapters of this work were devoted to the Casimir force between bi-isotropic spheres. The Casimir interaction is often computed with the proximity force approximation (PFA). Based on earlier calculations [33], we demonstrated that the PFA result can also be obtained for polarisation-mixing materials through an asymptotic expansion of the scattering formula. Unlike previous calculations for dielectric objects, we determined the PFA expression by considering all possible polarisation combinations in the scattering process. We introduced a recursive description for mixing of the reflection coefficients for fixed numbers of round-trips. We evaluated the round-trip contributions by using the method of generating functions. Furthermore, we also determined general expressions for PFA corrections. Additionally, we derived an expression for the Casimir free energy in the large-distance limit. Specifically, we evaluated the dipole-dipole and dipole-plane approximation for bi-isotropic materials.

We applied our findings for small and large distances to an idealized system, namely perfect electromagnetic conductor (PEMC) spheres. This model interpolates between a perfect electric and perfect magnetic conductor with a single parameter, allowing us to disentangle the interplay between material response, geometry and temperature. We studied the Casimir force between two dissimilar spheres for all distance and temperature regimes. The numerical calculation is based on a plane-wave method developed by [109], which we extended to bi-isotropic materials. Based on our earlier findings for general bi-isotropic spheres, we derived analytical results for several limiting cases between PEMCs. We used numerical results to discuss the Casimir interaction at intermediate separations and temperatures. We discovered that the Casimir force changes its sign for specific material parameters with increasing distance from repulsion to attraction. Hence, it allows for the existence of a stable equilibrium. Further analysis revealed that the equilibrium position can also change with temperature. Although PEMC materials constitute an idealized system, our results show that temperature can tune stable equilibria. To explore more realistic materials, we can consider a situation where the response of the PEMC is limited to certain frequencies. Whether a narrow-band response can lead to an equilibrium state or even a reduction in the Casimir force needs to be examined in the future.

A | Special functions and integrals

In this appendix, we provide definitions and limiting cases of several special functions, which we use throughout this thesis. Furthermore, we present results for certain integrals.

A.1 Modified Bessel function

Studying the scattering of electromagnetic waves at spherical objects for imaginary frequencies yields reflection coefficients expressed in terms of modified Bessel functions of the first kind $I_\lambda(z)$ and modified Hankel functions $K_\lambda(z)$.

We apply the Debye expansion to expand the reflection coefficients at large aspect ratios, as discussed in Section 4.2. For large orders of $\lambda \gg 1$, the Debye expansions of the modified Bessel functions are given by [185, Eqs. 10.41.3, 10.41.4]

$$I_\lambda(\lambda z) \approx \frac{1}{(2\pi\lambda)^{1/2}} \frac{\mathrm{e}^{\lambda\eta}}{(1+z^2)^{1/4}} \left(1 + \frac{U_1(p)}{\lambda}\right), \tag{A.1a}$$

$$K_\lambda(\lambda z) \approx \left(\frac{\pi}{2\lambda}\right)^{1/2} \frac{\mathrm{e}^{-\lambda\eta}}{(1+z^2)^{1/4}} \left(1 - \frac{U_1(p)}{\lambda}\right), \tag{A.1b}$$

where $\eta = \sqrt{1+z^2} - \operatorname{arcsinh}(1/z)$, $U_1 = (3p - 5p^3)/24$ with $p = 1/\sqrt{1+z^2}$. The Debye expansions of the derivatives are given by [185, Eqs. 10.41.5, 10.41.6]

$$I'_\lambda(\lambda z) \approx \frac{1}{(2\pi\lambda)^{1/2}} \frac{(1+z^2)^{1/4}\mathrm{e}^{\lambda\eta}}{z} \left(1 + \frac{V_1(p)}{\lambda}\right), \tag{A.2a}$$

$$K'_\lambda(\lambda z) \approx -\left(\frac{\pi}{2\lambda}\right)^{1/2} \frac{(1+z^2)^{1/4}\mathrm{e}^{-\lambda\eta}}{z} \left(1 - \frac{V_1(p)}{\lambda}\right) \tag{A.2b}$$

with $V_1(p) = (-9p + 7p^3)/24$. We are particularly interested in the logarithmic derivatives of the modified Bessel functions, which, according to the expressions above, yield

$$\frac{I'_\lambda(\lambda z)}{I_\lambda(\lambda z)} \approx \frac{\sqrt{1+z^2}}{z} \left[1 - \frac{1}{2\lambda} \frac{z^2}{(1+z^2)^{3/2}}\right], \tag{A.3a}$$

$$\frac{K'_\lambda(\lambda z)}{K_\lambda(\lambda z)} \approx -\frac{\sqrt{1+z^2}}{z} \left[1 + \frac{1}{2\lambda} \frac{z^2}{(1+z^2)^{3/2}}\right]. \tag{A.3b}$$

We apply [185, Eqs. 10.30.1, 10.30.2] to get the expansion of the modified Bessel functions for small arguments $x \ll 1$

$$I_{l+1/2}(x) \approx \sqrt{\frac{2}{\pi}} \frac{x^{l+1/2}}{(2l+1)!!} + \sqrt{\frac{1}{2\pi}} \frac{x^{l+5/2}}{(2l+3)!!}, \tag{A.4a}$$

$$K_{l+1/2}(x) \approx \sqrt{\frac{\pi}{2}} \frac{(2l-1)!!}{x^{l+1/2}}. \tag{A.4b}$$

We apply these formulas for the expansion of the reflection coefficients in the static limit, discussed in Sec. 4.3.

A.2 Angular function

The angular functions defined in Eq. (4.28) are expressed as function of associated Legendre polynomials $P_l^m(z)$ of degree l and order m, as follows

$$\pi_l(z) = P_l'(z) = \frac{P_l^1(z)}{\sqrt{z^2-1}}\,, \qquad \tau_l(z) = -z\pi_l(z) + l(l+1)P_l(z)\,. \tag{A.5}$$

For large orders l, we use the expansion for the Legendre polynomial given in [185, Eq. 14.15.13], which is based on the Debye expansion for the Bessel functions. We get

$$\frac{\pi_l(\cosh u)}{l(l+1)} \approx \frac{(-1)^{l-1}}{\lambda}\left(\frac{1}{2\pi\lambda\sinh^3 u}\right)^{1/2} \mathrm{e}^{\lambda u}\,, \tag{A.6a}$$

$$\frac{\tau_l(\cosh u)}{l(l+1)} \approx (-1)^l\left(\frac{1}{2\pi\lambda\sinh u}\right)^{1/2} \mathrm{e}^{\lambda u}\left(1-\frac{7}{8}\frac{\coth u}{\lambda}\right)\,, \tag{A.6b}$$

where $\lambda = l + 1/2$.

Using known results for the Legendre polynomials given in [185, Eq. 14.8.12], we obtain the following expansions for large arguments

$$\pi_l(z) \approx \frac{(2l)!}{2^l l!(l-1)!} z^{l-1}\,, \qquad \tau_l(z) \approx \frac{(2l)!}{2^l[(l-1)!]^2} z^l\,. \tag{A.7}$$

Note that $\tau_l(z) \approx zl\pi_l(z)$ in the limit $z \gg 1$.

A.3 Polylogarithm

The polylogarithm of order n is defined by [185, Eq. 25.12.10]

$$\mathrm{Li}_n(z) = \sum_{r=1}^{\infty} \frac{z^r}{r^n}\,. \tag{A.8}$$

The polylogartihms of order $n = 0$ and $n = 1$ are given by

$$\mathrm{Li}_0(z) = \frac{z}{1-z}\,, \qquad \mathrm{Li}_1(z) = -\log(1-z)\,. \tag{A.9}$$

The order of the polylogarithms can be lowered or increased by respectively differentiating or integrating with respect to the argument, as follows

$$z\frac{\mathrm{d}}{\mathrm{d}z}\mathrm{Li}_n(z) = \mathrm{Li}_{n-1}(z)\,, \tag{A.10}$$

$$\mathrm{Li}_{n+1}(z) = \int_0^z \frac{\mathrm{Li}_n(t)}{t}\mathrm{d}t\,. \tag{A.11}$$

Both expressions can be obtained directly from the series expansion given above.

In Part III of this work, we introduce various multivariant integrals over rational functions, which can be evaluated with the help of the polylogarithms. In particular, we define the following three integrals

$$
\begin{aligned}
\int_0^1 \frac{\mathrm{d}t_m}{t_m} \dots \int_0^{t_2} \frac{\mathrm{d}t_1}{t_1} \frac{ct_1 + dt_1^2 + et_1^3 + ft_1^4}{(1 - z_1 t_1)(1 - z_2 t_1)} &= \\
&= \frac{z_1^3 c + z_1^2 d + z_1 e + f}{z_1^3 (z_1 - z_2)} \mathrm{Li}_m(z_1) + \frac{z_2^3 c + z_2^2 d + z_2 e + f}{z_2^3 (z_2 - z_1)} \mathrm{Li}_m(z_2) \\
&\quad + \frac{e}{z_1 z_2} + \frac{f(z_1 + z_2)}{(z_1 z_2)^2} + \frac{1}{2^m} \frac{f}{z_1 z_2} ,
\end{aligned}
\tag{A.12}
$$

$$
\begin{aligned}
\int_0^1 \frac{\mathrm{d}t_m}{t_m} \dots \int_0^{t_2} \frac{\mathrm{d}t_1}{t_1} \frac{ct_1 + dt_1^2 + et_1^3 + ft_1^4}{[(1 - z_1 t_1)(1 - z_2 t_1)]^2} &= \\
&= \frac{2 z_1^3 z_2 c - z_1^2 (z_1 + z_2) d - 2 z_1^2 e - (3 z_1 - z_2) f}{z_1^2 (z_1 - z_2)^3} \mathrm{Li}_m(z_1) \\
&\quad + \frac{2 z_2^3 z_1 c - z_2^2 (z_1 + z_2) d - 2 z_2^2 e - (3 z_2 - z_1) f}{z_2^2 (z_2 - z_1)^3} \mathrm{Li}_m(z_2) \\
&\quad + \frac{z_1^3 c + z_1^2 d + z_1 e + f}{z_1^2 (z_1 - z_2)^2} \mathrm{Li}_{m-1}(z_1) + \frac{z_2^3 c + z_2^2 d + z_2 e + f}{z_2^2 (z_2 - z_1)^2} \mathrm{Li}_{m-1}(z_2) ,
\end{aligned}
\tag{A.13}
$$

$$
\begin{aligned}
\int_0^1 \frac{\mathrm{d}t_m}{t_m} \dots \int_0^{t_2} \frac{\mathrm{d}t_1}{t_1} \frac{cst_1 + ds^3 t_1^2 + es^5 t_1^3 + fs^4 t_1^4}{(1 - z_1 t_1)(1 - z_2 t_1)(1 - z_1 s^2 t_1)(1 - z_2 s^2 t_1)} &= \\
&= \frac{s z_1^3 c + s^3 z_1^2 d + s^5 z_1 e + s^5 f}{z_1^2 (s^2 - 1)(z_1 - z_2)(z_1 s^2 - z_2)(z_1 - s^2 z_2)} (z_2 - s^2 z_1) \mathrm{Li}_m(z_1) \\
&\quad + \frac{s z_2^3 c + s^3 z_2^2 d + s^5 z_2 e + s^5 f}{z_2^2 (s^2 - 1)(z_2 - z_1)(z_2 s^2 - z_1)(z_2 - s^2 z_1)} (z_1 - s^2 z_2) \mathrm{Li}_m(z_2) \\
&\quad + \frac{s (s^2 z_1)^3 c + s^3 (s^2 z_1)^2 d + s^5 s z_1 e + s^5 f}{(s^2 z_1)^2 (s^2 - 1)(z_1 - z_2)(z_1 s^2 - z_2)(z_1 - s^2 z_2)} (z_1 - s^2 z_2) \mathrm{Li}_m(s^2 z_1) \\
&\quad + \frac{s (s^2 z_2)^3 c + s^3 (s^2 z_2)^2 d + s^5 s z_2 e + s^5 f}{(s^2 z_2)^2 (s^2 - 1)(z_2 - z_1)(z_2 s^2 - z_1)(z_2 - s^2 z_1)} (z_2 - s^2 z_1) \mathrm{Li}_m(s^2 z_2) .
\end{aligned}
\tag{A.14}
$$

All three integrals can be evaluated by first performing a partial fraction decomposition of the integrand and then by applying (A.9) and (A.11). Alternatively, they can also be evaluated by using a standard library for symbolic mathematics like `SymPy` [218].

A.4 Generalized Lambert series

Here, we present a special case of the generalized Lambert series introduced by [189] as the so-called F-series. We follow the notation and results presented in Ref. [190], where the Lambert series is defined by

$$
\mathcal{L}_q(s, z) = \sum_{k=1}^{\infty} \frac{k^s q^{kx}}{1 - q^k} .
\tag{A.15}
$$

We will apply the Lambert series for the short-distance expansion of the Casimir free energy, which we carried out in Chap. D. For our purposes, we set $q = \exp(-\mu)$ with $\mu \leq 0$. The expansion of the

Lambert series for $q \to 1$ or equivalently $\mu \approx 0$ is discussed in Ref. [190]. For $s = 0$, the asymptotic expansion reads

$$\mathcal{L}_{\exp(-\mu)}(0, z) = -\frac{1}{\mu}\left[\psi(z) + \log(\mu) - \sum_{k=1}^{\infty} \frac{\zeta(1-k)}{k!} B_k(z)(-\mu)^k\right] , \tag{A.16}$$

where $\psi(z)$ defines the digamma function, while $B_k(z)$ accounts for the Bernoulli polynomial of degree k. For negative integers $s = -m$, the expansion of the Lambert series reads

$$\begin{aligned} \mathcal{L}_{\exp(-\mu)}(-m, z) = -\frac{1}{\mu}\Bigg\{ & [m\zeta'(1-m, z) + (\log(\mu) - H_{m-1})B_m(z)] \frac{(-\mu)^m}{m!} \\ & - \sum_{\substack{k=0 \\ k\neq m}}^{\infty} \frac{\zeta(1+m-k)}{k!} B_k(z)(-\mu)^k \Bigg\} . \end{aligned} \tag{A.17}$$

The first term in the expansion refers to the derivative of the Hurwitz-Zeta function $\zeta(s, z)$ with respect to the first argument. The Hurwitz-zeta function is a generalization of the Riemann zeta function with $\zeta(s) = \zeta(s, 1)$. H_n defines the harmonic number with $H_n = \sum_{k=1}^{n} 1/k$.

A.5 Bell polynomial

In this Section, we present a special class of multivariate polynomials known as the partial ordinary (o) Bell polynomials. They are defined using a generating function [194, 195]

$$\left(\sum_{n=1}^{\infty} x_n z^n\right)^k = \sum_{n=k}^{\infty} B^{\mathrm{o}}_{n,k}(x_1, x_2, \ldots, x_n) z^n . \tag{A.18}$$

The Bell polynomials of weight n and degree k, have the following representation

$$B^{\mathrm{o}}_{n,k}(x_1, x_2, \ldots, x_n) = \sum_{m_i} \frac{k!}{m_1! m_2! \cdots m_n!} x_1^{m_1} x_2^{m_2} \cdots x_n^{m_n} \quad \text{with} \quad \sum_{i=1}^{n} m_i = k \, , \sum_{i=1}^{n} i m_i = n \tag{A.19}$$

with the conventions

$$B_{0,0} = 1 \, , \qquad B_{n,0} = 0 \, . \tag{A.20}$$

A.6 Gaussian integral

In this Section, we review the results for one- and multidimensional Gaussian-type integrals, which we utilize throughout this work.

A.6.1 One dimensional Gaussian integral

First, we consider the following Gaussian integral over a single variable

$$\int \mathrm{d}x \exp\left(-\frac{1}{2}ax^2 + bx\right) = \sqrt{\frac{2\pi}{a}} \exp\left(\frac{b^2}{2a}\right) \tag{A.21}$$

which goes from $-\infty$ to ∞ and is valid for $a > 0$. We are particularly interested in the m-th moment, which is defined as

$$\langle x^m \rangle = \frac{\int \mathrm{d}x x^m \exp\left(-\frac{1}{2}ax^2\right)}{\int \mathrm{d}x \exp\left(-\frac{1}{2}ax^2\right)} \,. \tag{A.22}$$

When m takes odd values, the expression becomes zero. For even values of m $(m = 2n)$, we obtain:

$$\langle x^{2n} \rangle = (2n-1)!! \frac{1}{a^n} \,. \tag{A.23}$$

A.6.2 Saddle-point approximation

Throughout this work, we have to deal with integrals of the form [219]

$$I = \int \mathrm{d}x g(x) \exp(-af(x)) \tag{A.24}$$

which we evaluate for $a \gg 1$. We assume that f is an analytic function and has an isolated minimum at x_{sp}, called the saddle point (sp), which is defined by

$$\left.\frac{\mathrm{d}f(x)}{\mathrm{d}x}\right|_{x=x_{\mathrm{sp}}} = 0 \,, \qquad \left.\frac{\mathrm{d}^2 f(x)}{\mathrm{d}x^2}\right|_{x=x_{\mathrm{sp}}} < 0 \,. \tag{A.25}$$

The main contribution to the integral comes from $x \approx x_{\mathrm{sp}}$. All other contributions are exponentially suppressed for large a. We thus obtain the dominant contribution to the integral I by expanding f and g in a Taylor expansion around the saddle, with $f = \sum_{n=0}^{\infty} f_{\mathrm{sp}}^{(n)} (x - x_{\mathrm{sp}})^n / n!$, where $f_{\mathrm{sp}}^{(n)}$ denotes the n-th derivative of f evaluated at the saddle. A similar expansion can be carried out for g. Inserting the Taylor expansions in Eq. (A.24) and approximating the exponential with $\exp(-z) \approx 1 - z + z^2/2$, we obtain

$$\begin{aligned} I \approx \mathrm{e}^{-af_{\mathrm{sp}}} \int \mathrm{d}u \Bigg\{ & g_{\mathrm{sp}} + \frac{1}{2} g_{\mathrm{sp}}^{(2)} u^2 - \frac{a}{24} \left[4 g_{\mathrm{sp}}^{(1)} f_{\mathrm{sp}}^{(3)} + g_{\mathrm{sp}} f_{\mathrm{sp}}^{(4)} \right] u^4 \\ & + \frac{1}{72} \left[a^2 \left(f_{\mathrm{sp}}^{(3)} \right)^2 - 3a g_{\mathrm{sp}}^{(2)} f_{\mathrm{sp}}^{(4)} \right] u^6 \Bigg\} \mathrm{e}^{-\frac{a}{2} f_{\mathrm{sp}}^{(2)} u^2} \,, \end{aligned} \tag{A.26}$$

where we substituted $u = x - x_{\mathrm{sp}}$ and neglected all odd powers in u. We evaluate the integral with (A.23). The first two leading terms for $a \gg 1$, yield [219]

$$\begin{aligned} I \approx \mathrm{e}^{-af_{\mathrm{sp}}} \sqrt{\frac{2\pi}{a f_{\mathrm{sp}}^{(2)}}} \Bigg[& g_{\mathrm{sp}} + \frac{1}{2a} g_{\mathrm{sp}}^{(2)} \left(f_{\mathrm{sp}}^{(2)} \right)^{-1} - \frac{1}{8a} \left(4 g_{\mathrm{sp}}^{(1)} f_{\mathrm{sp}}^{(3)} + g_{\mathrm{sp}} f_{\mathrm{sp}}^{(4)} \right) \left(f_{\mathrm{sp}}^{(2)} \right)^{-2} \\ & + \frac{5}{24a} \left(f_{\mathrm{sp}}^{(3)} \right)^2 \left(f_{\mathrm{sp}}^{(2)} \right)^{-3} \Bigg] \,. \end{aligned} \tag{A.27}$$

A.6.3 Multidimensional Gaussian integral

We consider the multidimensional Gaussian integral

$$\int \mathrm{d}^n\mathbf{x} \exp\left(-\frac{1}{2}\mathbf{x}^t\mathbf{M}\mathbf{x} + \mathbf{J}^t\mathbf{x}\right) = \sqrt{\frac{(2\pi)^n}{\det\mathbf{M}}} \exp\left(\mathbf{J}^t\mathbf{M}^{-1}\mathbf{J}\right) , \tag{A.28}$$

where $\mathbf{M}$ is a real symmetric positive-definite n-dimensional matrix and $\mathbf{x}$ and $\mathbf{J}$ are n-dimensional vectors. Correlation functions are defined as

$$\langle\ldots\rangle = \frac{\int \mathrm{d}^n\mathbf{x} \ldots \exp\left(-\frac{1}{2}\mathbf{x}^t\mathbf{M}\mathbf{x}\right)}{\int \mathrm{d}^n\mathbf{x} \exp\left(-\frac{1}{2}\mathbf{x}^t\mathbf{M}\mathbf{x}\right)} , \tag{A.29}$$

where the dots ... are replaced by products of x_i. The correlation function is evaluated from (A.28) by taking derivatives with respect to J_i and setting $\mathbf{J}$ afterwards to zero. The 2-point correlation function, for example, yields

$$\langle x_i x_j\rangle = M^{-1}_{i,j} . \tag{A.30}$$

Correlation functions with odd numbers of points are zero, and correlation functions with even numbers of points can be expressed in terms of 2-point correlation functions by means of the Wick theorem [220]

$$\langle x_{j_1} x_{j_2} x_{j_3} \ldots x_{j_{2n}}\rangle = \sum_P M^{-1}_{P_1,P_2} M^{-1}_{P_3,P_4} \ldots M^{-1}_{P_{2n-1},P_{2n}} , \tag{A.31}$$

where P accounts for all non-equal pairings $(P_1, P_2)(P_3, P_4)\ldots(P_{2n-1}P_{2n})$ of the indices $j_1, j_2, \ldots j_{2n}$. In total, there are $(2n-1)!!$ distinct pairings.

B | Auxiliary calculations for the scattering of electromagnetic fields

In this appendix, we provide additional information and details on the discussion of the scattering formula in Sec. 2 and the asymptotic expansion of the Mie coefficients for a bi-isotropic sphere in Sec. 4.2.

B.1 Derivation of the scattering formula

In this Section, we want to show the equivalence between Eqs. (2.20) and (2.21). Here, we concentrate on the trace of the GTGT-operator, which, in position space is given by

$$\mathrm{tr}\,[\mathbb{G}_0\mathbb{T}_1\mathbb{G}_0\mathbb{T}_2] = \int_{V_2}\mathrm{d}^3\mathbf{r}\int_{V_1}\mathrm{d}^3\mathbf{s}\int_{V_1}\mathrm{d}^3\mathbf{t}\int_{V_2}\mathrm{d}^3\mathbf{u}\,\mathbb{G}_0(\mathbf{r},\mathbf{s})\mathbb{T}_1(\mathbf{s},\mathbf{t})\mathbb{G}_0(\mathbf{t},\mathbf{u})\mathbb{T}_2(\mathbf{u},\mathbf{r})\,. \tag{B.1}$$

The $\mathbb{T}$-matrices $\mathbb{T}_i(\mathbf{r},\mathbf{r}')$ are only non-zero if both $\mathbf{r},\mathbf{r}' \in V_i$, which is why we limited the spatial integration to the respective volumes of the scatterer. The two arguments of the free Green's function are thus located at the two scatterers. Consequently, $\mathbb{G}_0$ describes the propagation from one scatterer to another. The derivative of the trace expression with respect to the position O_1 of scatterer 1 yields

$$\begin{aligned}\nabla_{O_1}\mathrm{tr}\,[\mathbb{G}_0\mathbb{T}_1\mathbb{G}_0\mathbb{T}_2] = \int_{V_2}\mathrm{d}^3\mathbf{r}\int_{V_1}\mathrm{d}^3\mathbf{s}\int_{V_1}\mathrm{d}^3\mathbf{t}\int_{V_2}\mathrm{d}^3\mathbf{u}\,&[\nabla_s\mathbb{G}_0(\mathbf{r},\mathbf{s})\mathbb{T}_1(\mathbf{s},\mathbf{t})\mathbb{G}_0(\mathbf{t},\mathbf{u})\mathbb{T}_2(\mathbf{u},\mathbf{r})\\ &+\mathbb{G}_0(\mathbf{r},\mathbf{s})\nabla_s\mathbb{T}_1(\mathbf{s},\mathbf{t})\mathbb{G}_0(\mathbf{t},\mathbf{u})\mathbb{T}_2(\mathbf{u},\mathbf{r})\\ &+\mathbb{G}_0(\mathbf{r},\mathbf{s})\nabla_t\mathbb{T}_1(\mathbf{s},\mathbf{t})\mathbb{G}_0(\mathbf{t},\mathbf{u})\mathbb{T}_2(\mathbf{u},\mathbf{r})\\ &+\mathbb{G}_0(\mathbf{r},\mathbf{s})\mathbb{T}_1(\mathbf{s},\mathbf{t})\nabla_t\mathbb{G}_0(\mathbf{t},\mathbf{u})\mathbb{T}_2(\mathbf{u},\mathbf{r})]\,.\end{aligned} \tag{B.2}$$

Note that the Nabla operator only acts on the function to its right. We can use integration by parts for the first term and move the derivations past the free Green's function, which then cancels with the second expression. For the third expression, we can make use of the symmetry of the $\mathbb{T}$-operator, which thus leads to the expression in Eq. (2.20)

$$\begin{aligned}\nabla_{O_1}\mathrm{tr}\,[\mathbb{G}_0\mathbb{T}_1\mathbb{G}_0\mathbb{T}_2] = \int_{V_2}\mathrm{d}^3\mathbf{r}\int_{V_1}\mathrm{d}^3\mathbf{s}\int_{V_1}\mathrm{d}^3\mathbf{t}\int_{V_2}\mathrm{d}^3\mathbf{u}\,&[-\mathbb{G}_0(\mathbf{r},\mathbf{s})\nabla_s\mathbb{T}_1(\mathbf{s},\mathbf{t})\mathbb{G}_0(\mathbf{t},\mathbf{u})\mathbb{T}_2(\mathbf{u},\mathbf{r})\\ &+\mathbb{G}_0(\mathbf{r},\mathbf{s})\mathbb{T}_1(\mathbf{s},\mathbf{t})\nabla_t\mathbb{G}_0(\mathbf{t},\mathbf{u})\mathbb{T}_2(\mathbf{u},\mathbf{r})]\,.\end{aligned} \tag{B.3}$$

B.2 Asymptotic expansion for a large sphere and Fresnel reflection coefficients

In this Section, we provide the explicit expressions for the reflections coefficients of a bi-isotropic sphere in the large radii limit. According to our discussion in Sec. 4.2, the auxiliary functions (4.12) are given by

$$\begin{pmatrix} A_l^{\mathrm{L,R}} \\ B_l^{\mathrm{L,R}} \end{pmatrix} \approx \begin{pmatrix} a_0^{\mathrm{L,R}} \\ b_0^{\mathrm{L,R}} \end{pmatrix} + \frac{1}{2x} \begin{pmatrix} a_1^{\mathrm{L,R}} \\ b_1^{\mathrm{L,R}} \end{pmatrix}, \qquad \begin{pmatrix} V_l^{\mathrm{L,R}} \\ W_l^{\mathrm{L,R}} \end{pmatrix} \approx \begin{pmatrix} v_0^{\mathrm{L,R}} \\ w_0^{\mathrm{L,R}} \end{pmatrix} + \frac{1}{2x} \begin{pmatrix} v_1^{\mathrm{L,R}} \\ w_1^{\mathrm{L,R}} \end{pmatrix}, \tag{B.4}$$

where the leading order coefficients are denoted with the subscript '0' and are defined by

$$\begin{pmatrix} a_0^{\mathrm{L,R}} \\ b_0^{L,R} \end{pmatrix} = \begin{pmatrix} 1 & -m_{\mp} \\ m_{\mp} & -1 \end{pmatrix} \begin{pmatrix} \sqrt{1+\Lambda^2} \\ \sqrt{1+\frac{\Lambda^2}{m_{\mathrm{L,R}}^2}} \end{pmatrix}, \qquad \begin{pmatrix} v_0^{\mathrm{L,R}} \\ w_0^{L,R} \end{pmatrix} = \begin{pmatrix} 1 & m_{\mp} \\ m_{\mp} & 1 \end{pmatrix} \begin{pmatrix} \sqrt{1+\Lambda^2} \\ \sqrt{1+\frac{\Lambda^2}{m_{\mathrm{L,R}}^2}} \end{pmatrix} \tag{B.5}$$

while the leading-order corrections for $x \gg 1$, are denoted by the subscript 1 and yield

$$\begin{pmatrix} a_1^{\mathrm{L,R}} \\ b_1^{L,R} \end{pmatrix} = \begin{pmatrix} 1 & -m_{\mp} \\ m_{\mp} & -1 \end{pmatrix} \begin{pmatrix} \frac{\Lambda^2}{1+\Lambda^2} \\ \frac{\Lambda^2}{m_{\mathrm{L,R}}(m_{\mathrm{L,R}}^2+\Lambda^2)} \end{pmatrix}, \qquad \begin{pmatrix} v_1^{\mathrm{L,R}} \\ w_1^{L,R} \end{pmatrix} = \begin{pmatrix} 1 & m_{\mp} \\ m_{\mp} & 1 \end{pmatrix} \begin{pmatrix} -\frac{\Lambda^2}{1+\Lambda^2} \\ \frac{\Lambda^2}{m_{\mathrm{L,R}}(m_{\mathrm{L,R}}^2+\Lambda^2)} \end{pmatrix} \tag{B.6}$$

with the auxiliary variable $\Lambda = (l + 1/2)/x$. After substituting the above-given expansions into the definition of the Mie coefficients (4.11), (4.16), we obtain the following results for the coefficient $r_{p,p'}(\Lambda)$ of the asymptotic expansion defined in Eq. (4.33):

$$r_{\mathrm{TM,TM}}(\Lambda) = \frac{w_0^L a_0^R + w_0^R a_0^L}{w_0^L v_0^R + w_0^R v_0^L}, \qquad r_{\mathrm{TE,TE}}(\Lambda) = \frac{v_0^L b_0^R + v_0^R b_0^L}{w_0^L v_0^R + w_0^R v_0^L}, \tag{B.7}$$

and

$$r_{\mathrm{TE,TM}}(\Lambda) = 2\mathrm{i}\sqrt{1+\Lambda^2}\,\frac{m_-\sqrt{1+\Lambda^2/m_{\mathrm{R}}^2} - m_+\sqrt{1+\Lambda^2/m_{\mathrm{L}}^2}}{w_0^L v_0^R + w_0^R v_0^L}, \tag{B.8a}$$

$$r_{\mathrm{TE,TM}}(\Lambda) = 2\mathrm{i}\sqrt{1+\Lambda^2}\,\frac{m_-\sqrt{1+\Lambda^2/m_{\mathrm{L}}^2} - m_+\sqrt{1+\Lambda^2/m_{\mathrm{R}}^2}}{w_0^L v_0^R + w_0^R v_0^L}. \tag{B.8b}$$

In Section 4.2.2, we found that for large sphere radii, the leading term of the amplitude scattering matrix elements depends on $r_{p,p'}(\Lambda_{\mathrm{sp}})$ with $\Lambda_{\mathrm{sp}} = \mathrm{i}\cos(\Theta/2)$. In this limit, the above-given expressions coincide with the Fresnel reflection coefficients for a bi-isotropic plane

$$r_{p,p'}(\Lambda_{\mathrm{sp}}) \equiv r_{p,p'}(\theta_0), \tag{B.9}$$

where the incident angle is defined by $\theta_0 = (\pi - \Theta)/2$. Together with Snells'law

$$m_{\mathrm{L,R}} \sin(\theta_{\mathrm{L,R}}) = \sin(\theta_0), \tag{B.10}$$

we also introduce the transmitted angles $\theta_{\mathrm{L,R}}$, which are illustrated in Fig. B.1. From that, we recover the Fresnel reflection coefficients for a bi-isotropic plane [221]

$$r_{\mathrm{TM,TM}}(\theta_0) = \frac{(c_0 - m_- c_{\mathrm{L}})(c_{\mathrm{R}} + m_+ c_0) + (c_0 - m_+ c_{\mathrm{R}})(c_{\mathrm{L}} + m_- c_0)}{(m_- c_{\mathrm{L}} + c_0)(c_{\mathrm{R}} + m_+ c_0) + (m_+ c_{\mathrm{R}} + c_0)(c_{\mathrm{L}} + m_- c_0)}, \tag{B.11a}$$

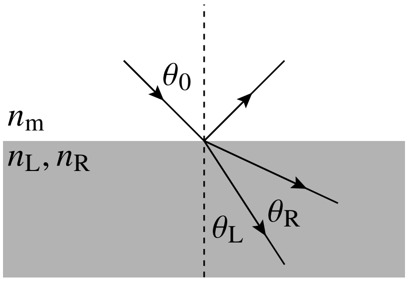

Figure B.1: Fresnel reflection. Reflection and transmission of a plane wave at a bi-isotropic half space. The wave is incident at an angle θ_0 and separates into two transmitted waves at angles θ_L and θ_R.

$$r_{\mathrm{TE,TE}}(\theta_0) = \frac{(m_- c_0 - c_\mathrm{L})\,(m_+ c_\mathrm{R} + c_0) + (m_+ c_0 - c_\mathrm{R})\,(m_- c_\mathrm{L} + c_0)}{(m_- c_\mathrm{L} + c_0)\,(c_\mathrm{R} + m_+ c_0) + (m_+ c_\mathrm{R} + c_0)\,(c_\mathrm{L} + m_- c_0)}\,, \tag{B.11b}$$

$$r_{\mathrm{TE,TM}}(\theta_0) = \frac{2\mathrm{i} c_0\,(m_- c_\mathrm{R} - m_+ c_\mathrm{L})}{(m_- c_\mathrm{L} + c_0)\,(c_\mathrm{R} + m_+ c_0) + (m_+ c_\mathrm{R} + c_0)\,(c_\mathrm{L} + m_- c_0)}\,, \tag{B.11c}$$

$$r_{\mathrm{TM,TE}}(\theta_0) = \frac{2\mathrm{i} c_0\,(m_- c_\mathrm{L} - m_+ c_\mathrm{R})}{(m_- c_\mathrm{L} + c_0)\,(c_\mathrm{R} + m_+ c_0) + (m_+ c_\mathrm{R} + c_0)\,(c_\mathrm{L} + m_- c_0)}\,, \tag{B.11d}$$

where we abbreviated the cosine of the incident and transmitted angles by

$$c_0 = \cos(\theta_0)\,, \qquad c_{\mathrm{L,R}} = \cos(\theta_{\mathrm{L,R}})\,. \tag{B.12}$$

C | Auxiliary calculations for the multipole expansion of optical forces

In this appendix, we provide calculations and background information supporting the results presented in Sec. 5. In particular, we present in Sec. C.1 the expression for the optical force on a spherical particle used in Sec. 5.2.3. In Sec. C.2, we discuss the multipole expansion of a generic electromagnetic field. Further, we discuss in Sec. C.3 the evaluation of the azimuthal integral presented in Eq. (5.18).

C.1 Multipole expansion of the optical force

In this Section, we provide the explicit force expression for an object in a light field. As discussed in Sec. 5.2, the optical force is calculated in a multipole basis with expansion coefficients $(e_{l,m}, f_{l,m})$ for the incident field and $(a_{l,m}, b_{l,m})$ for the scattered field. The optical force is furthermore separated into two parts, the scattering (scat) and the extinction (ext) contribution

$$\mathbf{F} = \mathbf{F}_{\text{scat}} + \mathbf{F}_{\text{ext}}\,. \tag{C.1}$$

We present the optical force in Cartesian coordinates $\mathbf{F} = F_x\hat{\mathbf{x}} + F_y\hat{\mathbf{y}} + F_z\hat{\mathbf{z}}$, where we will refer to F_z as axial force component and F_x and F_y define the transverse force components. The results are taken from [136].

C.1.1 Axial force components

The scattering contribution to the axial force component F_z is given by

$$F_{\text{scat},z} = -\frac{\epsilon_0\epsilon}{K^2}\sum_{l,m}\left\{\frac{U_{l+1,m}}{l+1}\text{Re}\left[\text{i}\left(a^*_{l+1,m}a_{l,m} + b^*_{l+1,m}b_{l,m}\right)\right] + \frac{m}{l(l+1)}\text{Re}\left(b^*_{l,m}a_{l,m}\right)\right\} \tag{C.2}$$

and the extinction term is defined by

$$\begin{aligned}F_{\text{ext},z} = -\frac{\epsilon_0\epsilon}{2K^2}\sum_{l,m}\Bigg\{&\frac{U_{l+1,m}}{l+1}\text{Re}\left[\text{i}\left(a^*_{l+1,m}e_{l,m} + b^*_{l+1,m}f_{l,m} + e^*_{l+1,m}a_{l,m} + f^*_{l+1,m}b_{l,m}\right)\right]\\ &+\frac{m}{l(l+1)}\text{Re}\left[a^*_{l,m}f_{l,m} + b^*_{l,m}e_{l,m}\right]\Bigg\}\,,\end{aligned} \tag{C.3}$$

where ϵ defines the dielectric function of the medium, in which the spherical object is immersed and K is the wave number. The summation indices l and m take the values $l = 1, \dots \infty$ and $m = -l, \dots l$. We furthermore introduced the coefficient

$$U_{l+1,m} = \sqrt{\frac{l(l+2)\left[(l+1)^2 - m^2\right]}{(2l+1)(2l+3)}}\,. \tag{C.4}$$

C.1.2 Transverse force components

Next, we present the multipole expansion of the transverse force components F_x and F_y. The scattering part is given by

$$\begin{aligned}\begin{Bmatrix} F_{\mathrm{scat},x} \\ F_{\mathrm{scat},y}\end{Bmatrix} = \frac{\epsilon_0\epsilon}{2K^2}\sum_{l,m}\Bigg\{ &\frac{V_{l+1,m}}{l+1}\begin{Bmatrix}-\mathrm{Im}\\ \mathrm{Re}\end{Bmatrix}\Big(a^*_{l+1,m+1}a_{l,m} + b^*_{l+1,m+1}b_{l,m} \\ &\qquad - a^*_{l+1,-(m+1)}a_{l,-m} - b^*_{l+1,-(m+1)}b_{l,-m}\Big) \\ &- \frac{c^+_{l,m}}{l(l+1)}\begin{Bmatrix}\mathrm{Re}\\ -\mathrm{Im}\end{Bmatrix}\Big(a^*_{l,m}b_{l,m+1}+b^*_{l,m}a_{l,m+1}\Big)\Bigg\}\end{aligned} \tag{C.5}$$

and the extinction terms are defined by

$$\begin{aligned}\begin{Bmatrix} F_{\mathrm{ext},x} \\ F_{\mathrm{ext},y}\end{Bmatrix} = \frac{\epsilon_0\epsilon}{4K^2}\sum_{l,m}\Bigg\{ &\frac{V_{l+1,m}}{l+1}\begin{Bmatrix}-\mathrm{Im}\\ \mathrm{Re}\end{Bmatrix}\Big(a^*_{l+1,m+1}e_{l,m} + b^*_{l+1,m+1}f_{l,m} \\ &\qquad + e^*_{l+1,m+1}a_{l,m} + f^*_{l+1,m+1}b_{l,m} \\ &\qquad - a^*_{l+1,-(m+1)}e_{l,-m} - b^*_{l+1,-(m+1)}f_{l,-m} \\ &\qquad - e^*_{l+1,-(m+1)}a_{l,-m} - f^*_{l+1,-(m+1)}b_{l,-m}\Big) \\ &- \frac{c^+_{l,m}}{l(l+1)}\begin{Bmatrix}\mathrm{Re}\\ -\mathrm{Im}\end{Bmatrix}\Big(a^*_{l,m}f_{l,m+1}+b^*_{l,m}e_{l,m+1}+a^*_{l,m+1}f_{l,m}+b^*_{l,m+1}e_{l,m}\Big)\Bigg\},\end{aligned} \tag{C.6}$$

where we introduced the following coefficients

$$V_{l+1,m} = \sqrt{\frac{l(l+2)(l+m+1)(l+m+2)}{(2l+1)(2l+3)}}, \qquad c^+_{l,m} = \sqrt{(l-m)(l+m+1)}\,. \tag{C.7}$$

For scattering problems with a cylinder symmetry, it is convenient to introduce cylindrical force components: $\mathbf{F} = F_\rho\hat{\boldsymbol{\rho}} + F_\varphi\hat{\boldsymbol{\varphi}} + F_z\hat{\mathbf{z}}$. The transverse force components F_ρ and F_φ can be obtained from F_x and F_y by a simple rotation about the azimuthal angle φ, as shown below

$$F_\rho = \mathrm{Re}\left[(F_x - \mathrm{i}F_y)\mathrm{e}^{\mathrm{i}\varphi}\right], \qquad F_\varphi = \mathrm{Im}\left[(F_x + \mathrm{i}F_y)\mathrm{e}^{-\mathrm{i}\varphi}\right]. \tag{C.8}$$

C.2 Evaluation of the multipole expansion coefficients

We consider an electromagnetic field $\mathbf{E}(\mathbf{r})$ with the multipole expansion

$$\mathbf{E}(\mathbf{r}) = \sum_{l,m}\left[e_{l,m}\mathbf{N}^{\mathrm{reg}}_{l,m}(\mathbf{r}) + f_{l,m}\mathbf{M}^{\mathrm{reg}}_{l,m}(\mathbf{r})\right]. \tag{C.9}$$

In the following, we present the evaluation of the expansion coefficients $e_{l,m}$ and $f_{l,m}$. According to (3.9), the magnetic modes are given by $\mathbf{M}^{\mathrm{reg}}_{l,m}(\mathbf{r}) = j_l(Kr)\mathbf{X}_{l,m}(\hat{\mathbf{r}})$, where the vector spherical harmonic $\mathbf{X}_{l,m}(\hat{\mathbf{r}})$ is defined in Eq. (3.10). We make use of the orthonormality of the vector spherical harmonics an thus multiply (C.9) with $\mathbf{X}^*_{l',m'}(\hat{\mathbf{r}})$ and integrate over the unit sphere, which leads to

$$f_{l',m'} j_{l'}(Kr) = \int_{S^2} \mathrm{d}\Omega_r \mathbf{X}^*_{l',m'}(\hat{\mathbf{r}}) \cdot \mathbf{E}(\mathbf{r})\,. \tag{C.10}$$

Next, we use the Fourier representation of the electric field with

$$\mathbf{E}(\mathbf{r}) = \int \frac{\mathrm{d}^3\mathbf{K}'}{(2\pi)^3} \frac{\delta(K-K')}{(K')^2} \mathbf{E}(\mathbf{K}') \mathrm{e}^{\mathrm{i}\mathbf{K}'\cdot\mathbf{r}}\,, \tag{C.11}$$

where we accounted for the fact that the modulus of the wave vector $\mathbf{K}$ is conserved. We insert the above-given expansion into (C.10) and apply spherical coordinates

$$\begin{aligned} f_{l',m'} j_{l'}(Kr) &= \int_{S^2} \mathrm{d}\Omega_r \mathbf{X}^*_{l',m'}(\hat{\mathbf{r}}) \int_0^\infty \frac{\mathrm{d}K'}{(2\pi)^3} \delta(K-K') \int_{S^2} \mathrm{d}\Omega_{K'} \mathrm{e}^{\mathrm{i}\mathbf{K}'\cdot\mathbf{r}} \mathbf{E}(\mathbf{K}') \\ &= \int_0^\infty \frac{\mathrm{d}K'}{(2\pi)^3} \delta(K-K') \int_{S^2} \mathrm{d}\Omega_{K'} 4\pi \mathrm{i}^{l'} j_{l'}(K'r) \mathbf{X}^*_{l',m'}(\hat{\mathbf{K}}') \cdot \mathbf{E}(\mathbf{K}')\,. \end{aligned} \tag{C.12}$$

In the second step, we evaluated the integral over the unit sphere in $\mathbf{K}'$-space with [98, p. 226] and introduced the vector spherical harmonic in reciprocal space

$$\mathbf{X}_{l,m}(\hat{\mathbf{K}}) = \frac{-\mathrm{i}(\hat{\mathbf{K}} \times \nabla_K) Y_l^m(\hat{\mathbf{K}})}{\sqrt{(l(l+1))}} = \frac{\mathrm{i}}{\sqrt{(l(l+1))}} \left[\frac{\hat{\theta}_K}{\sin\theta_K} \frac{\partial}{\partial\phi_K} - \hat{\phi}_K \frac{\partial}{\partial\theta_K} \right] Y_l^m(\hat{\mathbf{K}})\,. \tag{C.13}$$

After carrying out the integral over K', we find the following expression for the magnetic multipole expansion coefficients, in terms of the Fourier components of a given electric field

$$f_{l,m} = \frac{\mathrm{i}^l}{2\pi^2} \int_{S^2} \mathrm{d}\Omega_{K'} \mathbf{X}_{l,m}(\hat{\mathbf{K}}') \cdot \mathbf{E}(\mathbf{K}')\,. \tag{C.14}$$

The electric multipole expansion coefficients can be obtained from a similar expansion but with the Fourier components of the magnetic field instead of the electric field: $\mathbf{E}(\mathbf{K}) \to (\mathrm{i}\omega/K)\mathbf{B}(\mathbf{K}) = \mathrm{i}\hat{\mathbf{K}} \times \mathbf{E}(\mathbf{K})$, where we used the Maxwell equations to rewrite the magnetic field in terms of the electric field.

In a plane-wave expansion, the electric field is expressed in terms of the polarisation unit vectors $\hat{e}_{\mathrm{TM}}$ and $\hat{e}_{\mathrm{TE}}$. We present the scalar product of the vector spherical harmonics $\mathbf{X}_{l,m}(\hat{\mathbf{K}})$ with the polarisation unit vectors, which are defined in Eq. (3.2). We obtain

$$\mathbf{X}_{l,m}(\hat{\mathbf{K}}) \cdot \hat{e}_{\mathrm{TM}}(\hat{\mathbf{K}}) = \frac{\mathrm{i}}{\sqrt{(l(l+1))}} \frac{1}{\sin\theta_K} \frac{\partial Y_l^m(\hat{\mathbf{K}})}{\partial\phi_K} \tag{C.15a}$$

$$= \frac{1}{2\sqrt{l(l+1)}} \Big[\cos\theta_K \left(c^+_{l,m} Y_l^{m+1}(\hat{\mathbf{K}}) \mathrm{e}^{-\mathrm{i}\phi_K} + c^-_{l,m} Y_l^{m-1}(\hat{\mathbf{K}}) \mathrm{e}^{\mathrm{i}\phi_K} \right) \tag{C.15b}$$

$$-2m \sin\theta_K Y_l^m(\hat{\mathbf{K}}) \Big]\,,$$

$$\mathbf{X}_{l,m}(\hat{\mathbf{K}}) \cdot \hat{e}_{\mathrm{TE}}(\hat{\mathbf{K}}) = -\frac{\mathrm{i}}{\sqrt{(l(l+1))}} \frac{\partial Y_l^m(\hat{\mathbf{K}})}{\partial \theta_K} \tag{C.16a}$$

$$= \frac{1}{2\sqrt{l(l+1)}} \left[-c^{+}_{l,m} Y_l^{m+1}(\hat{\mathbf{K}}) \mathrm{e}^{-\mathrm{i}\phi_K} + c^{-}_{l,m} Y_l^{m-1}(\hat{\mathbf{K}}) \mathrm{e}^{\mathrm{i}\phi_K} \right] , \tag{C.16b}$$

where in both cases, we applied recursion relations for the spherical harmonics [98] and introduced

$$c^{\pm}_{l,m} = \sqrt{(l \mp m)(l \pm m + 1)} \, . \tag{C.17}$$

C.3 Multipole expansion of a focused laser beam

In this Section, we evaluate the azimuthal part of the integral representation of the focused vortex beam. According to Eq. (5.18) is the integral given by

$$I = \int_0^{2\pi} \mathrm{d}\phi \mathrm{e}^{\mathrm{i}\mathbf{K}_{\mathrm{w}} \cdot \mathbf{R}} \mathrm{e}^{\mathrm{i}A_{\mathrm{ast}} \cos(2(\phi_{\mathrm{ast}} - \phi))} \mathrm{e}^{-\mathrm{i}M\phi} \, . \tag{C.18}$$

We use spherical coordinates to express the scalar product of the wave vector $\mathbf{K}_{\mathrm{w}}$ and the position vector $\mathbf{R}$ and get $\mathbf{K}_{\mathrm{w}} \cdot \mathbf{R} = K_{\mathrm{w}} r_R \left[\sin(\theta_{\mathrm{w}}) \sin(\theta_R) \cos(\phi - \varphi_R) + \cos(\theta_R) \cos(\theta_{\mathrm{w}})\right]$ with $\phi_{\mathrm{w}} = \phi$. To extract the ϕ-dependence from the argument of the cosine functions, we are going to apply the Jacobi-Anger expansion [185, Eq. 10.12.1]

$$\exp\left(\frac{z}{2}(t - t^{-1})\right) = \sum_{n=-\infty}^{\infty} t^n J_n(z) \, , \tag{C.19}$$

where $J_n(z)$ is the Bessel function of the first kind. Furthermore, we use the expansion of the cosine in terms of exponential functions: $\mathrm{i}\cos(\Phi) = (t - t^{-1})/2$ with $t = \mathrm{i}\mathrm{e}^{\mathrm{i}\Phi}$. In our case, Φ takes the values $\phi - \varphi_R$ and $2(\phi_{\mathrm{ast}} - \phi)$, which leads to the following expression

$$\begin{aligned} I = \mathrm{e}^{\mathrm{i}K_{\mathrm{w}} r_R \cos(\theta_R) \cos(\theta_w)} \sum_{s=-\infty}^{\infty} \mathrm{i}^s J_s(A_{\mathrm{ast}}) \mathrm{e}^{2\mathrm{i}s\phi_{\mathrm{ast}}} \sum_{n=-\infty}^{\infty} \mathrm{i}^n J_n(K_{\mathrm{w}} r_R \sin(\theta_w) \sin(\theta_R)) \mathrm{e}^{-\mathrm{i}n\varphi_R} \\ \times \int_0^{2\pi} \mathrm{d}\phi \mathrm{e}^{\mathrm{i}(n-2s-M)\phi} \, . \end{aligned} \tag{C.20}$$

Only terms with $n = 2s + M$ yield a non-vanishing contribution, and we find

$$I = 2\pi \mathrm{i}^M \mathrm{e}^{-\mathrm{i}M\varphi_R} \mathrm{e}^{\mathrm{i}K_{\mathrm{w}} z_R \cos(\theta_w)} \sum_{s=-\infty}^{\infty} (-\mathrm{i})^s J_s(A_{\mathrm{ast}}) J_{2s+M}(K\rho_R \sin(\theta)) \mathrm{e}^{2\mathrm{i}s(\phi_{\mathrm{ast}} - \varphi_R)} \, , \tag{C.21}$$

where we expressed the position vector $\mathbf{R}$ in cylindrical coordinates (ρ_R, z_R, φ_R) and applied Snell' Law: $K_{\mathrm{w}} \sin(\theta_{\mathrm{w}}) = K \sin(\theta)$.

D | Auxiliary calculations for the universal Casimir interaction

In this appendix, we provide details on the results of the Casimir free energy in the zero-frequency limit discussed in Chap. 9. We present the small-distance approximation of the Casimir free energy for Dirichlet and Drude spheres in vacuum (see Sec. D.1 and Sec. D.2). The calculation in both cases relies on the representation of the analytical expression in terms of the Lambert series. Furthermore, we are also discussing an alternative representation of the Casimir free energy between a Drude sphere and a plane in Sec. D.3.

D.1 Two Dirichlet spheres in close proximity to each other

We found that the dimensionless Casimir free energy for a scalar field between two Dirichlet spheres can be expressed in terms of the derivative of the difference between two Lambert series (9.25)

$$f_{\mathrm{sc}} = \frac{\mathrm{d}}{\mathrm{d}(-\mu)} \left[\mathcal{L}_{\exp(-\mu)}(-2,1) - \mathcal{L}_{\exp(-2\mu)}(-2,1)\right] \,, \tag{D.1}$$

where we replaced $Z = \exp(-\mu)$. The parameter μ, defined in Eq. (9.21) goes to zero in the short-distance limit, which means $\exp(-\mu) \to 1$. We can thus apply the expansion of the Lambert series given in Eq. (A.17). The difference between the two Lambert series yields

$$\begin{aligned}\mathcal{L}_{\exp(-\mu)}&(-2,1) - \mathcal{L}_{\exp(-2\mu)}(-2,1) = \\ &= \frac{\mu}{2}\left[2\zeta'(-1) + 2B_2\log(2) - B_2 + B_2\log(\mu)\right] + \frac{1}{\mu}\sum_{\substack{k=0\\k\neq 2}}^{\infty}\frac{\zeta(3-k)}{k!}B_k\left(2^{k-1}-1\right)(-\mu)^k \,.\end{aligned} \tag{D.2}$$

We introduced the Bernoulli numbers using $B_k(z=1) = B_k$. We extract the term for $k=0$ from the sum and use that the Bernoulli numbers of odd orders are zero. Furthermore, we express the Riemann zeta function for negative integer arguments in terms of the Bernoulli numbers by applying [185, Eq. 25.6.3]: $\zeta(-n) = (-1)^n B_{n+1}/(n+1)$. We thus obtain

$$\begin{aligned}\mathcal{L}_{\exp(-\mu)}&(-2,1) - \mathcal{L}_{\exp(-2\mu)}(-2,1) = \\ &= \frac{\zeta(3)}{2\mu} + \mu\left[-\log(A) + \frac{\log(2)}{6} + \frac{\log(\mu)}{12}\right] + \sum_{n=1}^{\infty}\frac{B_{2n}}{2n}\frac{B_{2n+2}}{(2n+2)!}\left(2^{2n+1}-1\right)\mu^{2n+1} \,,\end{aligned} \tag{D.3}$$

where we have rewritten the derivative of the Riemann zeta function according to [185, Eq. 5.17.7]: $\zeta'(-1) = -B_2/2 - \log(A)$, with the Glaisher–Kinkelin constant $A = 1.282\ldots$. After taking the negative derivative with respect to μ, the small-distance expansion of the dimensionless Casimir free energy for two Dirichlet spheres yields

$$f_{\mathrm{sc}} = \frac{\zeta(3)}{2\mu^2} - \frac{1}{12}\log(\mu) - \frac{1}{12} + \log(A) - \frac{1}{6}\log(2) - \sum_{n=1}^{\infty}\frac{2n+1}{2n}\frac{B_{2n}B_{2n+2}}{(2n+2)!}\left(2^{2n+1}-1\right)\mu^{2n} \,. \tag{D.4}$$

D.2 Two Drude sphere in close proximity to each other

In Section 9.3, we discussed that the Casimir free energy of two Drude spheres equals the free energy of two Dirichlet spheres minus the monopole contributions. Since we have already determined the small-distance expansion for the Dirichlet spheres in the previous Section, we will present the expansion of the monopole terms. We use the representation introduced in Eq. (9.66), which we display again below for convenience

$$\begin{aligned}\Delta = -\log\{&[1 + J(3/2 - v)\, I(3/2 - v)]\,[1 + J(3/2 + v)\, I(3/2 + v)] \\ &- J(3/2 - v)\, J(3/2 + v)\, I^2(1)\}\,.\end{aligned} \tag{D.5}$$

The auxiliary functions $J(c)$ and $I(c)$ are respectively defined in Eqs. (9.64) and (9.65), which we will present here again

$$J(c) = \frac{1 - \mathrm{e}^{-2\mu(c-1)}}{\mathrm{e}^{-\mu(c-1)}}\,, \qquad I(c) = \mathcal{L}_{\exp(-\mu)}(0, c) - \mathcal{L}_{\exp(-2\mu)}(0, c)\,, \tag{D.6}$$

where we replaced $Z = \exp(-\mu)$ and the variable c takes the values $3/2 \pm v(\mu)$ and 1. $v(\mu)$ was introduced in Eq. (9.63)

$$v(\mu) = \frac{1}{2} - \frac{1}{2\mu}\left[\log(1 + \alpha_+ \mathrm{e}^{\mu}) - \log(1 + \alpha_+ \mathrm{e}^{-\mu})\right] \tag{D.7}$$

with α_+ defined in Eq. (9.53), which accounts for the ratio of the sphere radii.

The following presents the Taylor expansions of the above-given terms in the short-distance limit for $\mu \to 0$. We first expand $v(\mu)$ in a power series in μ, which we then use for $J(c = 3/2 \pm v(\mu))$ and $I(c = 3/2 \pm v(\mu))$.

D.2.1 Expansion of $v(\mu)$

By adding a zero $(\alpha_+ - \alpha_+)$ to the argument of the logarithms in Eq. (D.7), we find

$$\begin{aligned}v(\mu) - \frac{1}{2} &= -\frac{1}{2\mu}\left[\log\left(1 - \frac{\alpha_+(1 - \mathrm{e}^{\mu})}{1 + \alpha_+}\right) - \log\left(1 - \frac{\alpha_+(1 - \mathrm{e}^{-\mu})}{1 + \alpha_+}\right)\right] \\ &= \frac{1}{2\mu}\sum_{k=1}^{\infty}\frac{1}{k}\left(\frac{\alpha_+}{1 + \alpha_+}\right)^k \left[(1 - \mathrm{e}^{\mu})^k - (1 - \mathrm{e}^{-\mu})^k\right]\,,\end{aligned} \tag{D.8}$$

where we used that $|1 - \mathrm{e}^{\pm\mu}| < 1$ in the short distance regime and thus applied the Mercator series to expand the logarithms. To proceed with the expansion of $v(\mu)$, we apply the binomial formula to $(1 - \mathrm{e}^{\pm\mu})^k$ and use the series expansion of the exponential. We thus find

$$\begin{aligned}(1 - \mathrm{e}^{\mu})^k - (1 - \mathrm{e}^{-\mu})^k &= 2\sum_{j=1}^{k}\binom{k}{j}(-1)^j \sum_{n=0}^{\infty}\frac{(\mu j)^{2n+1}}{(2n+1)!} \\ &= 2\mu\sum_{n=0}^{\infty}\frac{\mu^{2l}}{(2n+1)!}(-1)^k k!\, S(2n+1, k)\,.\end{aligned} \tag{D.9}$$

In the second step, we carried out the sum over j by applying the definition of the Stirling numbers of the second kind $S(n,k)$ [185, Eq. 26.8.6]. Inserting the expression given above into Eq. (D.8) and interchanging the sum over k and n, we obtain the following power series expansion for $v(\mu)$

$$v(\mu) = \sum_{n=0}^{\infty} v_n \mu^{2n}\,, \tag{D.10}$$

where the coefficients for $n = 0$ and $n > 0$ are respectively given by

$$v_0 = \frac{1}{2}\frac{1-\alpha_+}{1+\alpha_+} = \frac{\sqrt{1-4u}}{2}\,, \qquad v_n = \frac{1}{(2n+1)!}\sum_{k=0}^{2n} k!S(2n+1,k+1)\,(v_0 - 1/2)^{k+1} \tag{D.11}$$

with u defined in Eq. (8.4). For convenience, we present the explicit expression for the first two coefficients

$$v_1 = -\frac{v_0}{3}u\,, \qquad v_2 = -\frac{v_0}{60}u(1-12u)\,. \tag{D.12}$$

Similarly we introduce the expansion for the auxiliary function $c(\mu) = 3/2 \pm v(\mu)$

$$c(\mu) = \sum_{n=0}^{\infty} c_n \mu^{2n}\,, \qquad c_0 = \frac{3}{2} \pm v_0\,, \qquad c_n = \pm v_n\,. \tag{D.13}$$

Note that the expansion coefficients of $v(\mu)$ fulfil $|v_n| \leq |v_0|$. The upper bound of $|v(v)|$ in the small distance regime is thus given by 1/2, which means $|c(\mu) - 1| \leq 1$.

D.2.2 Expansion of $J(c)$

Next, we are going to discuss the expansion of $J(c)$ given in Eq. (D.6), which we express in terms of the hyperbolic sine

$$J\,(c(\mu)) = 2\sinh\left[\mu(c(\mu)-1)\right] = 2\sum_{n=0}^{\infty}\frac{\left[\mu(c(\mu)-1)\right]^{2n+1}}{(2n+1)!}\,. \tag{D.14}$$

Recalling that $|c(\mu) - 1| \leq 1$, we applied the series expansion of the hyperbolic sine in the second step. In the following, we are going to expand the argument $(c(\mu) - 1)^{2n+1}$ in a power series in μ. We thus first insert the series expansion of $c(\mu)$ given in Eq. (D.13), which yields

$$(c(\mu)-1)^{2n+1} = \frac{1}{\mu^{4n+2}}\left(\sum_{l=0}^{\infty} c_l \mu^{2l+2} - \mu^2\right)^{2n+1}\,. \tag{D.15}$$

A further simplification can be obtained by using the generating function of the partial ordinary Bell polynomials (A.18), which allows us to extract the μ dependence and find

$$\begin{aligned}(c(\mu)-1)^{2n+1} &= \frac{1}{\mu^{4n+2}}\sum_{m=2n+1}^{\infty} B^{\mathrm{o}}_{m,2n+1}(c_0-1,c_1,c_2,\ldots)\mu^{2m}\\ &= \frac{1}{\mu^{2n}}\sum_{m=n}^{\infty} B^{\mathrm{o}}_{m+n+1,2n+1}(c_0-1,c_1,c_2,\ldots)\mu^{2m}\,.\end{aligned} \tag{D.16}$$

Note that we shifted the sum over m by $n+1$ in the second step. We insert the expansion from above in Eq. (D.14) and interchange the m- and n-sum and thus find for the Taylor expansion of $J(c(\mu))$

$$J\left(c(\mu)\right) = 2\mu \sum_{m=0}^{\infty} J_m(c)\mu^{2m}\,, \qquad J_m(c) = \sum_{n=0}^{m} \frac{B^{\circ}_{m+n+1,2n+1}(c_0-1, c_1, c_2, \dots)}{(2n+1)!}\,. \tag{D.17}$$

The first three expansion coefficients of $J(c = 3/2 \pm v)$ are together with (D.13) given by

$$J_0(3/2 \pm v) = B^{\mathrm{o}}_{1,1} = c_0 - 1 = \left(\frac{1}{2} \pm v_0\right)\,, \tag{D.18a}$$

$$J_1(3/2 \pm v) = B^{\mathrm{o}}_{2,1} + \frac{B^{\mathrm{o}}_{3,3}}{6} = c_1 + \frac{(c_0-1)^3}{6} = \frac{1-3u}{6}\left(\frac{1}{2} \pm v_0\right)\,, \tag{D.18b}$$

$$\begin{aligned} J_2(3/2 \pm v) &= B^{\mathrm{o}}_{3,1} + \frac{B^{\mathrm{o}}_{4,3}}{6} + \frac{B^{\mathrm{o}}_{5,5}}{120} = c_2 + \frac{(c_0-1)c_1}{2} + \frac{(c_0-1)^5}{120} \\ &= \frac{1-15u(1-3u)}{120}\left(\frac{1}{2} \pm v_0\right)\,. \end{aligned} \tag{D.18c}$$

D.2.3 Expansion of $I(c)$

Next, we derive the series expansion of $I(c)$ given in Eq. (D.6). Similar to the discussion for the scalar result (see Sec. D.1), we apply the asymptotic expansion of the Lambert series given in Sec. A.4, which leads to the following result

$$I(c(\mu)) = \frac{1}{2\mu}\left[\log 2 - \log\mu - \psi(c(\mu)) + \sum_{n=1}^{\infty} \frac{B_{2n}(2^{2n}-2)}{2n(2n)!} B_{2n}(c(\mu))\mu^{2n}\right]\,. \tag{D.19}$$

We again applied $B_k(1) = B_k$ and $\zeta(-n) = (-1)^n B_{n+1}/(n+1)$ together with the fact that only Bernoulli numbers of even orders yield a non-vanishing contribution. In the following, we are deriving the expansions of the digamma function $\psi(c(\mu))$ and of the Bernoulli polynomials $B_{2n}(c(\mu))$.

Expansion of the digamma function $\psi(c)$

We rewrite the argument of the digamma function as $\psi(1 + c - 1)$ and apply the Taylor series for $|c-1| < 1$ [185, Eq. 5.7.4], which yields

$$\psi\left(c(\mu)\right) = -\gamma - \sum_{k=1}^{\infty} \zeta(k+1)(-1)^k \left(c(\mu) - 1\right)^k \tag{D.20}$$

with the Euler-Mascheroni constant $\gamma = 0.57721\ldots$. Next, we insert the power series of $c(\mu)$, defined in Eq. (D.13) and apply the binomial formula to $(c-1)^k$

$$\begin{aligned}(c(\mu)-1)^k &= (c_0-1)^k + \sum_{n=1}^{k}\binom{k}{n}(c_0-1)^{k-n}\left(\sum_{m=1}^{\infty} c_m\mu^{2m}\right)^n \\ &= (c_0-1)^k + \sum_{n=1}^{k}\binom{k}{n}(c_0-1)^{k-n}\sum_{m=n}^{\infty} B^{\circ}_{m,n}(c_1,c_2,\ldots)\mu^{2m}\,.\end{aligned} \tag{D.21}$$

In the second step, we used the generating function for the Bell polynomials. After inserting the expression from above in Eq. (D.20) and interchanging the sum over k and n, we get the following expansion for the digamma function $\psi(c(\mu))$

$$\psi(c(\mu)) = \psi(c_0) + \sum_{m=1}^{\infty}\sum_{n=1}^{m}\frac{\psi^{(n)}(c_0)}{n!}B^{\circ}_{m,n}(c_1,c_2,\ldots)\mu^{2m}, \tag{D.22}$$

where $\psi^{(n)}(z) = d^n\psi(z)/dz^n$ refers to the polygamma functions which are the n-th derivatives of the digamma function.

Expansion of the Bernoulli polynomial $B_{2n}(c)$

To proceed with the expansion of $I(c(\mu))$ given in Eq. (D.19), we also need to expand the Bernoulli polynomial $B_{2n}(c(\mu))$. First, we apply the definition of the Bernoulli polynomials as an expansion over Bernoulli numbers

$$B_{2n}\left(c(\mu)\right) = \sum_{k=0}^{2n}\binom{2n}{k}B_k\left(c(\mu)\right)^{2n-k}\,. \tag{D.23}$$

With the series expansion of $c(\mu)$ given in Eq. (D.13) and the generating function of the ordinary partial Bell polynomials (A.18), we find

$$\begin{aligned}(c(\mu))^{2n-k} &= \frac{1}{\mu^{4n-2k}}\left(\sum_{n=1} c_{n-1}\mu^{2n}\right)^{2n-k} \\ &= \frac{1}{\mu^{4n-2k}}\sum_{m=2n-k}^{\infty} B^{\circ}_{m,2n-k}(c_0,c_1,c_2,\ldots)\mu^{2m}\,.\end{aligned} \tag{D.24}$$

We shift the sum over m by $n-k$ and insert the expansion above in Eq. (D.23), which yields

$$\begin{aligned}B_{2n}\left(c(\mu)\right) &= \frac{1}{\mu^{2n}}\sum_{k=0}^{2n}\binom{2n}{k}B_k\sum_{m=n}^{\infty}B^{\circ}_{m+n-k,2n-k}(c_0,c_1,\ldots)\mu^{2m} \\ &= \frac{1}{\mu^{2n}}\sum_{k=-n}^{n}\binom{2n}{k+n}B_{k+n}\sum_{m=n}^{\infty}B^{\circ}_{m+k,n-k}(c_0,c_1,\ldots)\mu^{2m}\,.\end{aligned} \tag{D.25}$$

In the second step, the sum over k was shifted by $-n$. We insert the result from above into Eq. (D.19) and find

$$\sum_{n=1}^{\infty}\frac{B_{2n}(2^{2n}-2)}{2n(2n)!}B_{2n}(c(\mu))\mu^{2n}=\sum_{m=1}^{\infty}\sum_{n=1}^{m}\frac{B_{2n}(2^{2n}-2)}{2n}\sum_{k=-n}^{n}\frac{B_{n+k}B^{\circ}_{m-k,n-k}(c_0,c_1,\ldots)}{(n-k)!(n+k)!}\mu^{2m}\,, \tag{D.26}$$

where we exchanged the summation over n and m, thus leading to a power series in μ.

Summary of the expansion of $I(c)$

We insert the expansions of the digamma function (D.22) and the Bernoulli polynomials (D.26) into Eq. (D.19) and find

$$I(c)=\frac{1}{2\mu}\sum_{m=0}^{\infty}I_m(c)\mu^{2m}\,. \tag{D.27}$$

The expansion coefficient $I_0(c)$ is given by

$$I_0(c)=\gamma_1-\log\mu-\psi(c_0)-\gamma\,, \tag{D.28}$$

where we added the Euler-Mascheroni constant γ and introduced $\gamma_1 = \gamma+\log 2$. The coefficients with $m>0$ are determined by

$$I_m(c)=\sum_{n=1}^{m}\left[\frac{B_{2n}(2^{2n}-2)}{2n}\sum_{k=-n}^{n}\frac{B_{n+k}B^{\circ}_{m-k,n-k}(c_0,c_1,\ldots)}{(n-k)!(n+k)!}-\frac{\psi^{(n)}(c_0)}{n!}B^{\circ}_{m,n}(c_1,c_2,\ldots)\right]\,. \tag{D.29}$$

Again, we provide the explicit expressions of the first three expansion coefficients for convenience. For $c=1$, we obtain

$$I_0(1)=\gamma_1-\log\mu\,,\qquad I_1(1)=\frac{1}{72}\,,\qquad I_2(1)=\frac{7}{43200} \tag{D.30}$$

and the first three coefficients for $c=3/2\pm v$ yield

$$I_0(3/2\pm v)=\gamma_1-\log\mu-\Psi_0^{(\pm)}\,, \tag{D.31a}$$

$$I_1(3/2\pm v)=-\Psi_1^{(\pm)}+\frac{1}{72}+\frac{2-u}{12}-\frac{1}{6}\left(\frac{1}{2}\mp v_0\right)\,, \tag{D.31b}$$

$$I_2(3/2\pm v)=-\Psi_2^{(\pm)}+\frac{7}{43200}-\frac{28+4u-73u^2}{1440}+\frac{7+13u}{360}\left(\frac{1}{2}\mp v_0\right)\,, \tag{D.31c}$$

where we introduced the abbreviation $\Psi_n^{(\pm)}$, which accounts for the coefficients of the Taylor expansion of the digamma function presented in Eq. (D.22)

$$\Psi_0^{(\pm)}=\psi^{(0)}(3/2\pm v_0)+\gamma\,, \tag{D.32a}$$

$$\Psi_1^{(\pm)}=\pm v_1\psi^{(1)}(3/2\pm v_0)\,, \tag{D.32b}$$

$$\Psi_2^{(\pm)}=\pm v_2\psi^{(1)}(3/2\pm v_0)+v_1^2\psi^{(2)}(3/2\pm v_0)/2\,. \tag{D.32c}$$

D.2.4 Leading expressions of the short-distance expansion

We summarize all results from above to determine the short-distance expansion of the monopole term. The variable μ is small for short distances. Hence, considering only terms up to the order of μ^4 is sufficient. We write $J(c) \approx 2\mu(J_0 + J_1\mu^2 + J_2\mu^4)$ with J_m given in Eq. (D.18) and $I(c) \approx (I_0 + I_1\mu^2 + I_2\mu^4)/(2\mu)$ with I_m given in Eq. (D.30) and (D.31) and insert the expansions into (D.5). After some algebraic transformations, we find the following small-distance expansion of the monopole terms

$$\Delta = -\log\left[\sum_{n=0}^{2} \frac{\epsilon_n(u)(\gamma_1 - \log\mu) + \delta_n(u)}{(2n+1)!}\mu^{2n} + O(\mu^6)\right] \tag{D.33}$$

with the expansion coefficients $\epsilon_n(u)$ and $\delta_n(u)$, which are only functions of the geometry parameter u. The zero-order coefficients are given by

$$\epsilon_0(u) = 1 - u\varphi_{0,0}\,, \tag{D.34a}$$

$$\delta_0(u) = 1 - \varphi_{0,1} + \frac{u}{2}\theta_{0,0} \tag{D.34b}$$

and the coefficients of the first-order yield

$$\epsilon_1(u) = (1-3u)(1-2u\varphi_{0,0}) + u(1-u-6\varphi_{1,0})\,, \tag{D.35a}$$

$$\begin{aligned}\delta_1(u) = {}& \frac{13-30u}{12} - 6\varphi_{1,1} + (1-3u)(u\theta_{0,0} - \varphi_{0,1})\\ &+ u\left[6\theta_{0,1} - \frac{13-6u}{12}\varphi_{0,0} + \varphi_{0,1}\right].\end{aligned} \tag{D.35b}$$

The second-order coefficients yield

$$\begin{aligned}\epsilon_2(u) = {}& -120u\varphi_{2,0} - \frac{u(14-22u-73u^2)}{6}\\ &+ (1-15u(1-3u))(1-2u\varphi_{0,0}) - \frac{10u(1-3u)^2}{3}\varphi_{0,0}\\ &+ \frac{20u(1-3u)}{3}(1-u-6\varphi_{1,0})\,,\end{aligned} \tag{D.36a}$$

$$\begin{aligned}\delta_2(u) = {}& \frac{10(1-3u)}{3}\left[\frac{13-30u}{12} - 6\varphi_{1,1}\right] + 120(u\theta_{0,2} - \varphi_{2,1})\\ &- \frac{833+120u-2190u^2}{360}(1-u\varphi_{0,0}) + \frac{u(7+13u)}{3}(2-\varphi_{0,1})\\ &- (1-15u(1-3u))(\varphi_{0,1} - u\theta_{0,0}) + \frac{5u(1-3u)^2}{3}\theta_{0,0}\\ &+ \frac{20u(1-3u)}{3}\left[6\theta_{0,1} - \frac{13-6u}{12}\varphi_{0,0} + \varphi_{0,1}\right]\\ &+ 60u\theta_{1,1} - \frac{5u(13-6u)}{3}\varphi_{1,0} + 20u\varphi_{1,1} + \frac{5u(1+5u+3u^2)}{18}\,.\end{aligned} \tag{D.36b}$$

We introduced abbreviations for the sums of the polygamma functions

$$\varphi_{n,m} = (1/2 + v_0)^m \Psi_n^{(+)} + (1/2 - v_0)^m \Psi_n^{(-)} . \tag{D.37}$$

For the products of polygamma functions, we defined

$$\theta_{n,m} = \Psi_n^{(+)} \Psi_m^{(-)} + \Psi_m^{(+)} \Psi_n^{(-)} . \tag{D.38}$$

Note that for the two limiting cases, $u = 0$ for the sphere-plane geometry and $u = 1/4$ for equal spheres, the coefficients v_1 and v_2 introduced in Eq. (D.12) vanish. Hence, $\varphi_{1,m}$ and $\varphi_{2,m}$ yield zero and all $\theta_{n,m}$ except for $\theta_{0,0}$ vanish. The resulting values for ϵ_n and δ_n are presented in Tab. 9.2.

D.3 Resummation of the plane-sphere result

Here, we compare our result for the monopole contribution in the plane-sphere geometry, given in Eq. (9.62) with the result reported in Ref. [24]. First, we expand our result by a factor $(1 - Z)$, which leads to

$$\Delta^{u=0} + \log(1 - Z) = \log \left[1 - Z + (1 - Z^2) \sum_{l=0}^{\infty} \frac{(1 - Z) Z^{4l+1}}{1 - Z^{2l+1}} \right] . \tag{D.39}$$

Next, we make use of the fact that $Z = \exp(-\mu) < 1$ and introduce the geometrical series $(1 - Z^2)^{-1} = \sum_{l=0}^{\infty} Z^{2l}$

$$\Delta^{u=0} + \log(1 - Z) = \log \left[1 - Z(1 - Z^2) \sum_{l=0}^{\infty} Z^{2l} + (1 - Z^2) \sum_{l=0}^{\infty} \frac{(1 - Z) Z^{4l+1}}{1 - Z^{2l+1}} \right] . \tag{D.40}$$

Finally, by summarizing the terms in the argument of the logarithm, we obtain

$$\Delta^{u=0} + \log(1 - Z) = \log \left[1 - \sum_{l=1}^{\infty} \frac{(1 - Z^2)(1 - Z^{2l}) Z^{2l+1}}{1 - Z^{2l+1}} \right] \tag{D.41}$$

which agrees with the result found by [24].

E | Auxiliary calculation for the round-trip approximation of the Casimir free energy

In this appendix, we provide additional information on the calculation of the triple round-trip expression of the Casimir free energy between a dielectric sphere and plane in an electrolyte.

We introduced the reflection matrix elements for a dielectric sphere in an electrolyte in Eq. (9.71) and the reflection matrix for a planar surface are given by the Fresnel coefficient (B.11) in the limit $\epsilon_\mathrm{s}/\epsilon_\mathrm{m} \to 0$ which yields: $\langle \mathbf{k}_j, \mathrm{TM}|\mathcal{R}_\mathrm{de}|\mathbf{k}_i, \mathrm{TM}\rangle = -1\delta^{(2)}(\mathbf{k}_i - \mathbf{k}_j)$. Inserting the reflection matrix elements in the trace expression, which is derived in Eq. (9.3), and performing the same variable transformation as we did for the sphere-sphere geometry in Sec. 9.4.1, we find for the trace over the 3-fold round-trip operator

$$\mathrm{tr}\mathcal{M}^3_\mathrm{ded} = \frac{\rho^3}{(2\pi)^3}\int_0^1 \mathrm{d}^3\mathbf{t}\int \mathrm{d}^3\mathbf{x}\int \mathrm{d}^3\mathbf{y}\,\mathrm{e}^{-x_1^2-x_2^2-x_3^2}\mathrm{e}^{-y_1^2-y_2^2-y_3^2}\prod_{i=1}^{3}\left[\cosh(\chi_i) - 2t_i\cosh(t_i\chi_i)\right] , \tag{E.1}$$

where the argument of the hyperbolic cosine is given by $\chi_i = \rho(x_i x_{i+1} + y_i y_{i+1})$ with $\rho = R/\mathcal{L}$. Note that $\mathcal{L} = R + L$ in the sphere-plane geometry. Similar to our discussion for the sphere-sphere geometry, the trace expression above is given by Gaussian-type integrals with the bilinear form

$$\mathbf{M}_3^{\pm}(\mathbf{t}) = \begin{pmatrix} 1 & \pm a t_1 & \pm a t_3 \\ \pm a t_1 & 1 & \pm a t_2 \\ \pm a t_3 & \pm a t_2 & 1 \end{pmatrix} , \qquad a = \rho/2\,. \tag{E.2}$$

For convenience, we introduced the variable $a = \rho/2$, which is related to the conformal distance scale $y = 1/\rho = 1 + L/R$, defined in Eq. (9.16), by

$$a = 1/2y\,. \tag{E.3}$$

After evaluating the Gaussian integral with (A.28), we obtain

$$\begin{aligned}\mathrm{tr}\mathcal{M}^3_\mathrm{ded} &= 4a^3\sum_{\sigma=\pm}\int \mathrm{d}^3\mathbf{t}\, t_1 t_2 t_3 \frac{\prod_{j=1}^{3}[\delta(t_j - 1) - 1]}{1 - a^2(t_1^2 + t_2^2 + t_3^2 + 2\sigma a t_1 t_2 t_3)} \\ &\equiv I_0 + I_1 + I_2 + I_3\,,\end{aligned} \tag{E.4}$$

where $\mathbf{t}^t = (t_1, t_2, t_3)$. After expanding the product over the δ-functions, we obtain four integrals denoted as I_k, which will be evaluated in the following. First, we compute the integral I_0, corresponding to the term with a product of four δ-functions. We thus obtain

$$I_0 = \frac{a^3}{2}\sum_{\sigma=\pm}\frac{1}{1 - a^2(3 + 2\sigma a)} = \frac{1}{2}\frac{y(4y^2 - 3)}{(4y^2 - 1)^2(y^2 - 1)}\,, \tag{E.5}$$

where we used Eq. (E.3) in the second step to express I_0 in terms of y. Note that this term agrees with the trace over the round-trip operator for a scalar field between the sphere and plane $I_0 = \mathrm{tr}\mathcal{M}^3_\mathrm{sc}$. Next, we discuss the term I_1, which corresponds to three integrals, each with a product of two δ-functions in the integrand. After carrying out the integral over the δ-functions, we obtain

$$\begin{aligned} I_1 &= -3a \sum_{\sigma=\pm} \int_0^1 \mathrm{d}t \frac{t}{1-a^2(2+t^2+2\sigma a t)} \\ &= \frac{3a}{2(1-a^2)} \left[2(1-a^2)\log(1-a^2) - 2(1-2a^2)\log(1-2a^2) + (1-2a^2)\log(1-4a^2) \right] , \end{aligned} \tag{E.6}$$

where we evaluated the integral over t by factorizing the denominator and applying (A.12). The term I_2 is given by three integrals, but with only one δ-function in the integrand, which thus leads to the following two-dimensional integral

$$I_2 = 6a^3 \sum_{\sigma=\pm} \int_0^1 \mathrm{d}^2\mathbf{t} \, \frac{t_1 t_2}{1-a^2\left(1+t_1^2+t_2^2+2\sigma a t_1 t_2\right)} \, . \tag{E.7}$$

The first integral over the rational function can be directly evaluated and leads to

$$\begin{aligned} I_2 = -\frac{3}{a} \int_0^\alpha \mathrm{d}\theta \Big\{ & \sin(\theta)\cos(\theta) \big[\log(\cos(\theta+2\alpha)\cos(\theta-2\alpha)) + 2\log(\cos(\theta)) \\ & \qquad - 2\log(\cos(\theta+\alpha)\cos(\theta-a)) \big] \\ & + \sin^2(\theta)\tan(\alpha) \left[2\log\left(\frac{\cos(\theta+\alpha)}{\cos(\theta-\alpha)}\right) - \log\left(\frac{\cos(\theta+2\alpha)}{\cos(\theta-2\alpha)}\right) \right] \Big\} , \end{aligned} \tag{E.8}$$

where we performed the following variable transformation

$$t = \sin(\theta)/a \tag{E.9}$$

with the upper integration limit given by $\alpha = \arcsin(a)$. The integral over the term in the first and second line can be obtained by integrating by parts, while for the integral over the expression in the third line we are using a variation of the integral representation of the imaginary part of the dilogarithm, which is given by [185, Eqs. 25.12.7 and 25.12.9]

$$\mathrm{Im}\left[\mathrm{Li}_2(-\mathrm{e}^{2\mathrm{i}\gamma})\right] = -2 \int_0^\gamma \mathrm{d}u \log\left(2\cos(u)\right) \, . \tag{E.10}$$

In summary, the integral I_2 yields

$$\begin{aligned} I_2 = \frac{3}{4a} \Big\{ & 8(1-a^2)\log(1-a^2) - 8(1-2a^2)\log(1-2a^2) + 2(1-4a^2)\log(1-4a^2) \\ & - \frac{a}{\sqrt{1-a^2}} \mathrm{Im}\left[\mathrm{Li}_2(-\mathrm{e}^{6\mathrm{i}\alpha}) - 4\mathrm{Li}_2(-\mathrm{e}^{4\mathrm{i}\alpha}) + \mathrm{Li}_2(-\mathrm{e}^{2\mathrm{i}\alpha})\right] \Big\} . \end{aligned} \tag{E.11}$$

Finally, we compute the integral I_3, which is given by

$$I_3 = -4a^3 \sum_{\sigma=\pm} \int_0^1 \mathrm{d}^3\mathbf{t} \, \frac{t_1 t_2 t_3}{1-a^2\left(t_1^2+t_2^2+t_3^2+2\sigma a t_1 t_2 t_3\right)} \, . \tag{E.12}$$

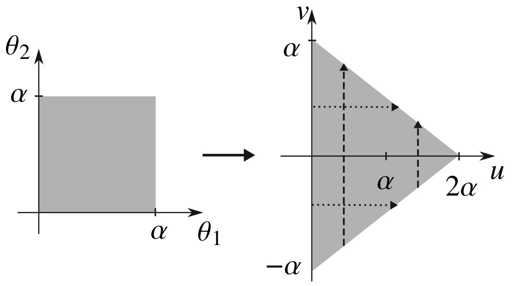

Figure E.1: Illustration of the coordinate transformation $(\theta_1, \theta_2) \to (u, v)$ defined in Eq. (E.14). The grey-shaded areas depict the integration interval. The dashed and dotted arrows illustrate the integration directions defined in Eqs. (E.15) and (E.16).

First, we evaluate the integral over t_3 and then transform the $t_{1,2}$-integrals with (E.9), which lead to

$$I_3 = \frac{1}{a^3}\int_0^\alpha \mathrm{d}\theta_1 \int_0^\alpha \mathrm{d}\theta_2 \Bigg\{ \left[\cos(u)\cos(v) - \cos^2(u)\right] \log\left(\frac{\cos(u-\alpha)\cos(u+\alpha)}{\cos^2(u)}\right) - \left[\cos(u)\cos(v) - \cos^2(v)\right] \log\left(\frac{\cos(v-\alpha)\cos(v+\alpha)}{\cos^2(v)}\right) \Bigg\}, \tag{E.13}$$

where the arguments of the cosines only depend on the sum and difference of θ_1 and θ_2

$$u = \theta_1 + \theta_2, \qquad v = \theta_1 - \theta_2 \,. \tag{E.14}$$

It is thus convenient to transform the integral over θ_1, θ_2 to an integral over u, v, as illustrated in Fig. E.1. There are two ways to change the integration limits when using the new variables, both given below

$$\int_0^\alpha \mathrm{d}\theta_1 \int_0^\alpha \mathrm{d}\theta_2 f(\theta_1+\theta_2, \theta_1-\theta_2) =$$

$$= \frac{1}{2}\left[\int_0^\alpha \mathrm{d}u \int_{-\alpha+u}^{\alpha-u} \mathrm{d}v + \int_\alpha^{2\alpha} \mathrm{d}u \int_{u-2\alpha}^{-u+2\alpha} \mathrm{d}v\right] f(u,v) \tag{E.15}$$

$$= \frac{1}{2}\left[\int_{-\alpha}^0 \mathrm{d}v \int_{-v}^{v+2\alpha} \mathrm{d}u + \int_0^\alpha \mathrm{d}v \int_v^{-v+2\alpha} \mathrm{d}u\right] f(u,v) \,. \tag{E.16}$$

Inserting the above given transformations into (E.13) and upon employing (E.10), we find after some algebraic transformations

$$\begin{aligned} I_3 = \frac{1}{8a^3}\Big\{ &\mathrm{Re}\left[6\mathrm{Li}_3(-\mathrm{e}^{4\mathrm{i}\alpha}) - 15\mathrm{Li}_3(-\mathrm{e}^{2\mathrm{i}\alpha}) + 10\mathrm{Li}_3(-1) - \mathrm{Li}_3(-\mathrm{e}^{6\mathrm{i}\alpha})\right] \\ &- 2a\sqrt{1-a^2}\,\mathrm{Im}\left[3\mathrm{Li}_2(-\mathrm{e}^{6\mathrm{i}\alpha}) - 12\mathrm{Li}_2(-\mathrm{e}^{4\mathrm{i}\alpha}) + 15\mathrm{Li}_2(-\mathrm{e}^{2\mathrm{i}\alpha})\right] \\ &+ 24(1-a^2)(2-a^2)\log(1-a^2) - 12(1-2a^2)(3-2a^2)\log(1-2a^2) \\ &+ 6(1-a^2)(1-4a^2)\log(1-4a^2)\Big\} \,. \end{aligned} \tag{E.17}$$

Combining (E.5), (E.6), (E.11) and (E.17), the trace over the 3-fold round-trip matrix yields

$$\begin{aligned}\mathrm{tr}\mathcal{M}_{\mathrm{ded}}^3 = \frac{1}{2}\frac{y(4y^2-3)}{(4y^2-1)^2(y^2-1)} + \frac{y}{2(4y^2-1)}\Bigg\{&12(32y^4-12y^2+1)\log\left(1-\frac{1}{4y^2}\right)\\ &-12(24y^4-14y^2+1)\log\left(1-\frac{1}{2y^2}\right)\\ &+3(16y^4-16y^2+1)\log\left(1-\frac{1}{y^2}\right)\\ &-2y^2(4y^2-1)\mathrm{Re}\left[\mathrm{Li}_3(-\mathrm{e}^{6\mathrm{i}\alpha})-6\mathrm{Li}_3(-\mathrm{e}^{4\mathrm{i}\alpha})+15\mathrm{Li}_3(-\mathrm{e}^{2\mathrm{i}\alpha})-10\mathrm{Li}_3(-1)\right]\\ &-12y^2\sqrt{4y^2-1}\mathrm{Im}\left[\mathrm{Li}_2(-\mathrm{e}^{6\mathrm{i}\alpha})-4\mathrm{Li}_2(-\mathrm{e}^{4\mathrm{i}\alpha})+5\mathrm{Li}_2(-\mathrm{e}^{2\mathrm{i}\alpha})\right]\Bigg\}\end{aligned} \tag{E.18}$$

with

$$\mathrm{e}^{2\mathrm{i}\alpha} = 1-2a^2+2\mathrm{i}a\sqrt{1-a^2} = \frac{2y^2-1+\mathrm{i}\sqrt{4y^2-1}}{2y^2}\,, \tag{E.19}$$

where we used the relation (E.3) to express the final result in terms of y.

F | Auxiliary calculation for the next-to-leading order in the saddle-point approximation

In this Section, we are going to derive the remaining contributions from the next-to-leading order of the saddle-point approximation of the Casimir free energy. According to our discussion in Sec. 10.2, the remaining parts of the saddle-point approximation are given by

$$\mathcal{F}^{(ii)}_{\mathrm{NTLO}}(\xi) = -\sum_{r=1}^{\infty} \frac{[\mathrm{tr}\mathcal{M}^r]^{(ii)}_{\mathrm{NTLO}}}{r}\,, \qquad [\mathrm{tr}\mathcal{M}^r]^{(ii)}_{\mathrm{NTLO}} = \frac{\pi R_{\mathrm{eff}}}{2r}\int \frac{\mathrm{d}^2\mathbf{k}_{\mathrm{sp}}}{(2\pi)^2}\kappa_{\mathrm{sp}}^{2r-1} g^{(b)}_{ij} M^{-1}_{i,j}\,, \tag{F.1}$$

where the integrand is given by (10.69)

$$g^{(b)}_{ij} M^{-1}_{i,j} = \frac{\mathrm{e}^{-2r\kappa_{\mathrm{sp}}L}}{\kappa_{\mathrm{sp}}^{2r}} \sum_{p_1,\dots,p_{2r}} \sum_{m,n=1}^{2r} d_\sigma(m-n) \sum_{\alpha=x,y} \frac{\partial^2}{\partial k_{m,\alpha}\partial k_{n,\alpha}} \left(\prod_{j=1}^{r} \rho^{(1)}_{p_{2j+1},p_{2j}} \rho^{(2)}_{p_{2j},p_{2j-1}} \right)_{\mathrm{sp}}\,. \tag{F.2}$$

The function $d_\sigma(k)$ arises from the Fourier transform of $M^{-1}_{i,j}$ and is defined in Eq. (10.56).

F.1 Derivatives of $\rho_{p,p'}$

Here, we present the derivatives of the function $\rho_{p,p'} = \rho_{p,p'}(\mathbf{k}_i, \mathbf{k}_j)$. According to Eq. (10.5) is $\rho_{p,p'}$ defined by

$$\rho_{p,p'} = A_{i,j} r_{p,p'} + (-1)^{p+p'} B_{i,j} r_{\bar{p},\bar{p}'} - (-1)^{p} C_{i,j} r_{\bar{p},p} + (-1)^{p'} D_{i,j} r_{p,\bar{p}'}\,. \tag{F.3}$$

Recall that $p = \mathrm{TE}\,(\mathrm{TM})$ is identified with 1 (2) in the exponents, and $\bar{p}$ denotes the 'opposite' polarisation of p. The Fresnel reflection coefficients $r_{p,p'} = r_{p,p'}(\mathbf{k}_i, \mathbf{k}_j)$ are defined in Eq. (B.11), while the polarisation-conversion coefficients $A_{i,j}$, $B_{i,j}$, $C_{i,j}$ and $D_{i,j}$ can be found in Eq. (4.29). First, we provide the derivatives of the polarisation-conversion coefficients evaluated at the saddle point (sp): $\mathbf{k}_i = \mathbf{k}_j = \mathbf{k}_{\mathrm{sp}}$. The single derivatives yield

$$\left.\frac{\partial C_{i,j}}{\partial k_{i,\alpha}}\right|_{\mathrm{sp}} = \pm\mathcal{K}\frac{k_{\mathrm{sp},\bar{\alpha}}}{2\kappa_{\mathrm{sp}}k_{\mathrm{sp}}^2} = -\left.\frac{\partial C_{i,j}}{\partial k_{j,\alpha}}\right|_{\mathrm{sp}} = -\left.\frac{\partial D_{i,j}}{\partial k_{i,\alpha}}\right|_{\mathrm{sp}} = \left.\frac{\partial D_{i,j}}{\partial k_{j,\alpha}}\right|_{\mathrm{sp}}\,, \tag{F.4}$$

where $\bar{\alpha} = y$ for $\alpha = x$ and vice versa. The upper (lower) sign corresponds to an incoming plane wave propagating in positive (negative) z-direction. The first derivatives of $A_{i,j}$ and $B_{i,j}$ vanish at the saddle point. For the double derivatives, we find

$$\sum_{\alpha=x,y}\left.\frac{\partial^2 A_{i,j}}{\partial k_{i,\alpha}^2}\right|_{\mathrm{sp}} = -\frac{\mathcal{K}^2}{2\kappa_{\mathrm{sp}}^2 k_{\mathrm{sp}}^2} = -\sum_{\alpha=x,y}\left.\frac{\partial^2 A_{i,j}}{\partial k_{i,\alpha}\partial k_{j,\alpha}}\right|_{\mathrm{sp}} = -\sum_{\alpha=x,y}\left.\frac{\partial^2 B_{i,j}}{\partial k_{i,\alpha}^2}\right|_{\mathrm{sp}} = \sum_{\alpha=x,y}\left.\frac{\partial^2 B_{i,j}}{\partial k_{i,\alpha}\partial k_{j,\alpha}}\right|_{\mathrm{sp}}\,. \tag{F.5}$$

Note, if both derivatives are taken at the second argument ($k_{j,\alpha}$), we yield the same result as for the derivatives taken at the first argument ($k_{i,\alpha}$). The derivatives of $C_{i,j}$ and $D_{i,j}$ yield

$$\sum_{\alpha=x,y} \left.\frac{\partial^2 C_{i,j}}{\partial k_{i,\alpha}^2}\right|_{\text{sp}} = \pm\frac{\mathcal{K}}{2\kappa_{\text{sp}}k_{\text{sp}}^2}\left[\frac{3\sin(2\phi_{\text{sp}})}{\kappa_{\text{sp}}^2}(\kappa_{\text{sp}}^2+k_{\text{sp}}^2)-2\right] = \sum_{\alpha=x,y} \left.\frac{\partial^2 D_{i,j}}{\partial k_{j,\alpha}^2}\right|_{\text{sp}}\,, \tag{F.6a}$$

$$\sum_{\alpha=x,y} \left.\frac{\partial^2 C_{i,j}}{\partial k_{j,\alpha}^2}\right|_{\text{sp}} = \pm\frac{\mathcal{K}}{2\kappa_{\text{sp}}k_{\text{sp}}^2}\left[2-\frac{\sin(2\phi_{\text{sp}})}{\kappa_{\text{sp}}^2}(5\kappa_{\text{sp}}^2+3k_{\text{sp}}^2)\right] = \sum_{\alpha=x,y} \left.\frac{\partial^2 D_{i,j}}{\partial k_{i,\alpha}^2}\right|_{\text{sp}}\,, \tag{F.6b}$$

$$\sum_{\alpha=x,y} \left.\frac{\partial^2 C_{i,j}}{\partial k_{j,\alpha}\partial k_{i,\alpha}}\right|_{\text{sp}} = \pm\mathcal{K}\frac{\sin(2\phi_{\text{sp}})}{\kappa_{\text{sp}}k_{\text{sp}}^4} = \sum_{\alpha=x,y} \left.\frac{\partial^2 D_{i,j}}{\partial k_{j,\alpha}\partial k_{i,\alpha}}\right|_{\text{sp}}\,. \tag{F.6c}$$

We integrate over the azimuth angle ϕ_{sp} in Eq. (F.1), hence all terms proportional to $\sin(2\phi_{\text{sp}})$ vanish and will thus be disregarded in the following. With the above-obtained expressions for the derivatives of the polarisation-conversion coefficients, we are able to derive the derivatives of $\rho_{p,p'}$. Derivatives with respect to a single component yield

$$\left.\frac{\partial \rho_{p,p'}}{\partial k_{i,\alpha}}\right|_{\text{sp}} = (r_{p,p'})_i \pm (-1)^{p-1}\frac{\mathcal{K}k_{\text{sp},\bar\alpha}}{2\kappa_{\text{sp}}k_{\text{sp}}^2}\left[r_{\bar p,p'}+(-1)^{p-p'}r_{p,\bar p'}\right]\,, \tag{F.7a}$$

$$\left.\frac{\partial \rho_{p,p'}}{\partial k_{j,\alpha}}\right|_{\text{sp}} = (r_{p,p'})_j \mp (-1)^{p-1}\frac{\mathcal{K}k_{\text{sp},\bar\alpha}}{2\kappa_{\text{sp}}k_{\text{sp}}^2}\left[r_{\bar p,p'}+(-1)^{p-p'}r_{p,\bar p'}\right]\,. \tag{F.7b}$$

All expressions are evaluated at the saddle point and for simplicity, we abbreviate the derivatives of the Fresnel reflection coefficients $\left(\partial_{k_{i,\alpha}} r_{p,p'}\right)_{\text{sp}}$ by $(r_{p,p'})_i$. For the double derivatives, we find

$$\begin{aligned}\sum_{\alpha=x,y} \left.\frac{\partial^2 \rho_{p,p'}}{\partial k_{i,\alpha}^2}\right|_{\text{sp}} &= \frac{\mathcal{K}^2}{2\kappa_{\text{sp}}^2k_{\text{sp}}^2}\left(-r_{p,p'}+(-1)^{p-p'}r_{\bar p,\bar p'}\right)+\left(r_{p,p'}\right)_{ii} \\ &\quad \pm(-1)^p\frac{\mathcal{K}}{\kappa_{\text{sp}}k_{\text{sp}}^2}\left(r_{\bar p,p'}+(-1)^{p-p'}r_{p,\bar p'}\right)\,,\end{aligned} \tag{F.8a}$$

$$\begin{aligned}\sum_{\alpha=x,y} \left.\frac{\partial^2 \rho_{p,p'}}{\partial k_{j,\alpha}^2}\right|_{\text{sp}} &= \frac{\mathcal{K}^2}{2\kappa_{\text{sp}}^2k_{\text{sp}}^2}\left(-r_{p,p'}+(-1)^{p-p'}r^{(t)}_{\bar p,\bar p'}\right)+\left(r_{p,p'}\right)_{jj} \\ &\quad \mp(-1)^p\frac{\mathcal{K}}{\kappa_{\text{sp}}k_{\text{sp}}^2}\left(r_{\bar p,p'}+(-1)^{p-p'}r_{p,\bar p'}\right)\,,\end{aligned} \tag{F.8b}$$

$$\sum_{\alpha=x,y} \left.\frac{\partial^2 \rho_{p,p'}}{\partial k_{j,\alpha}\partial k_{i,\alpha}}\right|_{\text{sp}} = \frac{\mathcal{K}^2}{2\kappa_{\text{sp}}^2k_{\text{sp}}^2}\left(r_{p,p'}-(-1)^{p-p'}r_{\bar p,\bar p'}\right)+\left(r_{p,p'}\right)_{ij}\,, \tag{F.8c}$$

where we also performed the sum over α as defined in Eq. (F.2).

F.2 General definitions

We already discussed in Sec. 10.2, that there are two types of terms in Eq. (F.2), which are also illustrated in Fig. 10.4. On the one hand, there are terms where we take both derivatives at one sphere during the r round-trips. We denote these terms with I in the following. They are illustrated in the left panel of Fig. 10.4. On the other hand, the two derivatives can also be taken at different points during the r round-trips as it is depicted in the right panel of Fig. 10.4. We denote these terms with J, so in total we write (F.2) as

$$g_{ij}^{(b)} M_{ij}^{-1} = I + J\,. \tag{F.9}$$

Before, we proceed with the evaluation of the two terms, we introduce the following notation for the derivatives of $\rho^{(t)}_{p_i,p_j}(\mathbf{k}_i, \mathbf{k}_j)$

$$d^{(t);1,2}_{p_i,p_j} = \frac{\left(\rho^{(t)}_{p_i,p_j}(\mathbf{k}_i, \mathbf{k}_j)\right)_{ij}}{r^{(t)}_{p_i,p_j}}\,. \tag{F.10}$$

The superscript takes values $t = 1, 2$ and distinguishes between spheres 1 and 2. The other superscripts determine whether the derivatives are taken with respect to the first or second argument of $\rho^{(t)}_{p_i,p_j}(\mathbf{k}_i, \mathbf{k}_j)$. Hence, the 1 denotes the derivative with respect to $k_{i,\alpha}$ and 2 the derivative with respect to $k_{j,\alpha}$. Moreover, we introduce for the products of Fresnel reflection coefficients (evaluated at the saddle point)

$$X_r^{(1,2)} = \prod_{j=1}^{r} r^{(1)}_{p_{2j-1},p_{2j}} r^{(2)}_{p_{2j},p_{2j+1}}\,. \tag{F.11}$$

The order of $r^{(t)}_{p,p'}$ is important in the following, which is why we added the superscript $(1, 2)$ to X.

F.3 Case I: Derivatives taken at one sphere

In case I, both derivatives in Eq. (F.2) are taken at one sphere. Within r round-trips, there are r possibilities for each sphere, we thus get

$$\begin{aligned} I = \frac{\mathrm{e}^{-2r\kappa_{\mathrm{sp}}L}}{\kappa_{\mathrm{sp}}^{2r}} \sum_{p_1,\dots,p_{2r}} \sum_{l=1}^{r} \Bigg\{ & \left[d(0)\left(d^{(1);1,1}_{p_{2l+1},p_{2l}} + d^{(1);2,2}_{p_{2l+1},p_{2l}}\right) + 2d_+(1) d^{(1);1,2}_{p_{2l+1},p_{2l}}\right] X_r^{(1,2)} \\ & + \left[d(0)\left(d^{(2);1,1}_{p_{2l},p_{2l-1}} + d^{(2);2,2}_{p_{2l},p_{2l-1}}\right) + 2d_-(1) d^{(2);1,2}_{p_{2l},p_{2l-1}}\right] X_r^{(2,1)} \Bigg\}\,. \end{aligned} \tag{F.12}$$

The terms proportional to $d(0)$ include the case, where both derivatives are taken with respect to the first or second argument of $\rho^{(t)}_{p,p'}$. For the terms proportional to $d_\pm(1)$, the derivatives are taken with respect to both arguments of $\rho^{(t)}_{p,p'}$. We can arbitrarily choose the point where the derivatives are taken due to the cyclic invariance of the summation indices. Without loss of generality, we will take the derivative in the first round-trip. The sum over l can thus be carried out, yielding a factor r.

Next, we use the results for the derivatives of $\rho^{(t)}_{pp'}$ which are given in Eq. (F.8). They allow us to write the derivatives given above in the following form

$$d^{(t);1,1}_{p,p'} + d^{(t);2,2}_{p,p'} = D^{(t)}_{I_0,p,p'} - D^{(t)}_{I_2,p,p'}\,, \tag{F.13a}$$

$$2d^{(t);1,2}_{p,p'} = D^{(t)}_{I_1,p,p'} + D^{(t)}_{I_2,p,p'}\,. \tag{F.13b}$$

The coefficient D_{I_0} and D_{I_1} account for the terms, where the derivatives are taken at the Fresnel reflection coefficients $r_{p,p'}$, they are given by

$$D^{(t)}_{I_0,p,p'} = \frac{\left(r^{(t)}_{p,p'}\right)_{ii}}{r^{(t)}_{p,p'}} + \frac{\left(r^{(t)}_{p,p'}\right)_{jj}}{r^{(t)}_{p,p'}}\,, \qquad D^{(t)}_{I_1,p,p'} = 2\frac{\left(r^{(t)}_{p,p'}\right)_{ij}}{r^{(t)}_{p,p'}} \tag{F.14}$$

while the coefficient D_{I_2} represents the terms, where we take the derivatives of the polarisation-conversion coefficients, which are given by

$$D^{(t)}_{I_2,p,p'} = \frac{\mathcal{K}^2}{\kappa_{\text{sp}}^2 k_{\text{sp}}^2}\frac{r^{(t)}_{p,p'} - (-1)^{p-p'} r^{(t)}_{\bar{p},\bar{p}'}}{r^{(t)}_{p,p'}}\,. \tag{F.15}$$

Hence, we can separate the terms in Eq. (F.12) into three different expression, based on the just introduced definition of the derivatives $I = I_0 + I_1 + I_2$ with

$$I_0 = r\frac{\mathrm{e}^{-2r\kappa_{\text{sp}}L}}{\kappa_{\text{sp}}^{2r}}\sum_{p_1,\dots,p_{2r}}\left[d(0)D^{(1)}_{I_0,p_1,p_2}X_r^{(1,2)} + d(0)D^{(2)}_{I_0,p_1,p_2}X_r^{(2,1)}\right]\,, \tag{F.16}$$

$$I_1 = r\frac{\mathrm{e}^{-2r\kappa_{\text{sp}}L}}{\kappa_{\text{sp}}^{2r}}\sum_{p_1,\dots,p_{2r}}\left[d_+(1)D^{(1)}_{I_1,p_1,p_2}X_r^{(1,2)} + d_-(1)D^{(2)}_{I_1,p_1,p_2}X_r^{(2,1)}\right]\,, \tag{F.17}$$

$$I_2 = r\frac{\mathrm{e}^{-2r\kappa_{\text{sp}}L}}{\kappa_{\text{sp}}^{2r}}\sum_{p_1,\dots,p_{2r}}\left[\left(d_+(1) - d(0)\right)D^{(1)}_{I_2,p_1,p_2}X_r^{(1,2)} + \left(d_-(1) - d(0)\right)D^{(2)}_{I_2,p_1,p_2}X_r^{(2,1)}\right]\,. \tag{F.18}$$

We are now going to determine the frequency contributions to $\mathcal{F}^{(ii)}_{\text{NTLO}}(\xi)$ defined in Eq. (F.1) for these three terms. Similar to our discussion in Sec. 10.1.2, we describe the different polarisation combinations recursively. The contribution from I_0 to the trace $[\text{tr}\mathcal{M}^r]^{(ii)}_{\text{NTLO}}$ yields

$$\left.[\text{tr}\mathcal{M}^r]^{(ii)}_{\text{NTLO}}\right|_{I_0} = \frac{R_{\text{eff}}}{4}\int\frac{\mathrm{d}^2\mathbf{k}_{\text{sp}}}{2\pi\kappa_{\text{sp}}}d(0)\left(h^{(1,2);\text{TM,TM}}_{I_0,r} + h^{(1,2);\text{TE,TE}}_{I_0,r} + h^{(2,1);\text{TM,TM}}_{I_0,r} + h^{(2,1);\text{TE,TE}}_{I_0,r}\right)\,. \tag{F.19}$$

Equivalent expressions can be derived for I_1 and I_2. For $r > 1$ the known recursion relation (10.26) holds, with

$$h^{(1,2);p,p'}_{I_n,r} = A_0^{(1,2);p\text{TM}}h^{(1,2);\text{TM},p'}_{I_n,r-1} + A_0^{(1,2);p,\text{TE}}h^{(1,2);\text{TM},p'}_{I_n,r-1}\,, \tag{F.20}$$

where $A_0^{(1,2);p,p'}$ describes a single round-trip similar to Eq. (10.27)

$$A_0^{(1,2);p,p'} = \left[r^{(1)}_{p,\text{TM}}r^{(2)}_{\text{TM},p'} + r^{(1)}_{p,\text{TE}}r^{(2)}_{\text{TE},p'}\right]\mathrm{e}^{-2\kappa_{\text{sp}}L}\,. \tag{F.21}$$

By exchanging the superscripts 1 and 2 in the expressions given above, one obtains the corresponding recursion relations for $h^{(2,1);p,p'}_{I_n,r}$. Note that the eigenvalues λ_1 and λ_2 of the round-trip matrix $\mathbf{A}_0$ are the same for the two superscripts (10.39)

$$\lambda_{1,2} = \frac{1}{2}\left[\text{tr}\mathbf{A}_0^{(1,2)} \pm \sqrt{\text{tr}^2\mathbf{A}_0^{(1,2)} - 4\det\mathbf{A}_0^{(1,2)}}\right] = \frac{1}{2}\left[\text{tr}\mathbf{A}_0^{(2,1)} \pm \sqrt{\text{tr}^2\mathbf{A}_0^{(2,1)} - 4\det\mathbf{A}_0^{(2,1)}}\right]\,. \tag{F.22}$$

The case $r = 1$ is discussed separately. Here, we have to take into account that we take the derivative at one of the spheres in the first round-trip, thus leading to

$$h^{(1,2);p,p'}_{I_n,1} = \left[D^{(1)}_{I_n,p,\mathrm{TM}} r^{(1)}_{p,\mathrm{TM}} r^{(2)}_{\mathrm{TM},p'} + D^{(1)}_{I_n,p,\mathrm{TE}} r^{(1)}_{p,\mathrm{TE}} r^{(2)}_{\mathrm{TE},p'}\right] \mathrm{e}^{-2\kappa_{\mathrm{sp}}L} \,. \tag{F.23}$$

Inserting the definitions for D_{I_0} and D_{I_1} in the above-given relation, we get

$$h^{(1,2);p,p'}_{I_0,1} = \left[\left(\left(r^{(1)}_{p,\mathrm{TM}}\right)_{ii} + \left(r^{(1)}_{p,\mathrm{TM}}\right)_{jj}\right) r^{(2)}_{\mathrm{TM},p'} + \left(\left(r^{(1)}_{p,\mathrm{TE}}\right)_{ii} + \left(r^{(1)}_{p,\mathrm{TE}}\right)_{jj}\right) r^{(2)}_{\mathrm{TE},p'}\right] \mathrm{e}^{-2\kappa_{\mathrm{sp}}L} \,, \tag{F.24}$$

$$h^{(1,2);p,p'}_{I_1,1} = \left[\left(r^{(1)}_{p,\mathrm{TM}}\right)_{ij} r^{(2)}_{\mathrm{TM},p'} + \left(r^{(1)}_{p,\mathrm{TE}}\right)_{ij} r^{(2)}_{\mathrm{TE},p'}\right] \mathrm{e}^{-2\kappa_{\mathrm{sp}}L} \,, \tag{F.25}$$

while we find for D_{I_2}, the following four relations for the first round-trip

$$h^{(1,2);\mathrm{TM},\mathrm{TM}}_{I_2,1} = \frac{\mathcal{K}^2}{\kappa^2_{\mathrm{sp}} k^2_{\mathrm{sp}}} \left[\Delta r^{(1)}_b r^{(2)}_{\mathrm{TM},\mathrm{TM}} + \Delta r^{(1)}_a r^{(2)}_{\mathrm{TE},\mathrm{TM}}\right] \mathrm{e}^{-2\kappa_{\mathrm{sp}}L} \,, \tag{F.26a}$$

$$h^{(1,2);\mathrm{TM},\mathrm{TE}}_{I_2,1} = \frac{\mathcal{K}^2}{\kappa^2_{\mathrm{sp}} k^2_{\mathrm{sp}}} \left[\Delta r^{(1)}_b r^{(2)}_{\mathrm{TM},\mathrm{TE}} + \Delta r^{(1)}_a r^{(2)}_{\mathrm{TE},\mathrm{TE}}\right] \mathrm{e}^{-2\kappa_{\mathrm{sp}}L} \,, \tag{F.26b}$$

$$h^{(1,2);\mathrm{TE},\mathrm{TM}}_{I_2,1} = \frac{\mathcal{K}^2}{\kappa^2_{\mathrm{sp}} k^2_{\mathrm{sp}}} \left[\Delta r^{(1)}_a r^{(2)}_{\mathrm{TM},\mathrm{TM}} - \Delta r^{(1)}_b r^{(2)}_{\mathrm{TE},\mathrm{TM}}\right] \mathrm{e}^{-2\kappa_{\mathrm{sp}}L} \,, \tag{F.26c}$$

$$h^{(1,2);\mathrm{TE},\mathrm{TE}}_{I_2,1} = \frac{\mathcal{K}^2}{\kappa^2_{\mathrm{sp}} k^2_{\mathrm{sp}}} \left[\Delta r^{(1)}_a r^{(2)}_{\mathrm{TM},\mathrm{TE}} - \Delta r^{(1)}_b r^{(2)}_{\mathrm{TE},\mathrm{TE}}\right] \mathrm{e}^{-2\kappa_{\mathrm{sp}}L} \,, \tag{F.26d}$$

where we defined

$$\Delta r^{(t)}_b = r^{(t)}_{\mathrm{TM},\mathrm{TM}} - r^{(t)}_{\mathrm{TE},\mathrm{TE}} \,, \qquad \Delta r^{(t)}_a = r^{(t)}_{\mathrm{TM},\mathrm{TE}} + r^{(t)}_{\mathrm{TE},\mathrm{TM}} \,. \tag{F.27}$$

After inserting the recursion relation (F.20) with (F.23) together with $d(0) = \kappa_{\mathrm{sp}}\left(r^2 + 3u - 1\right)/6rR_{\mathrm{eff}}$ into Eq. (F.19) and performing the round-trip sum, according to (F.1), the frequency contribution to the Casimir energy yields

$$\mathcal{F}^{(ii)}_{\mathrm{NTLO}}(\xi)\Bigg|_{I_0} = -\frac{1}{24}\int \frac{\mathrm{d}^2\mathbf{k}_{\mathrm{sp}}}{2\pi}\left[\mathcal{P}^{(1,2)}_{I_0,0} + \mathcal{P}^{(2,1)}_{I_0,0} + (3u-1)\left(\mathcal{P}^{(1,2)}_{I_0,2} + \mathcal{P}^{(2,1)}_{I_0,2}\right)\right] \,, \tag{F.28}$$

where we introduced for the round-trip sum over $h_{I_n,r}$ the following function

$$\mathcal{P}^{(1,2)}_{I_n,m} = \sum_{r=1}^{\infty} \frac{1}{r^m}\left[h^{(1,2);\mathrm{TM},\mathrm{TM}}_{I_n,r} + h^{(1,2);\mathrm{TE},\mathrm{TE}}_{I_n,r}\right] \,. \tag{F.29}$$

Similar to the discussion in Sec. 10.1.2, we evaluate the round-trip sum by rewriting $1/r^m$ in terms of m integrals over auxiliary variables and introduce generating functions for the round-trip sums

$$\mathcal{P}^{(1,2)}_{I_n,m} = \int_0^1 \frac{\mathrm{d}t_m}{t_m} \ldots \int_0^{t_2} \frac{\mathrm{d}t_1}{t_1}\left(H^{(1,2);\mathrm{TM},\mathrm{TM}}_{I_n}(t_1) + H^{(1,2);\mathrm{TE},\mathrm{TE}}_{I_n}(t_1)\right) \,. \tag{F.30}$$

The generating function is defined as

$$H_{I_n}^{(1,2);p,p'}(t) := \sum_{r=1}^{\infty} t^r h_{I_n,r}^{(1,2);p,p'} = t h_{I_n,1}^{(1,2);p,p'} + t \sum_{r=1}^{\infty} t^r h_{I_n,r+1}^{(1,2);p,p'} \,. \tag{F.31}$$

In the second step, we extracted the single-round-trip term and shifted the index of the remaining sum. The coefficients $h_{I_n,r+1}$ can now be rewritten with the above introduced recursion relation (F.20) and we find

$$H_{I_n}^{(1,2);p,p'}(t) = t h_{I_n,1}^{(1,2);p,p'} + t A_0^{(1,2);p,\mathrm{TM}} H_{I_n}^{(1,2);\mathrm{TM},p'}(t) + A_0^{(1,2);p,\mathrm{TE}} H_{I_n}^{(1,2);\mathrm{TM},p'}(t) \,. \tag{F.32}$$

We solve the expression for the generating functions and obtain

$$H_{I_n}^{(1,2);\mathrm{TM},\mathrm{TM}}(t) + H_{I_n}^{(1,2);\mathrm{TE},\mathrm{TE}}(t) = \frac{t c_{I_n}^{(1,2)} + t^2 d_{I_n}^{(1,2)}}{(1 - t\lambda_1)(1 - t\lambda_2)} \,, \tag{F.33}$$

where we introduced the eigenvalues $\lambda_{1,2}$ of the round-trip matrix given in Eq. (F.22) and the following expansion coefficients

$$c_{I_n}^{(1,2)} = h_{I_n,1}^{(1,2);\mathrm{TM},\mathrm{TM}} + h_{I_n,1}^{(1,2);\mathrm{TE},\mathrm{TE}} \,, \tag{F.34a}$$

$$\begin{aligned} d_{I_n}^{(1,2)} &= -h_{I_n,1}^{(1,2);\mathrm{TM},\mathrm{TM}} A_0^{(1,2);\mathrm{TE},\mathrm{TE}} - h_{I_n,1}^{(1,2);\mathrm{TE},\mathrm{TE}} A_0^{(1,2);\mathrm{TM},\mathrm{TM}} \\ &\quad + h_{I_n,1}^{(1,2);\mathrm{TE},\mathrm{TM}} A_0^{(1,2);\mathrm{TM},\mathrm{TE}} + h_{I_n,1}^{(1,2);\mathrm{TM},\mathrm{TE}} A_0^{(1,2);\mathrm{TE},\mathrm{TM}} \,. \end{aligned} \tag{F.34b}$$

The integrals over t_i in Eq. (F.30) can easily be evaluated with (A.12) and expressed in terms of polylogarithms. For $m > 0$, we get

$$\mathcal{P}_{I_n,m}^{(1,2)} = \frac{c_{I_n}^{(1,2)}\lambda_1 + d_{I_n}^{(1,2)}}{\lambda_1(\lambda_1 - \lambda_2)} \mathrm{Li}_m[\lambda_1] + \frac{c_{I_n}^{(1,2)}\lambda_2 + d_{I_n}^{(1,2)}}{\lambda_2(\lambda_2 - \lambda_1)} \mathrm{Li}_m[\lambda_2] \tag{F.35}$$

and for $m = 0$ we can employ the definition of the zero-order polylogarithm (A.9)

$$\mathcal{P}_{I_n,0}^{(1,2)} = \frac{c_{I_n}^{(1,2)} + d_{I_n}^{(1,2)}}{\lambda_1\lambda_2} \mathrm{Li}_0[\lambda_1]\mathrm{Li}_0[\lambda_2] \,. \tag{F.36}$$

For I_1, defined in Eq. (F.17) we use

$$d_\pm(1) = \frac{\kappa_{\rm sp}}{6rR_{\rm eff}}\left[r^2 - 3r\left(1 \mp \frac{R_1 - R_2}{R_1 + R_2}\right) + 2 - 3u \mp 3\frac{R_1 - R_2}{R_1 + R_2}\right] \tag{F.37}$$

and thus obtain for the free energy contribution

$$\begin{aligned}\mathcal{F}^{(ii)}_{\rm NTLO}(\xi)\Bigg|_{I_1} = -\frac{1}{24}\int\frac{{\rm d}^2\mathbf{k}_{\rm sp}}{2\pi}\Bigg\{&\mathcal{P}^{(1,2)}_{I_1,0} - 3\left(1 - \frac{R_1 - R_2}{R_1 + R_2}\right)\mathcal{P}^{(1,2)}_{I_1,1} + \left(2 - 3u - 3\frac{R_1 - R_2}{R_1 + R_2}\right)\mathcal{P}^{(1,2)}_{I_1,2}\\ &+\mathcal{P}^{(2,1)}_{I_1,0} - 3\left(1 + \frac{R_1 - R_2}{R_1 + R_2}\right)\mathcal{P}^{(2,1)}_{I_1,1} + \left(2 - 3u + 3\frac{R_1 - R_2}{R_1 + R_2}\right)\mathcal{P}^{(2,1)}_{I_1,2}\Bigg\}.\end{aligned} \tag{F.38}$$

For the case I_2, defined in Eq. (F.18), we apply

$$d_\pm(1) - d(0) = \frac{\kappa_{\rm sp}u}{rR_{\rm eff}}\left[-r\left(1 + \frac{R_{2/1}}{R_{1/2}}\right) + \frac{R_{2/1}}{R_{1/2}}\right], \tag{F.39}$$

where the upper (lower) sign corresponds to the first (second) index. The contribution to the free energy yields

$$\begin{aligned}\mathcal{F}^{(ii)}_{\rm NTLO}(\xi)\Bigg|_{I_2} = -\frac{u}{4}\int\frac{{\rm d}^2\mathbf{k}_{\rm sp}}{2\pi}\Bigg\{&-\left(1 + \frac{R_1}{R_2}\right)\mathcal{P}^{(2,1)}_{I_2,1} + \frac{R_1}{R_2}\mathcal{P}^{(2,1)}_{I_2,2}\\ &-\left(1 + \frac{R_2}{R_1}\right)\mathcal{P}^{(1,2)}_{I_2,1} + \frac{R_2}{R_1}\mathcal{P}^{(1,2)}_{I_2,2}\Bigg\}.\end{aligned} \tag{F.40}$$

Finally, we compare our results with known expressions for the limit of two dielectric spheres given in Ref. [109]. In this limit, the polarisation-changing reflections coefficients $r_{\rm TE,TM}$ and $r_{\rm TM,TE}$ vanish and the eigenvalues are given by $\lambda_1 = \phi_{\rm TM}$ and $\lambda_2 = \phi_{\rm TE}$ defined in Eq. (10.41). The coefficients (F.23) thus yield

$$h^{(1,2);p,p}_{I_0,1} = \left[\frac{(r^{(1)}_{p,p})_{jj}}{r^{(1)}_{p,p}} + \frac{(r^{(1)}_{p,p})_{ii}}{r^{(1)}_{p,p}}\right]\phi_p\,, \tag{F.41}$$

$$h^{(1,2);p,p}_{I_1,1} = \frac{(r^{(1)}_{p,p})_{ij}}{r^{(1)}_{p,p}}\phi_p\,, \tag{F.42}$$

$$h^{(1,2);p,p}_{I_2,1} = -(-1)^p\frac{\mathcal{K}^2}{k^2_{\rm sp}\kappa^2_{\rm sp}}\frac{\Delta r^{(1)}_b}{r^{(1)}_{p,p}}\phi_p\,. \tag{F.43}$$

It is now easy to show that Eq. (F.28) together with Eq. (F.41) and Eq. (F.38) together with Eq. (F.42) reproduce Eq. (6.63) of Ref. [109], while Eq. (F.40) together with Eq. (F.43) yields Eq. (6.67) of the same reference.

F.4 Case J: Derivatives taken at two spheres

In this Section, we will discuss the case J, where the derivatives are taken at different points during the r round-trips. As already depicted in Fig. 10.4, there are four contributions to J. Terms where both derivatives are taken at the same sphere are denoted by $J^{(1,1)}$ or $J^{(2,2)}$ and for derivatives at different spheres, we introduced $J^{(1,2)}$ or $J^{(2,1)}$. In total, we write

$$J = J^{(1,1)} + J^{(2,2)} + J^{(1,2)} + J^{(2,1)} \,. \tag{F.44}$$

$J^{(t,s)}$ accounts for round-trips where the first derivative is taken at sphere t and the second derivative at sphere s. In the following, we are discussing the cases $J^{(2,2)}$ and $J^{(2,1)}$ in detail. For $J^{(1,1)}$ and $J^{(1,2)}$ one only needs to exchange the indices 2 and 1 in the result for the discussed cases.

F.4.1 Cases $J^{(2,1)}$ and $J^{(1,2)}$

Similar to our discussion before, we make use of the cyclic invariance of the indices and take the first derivative always in the first round-trip. We start at sphere 2 ($d^{(2);1/2}_{p_2,p_1}$), where we take the derivative either with respect to $k_{2,\alpha}$ or $k_{1,\alpha}$. During the r round-trips, there are r possibilities of taking the derivative at sphere 1. Hence, we set $d^{(1);1/2}_{p_{2l+1},p_{2l}}$ and sum over $l = 1, \dots r$. The sum (F.2), thus yields

$$\begin{aligned} J^{(2,1)} = r\frac{\mathrm{e}^{-2r\kappa_{\mathrm{sp}}L}}{\kappa_{\mathrm{sp}}^{2r}} \sum_{p_1,\dots,p_{2r}} \sum_{l=1}^{r} \Big[& d_+(2l-1) d^{(2);1}_{p_2,p_1} d^{(1);1}_{p_{2l+1},p_{2l}} + d_-(2l-1) d^{(2);2}_{p_2,p_1} d^{(1);2}_{p_{2l+1},p_{2l}} \\ & + d(2l) d^{(2);2}_{p_2,p_1} d^{(1);1}_{p_{2l+1},p_{2l}} + d(2l-2) d^{(2);1}_{p_2,p_1} d^{(1);2}_{p_{2l+1},p_{2l}} \Big] X_r^{(2,1)} \,, \end{aligned} \tag{F.45}$$

where we used $2d(2l) = d_+(2l) + d_-(2l)$. The multiplicative factor r appearing in the expression above originates from the r possibilities of choosing the starting point at sphere 2. With the results for the derivatives of $\rho^{(t)}_{p,p'}$ determined in Eqs. (F.7a) and (F.7b), we find for the product of the derivatives

$$d^{(t);1/2}_{p,p'} d^{(s);1/2}_{q,q'} = E^{(t);p,p'}_{(s);q,q'} + F^{(t);p,p'}_{(s);q,q'} \,, \tag{F.46a}$$

$$d^{(t);1/2}_{p,p'} d^{(s);2/1}_{q,q'} = E^{(t);p,p'}_{(s);q,q'} - F^{(t);p,p'}_{(s);q,q'} \,. \tag{F.46b}$$

Here, the function $E^{(t);p,p'}_{(s);q,q'}$ takes the derivatives of the Fresnel coefficients into account

$$E^{(t);p,p'}_{(s);q,q'} = \frac{\left(r^{(t)}_{p,p'}\right)_i \left(r^{(s)}_{q,q'}\right)_j}{r^{(t)}_{q,p'} r^{(s)}_{q,q'}} \tag{F.47}$$

while $F^{(t);p,p'}_{(s);q,q'}$ contains the terms, where the derivatives are taken on the polarisation-conversion coefficients and thus yields

$$F^{(t);p,p'}_{(s);q,q'} = \pm\frac{\mathcal{K}^2}{4k_{\mathrm{sp}}^2\kappa_{\mathrm{sp}}^2} \frac{(-1)^p \left(r^{(t)}_{\bar{p},p'} + (-1)^{p-p'} r^{(t)}_{p,\bar{p}'}\right)}{r^{(t)}_{p,p'}} \frac{(-1)^q \left(r^{(s)}_{\bar{q},q'} + (-1)^{q-q'} r^{(s)}_{q,\bar{q}'}\right)}{r^{(s)}_{q,q'}} \,, \tag{F.48}$$

where the upper (lower) sign corresponds to $t = s$ ($t \neq s$). The above-introduced relations for the products of the derivatives, allows us to separate Eq. (F.45) into two terms: $J^{(2,1)} = J_F^{(2,1)} + J_E^{(2,1)}$ with

$$J_F^{(2,1)} = r\frac{\mathrm{e}^{-2r\kappa_{\text{sp}}L}}{\kappa_{\text{sp}}^{2r}} \sum_{p_1,\ldots,p_{2r}} \sum_{l=1}^{r} F^{(2);p_2,p_1}_{(1);p_{2l+1},p_{2l}} \Big(d_+(2l-1) + d_-(2l-1) - d(2l) - d(2l-2)\Big) X_r^{(2,1)}\,, \tag{F.49}$$

$$J_E^{(2,1)} = r\frac{\mathrm{e}^{-2r\kappa_{\text{sp}}L}}{\kappa_{\text{sp}}^{2r}} \sum_{p_1,\ldots,p_{2r}} \sum_{l=1}^{r} E^{(2);p_2,p_1}_{(1);p_{2l+1},p_{2l}} \Big(d_+(2l-1) + d_-(2l-1) + d(2l) + d(2l-2)\Big) X_r^{(2,1)}\,. \tag{F.50}$$

We evaluate the sums of $d_\pm(k)$ functions with (10.56) and get

$$d_+(2l-1) + d_-(2l-1) - d(2l) - d(2l-2) = -\frac{2\kappa_{\text{sp}}}{r(R_1+R_2)}\,, \tag{F.51}$$

$$d_+(2l-1) + d_-(2l-1) + d(2l) + d(2l-2) = \frac{\kappa_{\text{sp}}}{2r}\frac{4r^2 - 12r(2l-1) + 6(2l-1)^2 + 2}{3R_{\text{eff}}}\,. \tag{F.52}$$

We start with the evaluation of $J_F^{(2,1)}$, where the contribution to the trace yields

$$[\mathrm{tr}\mathcal{M}^r]^{(ii)}_{\text{NTLO}}\Bigg|_{J_F^{(2,1)}} = -\frac{u}{2}\int \frac{\mathrm{d}^2\mathbf{k}_{\text{sp}}}{2\pi}\frac{\mathrm{e}^{-2r\kappa_{\text{sp}}L}}{r} \sum_{p_1,\ldots,p_{2r}} \sum_{l=1}^{r} F^{(2);p_2,p_1}_{(1);p_{2l+1},p_{2l}} X_r^{(2,1)}\,. \tag{F.53}$$

We obtain the free energy by summing over all round-rips. As before, we compute the round-trip sum via a generating function and thus write

$$\begin{aligned}\mathcal{F}^{(ii)}_{\text{NTLO}}(\xi)\Bigg|_{J_F^{(2,1)}} &= \frac{u}{2}\int \frac{\mathrm{d}^2\mathbf{k}_{\text{sp}}}{2\pi}\sum_{r=1}^{\infty}\frac{\mathrm{e}^{-2r\kappa_{\text{sp}}L}}{r^2} \sum_{p_1,\ldots,p_{2r}} \sum_{l=1}^{r} F^{(2);p_2,p_1}_{(1);p_{2l+1}p_{2l}} X_r^{(2,1)} \\ &= -\frac{u}{8}\int \frac{\mathrm{d}^2\mathbf{k}_{\text{sp}}}{2\pi}\frac{\mathcal{K}^2}{k_{\text{sp}}^2\kappa_{\text{sp}}^2}\int_0^1\frac{\mathrm{d}t_1}{t_1}\int_0^{t_1}\frac{\mathrm{d}t}{t}\left(H^{(2,1);\text{TM},\text{TM}}(t,1) + H^{(2,1);\text{TE},\text{TE}}(t,1)\right)\,,\end{aligned} \tag{F.54}$$

where we introduced a generating function with two auxiliary variables

$$H^{(2,1);p,p'}(t,s) = \sum_{r=1}^{\infty} t^r \sum_{l=1}^{r} s^{2l-1} h_{r,l}^{(2,1);p,p'}\,. \tag{F.55}$$

The term s^{2l-1} accounts for the factors $(2l-1)$ in Eq. (F.50). We determine the generating function by applying recursion relations for $h_{r,l}$.

For $r \neq \{l, 1\}$ the known recursion relation holds

$$h_{r,l}^{(2,1);p,p'} = A_0^{(2,1);p,\text{TM}} h_{r-1,l}^{(2,1);\text{TM},p'} + A_0^{(2,1);p,\text{TE}} h_{r-1,l}^{(2,1);\text{TE},p'}\,. \tag{F.56}$$

For $l \neq 1$ is the beginning of the recursion ($r = 1$) given by

$$h_{1,l}^{(2,1);p,p'} = \hat{A}_0^{(2,1);p,p'}\,, \tag{F.57}$$

with (F.48) we find for the first round-trip, where the derivative is taken at sphere 2, the following expressions

$$\hat{A}_0^{(2,1);\mathrm{TM},\mathrm{TM}} = \left(\Delta r_a^{(2)} r_{\mathrm{TM},\mathrm{TM}}^{(1)} - \Delta r_b^{(2)} r_{\mathrm{TE},\mathrm{TM}}^{(1)}\right) \mathrm{e}^{-2\kappa_{\mathrm{sp}}L}\,, \tag{F.58a}$$

$$\hat{A}_0^{(2,1);\mathrm{TM},\mathrm{TE}} = \left(\Delta r_a^{(2)} r_{\mathrm{TM},\mathrm{TE}}^{(1)} - \Delta r_b^{(2)} r_{\mathrm{TE},\mathrm{TE}}^{(1)}\right) \mathrm{e}^{-2\kappa_{\mathrm{sp}}L}\,, \tag{F.58b}$$

$$\hat{A}_0^{(2,1);\mathrm{TE},\mathrm{TM}} = -\left(\Delta r_a^{(2)} r_{\mathrm{TE},\mathrm{TM}}^{(1)} + \Delta r_b^{(2)} r_{\mathrm{TM},\mathrm{TM}}^{(1)}\right) \mathrm{e}^{-2\kappa_{\mathrm{sp}}L}\,, \tag{F.58c}$$

$$\hat{A}_0^{(2,1);\mathrm{TE},\mathrm{TE}} = -\left(\Delta r_a^{(2)} r_{\mathrm{TE},\mathrm{TE}}^{(1)} + \Delta r_b^{(2)} r_{\mathrm{TM},\mathrm{TE}}^{(1)}\right) \mathrm{e}^{-2\kappa_{\mathrm{sp}}L}\,, \tag{F.58d}$$

where we introduced $\Delta r_a^{(2)}$ and $\Delta r_b^{(2)}$ defined in Eq. (F.27). For $r = l$ the derivative is taken at sphere 1 (see also Fig. F.1) and the recursion is thus given by

$$h_{l,l}^{(2,1);p,p'} = \tilde{A}_0^{(2,1);p,\mathrm{TM}} h_{l-1,l}^{(2,1);\mathrm{TM},p'} + \tilde{A}_0^{(2,1);p,\mathrm{TE}} h_{l-1,l}^{(2,1);\mathrm{TE},p'} \tag{F.59}$$

with

$$\tilde{A}_0^{(2,1);\mathrm{TM},\mathrm{TM}} = \left(r_{\mathrm{TM},\mathrm{TM}}^{(2)} \Delta r_a^{(1)} - r_{\mathrm{TM},\mathrm{TE}}^{(2)} \Delta r_b^{(1)}\right) \mathrm{e}^{-2\kappa_{\mathrm{sp}}L}\,, \tag{F.60a}$$

$$\tilde{A}_0^{(2,1);\mathrm{TM},\mathrm{TE}} = -\left(r_{\mathrm{TM},\mathrm{TM}}^{(2)} \Delta r_b^{(1)} + r_{\mathrm{TM},\mathrm{TE}}^{(2)} \Delta r_a^{(1)}\right) \mathrm{e}^{-2\kappa_{\mathrm{sp}}L}\,, \tag{F.60b}$$

$$\tilde{A}_0^{(2,1);\mathrm{TE},\mathrm{TM}} = \left(r_{\mathrm{TE},\mathrm{TM}}^{(2)} \Delta r_a^{(1)} - r_{\mathrm{TE},\mathrm{TE}}^{(2)} \Delta r_b^{(1)}\right) \mathrm{e}^{-2\kappa_{\mathrm{sp}}L}\,, \tag{F.60c}$$

$$\tilde{A}_0^{(2,1);\mathrm{TE},\mathrm{TE}} = -\left(r_{\mathrm{TE},\mathrm{TM}}^{(2)} \Delta r_b^{(1)} + r_{\mathrm{TE},\mathrm{TE}}^{(2)} \Delta r_a^{(1)}\right) \mathrm{e}^{-2\kappa_{\mathrm{sp}}L}\,. \tag{F.60d}$$

Special care is needed for the case $r = l = 1$, where both derivatives are taken within the first round-trip. Here, we obtain with (F.48), the following expressions for $h_{1,1}$

$$h_{1,1}^{(2,1);p,p} = \left(\Delta r_a^{(2)} \Delta r_a^{(1)} + \Delta r_b^{(2)} \Delta r_b^{(1)}\right) \mathrm{e}^{-2\kappa_{\mathrm{sp}}L}\,, \tag{F.61a}$$

$$h_{1,1}^{(2,1);p,\bar{p}} = (-1)^{p-1} \left(\Delta r_a^{(2)} \Delta r_b^{(1)} - \Delta r_b^{(2)} \Delta r_a^{(1)}\right) \mathrm{e}^{-2\kappa_{\mathrm{sp}}L}\,. \tag{F.61b}$$

Before we proceed with the evaluation of Eq. (F.54), we want to highlight that the recursion relations defined in Eqs. (F.56), (F.57) and (F.59) are also applicable to the other cases $J^{(t,s)}$. The only difference is the definition of $\hat{A}_0^{p,p'}$ and $\tilde{A}_0^{p,p'}$, which respectively define where the derivative is taken in the first and l-th round-trip.

In order to apply the recursion relations to the generating function in Eq. (F.55), we exchange the sum over r and l and separate the term $h_{l,l}$

$$H^{(2,1);\mathrm{TM},\mathrm{TM}}(t,s) = \sum_{l=1}^{\infty} \sum_{r=l+1}^{\infty} t^r s^{l-1} h_{r,l}^{(2,1),\mathrm{TM},\mathrm{TM}} + G^{(2,1),\mathrm{TM},\mathrm{TM}}(t,s)\,, \tag{F.62}$$

where we introduced a generating function $G^{(2,1);\mathrm{TM},\mathrm{TM}}$, which accounts for all polarisation combi-

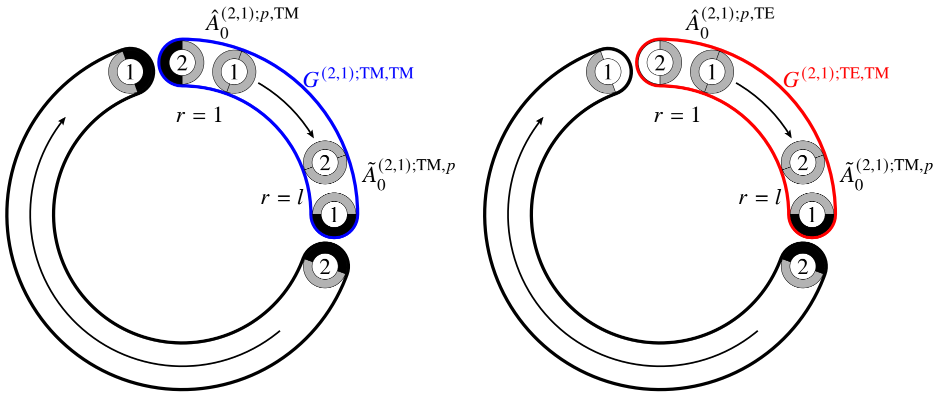

Figure F.1: Schematic illustration of the generation function $H^{(2,1),\mathrm{TM},\mathrm{TM}}$ defined in Eq. (F.65). The generating function accounts for scattering processes where the derivatives are taken at spheres 2 and 1. We start at the top of the two graphs, at sphere 2, and continue clockwise with our description of the graphs. Within the first round-trip, the incoming mode on sphere 2 is either TM-polarised (black half in the first graph) or TE-polarised (white half in the second graph). In both cases, the reflected wave can either be TM- or TE-polarised, which is why the second half of the sphere is coloured in grey. We take the first derivative at sphere 2 in the first round-trip. Hence, the first round-trip is described by $\hat{A}_0^{(2,1);p,\mathrm{TM}}$ (on the left) and $\hat{A}_0^{(2,1);p,\mathrm{TE}}$ (on the right). After l round-trips, we arrive at sphere 1 (end of the blue- or red-coloured line), where we again take a derivative. The outgoing wave is, in both cases, TM-polarised. Hence, the l-th round-trip is in both cases described by $\tilde{A}_0^{(2,1);\mathrm{TM},p}$. Between the first and l-th round-trip, various polarisation combinations are possible. The combinations are captured by functions $G^{(2,1);\mathrm{TM},\mathrm{TM}}$ and $G^{(2,1);\mathrm{TE},\mathrm{TM}}$.

nations between the first and l-th round-trip as illustrated in the left panel of Fig. F.1. The function is defined by

$$G^{(2,1);\mathrm{TM},\mathrm{TM}}(t,s) = \sum_{l=1}^{\infty} t^l s^{2l-1} h_{l,l}^{(2,1);\mathrm{TM},\mathrm{TM}} . \tag{F.63}$$

With the above introduced recursion relation (F.56) for $r \neq l, 1$, the generating function $H^{(2,1);\mathrm{TM},\mathrm{TM}}$ yields

$$\begin{aligned} H^{(2,1);\mathrm{TM},\mathrm{TM}}(t,s) = {} & tA_0^{(2,1);\mathrm{TM},\mathrm{TM}} H^{(2,1);\mathrm{TM},\mathrm{TM}}(t,s) + tA_0^{(2,1);\mathrm{TM},\mathrm{TE}} H^{(2,1);\mathrm{TE},\mathrm{TM}}(t,s) \\ & + G^{(2,1);\mathrm{TM},\mathrm{TM}}(t,s) . \end{aligned} \tag{F.64}$$

A similar recursion relation can be obtained for the other polarisation combinations, which can then be solved for $H^{(2,1);\mathrm{TM},\mathrm{TM}}$ and leads to

$$H^{(2,1);\mathrm{TM},\mathrm{TM}}(t,s) = \frac{\left(1 - tA_0^{(2,1);\mathrm{TE},\mathrm{TE}}\right) G^{(2,1);\mathrm{TM},\mathrm{TM}}(t,s) + tA_0^{(2,1);\mathrm{TM},\mathrm{TE}} G^{(2,1);\mathrm{TE},\mathrm{TM}}(t,s)}{\left(1 - tA_0^{(2,1);\mathrm{TE},\mathrm{TE}}\right)\left(1 - tA_0^{(2,1);\mathrm{TM},\mathrm{TM}}\right) - t^2 A_0^{(2,1);\mathrm{TM},\mathrm{TE}} A_0^{(2,1);\mathrm{TE},\mathrm{TM}}} . \tag{F.65}$$

We now determine an expression for the generating function $G^{(2,1);\mathrm{TM},\mathrm{TM}}$. First, we separate the $l = 1$ term and then we use the recursion relation (F.59) and shift the summation index. We thus obtain

$$\begin{aligned} G^{(2,1);\mathrm{TM},\mathrm{TM}}(t,s) = tsh_{1,1}^{(2,1);\mathrm{TM},\mathrm{TM}} + ts^2 \sum_{l=1}^{\infty} t^l s^{2l-1} \Big[& \tilde{A}_0^{(2,1);\mathrm{TM},\mathrm{TM}} h_{l,l+1}^{(2,1);\mathrm{TM},\mathrm{TM}} \\ & + \tilde{A}_0^{(2,1);\mathrm{TM},\mathrm{TE}} h_{l,l+1}^{(2,1);\mathrm{TE},\mathrm{TM}} \Big] \, . \end{aligned} \tag{F.66}$$

Now, the sum over $h_{l,l+1}^{(2,1);p,p'}$ can be carried out by applying the recursion (F.56) with (F.57), which leads to

$$\begin{aligned} G^{(2,1);\mathrm{TM},\mathrm{TM}}(t,s) &= tsh_{1,1}^{(2,1);\mathrm{TM},\mathrm{TM}} \\ &+ t^2 s^3 \tilde{A}_0^{(2,1);\mathrm{TM},\mathrm{TE}} \frac{\left(1 - ts^2 A_0^{(2,1);\mathrm{TM},\mathrm{TM}}\right) \hat{A}_0^{(2,1);\mathrm{TM},\mathrm{TE}} + ts^2 A_0^{(2,1);\mathrm{TE},\mathrm{TM}} \hat{A}_0^{(2,1);\mathrm{TM},\mathrm{TM}}}{\left(1 - ts^2 A_0^{(2,1);\mathrm{TE},\mathrm{TE}}\right)\left(1 - ts^2 A_0^{(2,1);\mathrm{TM},\mathrm{TM}}\right) - t^2 s^4 A_0^{(2,1);\mathrm{TM},\mathrm{TE}} A_0^{(2,1);\mathrm{TE},\mathrm{TM}}} \\ &+ t^2 s^3 \tilde{A}_0^{(2,1);\mathrm{TM},\mathrm{TM}} \frac{\left(1 - ts^2 A_0^{(2,1);\mathrm{TE},\mathrm{TE}}\right) \hat{A}_0^{(2,1);\mathrm{TM},\mathrm{TM}} + ts^2 A_0^{(2,1);\mathrm{TM},\mathrm{TE}} \hat{A}_0^{(2,1);\mathrm{TE},\mathrm{TM}}}{\left(1 - ts^2 A_0^{(2,1);\mathrm{TE},\mathrm{TE}}\right)\left(1 - ts^2 A_0^{(2,1);\mathrm{TM},\mathrm{TM}}\right) - t^2 s^4 A_0^{(2,1);\mathrm{TM},\mathrm{TE}} A_0^{(2,1);\mathrm{TE},\mathrm{TM}}} \, . \end{aligned} \tag{F.67}$$

We sort the terms according to the powers of the parameters t and s and get

$$G^{(2,1);\mathrm{TM},\mathrm{TM}}(t,s) = tsh_{1,1}^{(2,1);\mathrm{TM},\mathrm{TM}} + \frac{t^2 s^3 \delta^{\mathrm{TM},\mathrm{TM}} + t^3 s^5 \epsilon^{\mathrm{TM},\mathrm{TM}}}{(1 - \lambda_1 s^2 t)(1 - \lambda_2 s^2 t)} \, , \tag{F.68}$$

where we introduced the eigenvalues $\lambda_{1,2}$ given in Eq. (F.22) and defined the following expansion coefficients

$$\delta^{\mathrm{TM},\mathrm{TM}} = \hat{A}_0^{(2,1);\mathrm{TM},\mathrm{TM}} \tilde{A}_0^{(2,1);\mathrm{TM},\mathrm{TM}} + \hat{A}_0^{(2,1);\mathrm{TM},\mathrm{TE}} \tilde{A}_0^{(2,1);\mathrm{TE},\mathrm{TM}} \, , \tag{F.69a}$$

$$\begin{aligned} \epsilon^{\mathrm{TM},\mathrm{TM}} = &-A_0^{(2,1);\mathrm{TM},\mathrm{TM}} \hat{A}_0^{(2,1);\mathrm{TM},\mathrm{TE}} \tilde{A}_0^{(2,1);\mathrm{TE},\mathrm{TM}} - A_0^{(2,1);\mathrm{TE},\mathrm{TE}} \hat{A}_0^{(2,1);\mathrm{TM},\mathrm{TM}} \tilde{A}_0^{(2,1);\mathrm{TM},\mathrm{TM}} \\ &+ A_0^{(2,1);\mathrm{TM},\mathrm{TE}} \hat{A}_0^{(2,1);\mathrm{TE},\mathrm{TM}} \tilde{A}_0^{(2,1);\mathrm{TM},\mathrm{TM}} + A_0^{(2,1);\mathrm{TE},\mathrm{TM}} \hat{A}_0^{(2,1);\mathrm{TM},\mathrm{TM}} \tilde{A}_0^{(2,1);\mathrm{TM},\mathrm{TE}} \, . \end{aligned} \tag{F.69b}$$

The generating function $G^{(2,1);\mathrm{TE},\mathrm{TM}}$, appearing in Eq. (F.65) can be carried out similarly. In this case, we obtain

$$G^{(2,1);\mathrm{TE},\mathrm{TM}}(t,s) = \sum_{l=1}^{\infty} t^l s^{2l-1} h_{l,l}^{(2,1);\mathrm{TE},\mathrm{TM}} = tsh_{1,1}^{(2,1);\mathrm{TE},\mathrm{TM}} + \frac{t^2 s^3 \delta^{\mathrm{TE},\mathrm{TM}} + t^3 s^5 \epsilon^{\mathrm{TE},\mathrm{TM}}}{(1 - \lambda_1 s^2 t)(1 - \lambda_2 s^2 t)} \, , \tag{F.70}$$

where the expansion coefficients are now given by

$$\delta^{\mathrm{TE},\mathrm{TM}} = \hat{A}_0^{(2,1);\mathrm{TE},\mathrm{TM}} \tilde{A}_0^{(2,1);\mathrm{TE},\mathrm{TE}} + \hat{A}_0^{(2,1);\mathrm{TM},\mathrm{TM}} \tilde{A}_0^{(2,1);\mathrm{TE},\mathrm{TM}} \, , \tag{F.71a}$$

$$\begin{aligned} \epsilon^{\mathrm{TE},\mathrm{TM}} = &-A_0^{(2,1);\mathrm{TM},\mathrm{TM}} \hat{A}_0^{(2,1);\mathrm{TE},\mathrm{TM}} \tilde{A}_0^{(2,1);\mathrm{TE},\mathrm{TE}} - A_0^{(2,1);\mathrm{TE},\mathrm{TE}} \hat{A}_0^{(2,1);\mathrm{TM},\mathrm{TM}} \tilde{A}_0^{(2,1);\mathrm{TE},\mathrm{TM}} \\ &+ A_0^{(2,1);\mathrm{TM},\mathrm{TE}} \hat{A}_0^{(2,1);\mathrm{TE},\mathrm{TM}} \tilde{A}_0^{(2,1);\mathrm{TE},\mathrm{TM}} + A_0^{(2,1);\mathrm{TE},\mathrm{TM}} \hat{A}_0^{(2,1);\mathrm{TM},\mathrm{TM}} \tilde{A}_0^{(2,1);\mathrm{TE},\mathrm{TE}} \, . \end{aligned} \tag{F.71b}$$

The same rules apply to the generating function $H^{(2,1);\mathrm{TE},\mathrm{TE}}$, one simply has to exchange the superscripts TM and TE in all expressions given above. The sum of both functions yields

$$\begin{aligned}
&H^{(2,1);\mathrm{TM},\mathrm{TM}}(t,s) + H^{(2,1);\mathrm{TE},\mathrm{TE}}(t,s) = \\
&= s\frac{c_1^{(2,1)}t + d_1^{(2,1)}t^2}{(1-\lambda_1 t)(1-\lambda_2 t)} + \frac{d_2^{(2,1)}s^3t^2 + e_2^{(2,1)}s^3t^3 + e_3^{(2,1)}s^5t^3 + f_2^{(2,1)}s^5t^4}{(1-\lambda_1 t)(1-\lambda_2 t)(1-\lambda_1 s^2 t)(1-\lambda_2 s^2 t)}\,,
\end{aligned} \tag{F.72}$$

where the expansion coefficients are given by

$$c_1^{(2,1)} = h_{1,1}^{(2,1);\mathrm{TM},\mathrm{TM}} + h_{1,1}^{(2,1);\mathrm{TE},\mathrm{TE}}\,, \tag{F.73a}$$

$$\begin{aligned}
d_1^{(2,1)} &= -h_{1,1}^{(2,1);\mathrm{TM},\mathrm{TM}}A_0^{(2,1);\mathrm{TE},\mathrm{TE}} - h_{1,1}^{(2,1);\mathrm{TE},\mathrm{TE}}A_0^{(2,1);\mathrm{TM},\mathrm{TM}} \\
&\quad + h_{1,1}^{(2,1);\mathrm{TE},\mathrm{TM}}A_0^{(2,1);\mathrm{TM},\mathrm{TE}} + h_{1,1}^{(2,1);\mathrm{TM},\mathrm{TE}}A_0^{(2,1);\mathrm{TE},\mathrm{TM}}\,,
\end{aligned} \tag{F.73b}$$

$$d_2^{(2,1)} = \delta^{\mathrm{TM},\mathrm{TM}} + \delta^{\mathrm{TE},\mathrm{TE}}\,, \tag{F.73c}$$

$$\begin{aligned}
e_2^{(2,1)} &= -A_0^{(2,1);\mathrm{TE},\mathrm{TE}}\delta^{\mathrm{TM},\mathrm{TM}} - A_0^{(2,1);\mathrm{TM},\mathrm{TM}}\delta^{\mathrm{TE},\mathrm{TE}} \\
&\quad + A_0^{(2,1);\mathrm{TM},\mathrm{TE}}\delta^{\mathrm{TE},\mathrm{TM}} + A_0^{(2,1);\mathrm{TE},\mathrm{TM}}\delta^{\mathrm{TM},\mathrm{TE}}\,,
\end{aligned} \tag{F.73d}$$

$$e_3^{(2,1)} = \epsilon^{\mathrm{TM},\mathrm{TM}} + \epsilon^{\mathrm{TE},\mathrm{TE}}\,, \tag{F.73e}$$

$$\begin{aligned}
f_2^{(2,1)} &= -A_0^{(2,1);\mathrm{TE},\mathrm{TE}}\epsilon^{\mathrm{TM},\mathrm{TM}} - A_0^{(2,1);\mathrm{TM},\mathrm{TM}}\epsilon^{\mathrm{TE},\mathrm{TE}} \\
&\quad + A_0^{(2,1);\mathrm{TM},\mathrm{TE}}\epsilon^{\mathrm{TE},\mathrm{TM}} + A_0^{(2,1);\mathrm{TE},\mathrm{TM}}\epsilon^{\mathrm{TM},\mathrm{TE}}\,.
\end{aligned} \tag{F.73f}$$

We insert the generating functions (F.72) into Eq. (F.54) and perform the t_i-integrals with the help of (A.12) and (A.13). The free energy contribution of the case $J_F^{(2,1)}$, thus yields

$$\begin{aligned}
\mathcal{F}_{\mathrm{NTLO}}^{(ii)}(\xi)\bigg|_{J_F^{(2,1)}} = -\frac{u}{8}\int\frac{\mathrm{d}^2\mathbf{k}_{\mathrm{sp}}}{2\pi}\frac{\mathcal{K}^2}{k_{\mathrm{sp}}^2\kappa_{\mathrm{sp}}^2}\Bigg[&\frac{\lambda_1 c_1 + d_1}{\lambda_1(\lambda_1-\lambda_2)}\mathrm{Li}_2[\lambda_1] + \frac{\lambda_2 c_1 + d_1}{\lambda_2(\lambda_2-\lambda_1)}\mathrm{Li}_2[\lambda_2] \\
&+ \frac{-\lambda_1^2(\lambda_1+\lambda_2)d_2 - 2\lambda_1^2(e_2+e_3) - (3\lambda_1-\lambda_2)f_2}{\lambda_1^2(\lambda_1-\lambda_2)^3}\mathrm{Li}_2[\lambda_1] \\
&+ \frac{-\lambda_2^2(\lambda_1+\lambda_2)d_2 - 2\lambda_2^2(e_2+e_3) - (3\lambda_2-\lambda_1)f_2}{\lambda_2^2(\lambda_2-\lambda_1)^3}\mathrm{Li}_2[\lambda_2] \\
&+ \frac{\lambda_1^2 d_2 + \lambda_1(e_2+e_3) + f_2}{\lambda_1^2(\lambda_1-\lambda_2)^2}\mathrm{Li}_1[\lambda_1] \\
&+ \frac{\lambda_2^2 d_2 + \lambda_2(e_2+e_3) + f_2}{\lambda_2^2(\lambda_2-\lambda_1)^2}\mathrm{Li}_1[\lambda_2]\Bigg]\,.
\end{aligned} \tag{F.74}$$

If there are no polarisation-mixing reflections coefficient, the eigenvalues $\lambda_{1,2}$ are given by $\phi_{\mathrm{TM},\mathrm{TE}}$ defined in Eq. (10.41) and the expansion coefficients reduce to: $c_1 = 2\Delta r_b^{(1)}\Delta r_b^{(1)}\mathrm{e}^{-2\kappa_{\mathrm{sp}}L}$, $d_1 = -(\lambda_1+\lambda_2)\Delta r_b^{(1)}\Delta r_b^{(1)}\mathrm{e}^{-2\kappa_{\mathrm{sp}}L}$, $d_2 = -d_1$, $e_2 + e_3 = (\lambda_1+\lambda_2)d_1$ and $f_2 = \lambda_1\lambda_2 d_2$. Equation (F.74) then agrees with the first part of Eq. (6.66) of Ref. [109].

Next, we are going to discuss the contribution of $J_E^{(2,1)}$ given in Eq. (F.50). Together with (F.52), the trace over the round-trip operator yields

$$[\mathrm{tr}\mathcal{M}^r]^{(ii)}_{\mathrm{NTLO}}\Bigg|_{J_E^{(2,1)}} = \frac{1}{24}\int\frac{\mathrm{d}^2\mathbf{k}_{\mathrm{sp}}}{2\pi}\frac{\mathrm{e}^{-2r\kappa_{\mathrm{sp}}L}}{r}\sum_{p_1,\dots,p_{2r}}\sum_{l=1}^{r}E^{(2);p_2,p_1}_{(1);p_{2l+1}p_{2l}}X_r^{(2,1)} \\ \times\left(4r^2-12r(2l-1)+6(2l-1)^2+2\right)\,. \tag{F.75}$$

After summing over all round-trips, we obtain for the free energy contribution from $J_E^{(2,1)}$

$$\begin{aligned}\mathcal{F}^{(ii)}_{\mathrm{NTLO}}(\xi)\Bigg|_{J_E^{(2,1)}} = -\frac{1}{24}\int\frac{\mathrm{d}^2\mathbf{k}_{\mathrm{sp}}}{2\pi}\Bigg[&4\left(H^{(2,1);\mathrm{TM,TM}}(1,1)+H^{(2,1);\mathrm{TM,TM}}(1,1)\right)\\ &-12\left(\frac{\mathrm{d}}{\mathrm{d}s}\int_0^1\frac{\mathrm{d}t}{t}H^{(2,1);\mathrm{TM,TM}}(t,s)+H^{(2,1);\mathrm{TM,TM}}(t,s)\right)_{s=1}\\ &+6\left(\frac{\mathrm{d}}{\mathrm{d}s}s\frac{\mathrm{d}}{\mathrm{d}s}\int_0^1\frac{\mathrm{d}t_1}{t_1}\int_0^{t_1}\frac{\mathrm{d}t}{t}H^{(2,1);\mathrm{TM,TM}}(t,s)+H^{(2,1);\mathrm{TM,TM}}(t,s)\right)_{s=1}\\ &+2\int_0^1\frac{\mathrm{d}t_1}{t_1}\int_0^{t_1}\frac{\mathrm{d}t}{t}\left(H^{(2,1);\mathrm{TM,TM}}(t,1)+H^{(2,1);\mathrm{TM,TM}}(t,1)\right)\Bigg]\,.\end{aligned} \tag{F.76}$$

Note that we used that derivatives of the generating functions $H(t,s)$ with respect to s yield a factor $2l-1$ in the l-sum of (F.55). The generating functions have the same form as (F.72) with the same expansion coefficient, only the definitions of $\hat{A}_0^{(2,1);p,p'}$ and $\tilde{A}_0^{(2,1);p,p'}$ change to

$$\hat{A}_0^{(2,1);p,p'} = \left[\left(r^{(2)}_{p,\mathrm{TM}}\right)_i r^{(1)}_{\mathrm{TM},p'}+\left(r^{(2)}_{p,\mathrm{TE}}\right)_i r^{(1)}_{\mathrm{TE},p'}\right]\mathrm{e}^{-2\kappa_{\mathrm{sp}}L}\,, \tag{F.77}$$

$$\tilde{A}_0^{(2,1);p,p'} = \left[r^{(2)}_{p,\mathrm{TM}}\left(r^{(1)}_{\mathrm{TM},p'}\right)_i+r^{(2)}_{p,\mathrm{TE}}\left(r^{(1)}_{\mathrm{TE},p'}\right)_i\right]\mathrm{e}^{-2\kappa_{\mathrm{sp}}L} \tag{F.78}$$

and $h_{1,1}^{(2,1);p,p'}$ is given by

$$h_{1,1}^{(2,1);p,p'} = \left[\left(r^{(2)}_{p,\mathrm{TM}}\right)_i\left(r^{(1)}_{\mathrm{TM},p'}\right)_i+\left(r^{(2)}_{p,\mathrm{TM}}\right)_i\left(r^{(1)}_{\mathrm{TM},p'}\right)_i\right]\mathrm{e}^{-2\kappa_{\mathrm{sp}}L}\,. \tag{F.79}$$

We use the results (A.12), (A.13) and (A.14) for the integrals in Eq. (F.76). The derivatives with respect to s can be carried out by applying the relation (A.10) $z\partial_z \mathrm{Li}_n[z] = \mathrm{Li}_{n-1}[z]$. We then find

$$
\begin{aligned}
\mathcal{F}^{(ii)}_{\mathrm{NTLO}}(\xi)\Big|_{J_E^{(2,1)}} = -\frac{1}{24}\int \frac{\mathrm{d}^2\mathbf{k}_{\mathrm{sp}}}{2\pi}\Bigg[& \frac{4(c_1+d_1)}{\lambda_1\lambda_2}\mathrm{Li}_0[\lambda_1]\mathrm{Li}_0[\lambda_2] \\
& + \frac{4(d_2+e_2+e_3+f_2)}{\lambda_1\lambda_2}\mathrm{Li}_{-1}[\lambda_1]\mathrm{Li}_{-1}[\lambda_2] \\
& - \frac{4(\lambda_1^2 d_2+\lambda_1(e_2+e_3)+f_2)}{\lambda_1^2(\lambda_1-\lambda_2)^2}\mathrm{Li}_{-1}[\lambda_1] - \frac{4(\lambda_2^2 d_2+\lambda_2(e_2+e_3)+f_2)}{\lambda_2^2(\lambda_1-\lambda_2)^2}\mathrm{Li}_{-1}[\lambda_2] \\
& - \frac{12(c_1\lambda_1+d_1)}{\lambda_1(\lambda_1-\lambda_2)}\mathrm{Li}_1[\lambda_1] + \frac{12(c_1\lambda_2+d_1)}{\lambda_2(\lambda_1-\lambda_2)}\mathrm{Li}_1[\lambda_2] \\
& + \frac{12(d_2\lambda_1^2+2e_2\lambda_1+f_2)}{\lambda_1^2(\lambda_1-\lambda_2)^2}\mathrm{Li}_1[\lambda_1] + \frac{12(d_2\lambda_2^2+2e_2\lambda_2+f_2)}{\lambda_2^2(\lambda_1-\lambda_2)^2}\mathrm{Li}_1[\lambda_2] \\
& + \frac{24(2d_2\lambda_1\lambda_2+(e_2+e_3)(\lambda_1+\lambda_2)+2f_2)}{(\lambda_1-\lambda_2)^4}\left(\mathrm{Li}_1[\lambda_1]+\mathrm{Li}_1[\lambda_2]\right) \\
& + \frac{8(c_1\lambda_1+d_1)}{\lambda_1(\lambda_1-\lambda_2)}\mathrm{Li}_2[\lambda_1] - \frac{8(c_1\lambda_2+d_1)}{\lambda_2(\lambda_1-\lambda_2)}\mathrm{Li}_2[\lambda_2] \\
& - \frac{8(d_2\lambda_1^2(\lambda_1+\lambda_2)+2(e_2+e_3)\lambda_1^2+f_2(3\lambda_1-\lambda_2))}{\lambda_1^2(\lambda_1-\lambda_2)^3}\mathrm{Li}_2[\lambda_1] \\
& + \frac{8(d_2\lambda_2^2(\lambda_1+\lambda_2)+2(e_2+e_3)\lambda_2^2+f_2(3\lambda_2-\lambda_1))}{\lambda_2^2(\lambda_1-\lambda_2)^3}\mathrm{Li}_2[\lambda_2] \\
& - \frac{48(d_2\lambda_1\lambda_2(\lambda_1+\lambda_2)+2e_2\lambda_1\lambda_2+e_3(\lambda_1^2+\lambda_2^2)+f_2(\lambda_1+\lambda_2))}{(\lambda_1-\lambda_2)^5}\left(\mathrm{Li}_2[\lambda_1]-\mathrm{Li}_2[\lambda_2]\right)\Bigg].
\end{aligned}
\tag{F.80}
$$

The expression vanishes in the limit of dielectric spheres, which is in agreement with the discussion in Ref. [109]. After evaluating the expansion coefficients for dielectrics and inserting them in the expression above, one finds that all terms cancel each other out. However, this can also already be seen in Eq. (F.75), where the coefficient $E^{(2);p_2,p_1}_{(1);p_{2l+1}p_{2l}}$ does not depend on l for dielectrics and the sum over l yields $\sum_{l=1}^{r}\left(4r^2-12r(2l-1)+6(2l-1)^2+2\right)=0$.

F.4.2 Cases $J^{(1,1)}$ and $J^{(2,2)}$

Next, we examine the case $J^{(2,2)}$. Again, we start at sphere 2 and take the derivative of $\rho^{(2)}_{p_2,p_1}$. For the next derivative, we have $(r-1)$ possibilities, $d^{(2);1/2}_{p_{2l},p_{2l-1}}$ with $l = 2,\dots r$. Considering all combinations in Eq. (F.2), we find

$$\begin{aligned} J^{(2,2)} = r\frac{\mathrm{e}^{-2r\kappa_{\mathrm{sp}}L}}{\kappa_{\mathrm{sp}}^{2r}} \sum_{p_1,\dots,p_{2r}} \sum_{l=2}^{r} \Big[& d(2l-2)d^{(2);1}_{p_2,p_1}d^{(2);1}_{p_{2l},p_{2l-1}} + d_+(2l-3)d^{(2);1}_{p_2,p_1}d^{(2);2}_{p_{2l},p_{2l-1}} \\ & + d_-(2l-1)d^{(2);2}_{p_2,p_1}d^{(2);1}_{p_{2l},p_{2l-1}} + d(2l-2)d^{(2);2}_{p_2,p_1}d^{(2);2}_{p_{2l},p_{2l-1}}\Big] X^{(2,1)}_r \,. \end{aligned} \tag{F.81}$$

Similar to before, we use (F.46a) and (F.46b) which allows us to separate $J^{(2,2)}$ into two terms $J^{(2,2)} = J^{(2,2)}_F + J^{(2,2)}_E$ with

$$J^{(2,2)}_F = r\frac{\mathrm{e}^{-2r\kappa_{\mathrm{sp}}L}}{\kappa_{\mathrm{sp}}^{2r}} \sum_{p_1,\dots,p_{2r}} \sum_{l=2}^{r} F^{(2);p_2,p_1}_{(2);p_{2l},p_{2l-1}} \Big(2d(2l-2) - d_-(2l-1) - d_+(2l-3)\Big) X^{(2,1)}_r \,, \tag{F.82}$$

$$J^{(2,2)}_E = r\frac{\mathrm{e}^{-2r\kappa_{\mathrm{sp}}L}}{\kappa_{\mathrm{sp}}^{2r}} \sum_{p_1,\dots,p_{2r}} \sum_{l=2}^{r} E^{(2);p_2,p_1}_{(2);p_{2l},p_{2l-1}} \Big(2d(2l-2) + d_-(2l-1) + d_+(2l-3)\Big) X^{(2,1)}_r \,, \tag{F.83}$$

where E and F can be found in Eqs. (F.47) and (F.48). Next, we determine the sum over the $d_\pm$-functions, appearing in the expression above, which yield

$$2d(2l-2) - d_-(2l-1) - d_+(2l-3) = -\frac{2\kappa_{\mathrm{sp}}}{r(R_1+R_2)}\frac{R_1}{R_2} \,, \tag{F.84}$$

$$\begin{aligned} & 2d(2l-2) + d_-(2l-1) + d_+(2l-3) = \\ & = \frac{\kappa_{\mathrm{sp}}}{2r}\frac{1}{3R_{\mathrm{eff}}}\left[2\left(1 + 3\frac{R_1-R_2}{R_1+R_2}\right) + 4r^2 - 12r(2l-2) + 6(2l-2)^2\right] . \end{aligned} \tag{F.85}$$

We start again by first evaluating the case $J^{(2,2)}_F$. Here the contribution to the free energy yields

$$\begin{aligned} \mathcal{F}^{(ii)}_{\mathrm{NTLO}}(\xi)\Big|_{J^{(2,2)}_F} &= \frac{u}{2}\frac{R_1}{R_2}\int \frac{\mathrm{d}^2\mathbf{k}_{\mathrm{sp}}}{2\pi} \sum_{r=1}^{\infty} \frac{\mathrm{e}^{-2r\kappa_{\mathrm{sp}}L}}{r^2} \sum_{p_1,\dots,p_{2r}} \sum_{l=1}^{r} F^{(2);p_2,p_1}_{(2);p_{2l},p_{2l-1}} X^{(2,1)}_r \\ &= \frac{u}{8}\frac{R_1}{R_2}\int \frac{\mathrm{d}^2\mathbf{k}_{\mathrm{sp}}}{2\pi} \frac{\mathcal{K}^2}{k_{\mathrm{sp}}^2\kappa_{\mathrm{sp}}} \int_0^1 \frac{\mathrm{d}t_1}{t_1} \int_0^{t_1} \frac{\mathrm{d}t}{t} \left(H^{(2,1);\mathrm{TM,TM}}(t,1) + H^{(2,1);\mathrm{TE,TE}}(t,1)\right) , \end{aligned} \tag{F.86}$$

where the generating function is given by

$$H^{(2,1);p,p}(t,s) = \sum_{r=2}^{\infty} t^r \sum_{l=2}^{r} s^{2l-2} h^{(2,1);p,p}_{r,l} \,. \tag{F.87}$$

Note that the exponent of the parameter s is now given by $(2l-2)$ to account for the terms in Eq. (F.85). The recursion relations for $h^{(2,1);p,p'}_{r,l}$ are given in Eqs. (F.56), (F.59) and (F.57). We then find for the generating functions

$$H^{(2,1);\mathrm{TM,TM}}(t,s)+H^{(2,1);\mathrm{TE,TE}}(t,s)=\frac{d_2^{(2,1)}s^2t^2+e_2^{(2,1)}s^2t^3+e_3^{(2,1)}s^4t^3+f_2^{(2,1)}s^4t^4}{(1-\lambda_1 t)(1-\lambda_2 t)(1-\lambda_1 s^2 t)(1-\lambda_2 s^2 t)}\,. \tag{F.88}$$

The expansion coefficients $d_2^{(2,1)}$, $e_2^{(2,1)}$ and $f_2^{(2,1)}$ are the same as before, only that the definition of $\hat{A}_0^{(2,1);p,p'}$ and $\tilde{A}_0^{(2,1);p,p'}$ changed to

$$\hat{A}_0^{(2,1);\mathrm{TM,TM}}=\tilde{A}_0^{(2,1);\mathrm{TM,TM}}=\left(\Delta r_a^{(2)}r_{\mathrm{TM,TM}}^{(1)}-\Delta r_b^{(2)}r_{\mathrm{TE,TM}}^{(1)}\right)\mathrm{e}^{-2\kappa_{\mathrm{sp}}L}\,, \tag{F.89a}$$

$$\hat{A}_0^{(2,1);\mathrm{TM,TE}}=\tilde{A}_0^{(2,1);\mathrm{TM,TE}}=\left(\Delta r_a^{(2)}r_{\mathrm{TM,TE}}^{(1)}-\Delta r_b^{(2)}r_{\mathrm{TE,TE}}^{(1)}\right)\mathrm{e}^{-2\kappa_{\mathrm{sp}}L}\,, \tag{F.89b}$$

$$\hat{A}_0^{(2,1);\mathrm{TE,TM}}=\tilde{A}_0^{(2,1);\mathrm{TE,TM}}=-\left(\Delta r_a^{(2)}r_{\mathrm{TE,TM}}^{(1)}+\Delta r_b^{(2)}r_{\mathrm{TM,TM}}^{(1)}\right)\mathrm{e}^{-2\kappa_{\mathrm{sp}}L}\,, \tag{F.89c}$$

$$\hat{A}_0^{(2,1);\mathrm{TE,TE}}=\tilde{A}_0^{(2,1);\mathrm{TE,TE}}=-\left(\Delta r_a^{(2)}r_{\mathrm{TE,TE}}^{(1)}+\Delta r_b^{(2)}r_{\mathrm{TM,TE}}^{(1)}\right)\mathrm{e}^{-2\kappa_{\mathrm{sp}}L}\,. \tag{F.89d}$$

After carrying out the t_i-integrals with Eq. (A.13), we get

$$\begin{aligned}\mathcal{F}_{\mathrm{NTLO}}^{(ii)}(\xi)\bigg|_{J_F^{(2,2)}}=\frac{u}{8}\frac{R_1}{R_2}\int\frac{\mathrm{d}^2\mathbf{k}_{\mathrm{sp}}}{2\pi}\frac{\mathcal{K}^2}{k_{\mathrm{sp}}^2\kappa_{\mathrm{sp}}^2}\Bigg[&\frac{\lambda_1^2d_2+\lambda_1(e_2+e_3)+f_2}{\lambda_1^2(\lambda_1-\lambda_2)^2}\mathrm{Li}_1[\lambda_1]\\&+\frac{\lambda_2^2d_2+\lambda_2(e_2+e_3)+f_2}{\lambda_2^2(\lambda_2-\lambda_1)^2}\mathrm{Li}_1[\lambda_2]\\&+\frac{-\lambda_1^2(\lambda_1+\lambda_2)d_2-2\lambda_1^2(e_2+e_3)-(3\lambda_1-\lambda_2)f_2}{\lambda_1^2(\lambda_1-\lambda_2)^3}\mathrm{Li}_2[\lambda_1]\\&+\frac{-\lambda_2^2(\lambda_1+\lambda_2)d_2-2\lambda_2^2(e_2+e_3)-(3\lambda_2-\lambda_1)f_2}{\lambda_2^2(\lambda_2-\lambda_1)^3}\mathrm{Li}_2[\lambda_2]\Bigg]\,.\end{aligned} \tag{F.90}$$

The expansion coefficients reduce to $d_2=2r_{\mathrm{TM,TM}}^{(1)}r_{\mathrm{TE,TE}}^{(1)}(\Delta r_b^{(2)}\mathrm{e}^{-2\kappa_{\mathrm{sp}}L})^2$, $e_2+e_3=-(\lambda_1+\lambda_2)d_2$ and $f_2=\lambda_1\lambda_2d_2$. Equation (F.91) then reproduces Eq. (6.66) of Ref. [109].

Finally, for $J_E^{(2,2)}$ defined in Eq. (F.83), the free energy contributions reads

$$\begin{aligned}\mathcal{F}_{\mathrm{NTLO}}^{(ii)}(\xi)\bigg|_{J_E^{(2,2)}}=-\frac{1}{24}\int\frac{\mathrm{d}^2\mathbf{k}_{\mathrm{sp}}}{2\pi}\Bigg[&4\left(H^{(2,1);\mathrm{TM,TM}}(1,1)+H^{(2,1);\mathrm{TM,TM}}(1,1)\right)\\&-12\left(\frac{\mathrm{d}}{\mathrm{d}s}\int_0^1\frac{\mathrm{d}t}{t}H^{(2,1);\mathrm{TM,TM}}(t,s)+H^{(2,1);\mathrm{TM,TM}}(t,s)\right)_{s=1}\\&+6\left(\frac{\mathrm{d}}{\mathrm{d}s}s\frac{\mathrm{d}}{\mathrm{d}s}\int_0^1\frac{\mathrm{d}t_1}{t_1}\int_0^{t_1}\frac{\mathrm{d}t}{t}H^{(2,1);\mathrm{TM,TM}}(t,s)+H^{(2,1);\mathrm{TM,TM}}(t,s)\right)_{s=1}\\&+2\left(1+3\frac{R_1-R_2}{R_1+R_2}\right)\int_0^1\frac{\mathrm{d}t_1}{t_1}\int_0^{t_1}\frac{\mathrm{d}t}{t}\left(H^{(2,1);\mathrm{TM,TM}}(t,1)+H^{(2,1);\mathrm{TM,TM}}(t,1)\right)\Bigg]\,.\end{aligned} \tag{F.91}$$

The generating functions are again given by (F.88), however the definition of $\hat{A}_0^{(2,1);p,p'}$ and $\tilde{A}_0^{(2,1);p,p'}$

changed to

$$\hat{A}_0^{(2,1);p,p'} = \tilde{A}_0^{(2,1);p,p'} = \left[\left(r^{(2)}_{p,\mathrm{TM}}\right)_i r^{(1)}_{\mathrm{TM},p'} + \left(r^{(2)}_{p,\mathrm{TE}}\right)_i r^{(1)}_{\mathrm{TE},p'}\right] \mathrm{e}^{-2\kappa_{\mathrm{sp}}L} . \tag{F.92}$$

Note also that we used that derivatives of $H(t,s)$ with respect to s yield a factor $(2l-2)$ in the l-sum in Eq. (F.87). Applying the integrals (A.13) and (A.14) together with the relation for derivatives of polylogarithms, we obtain

$$\begin{aligned}
\mathcal{F}^{(ii)}_{\mathrm{NTLO}}(\xi)\Big|_{J_E^{(2,2)}} = -\frac{1}{24}\int \frac{\mathrm{d}^2\mathbf{k}_{\mathrm{sp}}}{2\pi}\Bigg\{ & 4(d_2+e_2+e_3+f_2)\frac{\mathrm{Li}_{-1}[\lambda_1]\mathrm{Li}_{-1}[\lambda_2]}{\lambda_1\lambda_2} \\
& - \frac{4(d_2\lambda_1^2+(e_2+e_3)\lambda_1+f_2)}{\lambda_1^2(\lambda_1-\lambda_2)^2}\mathrm{Li}_{-1}[\lambda_1] - \frac{4(d_2\lambda_2^2+(e_2+e_3)\lambda_2+f_2)}{\lambda_2^2(\lambda_1-\lambda_2)^2}\mathrm{Li}_{-1}[\lambda_2] \\
& + \frac{24(2d_2\lambda_1\lambda_2+(e_2+e_3)(\lambda_1+\lambda_2)+2f_2)}{(\lambda_1-\lambda_2)^4}\left(\mathrm{Li}_1[\lambda_1]+\mathrm{Li}_1[\lambda_2]\right) \\
& - \frac{24(2d_2\lambda_1\lambda_2+(e_2+e_3)(\lambda_1+\lambda_2)+2f_2)}{(\lambda_1-\lambda_2)^5}(\lambda_1+\lambda_2)\left(\mathrm{Li}_2[\lambda_1]-\mathrm{Li}_2[\lambda_2]\right) \\
& + 6\left(1+\frac{R_1-R_2}{R_1+R_2}\right)\left[\frac{\lambda_1^2 d_2+\lambda_1(e_2+e_3)+f_2}{\lambda_1^2(\lambda_1-\lambda_2)^2}\mathrm{Li}_1[\lambda_1] + \frac{\lambda_2^2 d_2+\lambda_2 e_2+f_2}{\lambda_2^2(\lambda_2-\lambda_1)^2}\mathrm{Li}_1[\lambda_2]\right] \\
& + 2\left(1+3\frac{R_1-R_2}{R_1+R_2}\right)\left[\frac{-\lambda_1^2(\lambda_1+\lambda_2)d_2-2\lambda_1^2(e_2+e_3)-(3\lambda_1-\lambda_2)f_2}{\lambda_1^2(\lambda_1-\lambda_2)^3}\mathrm{Li}_2[\lambda_1]\right. \\
& \qquad \left. + \frac{-\lambda_2^2(\lambda_1+\lambda_2)d_2-2\lambda_2^2(e_2+e_3)-(3\lambda_2-\lambda_1)f_2}{\lambda_2^2(\lambda_2-\lambda_1)^3}\mathrm{Li}_2[\lambda_2]\right]\Bigg\} .
\end{aligned} \tag{F.93}$$

The expansion coefficients yield

$$\begin{aligned}
d_2 &= \left[r^{(1)}_{\mathrm{TM,TM}}(r^{(2)}_{\mathrm{TM,TM}})_i \mathrm{e}^{-2\kappa_{\mathrm{sp}}L}\right]^2 + \left[r^{(1)}_{\mathrm{TE,TE}}(r^{(2)}_{\mathrm{TE,TE}})_i \mathrm{e}^{-2\kappa_{\mathrm{sp}}L}\right]^2 , \\
e_2+e_3 &= -2\phi_{\mathrm{TE}}\left[r^{(1)}_{\mathrm{TM,TM}}(r^{(2)}_{\mathrm{TM,TM}})_i \mathrm{e}^{-2\kappa_{\mathrm{sp}}L}\right]^2 - 2\phi_{\mathrm{TM}}\left[r^{(1)}_{\mathrm{TE,TE}}(r^{(2)}_{\mathrm{TE,TE}})_i \mathrm{e}^{-2\kappa_{\mathrm{sp}}L}\right]^2 , \\
f_2 &= \phi_{\mathrm{TE}}^2\left[r^{(1)}_{\mathrm{TM,TM}}(r^{(2)}_{\mathrm{TM,TM}})_i \mathrm{e}^{-2\kappa_{\mathrm{sp}}L}\right]^2 + \phi_{\mathrm{TM}}^2\left[r^{(1)}_{\mathrm{TE,TE}}(r^{(2)}_{\mathrm{TE,TE}})_i \mathrm{e}^{-2\kappa_{\mathrm{sp}}L}\right]^2
\end{aligned}$$

for dielectric spheres and Eq. (F.93) then agrees with Eq. (6.63) of Ref. [109].

F.5 Application to PEMC spheres

In this Section, we apply the results we derived in the previous Section for general bi-isotropic spheres to the idealized system of PEMCs. The Fresnel reflection coefficients of PEMCs only depend on the material parameter θ. They yield (4.34):

$$r_{\mathrm{TM,TM}} = -r_{\mathrm{TE,TE}} = \cos(2\theta)\,, \qquad r_{\mathrm{TM,TE}} = r_{\mathrm{TE,TM}} = -\sin(2\theta)\,.$$

This particularly means that only terms in Eq. (F.2), where derivatives are taken at the polarisation-conversion coefficients $A_{i,j}$, $B_{i,j}$, $C_{i,j}$ and $D_{i,j}$ contribute.

For the case I, discussed in Sec. F.3, this means only (F.40) is not vanishing

$$\mathcal{F}^{(ii)}_{\mathrm{NTLO}}(\xi)\bigg|_{I} = -\frac{u}{4}\int\frac{\mathrm{d}^2\mathbf{k}_{\mathrm{sp}}}{2\pi}\left\{-\left(1+\frac{R_1}{R_2}\right)\mathcal{P}^{(2,1)}_{I,1}+\frac{R_1}{R_2}\mathcal{P}^{(2,1)}_{I,2}-\left(1+\frac{R_2}{R_1}\right)\mathcal{P}^{(1,2)}_{I,1}+\frac{R_2}{R_1}\mathcal{P}^{(1,2)}_{I,2}\right\} \tag{F.94}$$

with (F.35)

$$\mathcal{P}^{(1,2)}_{I,m} = \frac{c^{(1,2)}_I\lambda_1 + d^{(1,2)}_I}{\lambda_1(\lambda_1-\lambda_2)}\mathrm{Li}_m[\lambda_1] + \frac{c^{(1,2)}_I\lambda_2 + d^{(1,2)}_I}{\lambda_2(\lambda_2-\lambda_1)}\mathrm{Li}_m[\lambda_2]\,. \tag{F.95}$$

The eigenvalues of the round-trip matrix for two PEMC plates is given by (11.2)

$$\lambda_{1/2} = \exp(\pm 2\mathrm{i}\delta)\exp(-2\kappa_{\mathrm{sp}}L)\,,$$

where $\delta = |\theta_1 - \theta_2|$. The expansion coefficients, defined in Eq. (F.34) simplify to $c^{(1,2)}_I = c^{(2,1)}_I = 4\mathcal{K}^2\cos(2\delta)\mathrm{e}^{-2\kappa_{\mathrm{sp}}L}/(\kappa_{\mathrm{sp}}k_{\mathrm{sp}})^2$ and $d^{(1,2)}_I = d^{(2,1)}_I = -4\mathcal{K}^2\mathrm{e}^{-4\kappa_{\mathrm{sp}}L}/(\kappa_{\mathrm{sp}}k_{\mathrm{sp}})^2$.

Next, we present the expressions from case J, discussed in Sec. F.4, which are not vanishing. For the case $J^{(2,1)}$ only expression (F.74) contributes, with

$$\begin{aligned}\mathcal{F}^{(ii)}_{\mathrm{NTLO}}(\xi)\bigg|_{J^{(2,1)}} = -\frac{u}{8}\int\frac{\mathrm{d}^2\mathbf{k}_{\mathrm{sp}}}{2\pi}\frac{\mathcal{K}^2}{k^2_{\mathrm{sp}}\kappa^2_{\mathrm{sp}}}\Bigg[&\frac{\lambda_1 c_1 + d_1}{\lambda_1(\lambda_1-\lambda_2)}\mathrm{Li}_2[\lambda_1] + \frac{\lambda_2 c_1 + d_1}{\lambda_2(\lambda_2-\lambda_1)}\mathrm{Li}_2[\lambda_2] \\ &+ \frac{-\lambda_1^2(\lambda_1+\lambda_2)d_2 - 2\lambda_1^2(e_2+e_3) - (3\lambda_1-\lambda_2)f_2}{\lambda_1^2(\lambda_1-\lambda_2)^3}\mathrm{Li}_2[\lambda_1] \\ &+ \frac{-\lambda_2^2(\lambda_1+\lambda_2)d_2 - 2\lambda_2^2(e_2+e_3) - (3\lambda_2-\lambda_1)f_2}{\lambda_2^2(\lambda_2-\lambda_1)^3}\mathrm{Li}_2[\lambda_2] \\ &+ \frac{\lambda_1^2 d_2 + \lambda_1(e_2+e_3) + f_2}{\lambda_1^2(\lambda_1-\lambda_2)^2}\mathrm{Li}_1[\lambda_1] \\ &+ \frac{\lambda_2^2 d_2 + \lambda_2(e_2+e_3) + f_2}{\lambda_2^2(\lambda_2-\lambda_1)^2}\mathrm{Li}_1[\lambda_2]\Bigg]\,,\end{aligned} \tag{F.96}$$

where the expansion coefficients for PEMC spheres yield: $c_1 = 8\cos(2\delta)\mathrm{e}^{-2\kappa_{\mathrm{sp}}L}$, $d_1 = -8\mathrm{e}^{-4\kappa_{\mathrm{sp}}L}$ and $d_2 = -8\cos(4\delta)\mathrm{e}^{-4\kappa_{\mathrm{sp}}L}$, $e_2 + e_3 = -16\cos(2\delta)\mathrm{e}^{-6\kappa_{\mathrm{sp}}L}$, $f_2 = 8\mathrm{e}^{-8\kappa_{\mathrm{sp}}L}$. We get the same result for the case $J^{(1,2)}$.

For $J^{(2,2)}$ only (F.91) yields a non-vanishing contribution with

$$\begin{aligned}\mathcal{F}^{(ii)}_{\mathrm{NTLO}}(\xi)\Big|_{J^{(2,2)}} = \frac{u}{8}\frac{R_1}{R_2}\int\frac{\mathrm{d}^2\mathbf{k}_{\mathrm{sp}}}{2\pi}\frac{\mathcal{K}^2}{k_{\mathrm{sp}}^2\kappa_{\mathrm{sp}}^2}\Bigg[&\frac{\lambda_1^2 d_2+\lambda_1(e_2+e_3)+f_2}{\lambda_1^2(\lambda_1-\lambda_2)^2}\mathrm{Li}_1[\lambda_1]\\ &+\frac{\lambda_2^2 d_2+\lambda_2(e_2+e_3)+f_2}{\lambda_2^2(\lambda_2-\lambda_1)^2}\mathrm{Li}_1[\lambda_2]\\ &+\frac{-\lambda_1^2(\lambda_1+\lambda_2)d_2-2\lambda_1^2(e_2+e_3)-(3\lambda_1-\lambda_2)f_2}{\lambda_1^2(\lambda_1-\lambda_2)^3}\mathrm{Li}_2[\lambda_1]\\ &+\frac{-\lambda_2^2(\lambda_1+\lambda_2)d_2-2\lambda_2^2(e_2+e_3)-(3\lambda_2-\lambda_1)f_2}{\lambda_2^2(\lambda_2-\lambda_1)^3}\mathrm{Li}_2[\lambda_2]\Bigg].\end{aligned} \tag{F.97}$$

The expansion coefficients are given by: $d_2 = -8\cos(4\delta)\mathrm{e}^{-4\kappa_{\mathrm{sp}}L}$, $e_2 + e_3 = 16\cos(2\delta)\mathrm{e}^{-6\kappa_{\mathrm{sp}}L}$ and $f_2 = -8\mathrm{e}^{-8\kappa_{\mathrm{sp}}L}$. For $J^{(1,1)}$ only the pre-factor R_1/R_2 in the expression above has to be replaced by R_2/R_1.

After inserting all expansion coefficients in the respective expression, we find that the case I and J precisely cancel each other out, so $\mathcal{F}^{(ii)}_{\mathrm{NTLO}}(\xi) = 0$ for two PEMC spheres.

Bibliography

1. Ashkin, A. Acceleration and Trapping of Particles by Radiation Pressure. *Phys. Rev. Lett.* **24,** 156–159. doi:`10.1103/PhysRevLett.24.156` (1970).
2. Ng, J., Lin, Z. & Chan, C. T. Theory of Optical Trapping by an Optical Vortex Beam. *Phys. Rev. Lett.* **104,** 103601. doi:`10.1103/PhysRevLett.104.103601` (2010).
3. Ether, D. S. *et al.* Probing the Casimir force with optical tweezers. *Europhys. Lett.* **112,** 44001. doi:`10.1209/0295-5075/112/44001` (2015).
4. Pires, L. B. *et al.* Probing the screening of the Casimir interaction with optical tweezers. *Phys. Rev. Res.* **3,** 033037. doi:`10.1103/PhysRevResearch.3.033037` (2021).
5. Casimir, H. B. G. On the attraction between two perfectly conducting plates. *Proc. Kon. Ned. Akad. Wetenschappen* **51,** 79 (1948).
6. Feinberg, J., Mann, A. & Revzen, M. Casimir Effect: The Classical Limit. *Ann. Phys.* **288,** 103–136. doi:`10.1006/aphy.2000.6118` (2001).
7. Gelbwaser-Klimovsky, D., Graham, N., Kardar, M. & Krüger, M. Equilibrium forces on nonreciprocal materials. *Phys. Rev. B* **106,** 115106. doi:`10.1103/PhysRevB.106.115106` (2022).
8. Lindell, I. V., Sihvola, A. H., Tretyakov, S. & Viitanen, A. *Electromagnetic waves in chiral and bi-isotropic media* ISBN: 0890066841 (Artech House, Norwood, 1994).
9. Lamoreaux, S. K. Demonstration of the Casimir Force in the 0.6 to 6μm Range. *Phys. Rev. Lett.* **78,** 5–8. doi:`10.1103/PhysRevLett.78.5` (1997).
10. Munday, J. N., Capasso, F. & Parsegian, V. A. Measured long-range repulsive Casimir–Lifshitz forces. *Nature* **457,** 170–173. doi:`10.1038/nature07610` (2009).
11. London, F. Zur Theorie und Systematik der Molekularkräfte. *Z. Physik* **63,** 245–279 (1930).
12. Casimir, H. B. G. & Polder, D. The Influence of Retardation on the London-van der Waals Forces. *Phys. Rev.* **73,** 360–372. doi:`10.1103/PhysRev.73.360` (1948).
13. Lifshitz, E. The Theory of Molecular Attractive Forces between Solids. *Sov. Phys. JETP* **2,** 73 (1956).
14. I.E. Dzyaloshinskii, E. L. & Pitaevskii, L. The general theory of van der Waals forces. *Adv. Phys.* **10,** 165–209. doi:`10.1080/00018736100101281` (1961).
15. Fiedler, J. *et al.* Perspectives on weak interactions in complex materials at different length scales. *Phys. Chem. Chem. Phys.* **25,** 2671–2705. doi:`10.1039/D2CP03349F` (2023).
16. Sparnaay, M. Measurements of attractive forces between flat plates. *Physica* **24,** 751–764. doi:`10.1016/S0031-8914(58)80090-7` (1958).
17. Mohideen, U. & Roy, A. Precision Measurement of the Casimir Force from 0.1 to 0.9μm. *Phys. Rev. Lett.* **81,** 4549–4552. doi:`10.1103/PhysRevLett.81.4549` (1998).
18. Decca, R. S., López, D., Fischbach, E. & Krause, D. E. Measurement of the Casimir Force between Dissimilar Metals. *Phys. Rev. Lett.* **91,** 050402. doi:`10.1103/PhysRevLett.91.050402` (2003).

19. Garrett, J. L., Somers, D. A. T. & Munday, J. N. Measurement of the Casimir Force between Two Spheres. *Phys. Rev. Lett.* **120,** 040401. doi:`10.1103/PhysRevLett.120.040401` (2018).

20. Gong, T., Corrado, M. R., Mahbub, A. R., Shelden, C. & Munday, J. N. Recent progress in engineering the Casimir effect – applications to nanophotonics, nanomechanics, and chemistry. *Nanophotonics* **10,** 523–536. doi:`10.1515/nanoph-2020-0425` (2021).

21. Lambrecht, A., Maia Neto, P. A. & Reynaud, S. The Casimir effect within scattering theory. *New J. Phys.* **8,** 243. doi:`10.1088/1367-2630/8/10/243` (2006).

22. Emig, T., Graham, N., Jaffe, R. L. & Kardar, M. Casimir Forces between Arbitrary Compact Objects. *Phys. Rev. Lett.* **99,** 170403. doi:`10.1103/PhysRevLett.99.170403` (2007).

23. Rahi, S. J., Emig, T., Graham, N., Jaffe, R. L. & Kardar, M. Scattering theory approach to electrodynamic Casimir forces. *Phys. Rev. D* **80,** 085021. doi:`10.1103/PhysRevD.80.085021` (2009).

24. Bimonte, G. & Emig, T. Exact Results for Classical Casimir Interactions: Dirichlet and Drude Model in the Sphere-Sphere and Sphere-Plane Geometry. *Phys. Rev. Lett.* **109,** 160403. doi:`10.1103/PhysRevLett.109.160403` (2012).

25. Zhao, R., Luo, Y., Fernández-Domínguez, A. I. & Pendry, J. B. Description of van der Waals Interactions Using Transformation Optics. *Phys. Rev. Lett.* **111,** 033602. doi:`10.1103/PhysRevLett.111.033602` (2013).

26. Bimonte, G. Beyond-proximity-force-approximation Casimir force between two spheres at finite temperature. II. Plasma versus Drude modeling, grounded versus isolated spheres. *Phys. Rev. D* **98,** 105004. doi:`10.1103/PhysRevD.98.105004` (2018).

27. Maia Neto, P. A. *et al.* Scattering theory of the screened Casimir interaction in electrolytes. *Eur. Phys. J. D* **73,** 178. doi:`10.1140/epjd/e2019-100225-8` (2019).

28. Spreng, B. *et al.* Universal Casimir attraction between filaments at the cell scale. *New J. Phys.* **26,** 013009. doi:`10.1088/1367-2630/ad1846` (2024).

29. Parsegian, V. & Ninham, B. Toward the correct calculation of van der Waals interactions between lyophobic colloids in an aqueous medium. *J. Colloid Interface Sci.* **37,** 332–341. doi:`10.1016/0021-9797(71)90301-8` (1971).

30. Hamaker, H. The London—van der Waals attraction between spherical particles. *Physica* **4,** 1058–1072. doi:`10.1016/S0031-8914(37)80203-7` (1937).

31. Gies, H. & Klingmüller, K. Casimir Effect for Curved Geometries: Proximity-Force- Approximation Validity Limits. *Phys. Rev. Lett.* **96,** 220401. doi:`10.1103/PhysRevLett.96.220401` (2006).

32. Liu, Y., Xie, H., Li, C., Jeng, D.-S. & Zhang, B. N. Influence of Particle Geometry on Dispersion Forces. *Phys. Rev. Appl.* **19,** 044019. doi:`10.1103/PhysRevApplied.19.044019` (2023).

33. Spreng, B., Hartmann, M., Henning, V., Maia Neto, P. A. & Ingold, G.-L. Proximity force approximation and specular reflection: Application of the WKB limit of Mie scattering to the Casimir effect. *Phys. Rev. A* **97,** 062504. doi:`10.1103/PhysRevA.97.062504` (2018).

34. Henning, V., Spreng, B., Hartmann, M., Ingold, G.-L. & Maia Neto, P. A. Role of diffraction in the Casimir effect beyond the proximity force approximation. *J. Opt. Soc. Am. B* **36,** C77. doi:`10.1364/JOSAB.36.000C77` (2019).

35. Henning, V., Spreng, B., Maia Neto, P. A. & Ingold, G.-L. Casimir Interaction between a Plane and a Sphere: Correction to the Proximity-Force Approximation at Intermediate Temperatures. *Universe* **7,** 129. doi:`10.3390/universe7050129` (2021).

36. Woods, L. M. *et al.* Materials perspective on Casimir and van der Waals interactions. *Rev. Mod. Phys.* **88,** 045003. doi:`10.1103/RevModPhys.88.045003` (2016).

37. Lu, B.-S. The Casimir Effect in Topological Matter. *Universe* **7,** 237. doi:`10.3390/universe7070237` (2021).

38. Serry, F. M., Walliser, D. & Maclay, G. J. The role of the casimir effect in the static deflection and stiction of membrane strips in microelectromechanical systems (MEMS). *J. Appl. Phys.* **84,** 2501–2506. doi:`10.1063/1.368410` (1998).

39. Kenneth, O. & Klich, I. Opposites Attract: A Theorem about the Casimir Force. *Phys. Rev. Lett.* **97,** 160401. doi:`10.1103/PhysRevLett.97.160401` (2006).

40. Rahi, S. J., Kardar, M. & Emig, T. Constraints on Stable Equilibria with Fluctuation-Induced (Casimir) Forces. *Phys. Rev. Lett.* **105,** 070404. doi:`10.1103/PhysRevLett.105.070404` (2010).

41. Rodriguez, A. W. *et al.* Nontouching Nanoparticle Diclusters Bound by Repulsive and Attractive Casimir Forces. *Phys. Rev. Lett.* **104,** 160402. doi:`10.1103/PhysRevLett.104.160402` (2010).

42. Rodriguez, A. W. *et al.* Achieving a Strongly Temperature-Dependent Casimir Effect. *Phys. Rev. Lett.* **105,** 060401. doi:`10.1103/PhysRevLett.105.060401` (2010).

43. Boyer, T. H. Van der Waals forces and zero-point energy for dielectric and permeable materials. *Phys. Rev. A* **9,** 2078–2084. doi:`10.1103/PhysRevA.9.2078` (1974).

44. Rosa, F. S. S., Dalvit, D. A. R. & Milonni, P. W. Casimir-Lifshitz Theory and Metamaterials. *Phys. Rev. Lett.* **100,** 183602. doi:`10.1103/PhysRevLett.100.183602` (2008).

45. Yannopapas, V. & Vitanov, N. V. First-Principles Study of Casimir Repulsion in Metamaterials. *Phys. Rev. Lett.* **103,** 120401. doi:`10.1103/PhysRevLett.103.120401` (2009).

46. Zhao, R., Zhou, J., Koschny, T., Economou, E. N. & Soukoulis, C. M. Repulsive Casimir Force in Chiral Metamaterials. *Phys. Rev. Lett.* **103,** 103602. doi:`10.1103/PhysRevLett.103.103602` (2009).

47. Grushin, A. G. & Cortijo, A. Tunable Casimir Repulsion with Three-Dimensional Topological Insulators. *Phys. Rev. Lett.* **106,** 020403. doi:`10.1103/PhysRevLett.106.020403` (2011).

48. Grushin, A. G., Rodriguez-Lopez, P. & Cortijo, A. Effect of finite temperature and uniaxial anisotropy on the Casimir effect with three-dimensional topological insulators. *Phys. Rev. B* **84,** 045119. doi:`10.1103/PhysRevB.84.045119` (2011).

49. Rodriguez-Lopez, P. Casimir repulsion between topological insulators in the diluted regime. *Phys. Rev. B* **84,** 165409. doi:`10.1103/PhysRevB.84.165409` (2011).

50. Nie, W., Zeng, R., Lan, Y. & Zhu, S. Casimir force between topological insulator slabs. *Phys. Rev. B* **88,** 085421. doi:`10.1103/PhysRevB.88.085421` (2013).
51. Rodriguez-Lopez, P. & Grushin, A. G. Repulsive Casimir Effect with Chern Insulators. *Phys. Rev. Lett.* **112,** 056804. doi:`10.1103/PhysRevLett.112.056804` (2014).
52. Fuchs, S. *et al.* Casimir-Lifshitz force for nonreciprocal media and applications to photonic topological insulators. *Phys. Rev. A* **96,** 062505. doi:`10.1103/PhysRevA.96.062505` (2017).
53. Wilson, J. H., Allocca, A. A. & Galitski, V. Repulsive Casimir force between Weyl semimetals. *Phys. Rev. B* **91,** 235115. doi:`10.1103/PhysRevB.91.235115` (2015).
54. Ema, Y., Hazumi, M., Iizuka, H., Mukaida, K. & Nakayama, K. Zero Casimir force in axion electrodynamics and the search for a new force. *Phys. Rev. D* **108,** 016009. doi:`10.1103/PhysRevD.108.016009` (2023).
55. Pappakrishnan, V. K., Mundru, P. C. & Genov, D. A. Repulsive Casimir force in magnetodielectric plate configurations. *Phys. Rev. B* **89,** 045430. doi:`10.1103/PhysRevB.89.045430` (2014).
56. Rode, S., Bennett, R. & Buhmann, S. Y. Casimir effect for perfect electromagnetic conductors (PEMCs): a sum rule for attractive/ repulsive forces. *New J. Phys.* **20,** 043024. doi:`10.1088/1367-2630/aaaa44` (2018).
57. Li, Y., Zhou, L.-M. & Zhao, N. Anomalous motion of a particle levitated by Laguerre–Gaussian beams. *Opt. Lett.* **46,** 106–109. doi:`10.1364/OL.405696` (2021).
58. Ether, D. S. *et al.* Double-layer force suppression between charged microspheres. *Phys. Rev. E* **97,** 022611. doi:`10.1103/PhysRevE.97.022611` (2018).
59. Hartmann, M., Ingold, G.-L. & Maia Neto, P. A. Advancing numerics for the Casimir effect to experimentally relevant aspect ratios. *Phys. Scr.* **93,** 114003. doi:`10.1088/1402-4896/aae34e` (2018).
60. G. Volpe et al. Roadmap for optical tweezers. *J. Phys. Photonics* **5,** 022501. doi:`10.1088/2515-7647/acb57b` (2023).
61. Ashkin, A., Dziedzic, J. M., Bjorkholm, J. E. & Chu, S. Observation of a single-beam gradient force optical trap for dielectric particles. *Opt. Lett.* **11,** 288–290. doi:`10.1364/OL.11.000288` (1986).
62. Bustamante, C. J., Chemla, Y. R., Liu, S. & Wang, M. D. Optical tweezers in single-molecule biophysics. *Nat. Rev. Methods Primers* **1,** 25. doi:`10.1038/s43586-021-00021-6` (2021).
63. Otte, E. & Denz, C. Optical trapping gets structure: Structured light for advanced optical manipulation. *Appl. Phys. Rev.* **7,** 041308. doi:`10.1063/5.0013276` (2020).
64. Yang, Y., Ren, Y., Chen, M., Arita, Y. & Rosales-Guzmán, C. Optical trapping with structured light: a review. *Adv. Photon.* **3,** 034001. doi:`10.1117/1.AP.3.3.034001` (2021).
65. Forbes, A., de Oliveira, M. & Dennis, M. R. Structured light. *Nat. Photonics* **15,** 253–262 (2021).
66. Curtis, J. E. & Grier, D. G. Structure of Optical Vortices. *Phys. Rev. Lett.* **90,** 133901. doi:`10.1103/PhysRevLett.90.133901` (2003).

67. Zhao, Y., Edgar, J. S., Jeffries, G. D. M., McGloin, D. & Chiu, D. T. Spin-to-Orbital Angular Momentum Conversion in a Strongly Focused Optical Beam. *Phys. Rev. Lett.* **99,** 073901. doi:`10.1103/PhysRevLett.99.073901` (2007).
68. Simpson, N. B., Dholakia, K., Allen, L. & Padgett, M. J. Mechanical equivalence of spin and orbital angular momentum of light - an optical spanner. *Opt. Lett.* **22,** 52–54. doi:`10.1364/OL.22.000052` (1997).
69. Padgett, M. & Leach, J. in *Structured Light and Its Applications* (ed ANDREWS, D. L.) 237–248 (Academic Press, Burlington, 2008). ISBN: 978-0-12-374027-4. doi:`10.1016/B978-0-12-374027-4.00009-8`.
70. Silva, P. D. S., Casana, R. & Ferreira, M. M. Symmetric and antisymmetric constitutive tensors for bi-isotropic and bi-anisotropic media. *Phys. Rev. A* **106,** 042205. doi:`10.1103/PhysRevA.106.042205` (2022).
71. Jackson, J. D. *Classical electrodynamics* Third edition. ISBN: 9781119770763 (Wiley, Singapore, 2021).
72. Glauber, R. J. & Lewenstein, M. Quantum optics of dielectric media. *Phys. Rev. A* **43,** 467–491. doi:`10.1103/PhysRevA.43.467` (1991).
73. Philbin, T. G. Canonical quantization of macroscopic electromagnetism. *New J. Phys.* **12,** 123008. doi:`10.1088/1367-2630/12/12/123008` (2010).
74. Tellegen, B. D. H. The gyrator, a new electric network element. *Philips Res. Rep.* **3,** 81–101 (1948).
75. Kong, J. A. Theorems of bianisotropic media. *Proc. IEEE* **60,** 1036–1046. doi:`10.1109/PROC.1972.8851` (1972).
76. Buhmann, S. Y., Butcher, D. T. & Scheel, S. Macroscopic quantum electrodynamics in nonlocal and nonreciprocal media. *New J. Phys.* **14,** 083034. doi:`10.1088/1367-2630/14/8/083034` (2012).
77. Caloz, C. *et al.* Electromagnetic Nonreciprocity. *Phys. Rev. Appl.* **10,** 047001. doi:`10.1103/PhysRevApplied.10.047001` (2018).
78. Lindell, I. V. & Sihvola, A. H. Perfect Electromagnetic Conductor. *J. Electromagn. Waves Appl.* **19,** 861–869. doi:`10.1163/156939305775468741` (2005).
79. Bohren, C. F. Light scattering by an optically active sphere. *Chem. Phys. Lett.* **29,** 458–462. doi:`10.1016/0009-2614(74)85144-4` (1974).
80. Bohren, C. F. & Huffman, D. R. *Absorption and Scattering of Light by Small Particles* Chap. 4. ISBN: 978-0-471-29340-8. doi:`10.1002/9783527618156` (Wiley-VCH, Weinheim, 2004).
81. Intravaia, F. How Modes Shape Casimir Physics. *International Journal of Modern Physics A* **37,** 2241014. doi:`10.1142/S0217751X22410147` (2022).
82. Krüger, M., Bimonte, G., Emig, T. & Kardar, M. Trace formulas for nonequilibrium Casimir interactions, heat radiation, and heat transfer for arbitrary objects. *Phys. Rev. B* **86,** 115423. doi:`10.1103/PhysRevB.86.115423` (2012).

83. Reid, M. T. H., White, J. & Johnson, S. G. Fluctuating surface currents: An algorithm for efficient prediction of Casimir interactions among arbitrary materials in arbitrary geometries. *Phys. Rev. A* **88,** 022514. doi:`10.1103/PhysRevA.88.022514` (2013).

84. Landau, L. D. & Lifshitz, E. M. *Electrodynamics of Continuous Media* ISBN: 0-08-030276-9 (Pergamon Press, Qxford, 1984).

85. Guérout, R., Ingold, G.-L., Lambrecht, A. & Reynaud, S. Accounting for Dissipation in the Scattering Approach to the Casimir Energy. *Symmetry* **10,** 37. doi:`10.3390/sym10020037` (2018).

86. Bimonte, G., Emig, T., Kardar, M. & Krüger, M. Nonequilibrium Fluctuational Quantum Electrodynamics: Heat Radiation, Heat Transfer, and Force. *Annu. Rev. Condens. Matter Phys.* **8,** 119–143. doi:`10.1146/annurev-conmatphys-031016-025203` (2017).

87. Landau, L. D. & Lifshitz, E. M. *Electrodynamics of Continuous Media* (Pergamon Press, Oxford, 1963).

88. Agarwal, G. S. Quantum electrodynamics in the presence of dielectrics and conductors. I. Electromagnetic-field response functions and black-body fluctuations in finite geometries. *Phys. Rev. A* **11,** 230–242. doi:`10.1103/PhysRevA.11.230` (1975).

89. Venkataram, P. S., Hermann, J., Tkatchenko, A. & Rodriguez, A. W. Fluctuational electrodynamics in atomic and macroscopic systems: van der Waals interactions and radiative heat transfer. *Phys. Rev. B* **102,** 085403. doi:`10.1103/PhysRevB.102.085403` (2020).

90. Lippmann, B. A. & Schwinger, J. Variational Principles for Scattering Processes. I. *Phys. Rev.* **79,** 469–480. doi:`10.1103/PhysRev.79.469` (1950).

91. Guérout, R., Lambrecht, A., Milton, K. A. & Reynaud, S. Derivation of the Lifshitz-Matsubara sum formula for the Casimir pressure between metallic plane mirrors. *Phys. Rev. E* **90,** 042125. doi:`10.1103/PhysRevE.90.042125` (2014).

92. Minkowski, H. Die Grundgleichungen für die elektromagnetischen Vorgänge in bewegten Körpern. *Math. Ann.* **68,** 472–525 (1910).

93. Brevik, I. Experiments in phenomenological electrodynamics and the electromagnetic energy-momentum tensor. *Phys. Rep.* **52,** 133–201. doi:`10.1016/0370-1573(79)90074-7` (1979).

94. Nieto-Vesperinas, M. & Xu, X. The complex Maxwell stress tensor theorem: The imaginary stress tensor and the reactive strength of orbital momentum. A novel scenery underlying electromagnetic optical forces. *Light Sci. Appl.* **11,** 297. doi:`10.1038/s41377-022-00979-2` (2022).

95. Nieto-Vesperinas, M. *Scattering and Diffraction in Physical Optics* 2nd. doi:`10.1142/5833` (World Scientific, 2006).

96. Santos, F. C., Passos Sobrinho, J. J. & Tort, A. C. Electromagnetic field correlators, Maxwell stress tensor, and the Casimir effect for parallel walls. *Braz. J. Phys.* **35,** 657–666. doi:`10.1590/S0103-97332005000400013` (2005).

97. Canaguier-Durand, A. *Multipolar scattering expansion for the Casimir effect in the sphere-plane geometry* PhD thesis (Pierre and Marie Curie University, 2011).

98. Varshalovich, D., Moskalev, A. & Khersonskii, V. *Quantum Theory of Angular Momentum* (World Scientific, 1988).
99. Afonin, A. A., Godlevskaya, A. N., Kapshai, V. N. & Serdyukov, A. N. Spherical electromagnetic waves and quantization of an electro-magnetic field in a naturally gyrotropic medium. *J. Appl. Spectrosc.* **45,** 877–881. doi:`10.1007/BF00657478` (1986).
100. Ji, J.-Y., Lee, C.-W., Noh, J. & Jhe, W. Quantum electromagnetic fields in the presence of a dielectric microsphere. *J. Phys. B: At. Mol. Opt. Phys.* **33,** 4821. doi:`10.1088/0953-4075/33/21/324` (2000).
101. Schoger, T., Spreng, B., Ingold, G.-L. & Maia Neto, P. A. Casimir effect between spherical objects: Proximity-force approximation and beyond using plane waves. *Int. J. Mod. Phys. A* **37,** 2241009. doi:`10.1142/S0217751X22410093` (2022).
102. Shanker, B. & Lakhtakia, A. Scattering of Beltrami fields by anisotropic impedance spheres. *Electromagnetics* **12,** 217–229. doi:`10.1080/02726349208908312` (1992).
103. Athanasiadis, C., Costakis, G. & Stratis, I. On some properties of Beltrami fields in chiral media. *Rep. Math. Phys.* **45,** 257–271. doi:`10.1016/S0034-4877(00)89036-9` (2000).
104. Nussenzveig, H. M. *Diffraction Effects in Semiclassical Scattering* isbn: 0-521-38318-8 (Cambridge University Press, Cambridge, 1992).
105. Lentz, W. J. Generating Bessel functions in Mie scattering calculations using continued fractions. *Appl. Opt.* **15,** 668–671. doi:`10.1364/AO.15.000668` (1976).
106. Canaguier-Durand, A., Maia Neto, P. A., Lambrecht, A. & Reynaud, S. Thermal Casimir effect for Drude metals in the plane-sphere geometry. *Phys. Rev. A* **82,** 012511. doi:`10.1103/PhysRevA.82.012511` (2010).
107. Messina, R., Maia Neto, P. A., Guizal, B. & Antezza, M. Casimir interaction between a sphere and a grating. *Phys. Rev. A* **92,** 062504. doi:`10.1103/PhysRevA.92.062504` (2015).
108. Van de Hulst, H. C. *Light Scattering by Small Particles* Chap. 12. isbn: 978-0-486-64228-4 (Dover Publications, New York, 1981).
109. Spreng, B. *Plane-wave approach to the Casimir interaction between colloid particles* PhD thesis (Universität Augsburg, 2021).
110. Abbe, E. Beiträge zur Theorie des Mikroskops und der mikroskopischen Wahrnehmung. *Archiv f. mikrosk. Anatomie* **9,** 413–468 (1873).
111. Barton, J. P., Alexander, D. R. & Schaub, S. A. Theoretical determination of net radiation force and torque for a spherical particle illuminated by a focused laser beam. *J. Appl. Phys.* **66,** 4594–4602. doi:`10.1063/1.343813` (1989).
112. Lax, M., Louisell, W. H. & McKnight, W. B. From Maxwell to paraxial wave optics. *Phys. Rev. A* **11,** 1365–1370. doi:`10.1103/PhysRevA.11.1365` (1975).
113. Quabis, S., Dorn, R., Eberler, M., Glöckl, O. & Leuchs, G. Focusing light to a tighter spot. *Opt. Commun.* **179,** 1–7. doi:`10.1016/S0030-4018(99)00729-4` (2000).
114. Stratton, J. A. & Chu, L. J. Diffraction Theory of Electromagnetic Waves. *Phys. Rev.* **56,** 99–107. doi:`10.1103/PhysRev.56.99` (1939).

115. Richards, B. & Wolf, E. Electromagnetic diffraction in optical systems, II. Structure of the image field in an aplanatic system. *Proc. R. Soc. Lond. Ser. A* **253,** 358–379. doi:`10.1098/rspa.1959.0200` (1959).

116. Viana, N. B. *et al.* Towards absolute calibration of optical tweezers. *Phys. Rev. E* **75,** 021914. doi:`10.1103/PhysRevE.75.021914` (2007).

117. Dutra, R. S., Viana, N. B., Maia Neto, P. A. & Nussenzveig, H. M. Absolute calibration of forces in optical tweezers. *Phys. Rev. A* **90,** 013825. doi:`10.1103/PhysRevA.90.013825` (2014).

118. Monteiro, P. B., Maia Neto, P. A. & Nussenzveig, H. M. Angular momentum of focused beams: Beyond the paraxial approximation. *Phys. Rev. A* **79,** 033830. doi:`10.1103/PhysRevA.79.033830` (2009).

119. Goubau, G. & Schwering, F. On the guided propagation of electromagnetic wave beams. *IRE Trans. Antennas Propag.* **9,** 248–256. doi:`10.1109/TAP.1961.1144999` (1961).

120. Seghilani, M. S. *et al.* Vortex Laser based on III-V semiconductor metasurface: direct generation of coherent Laguerre-Gauss modes carrying controlled orbital angular momentum. *Sci. Rep.* **6,** 38156. doi:`10.1038/srep38156` (2016).

121. Wolf, E. Electromagnetic Diffraction in Optical Systems. I. An Integral Representation of the Image Field. *Proc. R. Soc. Lond. A. Math. Phys. Sci.* **253,** 349–357 (1959).

122. Wolf, E. & Li, Y. Conditions for the validity of the Debye integral representation of focused fields. *Opt. Commun.* **39,** 205–210. doi:`10.1016/0030-4018(81)90107-3` (1981).

123. Neves, A. A. R. & Cesar, C. L. Analytical calculation of optical forces on spherical particles in optical tweezers: tutorial. *J. Opt. Soc. Am. B* **36,** 1525–1537. doi:`10.1364/JOSAB.36.001525` (2019).

124. Collins, S. A. Lens-System Diffraction Integral Written in Terms of Matrix Optics. *J. Opt. Soc. Am.* **60,** 1168–1177. doi:`10.1364/JOSA.60.001168` (1970).

125. Zhi-Ming, Z., Ji-Xiong, P. & Xi-Qing, W. Tight Focusing of Radially and Azimuthally Polarized Vortex Beams through a Dielectric Interface. *Chin. Phys. Lett.* **25,** 1664. doi:`10.1088/0256-307X/25/5/039` (2008).

126. Kim, J., Wang, Y. & Zhang, X. Calculation of vectorial diffraction in optical systems. *J. Opt. Soc. Am. A* **35,** 526–535. doi:`10.1364/JOSAA.35.000526` (2018).

127. Ranasinghesagara, J. C., Potma, E. O. & Venugopalan, V. Modeling nonlinear optical microscopy in scattering media, part I. Propagation from lens to focal volume: tutorial. *J. Opt. Soc. Am. A* **40,** 867–882. doi:`10.1364/JOSAA.478712` (2023).

128. Novotny, L. & Hecht, B. *Principles of Nano-Optics* 2nd ed. (Cambridge University Press, 2012).

129. Dutra, R. S., Viana, N. B., Maia Neto, P. A. & Nussenzveig, H. M. Absolute calibration of optical tweezers including aberrations. *Appl. Phys. Lett.* **100,** 131115. doi:`10.1063/1.3699273` (2012).

130. Neves, A. A. R. *et al.* Axial optical trapping efficiency through a dielectric interface. *Phys. Rev. E* **76,** 061917. doi:`10.1103/PhysRevE.76.061917` (2007).

131. Török, P., Varga, P., Laczik, Z. & Booker, G. R. Electromagnetic diffraction of light focused through a planar interface between materials of mismatched refractive indices: an integral representation. *J. Opt. Soc. Am. A* **12,** 325–332. doi:`10.1364/JOSAA.12.000325` (1995).

132. Abbe Hon., E. VII.—On the Estimation of Aperture in the Microscope. *J. R. Microsc. Soc.* **1,** 388–423. doi:`10.1111/j.1365-2818.1881.tb05909.x` (1881).

133. Mazolli, A., Maia Neto, P. A. & Nussenzveig, H. M. Theory of Trapping Forces in Optical Tweezers. *Proc. R. Soc. London Ser. A* **459,** 3021–3041 (2003).

134. Maheu, B., Gouesbet, G. & Grehan, G. A concise presentation of the generalized Lorenz-Mie theory for arbitrary location of the scatterer in an arbitrary incident profile. *J. Opt.* **19,** 59. doi:`10.1088/0150-536X/19/2/002` (1988).

135. Neves, A. A. R. & Cesar, C. L. Analytical calculation of optical forces on spherical particles in optical tweezers: tutorial. *J. Opt. Soc. Am. B* **36,** 1525–1537. doi:`10.1364/JOSAB.36.001525` (2019).

136. Schoger, T. *Influence of light reverberation on optical tweezers* mastersthesis (Universität Augsburg, 2019).

137. De Sousa Dutra, R. *Parametrizando uma Pinça Otica: Efeitos de Aberraçoes e Absorçao* PhD thesis (UFRJ, 2011).

138. Harada, Y. & Asakura, T. Radiation forces on a dielectric sphere in the Rayleigh scattering regime. *Opt. Commun.* **124,** 529–541. doi:`10.1016/0030-4018(95)00753-9` (1996).

139. Gussgard, R., Lindmo, T. & Brevik, I. Calculation of the trapping force in a strongly focused laser beam. *J. Opt. Soc. Am. B* **9,** 1922–1930. doi:`10.1364/JOSAB.9.001922` (1992).

140. Lakhtakia, A., Varadan, V. K. & Varadan, V. V. Scattering and absorption characteristics of lossy dielectric, chiral, nonspherical objects. *Appl. Opt.* **24,** 4146–4154. doi:`10.1364/AO.24.004146` (1985).

141. Ashkin, A. Forces of a single-beam gradient laser trap on a dielectric sphere in the ray optics regime. *Biophys. J.* **61,** 569–582. doi:`10.1016/S0006-3495(92)81860-X` (1992).

142. Diniz, K. *et al.* Negative optical torque on a microsphere in optical tweezers. *Opt. Express* **27,** 5905–5917. doi:`10.1364/OE.27.005905` (2019).

143. Harris, C. R. *et al.* Array programming with NumPy. *Nature* **585,** 357–362. doi:`10.1038/s41586-020-2649-2` (2020).

144. Virtanen, P. *et al.* SciPy 1.0: Fundamental Algorithms for Scientific Computing in Python. *Nature Methods* **17,** 261–272. doi:`10.1038/s41592-019-0686-2` (2020).

145. Lam, S. K., Pitrou, A. & Seibert, S. *Numba: a LLVM-based Python JIT compiler* in *Proceedings of the Second Workshop on the LLVM Compiler Infrastructure in HPC* (Association for Computing Machinery, Austin, Texas, 2015). ISBN: 9781450340052. doi:`10.1145/2833157.2833162`.

146. Nieminen, T. A., Stilgoe, A. B., Heckenberg, N. R. & Rubinsztein-Dunlop, H. Angular momentum of a strongly focused Gaussian beam. *J. Opt. A: Pure Appl. Opt.* **10,** 115005. doi:`10.1088/1464-4258/10/11/115005` (2008).

147. Yu, H. & She, W. Radiation torques exerted on a sphere by focused Laguerre-Gaussian beams. *Phys. Rev. A* **92,** 023844. doi:`10.1103/PhysRevA.92.023844` (2015).

148. Ganic, D., Gan, X. & Gu, M. Focusing of doughnut laser beams by a high numerical-aperture objective in free space. *Opt. Express* **11,** 2747–2752. doi:`10.1364/OE.11.002747` (2003).

149. Zhou, L.-M., Xiao, K.-W., Chen, J. & Zhao, N. Optical levitation of nanodiamonds by doughnut beams in vacuum. *Laser Photon. Rev.* **11,** 1600284. doi:`10.1002/lpor.201600284` (2017).

150. Zhang, X., Qiu, J., Li, X., Zhao, J. & Liu, L. Complex refractive indices measurements of polymers in visible and near-infrared bands. *Appl. Opt.* **59,** 2337–2344. doi:`10.1364/AO.383831` (2020).

151. Daimon, M. & Masumura, A. Measurement of the refractive index of distilled water from the near-infrared region to the ultraviolet region. *Appl. Opt.* **46,** 3811–3820. doi:`10.1364/AO.46.003811` (2007).

152. Fonseca, A. L. *et al.* Tailoring bistability in optical tweezers with vortex beams and spherical aberration. *arXiv:2311.04737* (2023).

153. Diniz, K. *et al.* Precise in situ radius measurement of individual optically trapped microspheres using negative optical torque exerted by focused vortex beams. *arXiv:2312.17332* (2023).

154. Maia Neto, P. A. & Nussenzveig, H. M. Theory of optical tweezers. *Europhys. Lett.* **50,** 702. doi:`10.1209/epl/i2000-00327-4` (2000).

155. Zhang, J., Albelda, M. T., Liu, Y. & Canary, J. W. Chiral nanotechnology. *Chirality* **17,** 404–420. doi:`10.1002/chir.20178` (2005).

156. Mun, J. *et al.* Electromagnetic chirality: from fundamentals to nontraditional chiroptical phenomena. *Light Sci. Appl.* **9,** 139. doi:`10.1038/s41377-020-00367-8` (2020).

157. Genet, C. Chiral Light–Chiral Matter Interactions: an Optical Force Perspective. *ACS Photonics* **9,** 319–332. doi:`10.1021/acsphotonics.1c01130` (2022).

158. Ali, R., Pinheiro, F. A., Dutra, R. S., Rosa, F. S. S. & Maia Neto, P. A. Enantioselective manipulation of single chiral nanoparticles using optical tweezers. *Nanoscale* **12,** 5031–5037. doi:`10.1039/C9NR09736H` (2020).

159. Ali, R., Pinheiro, F. A., Dutra, R. S., Rosa, F. S. S. & Maia Neto, P. A. Probing the optical chiral response of single nanoparticles with optical tweezers. *J. Opt. Soc. Am. B* **37,** 2796–2803. doi:`10.1364/JOSAB.398934` (2020).

160. Li, M., Yan, S., Zhang, Y., Chen, X. & Yao, B. Optical separation and discrimination of chiral particles by vector beams with orbital angular momentum. *Nanoscale Adv.* **3,** 6897–6902. doi:`10.1039/D1NA00530H` (2021).

161. Zhan, Q. Cylindrical vector beams: from mathematical concepts to applications. *Adv. Opt. Photon.* **1,** 1–57. doi:`10.1364/AOP.1.000001` (2009).

162. Pecora, R. Dynamic Light Scattering Measurement of Nanometer Particles in Liquids. *J. Nanoparticle Res.* **2,** 123–131. doi:`10.1023/A:1010067107182` (2000).

163. Yevick, A., Hannel, M. & Grier, D. G. Machine-learning approach to holographic particle characterization. *Opt. Express* **22,** 26884–26890. doi:`10.1364/OE.22.026884` (2014).

164. Midtvedt, B. *et al.* Fast and Accurate Nanoparticle Characterization Using Deep-Learning-Enhanced Off-Axis Holography. *ACS Nano* **15,** 2240–2250. doi:`10.1021/acsnano.0c06902` (2021).

165. Altman, L. E. & Grier, D. G. Machine learning enables precise holographic characterization of colloidal materials in real time. *Soft Matter* **19,** 3002–3014. doi:`10.1039/D2SM01283A` (2023).

166. Malagnino, N., Pesce, G., Sasso, A. & Arimondo, E. Measurements of trapping efficiency and stiffness in optical tweezers. *Opt. Commun.* **214,** 15–24. doi:`10.1016/S0030-4018(02)02119-3` (2002).

167. Pedregosa, F. *et al.* Scikit-learn: Machine Learning in Python. *J. Mach. Learn. Res.* **12,** 2825–2830 (2011).

168. Dembinski, H. & et al., P. O. *scikit-hep/iminuit* 2020. doi:`10.5281/zenodo.3949207`.

169. Hartmann, M., Ingold, G.-L. & Maia Neto, P. A. Plasma versus Drude Modeling of the Casimir Force: Beyond the Proximity Force Approximation. *Phys. Rev. Lett.* **119,** 043901. doi:`10.1103/PhysRevLett.119.043901` (2017).

170. Bimonte, G. Classical Casimir interaction of a perfectly conducting sphere and plate. *Phys. Rev. D* **95,** 065004. doi:`10.1103/PhysRevD.95.065004` (2017).

171. Spreng, B., Maia Neto, P. A. & Ingold, G.-L. Plane-wave approach to the exact van der Waals interaction between colloid particles. *J. Chem. Phys.* **153,** 024115. doi:`10.1063/5.0011368` (2020).

172. Klich, I. & Kenneth, O. Casimir effect: The TGTG formula. *J. Phys.: Conf. Ser.* **161,** 012020. doi:`10.1088/1742-6596/161/1/012020` (2009).

173. Maghrebi, M. F. Diagrammatic expansion of the Casimir energy in multiple reflections: Theory and applications. *Phys. Rev. D* **83,** 045004. doi:`10.1103/PhysRevD.83.045004` (2011).

174. Zandi, R., Emig, T. & Mohideen, U. Quantum and thermal Casimir interaction between a sphere and a plate: Comparison of Drude and plasma models. *Phys. Rev. B* **81,** 195423. doi:`10.1103/PhysRevB.81.195423` (2010).

175. Umrath, S., Hartmann, M., Ingold, G.-L. & Maia Neto, P. A. Disentangling geometric and dissipative origins of negative Casimir entropies. *Phys. Rev. E* **92,** 042125. doi:`10.1103/PhysRevE.92.042125` (2015).

176. Stein, S. Addition theorems for spherical wave functions. *Q. Appl. Math.* **19,** 15–24 (1961).

177. Schoger, T. & Ingold, G.-L. Classical Casimir free energy for two Drude spheres of arbitrary radii: A plane-wave approach. *SciPost Phys. Core* **4,** 011. doi:`10.21468/SciPostPhysCore.4.2.011` (2021).

178. Schoger, T. *et al.* Universal Casimir interactions in the sphere–sphere geometry. *Int. J. Mod. Phys. A* **37,** 2241005. doi:`10.1142/S0217751X22410056` (2022).

179. Schoger, T., Spreng, B., Ingold, G.-L., Maia Neto, P. A. & Reynaud, S. Universal Casimir Interaction between Two Dielectric Spheres in Salted Water. *Phys. Rev. Lett.* **128,** 230602. doi:`10.1103/PhysRevLett.128.230602` (2022).

180. Sauer, F. *Die Temperaturabhängigkeit von Dispersionskräften* German. PhD thesis (Universität Göttingen, 1962).
181. Mehra, J. Temperature correction to the Casimir effect. *Physica* **37,** 145–152. doi:`10.1016/0031-8914(67)90115-2` (1967).
182. Bimonte, G. Beyond-proximity-force-approximation Casimir force between two spheres at finite temperature. *Phys. Rev. D* **97,** 085011. doi:`10.1103/PhysRevD.97.085011` (2018).
183. Molinari, L. Transfer matrices and tridiagonal-block Hamiltonians with periodic and scattering boundary conditions. *J. Phys. A: Math. Gen.* **30,** 983–997. doi:`10.1088/0305-4470/30/3/021` (1997).
184. Molinari, L. G. Determinants of block tridiagonal matrices. *Linear Algebra Appl.* **429,** 2221–2226. doi:`10.1016/j.laa.2008.06.015` (2008).
185. *NIST Digital Library of Mathematical Functions* http://dlmf.nist.gov/, Release 1.0.28 of 2020-09-15. F. W. J. Olver, A. B. Olde Daalhuis, D. W. Lozier, B. I. Schneider, R. F. Boisvert, C. W. Clark, B. R. Miller, B. V. Saunders, H. S. Cohl, and M. A. McClain, eds.
186. Bromwich, T. J. I. Conformal Space Transformations. *Proc. London Math. Soc.* **s1-33,** 185–192. doi:`10.1112/plms/s1-33.1.185` (1900).
187. Burkhardt, T. W. & Eisenriegler, E. Casimir Interaction of Spheres in a Fluid at the Critical Point. *Phys. Rev. Lett.* **74,** 3189–3192. doi:`10.1103/PhysRevLett.74.3189` (1995).
188. Eisenriegler, E. & Ritschel, U. Casimir forces between spherical particles in a critical fluid and conformal invariance. *Phys. Rev. B* **51,** 13717–13734. doi:`10.1103/PhysRevB.51.13717` (1995).
189. Garvin, M. C. A Generalized Lambert Series. *Am. J. Math.* **58,** 507–513. doi:`10.2307/2370967` (1936).
190. Banerjee, S. & Wilkerson, B. Asymptotic expansions of Lambert series and related q-series. *Int. J. Number Theory* **13,** 2097–2113. doi:`10.1142/S1793042117501135` (2017).
191. Gover, M. J. C. & Barnett, S. Inversion of Toeplitz Matrices which are not Strongly Non-singular. *IMA J. Numer. Anal.* **5,** 101–110. doi:`10.1093/imanum/5.1.101` (1985).
192. Gover, M. J. C. The eigenproblem of a tridiagonal 2-Toeplitz matrix. *Linear Algebr. Appl.* **197-198,** 63–78. doi:`10.1016/0024-3795(94)90481-2` (1994).
193. Kilic, E. & Arikan, T. Evaluation of Hessenberg Determinants via Generating Function Approach. *Filomat* **31,** 4945–4962. doi:`10.2298/FIL1715945K` (2017).
194. Comtet, L. *Advanced combinatorics* ISBN: 90-277-0380-9 (D. Reidel, Dordrecht, 1974).
195. Port, D. *Polynomial maps with applications to combinatorics and probability theory* PhD thesis (Massachusetts Institute of Technology, 1994).
196. Fosco, C. D., Lombardo, F. C. & Mazzitelli, F. D. Casimir free energy at high temperatures: Grounded versus isolated conductors. *Phys. Rev. D* **93,** 125015. doi:`10.1103/PhysRevD.93.125015` (2016).
197. Maxwell, J. C. *A Treatise on Electricity and Magnetism* §173 (Clarendon Press., Oxford, 1873).

198. Smythe, W. C. *Static and Dynamic Electricity* Chap. 5. isbn: 978-0891169178 (McGraw-Hill, New York, 1950).

199. Balian, R. & Duplantier, B. Electromagnetic waves near perfect conductors. II. Casimir effect. *Ann. Phys. (N.Y.)* **112,** 165–208. doi:`10.1016/0003-4916(78)90083-0` (1978).

200. Wirzba, A. The Casimir effect as a scattering problem. *J. Phys. A: Math. Theor.* **41,** 164003. doi:`10.1088/1751-8113/41/16/164003` (2008).

201. Bitbol, A.-F., Berthoumieux, H., Spreng, B., Maia Neto, P. A. & Reynaud, S. A universal attractive interaction between filaments at the cell scale. arXiv:2304.06006 (2023).

202. Derjaguin, B. Untersuchungen fiber die Reibung und Adh ision, IV. Theorie des Anhaftens kleiner Teilchen. *Kolloid-Z.* **69,** 155–164. doi:`10.1007/BF01433225` (1934).

203. Schaden, M. & Spruch, L. Infinity-free semiclassical evaluation of Casimir effects. *Phys. Rev. A* **58,** 935–953. doi:`10.1103/PhysRevA.58.935` (1998).

204. Jaffe, R. L. & Scardicchio, A. Casimir Effect and Geometric Optics. *Phys. Rev. Lett.* **92,** 070402. doi:`10.1103/PhysRevLett.92.070402` (2004).

205. Hansen, E. R. *A table of series and products* isbn: 0138819386 (Prentice-Hall, Englewood Cliffs, NJ, 1975).

206. Ingold, G.-L. *et al.* Geometric origin of negative Casimir entropies: A scattering-channel analysis. *Phys. Rev. E* **91,** 033203. doi:`10.1103/PhysRevE.91.033203` (2015).

207. Feinberg, G. & Sucher, J. General Form of the Retarded van der Waals Potential. *J. Chem. Phys.* **48,** 3333–3334. doi:`10.1063/1.1669611` (1968).

208. Schoger, T. & Ingold, G.-L. Switching the sign of the Casimir force between two PEMC spheres. arXiv:2401.14738 (2024).

209. Asorey, M. & Muñoz-Castañeda, J. Attractive and repulsive Casimir vacuum energy with general boundary conditions. *Nucl. Phys. B* **874,** 852–876. doi:`10.1016/j.nuclphysb.2013.06.014` (2013).

210. Teo, L. P. Casimir effect between two spheres at small separations. *Phys. Rev. D* **85,** 045027. doi:`10.1103/PhysRevD.85.045027` (2012).

211. Muñoz-Castañeda, J. M., Santamaría-Sanz, L., Donaire, M. & Tello-Fraile, M. Thermal Casimir effect with general boundary conditions. *Eur. Phys. J. C* **80,** 793. doi:`10.1140/epjc/s10052-020-8348-1` (2020).

212. Bimonte, G., Emig, T., Jaffe, R. L. & Kardar, M. Casimir forces beyond the proximity approximation. *Europhys. Lett.* **97,** 50001. doi:`10.1209/0295-5075/97/50001` (2012).

213. Teo, L. P. Material dependence of Casimir interaction between a sphere and a plate: First analytic correction beyond proximity force approximation. *Phys. Rev. D* **88,** 045019. doi:`10.1103/PhysRevD.88.045019` (2013).

214. Rodriguez-Lopez, P. Casimir energy and entropy in the sphere-sphere geometry. *Phys. Rev. B* **84,** 075431. doi:`10.1103/PhysRevB.84.075431` (2011).

215. Pirozhenko, I. G. & Bordag, M. Casimir repulsion in sphere-plate geometry. *Phys. Rev. D* **87,** 085031. doi:`10.1103/PhysRevD.87.085031` (2013).

216. Oosthuyse, T. & Dudal, D. Interplay between chiral media and perfect electromagnetic conductor plates: Repulsive vs. attractive Casimir force transitions. *SciPost Phys.* **15,** 213. doi:`10.21468/SciPostPhys.15.5.213` (2023).

217. Bimonte, G. *et al.* Measurement of the Casimir Force between 0.2 and 8µm: Experimental Procedures and Comparison with Theory. *Universe* **7,** 93. doi:`10.3390/universe7040093` (2021).

218. Meurer, A. *et al.* SymPy: symbolic computing in Python. *PeerJ Computer Science* **3,** e103. doi:`10.7717/peerj-cs.103` (2017).

219. Schafer, R. & Kouyoumjian, R. Higher order terms in the saddle point approximation. *Proc. IEEE* **55,** 1496–1497. doi:`10.1109/PROC.1967.5863` (1967).

220. Wick, G. C. The Evaluation of the Collision Matrix. *Phys. Rev.* **80,** 268–272. doi:`10.1103/PhysRev.80.268` (1950).

221. Lindell, I., Sihvola, A. & Viitanen, A. Reflection and transmission of plane waves at a planar interface between isotropic and bi-isotropic media. *NASA STI/Recon Technical Report N* **92,** 21280 (1991).

List of Abbreviations

PEMC	perfect electromagnetic conductor, see p. 2
PMC	perfect magnetic conductor, see p. 3
PEC	perfect electric conductor, see p. 3
PFA	proximity force approximation, see p. x
PWS	pairwise summation, see p. x
M	magnetic, see p. 12
E	electric, see p. 12
TE	transversal electric, see p. 11
TM	transversal magnetic, see p. 11
inc	incident, see p. 14
out	outgoing, see p. 13
reg	regular, see p. 13
scat	scattered, see p. 14
sp	saddle point, see p. 22
LG	Laguerre-Gaussian, see p. 30
MD	Mie-Debye, see p. 39
MDSA	Mie-Debye Spherical Aberration, see p. 39
MDSA+	Mie-Debye Spherical Aberration + Astigmatism, see p. 39
L	left, see p. 3
R	right, see p. 3
rs	reference surface, see p. 31
eff	effective, see p. 61
dip	dipole, see p. 109
ext	extinction, see p. 35
e	even, see p. 77
o	odd, see p. 77
F	Fresnel plane, see p. 11
S	scattering plane, see p. 18
NTLO	next-to-leading-order, see p. 104
LO	leading-order, see p. 95
rm	rational model, see p. 89
pp	plane-plane, see p. 93

Acknowledgements

First and foremost, I want to thank my supervisor, Gert-Ludwig Ingold, for his supervision and constant support and guidance throughout my academic journey, starting from my Bachelor's thesis in 2017 and continuing through my PhD. I learned a lot from our discussions over the years. I am also very thankful to my supervisor for the numerous opportunities to attend conferences. I am very grateful to Paulo Maia Neto, who introduced me to optical tweezers and with whom I have collaborated since my Master's thesis. I am also grateful for our helpful discussions on Casimir physics. Furthermore, I sincerely thank Serge Reynaud for our interesting discussions on the Casimir effect in biological systems. Special gratitude goes to Benjamin Spreng for his invaluable assistance with numerical results. I am also thankful to Kainã Diniz, Arthur L. Fonseca, Rafael S. Dutra, and Nathan B. Viana from UFRJ for our discussions on the optical tweezers experiment.

I also want to thank Abhinav Sharma and Felipe Siqueira de Souza da Rosa for examining this thesis. Moreover, I would also like to thank all current and former members of the TP1 chair and the current members of the quantum information and quantum computing chair.

Moreover, I'd like to thank the "Frauenbeauftragte der MNTF Augsburg" for their financial support for my attendance at a conference.

Abschließend möchte ich noch meinen Eltern und meinen Bruder für die Unterstützung während meines gesamten Studiums und der Zeit während der Doktorarbeit Danken.